Design, Fabrication and Evaluation of a Label-free Silicon-on-Insulator "Lab on a Chip" Optical Biosensor

Najla Najeeb

Department of Electrical and Electronic Engineering
University of Nottingham

This thesis is submitted for the degree of

Doctor of Philosophy

August 2017

I would like to dedicate this thesis to my loving parents and siblings…

ACKNOWLEDGEMENTS

I am extremely grateful to my supervisors Professor Trevor Benson and Dr. Yaping Zhang for their excellent guidance, kindness and patience during the course of this PhD. As my mentors, they have taught me and provided me with opportunities more than I could ever give them credit for.

I would also like to thank Dr. Chris Mellor for his expert advice and help during the fabrication process. I wish to acknowledge the assistance provided by Dr. Jasbinder Chauhan and Dave in the clean room.

I am grateful for the encouraging discussions with Professor Angela Seddon and the assistance of Dr. David Furniss in the dark room.

I would like to thank Dr. Noah Russell for his help and guidance in the fabrication of the microfluidics for this project.

Many thanks to Professor Paul O' Shea, Dr. John Moses, Dr. Joanna Richens and Dr. Kimberley Powell for their advice and help on the surface functionalisation of silicon.

From the City University of Hong Kong, I wish to thank Professor Edwin Pun and Dr. Polis Wong for the fabrication of biosensors and Dr. Sai Tak Chu and Dr. Alex Chun-Yuen Wong for their collaboration on surface functionalisation.

And I also wish to thank Professor Jun Zhou from Ningbo University, Professor Daoxing Dai and Ming Zhang from Zhejiang University for their fabrication and testing of biosensors.

I would like to thank Professor Graham Reed and Dr. Ali Khokhar from The University of Southampton and Dr. Graham Sharp from The University of Glasgow for the fabrication of biosensors.

Finally, I would like to thank my colleagues in the GGIEMR, Nottingham UK campus and at Nottingham China campus for making this experience memorable.

ABSTRACT

This thesis presents the design, fabrication and testing on a Silicon-on-Insulator (SOI) "lab on a chip" immunosensors based on interferometer technology capable of label-free, real time, parallel detection and identification of multiple analytes with extremely high sensitivity.

The basic principles for the biosensor device are evanescent wave sensing and interferometry. Light is guided through a high index contrast photonic wire by total internal reflection. The high index contrast core-cladding photonic wires supporting a vector TM-like mode can be designed to have extremely high sensing sensitivity for low analyte volumes. The optical field decays rapidly from the surface of the waveguide, penetrating into a test solution by ≈178nm. When a chemical, biochemical or biological reaction takes place in the sensing area, i.e. in the region of the decaying field near the surface, the light propagating through the sensing channel will experience a change in its effective refractive index causing a phase change per unit propagation length. With a reference channel built-in on chip, the resulting phase difference between the sensing and reference channels can be detected with a very high sensitivity of detection.

The first sensor studied consists of Mach-Zehnder interferometers (MZIs) fabricated with silicon photonic wires. For a MZI with a sensing length of 1000µm the theoretical sensitivity is 3.1×10^{-7} Refractive Index Units (RIUs). Sensitivity is further increased by incorporating spiral waveguides to increase the length of the interferometer arms within a given wafer footprint. A spiral of four turns gives a sensing arm length of 3145µm, which takes up an area of $0.06mm^2$ and gives a theoretical MZI sensitivity of 9.9×10^{-8} RIUs. The sensitivity of detection of the biosensors developed is at least 10-100 times more sensitive than that of current commercial products. Parallel detection is achieved by exciting multiple sensors in parallel using a 1xN Multimode interferometer (MMI) where N≤20.

The second sensor considered is a label-free self-aligned Plasmonic Interferometer (PI). The interfering plasmonic modes are excited on either side of a thin gold layer embedded into a silicon photonic wire. Only the mode on the upper surface interacts with the analyte. The resonant wavelength is thus sensitive to the analyte index. The PI designed for this project is 13µm in length and gives a predicted system wavelength shift responsivity of 500nm/RIU.

To guide the way towards the successful design of these sensors commercial software is used to perform detailed simulation evaluations of straight and curved waveguides, Mach Zehnder Interferometers (MZIs), Plasmonic Interferometers (PIs), Multimode interferometers (MMIs), Directional Couplers (DCs), Y-junction splitters and Spot size converters.

So that the proposed biosensors can operate as an immunosensor, two methods of selective surface functionalisation are developed to immobilise the antibodies on to the sensor waveguides. The first method attached a non-uniform layer of amine functional group to surface of silicon via a hydrosilylation process. The second method attached a uniform layer of amine functional group to the surface of silicon dioxide via a hydroxylation and silanisation process. Attaching a fluorescent tag to the amine functional groups allowed the imaging and assessment of the surface modification and selectivity.

Four sets of biosensor devices were fabricated and tested showing promising results.

Publications

[1] **N. Najeeb**, Y. Zhang, C.J. Mellor, D. Furniss, P O'Shea, J. Richens, E.Y.B. Pun, P.W.H. Wong, J.E. Moses, K.J. Powell, T.M. Benson, "Optical interferometric techniques for parallel bio-sensing," in *Biosensors 2014*, Melbourne Australia, 25-31 May 2014.

[2] **N. Najeeb**, Y. Zhang, C. Mellor, and T. Benson, "Photonic biosensor chip for early-stage cancer diagnosis," in *Transparent Optical Networks (ICTON), 2015 17th International Conference on*, 2015, pp. 1-4.

[3] **N. Najeeb**, Y. Zhang, C. Mellor, and T. Benson, "Design, Fabrication and Demonstration of a 1x20 Multimode Interference Splitter for Parallel Biosensing Applications," in *Journal of Physics: Conference Series*, 2016, p. 012027.

Oral Presentations (by the author)

[4] "Label-Free Silicon-on-Insulator "Lab on a chip" Optical Biosensors based on Interferometers," in *Lab-on-a-Chip Asia*, 20-21 November 2014, 20-21 November 2014.

[5] "Design, Fabrication and Demonstration of a 1x20 Multimode Interference Splitter," in *IEEE 8th International Conference on Advanced Infocomm Technology (ICAIT 2015)*, Hangzhou, China, 25-27 October 2015.

TABLE OF CONTENTS

NOMENCLATURE

ROMAN SYMBOLS

$\underline{A}$	An oscillating wave
a	Asymmetry factor
$\underline{B}$	Magnetic flux density
c	Velocity of light in free space
d	Edge to edge distance between two ridge waveguides in a directional coupler
$\underline{D}$	Electric flux density
d_p	Penetration depth of evanescent field
$\underline{E}$	Electric field amplitude
E_i	Incident light ray
E_r	Reflected ray of light
E_t	Transmitted ray of light
g	Egde to egde gap between two ridge waveguides in a slot waveguide
h	Planck's constant
$\underline{H}$	Magnetic field amplitude
h	Height of waveguide
j	Imaginary number
k_0	Free space vector
k_p	wavevector of the plasmon mode
L	Length
L_c	Length of directional coupler for complete power transfer
L_{MMI}	Length of multimode interferometer cavity
m	Mode number
N	Number of outputs of a multimode interferometer
n_1	Refractive index of upper cladding
n_2	Refractive index of propergating medium or core
n_3	Refractive index of lower cladding
n_c	Cover/upper cladding index
n_e	Even supermode effective refractive index

N_{eff}	Effective index
n_o	Odd supermode effective refractive index
P	Position on the S-function curve
P	Poynting vector
P_{lhs}	Left hand side offset from the z-axis
P_{rhs}	Right hand side offset from the z-axis
R	Radius of curvature
R_{min}	Minimum radius of curvature
S	Sensitivity
t	Thickness of adsorbed layer
t	Time
T_L	Taper length
T_w	Taper width
V	Normalised frequency of waveguide
w	width of ridge waveguide
W_{MMI}	Width of multimode interferometer cavity
Z	Length along the z-axis
z_{in}	Initial z value in the z-axis

Greek Symbols

β	Propagation constant
Γ	Confinement factor
Δ	Change/difference
ε	Permittivity
ε_0	Permittivity in a vacuum
ε_d	Complex dielectric constant of a dielectric
ε_m	Complex dielectric constant of a metal film
ε_r	Relative permittivity
ϑ	Angle
ϑ_1	Angle of transmission
ϑ_2	Angle of reflection
ϑ_c	Critical angle
λ_0	Wavelength of light in free space
λ_{UV}	Wavelength of ultraviolet lamp

μ	Permeability
μ_0	Permeability in a vacuum
μ_r	Relative permeability
π	Pi ≈ 3.14142
ρ	Distance between output waveguides
φ	Phase of light
ω	Angular frequency

ACRONYMS/ABBREVIATIONS

APTES	(3-Aminopropyl)triethoxysilane
BPM	Beam Propagation Method
CAD	Computer aided design
Chalc	Chalcogenide
COOH	Carboxyl
EF	Evanescent field
EM	Electromagnetic
EME	Eigenmode expansion
FD-BPM	Finite-difference beam propagation method
FE-BPM	Finite element beam propagation method
FEM	Finite element method
FFT-BPM	Fast Fourier transform beam propagation method
FIR	Far infra-red
FITC	Fluorescein isothiocyanate
GDS	Graphic database system
H	Hydrogen
H_2O_2	Hydrogen peroxide
H_2SO_4	Sulphuric acid
HCl	Hydrochloric acid
HF	Hydrofluoric
ICP	Inductively coupled plasma
LED	Light emitting diode
MIR	Mid infra-red
MMI	Multimode interferometer
MZI	Mach-Zehnder interferometer

NH_2	Amine
NIR	Near infra-red
OH	Hydroxide
PBS	Phosphate buffer solution
PDMS	Polydimethylsiloxane
PEB	Post-exposure bake
POC	Point-of-care
RIE	Reactive ion etching
RIU	Refractive index units
RT	Room temperature
SAM	Self-assembled monolayer
SEM	Scanning electron microscope
Si_3N_4	Silicon nitride
SiH_4	Silane
SiO_2	Silicon dioxide
SOI	Silicon-on-Insulator
SP	Surface plasmon
SPP	Surface plasmon polaritons
SPR	Surface plasmon resonance
SU-8	Glycidyl-ether-bisphenol-A
t-BOC	t-Butyoxycarbonyl
TE	Transverse electric
TFA	Trifluoroacetic acid
TIR	Total internal reflection
TM	Transverse magnetic
UV	Ultraviolet
VLSI	Very large-scale integration

Mathematical Operators and Symbols

δ	Partial differential
$\nabla\cdot$	Divergence operator
$\nabla\times$	Curl operator
∇^2	Laplacian operator
$\perp$	Transverse

Chapter 1

1 INTRODUCTION

In 1956 Leland C Clark Jnr. published a definitive paper on the oxygen electrode known as the Clark electrode [1.1]. This was a visual oxygen sensor that later evolved into an amperometric enzyme electrode for glucose in 1962 [1.2]. An amperometric biosensor measures the motion of electrons (current) during a chemical reaction to determine the approximate concentration of a certain molecule in an analyte such as the concentration of glucose in blood. This simple device founded the field of biosensors which has now brought together research communities from various fields such as VLSI, physics, chemistry and materials science to develop more sophisticated, reliable and mature biosensing devices that make measurements in complex matrices.

This rapidly evolving and expanding global market is expected to reach USD 21.17 billion by the year 2020 and forecasts are that optical biosensors will be the most lucrative technology in the global biosensor market [1.3]. Figure 1.1 displays the global biosensor market segmented by application, technology and end-use.

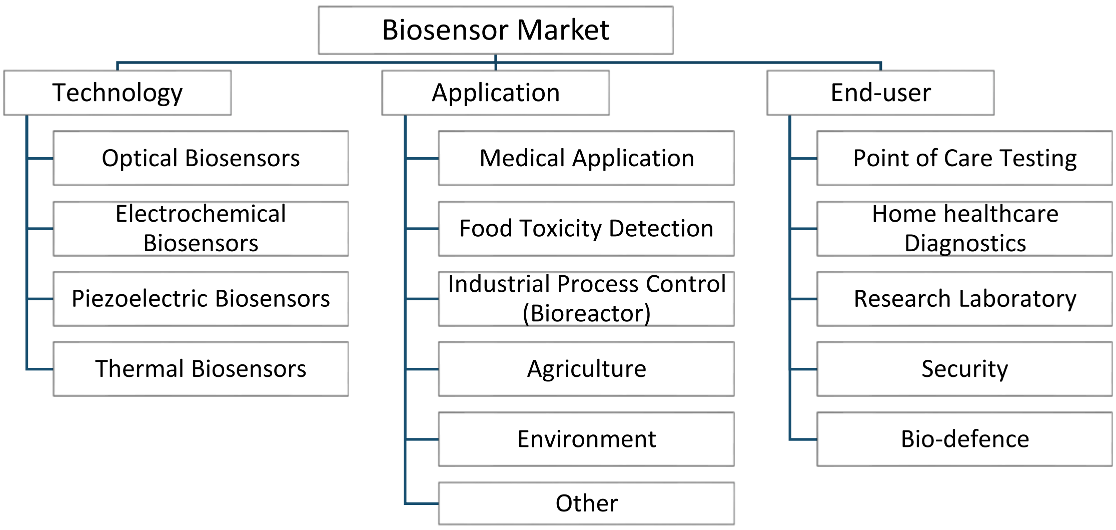

Figure 1.1: Global biosensor market segmented by application, technology and end-use [1.3].

A biosensor is a sensor that converts a chemical or biochemical interaction into a signal that can be displayed or read. Figure 1.2 shows a schematic illustration of the main components of a biosensor.

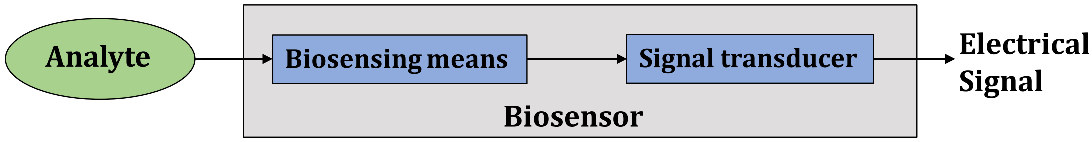

Figure 1.2: Schematic illustration of the main components of a biosensor.

The analyte is a substance that consists of a chemical or pathogen that will be undergoing analysis, such as a blood sample or a contaminated sample of water. The analyte is inserted to the bioreceptor or bioelement layer of the biosensor which can be an enzyme, antibody, nucleic acid, tissue, microbial or polysaccharides. The transducer is the sensor element that detects the interaction between the biorecepter layer and the analyte in the form of a change in electric potential, current, conductance, impedance, intensity and phase change of electromagnetic (EM) radiation, mass, temperature or viscosity.

Biosensors can be classified according to the bioreceptor and transducing system used. A sensor that uses antibodies as a bioreceptor is called an immunosensor and a transducer that measures a change in the propagation of optical radiation is known as an optical biosensor. This project is based on the design and fabrication of an optical Immunosensor where the components of an analyte combine with the antibody and this results in a change in an optical signal. This is explained in more detail below.

1.1 Optical Biosensor

Optical biosensors can be defined as sensor devices which make use of optical principles for the transduction of a biochemical interaction into a suitable output signal. A substantial number of measurements can be made based on emission, absorption, fluorescence, refractometry and polarimetry. Based on the measurements taken optical biosensors can be conveniently categorised into three types; Surface plasmon resonance (SPR), Evanescent Field and Photonic Crystal.

1.1.1 Surface plasmon resonance (SPR) sensor

SPR was first demonstrated by Otto in 1968 [1.4] and modified by Kretschmann [1.5]. The first SPR immunosensors were published in 1983 by Liedberg *et al.* [1.6] and it has been the most common and commercialised optical biosensor since 1990 when it was first commercialised by Biacore [1.7]. SPR occurs when the frequency of an incident wave matches the natural frequency of the oscillating electron on the surface (Surface plasmon waves) of a metal (typically gold or silver) causing a resonance condition. Any molecules on the surface will cause a change in the local refractive index which shifts the resonant condition of the Surface plasmon waves as shown in Figure 1.3 [1.7].

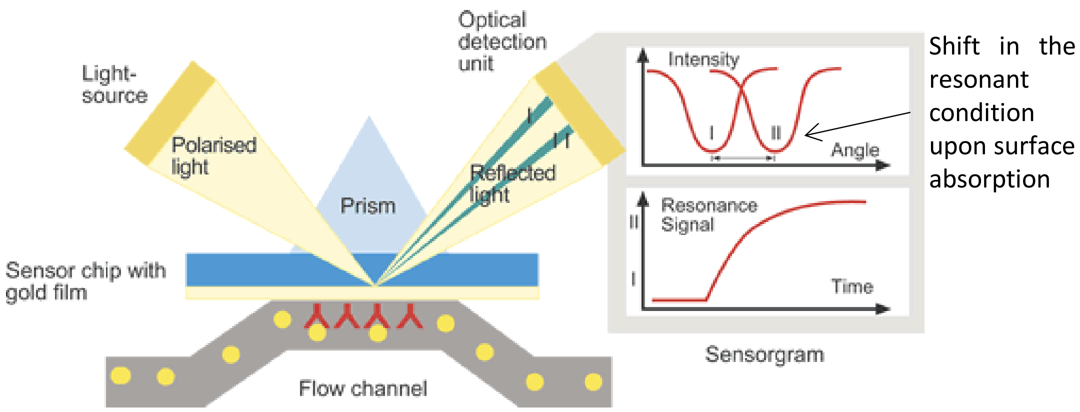

Figure 1.3: Schematic illustration of an SPR measurement system [1.7].

1.1.2 Evanescent field sensors

The evanescent field is the light that decays exponentially outwards from the sensor chip surface as will be explained in Chapter 2. Evanescent field sensors usually operate in interferometry based systems and one of the most common interferometers is the Mach-Zehnder interferometer (MZI) [1.8] whose operation will be explained in more detail in Chapter 2. Other evanescent field based sensors are Young interferometers [1.9, 10] and ring resonators [1.11]. The sensor measures a change in refractive index caused by the interaction of the analyte with the biorecepetor layer. The change in refractive index causes a phase change in the light and a subsequent change in the light intensity measured by a photodetector.

Figure 1.4a shows a MZI with spiral waveguides and Figure 1.4b shows a ring resonator with spiral waveguides. Figure 1.4c is an illustration of the sensor window of an evanescent field sensor showing the target molecules binding to the receptor molecules causing a change in the refractive index of the waveguide surface resulting in a phase shift in the propagating light.

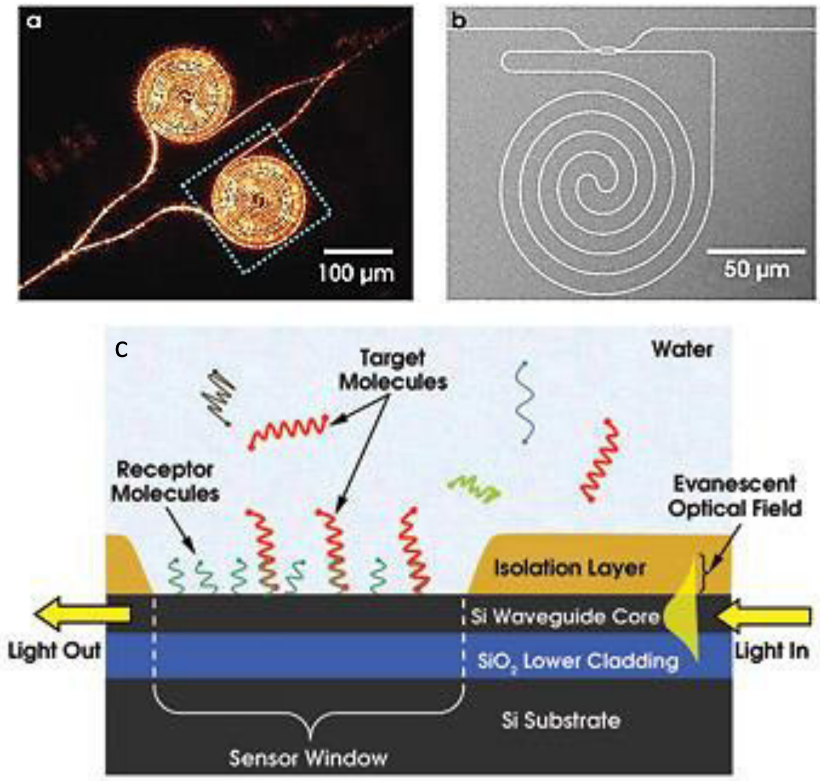

Figure 1.4: a) Infrared image of a MZI with 2mm long spiral waveguides taken while guiding 1550nm light, b) electron microscope (SEM) image of a ring resonator with 1.3mm long spiral waveguides and c) schematic illustration of a sensor window of an evanescent field sensor [1.12].

1.1.3 Photonic crystal sensor

A photonic crystal has periodic microstructures that create photonic band gaps which prevent light travelling through the structure at certain frequencies [1.13]. By introducing defects to the periodic structure certain frequencies of light become resonantly confined within the defects. A change in refractive index caused by the analyte induces a change in the resonant frequency which is then used to analyse the analyte. Figure 1.5 shows a scanning electron microscopy (SEM) image of a typical photonic crystal device, [1.14]

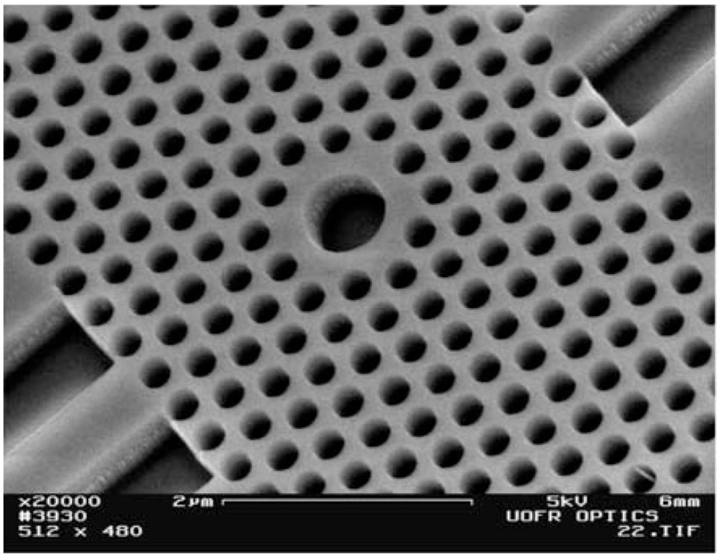

Figure 1.5: Image of a typical Photonic crystal device [1.14].

1.1.4 Performance of optical biosensors

Sensitivity, assay sensitivity and resolution are some of the methods used to compare the performance of optical biosensors.

Sensitivity for optical biosensors is the measure of how efficiently the electromagnetic field couples and changes to biomolecules in contact with the sensor surface [1.15]. For a waveguide based evanescent field sensor, the transducer sensitivity is given in terms of change in effective refractive index (ΔN_{eff}) of the waveguide per change in cover index (Δn_c). $\Delta N_{eff}/\Delta n_c$ represents the sensitivity of the waveguide and is not dependent on the target molecule binding with the antibody or the sensitivity of the detection instruments.

Assay sensitivity is defined at the minimum detectable concentration of an analyte and is defined in units of moles/volume or mass/volume [1.15]. Assay sensitivity depends on the waveguide sensitivity as well as efficient binding of the target molecules with the antibodies.

Resolution or limit of detection refers to the smallest change in Δn_c that can be measured and is expressed as Refractive Index Units (RIUs). To determine the resolution of the sensor, the phase resolution of the detection instrumentation must also be considered which in this project is assumed to be $2\pi \times 10^{-4}$ rads [1.16].

The best resolutions for SPR, MZI and photonic crystal sensors in the literature are $1\text{x}10^{-8}$ RIU [1.17], $1\text{x}10^{-7}$ RIU [1.16] and $7\text{x}10^{-5}$ RIU [1.18] respectively.

In addition to sensitivity, assay sensitivity and resolution, factors such as ease of use, sensor cost, detection instrumentation and throughput must also be considered when designing a packaged commercial optical biosensor [1.15].

1.2 WHY OPTICAL BIOSENSORS?

Although the most commercially successful biosensors are the amperometric glucose biosensors due to their abundant market, biosensors are used for a large number of applications ranging from biomedical, pharmaceutical, environmental, security to food analysis.

Rapid detection and identification of microorganisms is a pressing issue in fields ranging from clinical diagnostics and the monitoring of food-borne pathogens to the detection of biological warfare agents [1.19]. As the potential threat of bio-terrorism increases, there is a need for a device that can quickly, reliably, and accurately detect contaminants in the atmosphere [1.20]. Current methods used to monitor antimicrobials in animals produced for human consumption are simple and inexpensive, but slow for real-time measurements and is crucial to have quick and accurate tests [1.21]. Point-of-care (POC) diagnostics would greatly benefit from faster, more accurate, low-cost and portable devices [1.22].

Furthermore, biosensors need to provide real-time measurements, a high degree of automation, and improved throughput and sensitivity. They should be less expensive than sophisticated physical-chemical instrumentation, require less time for analysis, and be capable of being used by semi-skilled people.

Optical biosensors are preferred due to their potential sensitivity, portability, wider bandwidth, real time and remote sensing, immunity to electromagnetic interference and because they can provide parallel detection and identification within a single device. The technology of integrated optics allows the integration of many passive and active optical components such as fibres, emitters, detectors and waveguides allowing the development of “Lab on a Chip” devices.

“Lab on a Chip” usually refers to a device that integrates one or several laboratory functions on a single chip and generally varies in size from micrometres to millimetres as shown in Figure 1.6 [1.23]

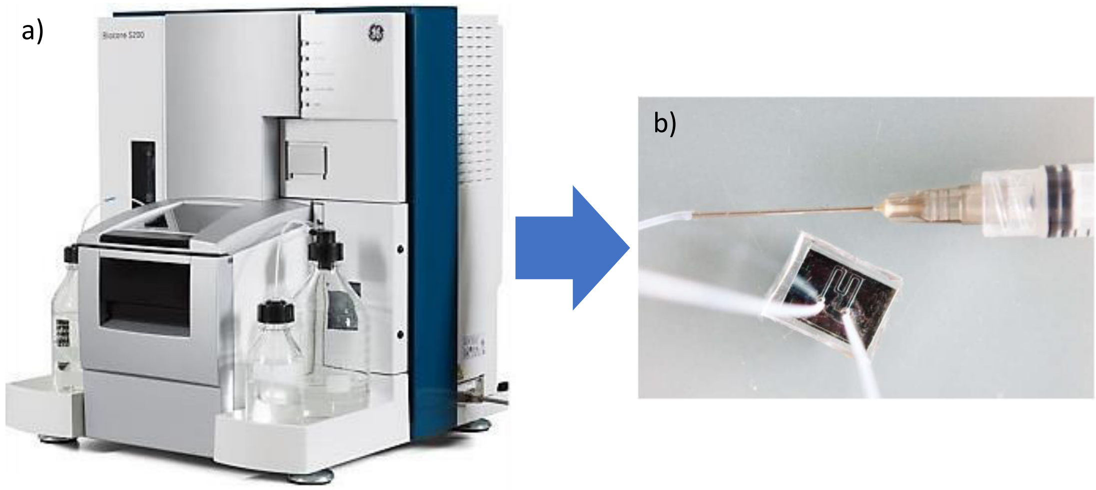

Figure 1.6: a) Biacore S200 biosensor based on Surface plasmon Resonance Technology [1.7] and b) SOI ‘Lab on a Chip’ biosensor packaged with PDMS microfluidics [1.23].

Despite the growing focus on research and development and the large amounts of literature available, very few commercial implementations have been demonstrated. This may be the result of developing and improving individual aspects of the sensor rather than the sensor as a whole as it is an interdisciplinary research project. Another reason may be the difficulty in producing low-cost, sensitive and portable detection systems.

1.3 AIM AND THESIS OVERVIEW

The Aim of this project is the research and development of next generation optical biosensors which are capable of label-free, real time, parallel detection and the identification of multiple analytes in multiple samples with extremely high detection sensitivity.

Chapter 2 presents a brief introduction to electromagnetic theory and the concept of evanescent field sensors. The material and waveguide height of a slab waveguide are optimised for maximum sensitivity while considering biocompatibility, fabrication and integration.

In Chapter 3, commercial software based on the Beam propagation method (BPM) and the Eigenmode expansion (EME) method are used to design and simulate the components of an evanescent field biosensor. At first the waveguide height and width are optimized for maximum sensitivity. Then the propagation loss and curvature loss are evaluated. Finally, the components of the biosensor are designed and optimized. Figure 1.7 shows a schematic diagram of the proposed biosensor layout which is realised in a Silicon-on-Insulator (SOI) wafer and is made of an input coupler, a 1xN splitter (where N is the number of outputs), bent guide separators, sensors, output couplers and the microfluidics layer.

Light is not directly coupled in to the silicon waveguide as the waveguide has a cross-section much smaller than that of the input beam and therefore the coupling loss will be high. The light may be efficiently coupled through a spot size converter such as an SU-8 taper (SU-8 is a polymer with good transmission properties and low insertion loss [1.24-26] as explained in section 4.5) or by using a grating coupler which is more compact but is associated with a high insertion loss. The same method is used to couple light out of the waveguide as well. A 1xN multimode interferometer (MMI) is used to split the input light into many outputs by the self-imaging principle as explained in section 3.4. Other methods of splitting light by cascading Y-junction splitters and cascading directional couplers (DCs) are also presented in section 3.4.5.

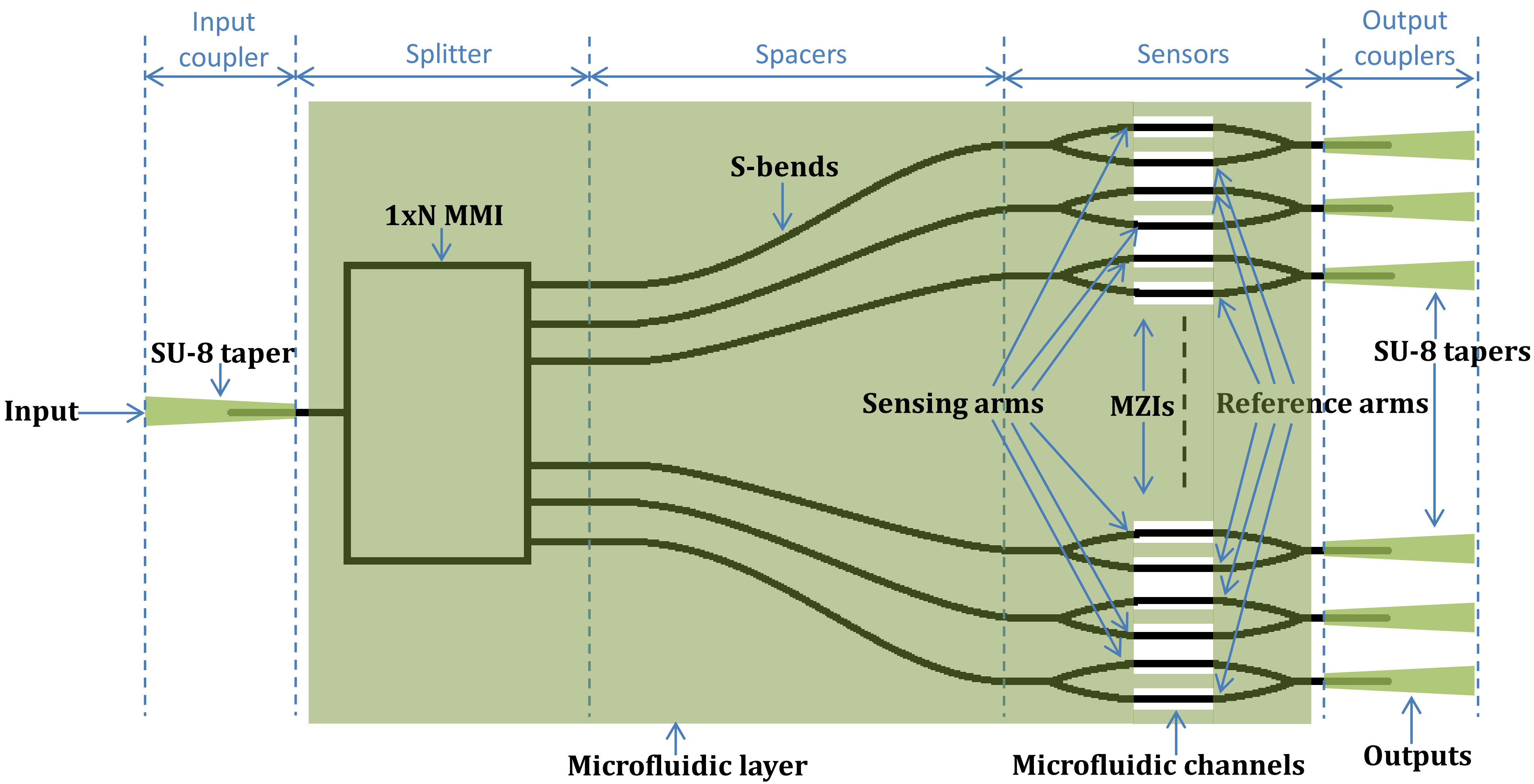

Figure 1.7: Schematic diagram of the proposed biosensor layout which is made of an input coupler, a 1xN splitter (where N is the number of outputs), separators, sensors, output couplers and the microfluidics layer.

Each MMI output connects to a Mach-Zehnder interferometer (MZI) via a spacer. A spacer is made of an S-bend or S-function waveguide and is used to space the MZIs on the chip. Each MZI has a sensing arm and a reference arm that superimposes the light at the output of the MZI as explained in more detail in section 3.2. The use of multiple MZIs enables parallel detection.

Chapter 4 presents in detail the processing techniques used for the fabrication of the biosensor including the microfluidics layer. The microfluidics' layer controls the flow of the analyte by transporting them in and out of the sensing and reference arms via micrometre scaled channels.

For the biosensor to work as a heterogenous sensor, a bioreceptor layer must be developed on the sensing arm of the MZI. Chapter 5 presents an introduction to the bioreceptor layer and some preliminary results on the surface functionalisation of silicon and silicon dioxide for the attachment of antibodies on the silicon waveguides.

Chapter 6 evaluates the fabricated devices optically. Results presented show successful realisation of waveguides, power splitters, spot size converters, grating couplers, MZIs and PIs.

Chapter 7 summarises the conclusions of the work undertaken for this PhD and suggests possible future work.

REFERENCES

[1.1] Leland C. Clark Jr., "Monitor and control of blood and tissue oxygen tensions," *American Society for Artificial Internal Organs,* vol. 2, pp. 41-48, 1956.

[1.2] Leland C. Clark Jr. and C. Lyons, "Electrode systems for continuous monitoring in cardiovascular surgery," *Annuals of the New York Academy of Sciences,* vol. 102, pp. pages 29-45, 1962.

[1.3] *Biosensors Market Analysis*. Available: http://www.grandviewresearch.com/

[1.4] A. Otto, "Excitation of nonradiative surface plasma waves in silver by the method of frustrated total reflection," *Zeitschrift für Physik,* vol. 216, pp. 398-410, 1968.

[1.5] E. Kretschmann, "Decay of non radiative surface plasmons into light on rough silver films. Comparison of experimental and theoretical results," *Optics Communications,* vol. 6, pp. 185-187, 1972.

[1.6] B. Liedberg, C. Nylander, and I. Lunström, "Surface plasmon resonance for gas detection and biosensing," *Sensors and Actuators,* vol. 4, pp. 299-304, 1983.

[1.7] (Accessed 28 May 2017). *Biacore* Available: http://www.biacore.com/lifesciences/index.html

[1.8] B. Sepulveda, J. S. Del Rio, M. Moreno, F. Blanco, K. Mayora, C. Domínguez, and L. M. Lechuga, "Optical biosensor microsystems based on the integration of highly sensitive Mach–Zehnder interferometer devices," *Journal of Optics A: Pure and Applied Optics,* vol. 8, p. S561, 2006.

[1.9] A. Ymeti, J. S. Kanger, R. Wijn, P. V. Lambeck, and J. Greve, "Development of a multichannel integrated interferometer immunosensor," *Sensors and Actuators B: Chemical,* vol. 83, pp. 1-7, 2002.

[1.10] A. Ymeti, J. S. Kanger, J. Greve, G. A. J. Besselink, P. V. Lambeck, R. Wijn, and R. G. Heideman, "Integration of microfluidics with a four-channel integrated optical Young interferometer immunosensor," *Biosensors and Bioelectronics,* vol. 20, pp. 1417-1421, 2005.

[1.11] D. X. Xu, A. Densmore, A. Delâge, P. Waldron, R. McKinnon, S. Janz, J. Lapointe, G. Lopinski, T. Mischki, E. Post, P. Cheben, and J. H. Schmid, "Folded cavity SOI microring sensors for highsensitivity and real time measurement of biomolecular binding," *Opt. Express,* vol. 16, pp. 15137-15148, 2008.

[1.12] S. Janz, "Food and Water Safety," in *Photonics Media*, ed. www.photonics.com: National Research Council of Canada, 2008.

[1.13] J. D. Joannopoulos, S. G. Johnson, J. N. Winn, and R. D. Meade, *Photonic crystals: molding the flow of light*. New Jersey: Princeton University Press, 2011.

[1.14] M. R. Lee and P. M. Fauchet, "Nanoscale microcavity sensor for single particle detection," *Opt. Lett.,* vol. 32, pp. 3284-3286, 2007.

[1.15] B. T. Cunningham, *Label-free optical biosensors: An Introduction*. New York: Cambridge University Press, 2009.

[1.16] R. G. Heideman and P. V. Lambeck, "Remote opto-chemical sensing with extreme sensitivity: design, fabrication and performance of a pigtailed integrated optical phase-modulated Mach–Zehnder interferometer system," *Sensors and Actuators B: Chemical,* vol. 61, pp. 100-127, 1999.

[1.17] N. Tao, S. Boussaad, W. Huang, R. Arechabaleta, and J. Dagnese, "High resolution surface plasmon resonance spectroscopy," *Review of Scientific Instruments,* vol. 70, pp. 4656-4660, 1999.

[1.18] S. Mandal and D. Erickson, "Nanoscale optofluidic sensor arrays," *Opt. Express,* vol. 16, pp. 1623-1631, 2008.

[1.19] J. Mairhofer, K. Roppert, and P. Ertl, "Microfluidic systems for pathogen sensing: a review," *Sensors,* vol. 9, pp. 4804-4823, 2009.

[1.20] F. S. Ligler and D. Phil, "Biosensors for detection of bioterrorist threats," in *Optical Chemical Sensors*, ed Erice: Springer, 2006, pp. 437-455.

[1.21] A.-C. Huet, P. Delahaut, T. Fodey, S. A. Haughey, C. Elliott, and S. Weigel, "Advances in biosensor-based analysis for antimicrobial residues in foods," *TrAC Trends in Analytical Chemistry,* vol. 29, pp. 1281-1294, 2010.

[1.22] S. Choi, M. Goryll, L. Y. M. Sin, P. K. Wong, and J. Chae, "Microfluidic-based biosensors toward point-of-care detection of nucleic acids and proteins," *Microfluidics and Nanofluidics,* vol. 10, pp. 231-247, 2011.

[1.23] K. de Vos, J. Girones, T. Claes, Y. De Koninck, S. Popelka, E. Schacht, R. Baets, and P. Bienstman, "Multiplexed antibody detection with an array of silicon-on-insulator microring resonators," *Photonics Journal, IEEE,* vol. 1, pp. 225-235, 2009.

[1.24] D. Esinenco, S. Psoma, M. Kusko, A. Schneider, and R. Muller, "SU-8 micro-biosensor based on Mach-Zehnder interferometer," *Rev. Adv. Mater. Sci,* vol. 10, pp. 295-299, 2005.

[1.25] B. Shew, C. Kuo, Y. Huang, and Y. Tsai, "UV-LIGA interferometer biosensor based on the SU-8 optical waveguide," *Sensors and Actuators A: Physical,* vol. 120, pp. 383-389, 2005.

[1.26] B. Y. Shew, Y. C. Cheng, and Y. H. Tsai, "Monolithic SU-8 micro-interferometer for biochemical detections," *Sensors and Actuators A: Physical,* vol. 141, pp. 299-306, 2008.

Chapter 2

2 WAVEGUIDE DESIGN CONCEPT AND PRINCIPLES

In this chapter, a brief introduction to basic electromagnetic theory and evanescent field sensors is presented. Methods of quantifying the sensitivity of the sensors and optimising the waveguides to obtain maximum sensitivity are shown.

2.1 INTRODUCTION TO PLANAR DIELECTRIC WAVEGUIDE THEORY

To explain propagation of light in a waveguide a ray optics model is explained first as shown in Figure 2.1. An incident light ray, E_i, propagating in a medium of refractive index, n_2, at an angle of θ_2 towards the interface between the two media will in general partially transmit a ray of light, E_t at angle θ_1 in a medium of refractive index n_1 and partially reflect a ray of light, E_r at an angle of θ_2 in the medium of refractive index n_2 where n_2>n_1 as shown in Figure 2.1a.

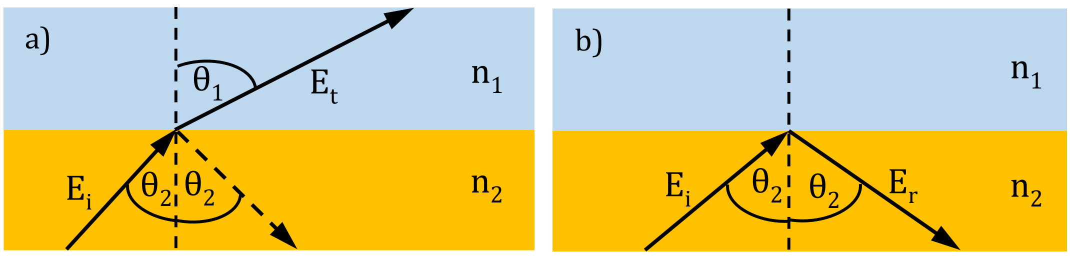

Figure 2.1: a) Light rays refracted and reflected and the interface of two media and b) total internal reflection at two interfaces when ϑ_2 exceeds the critical angle.

The relationship between the angles and refractive indices is given by Snell's law:

$$n_1 sin\theta_1 = n_2 sin\theta_2 \tag{2.1}$$

As θ_2 increases, θ_1 will reach 90˚ and $sin\theta_1$ becomes 1. At this point θ_2 is known as the critical angle, θ_c, and Snell's law becomes:

$$sin\theta_2 = \frac{n_1}{n_2} \tag{2.2}$$

If θ_2 becomes larger than the critical angle then no light is transmitted; instead it is all reflected as shown in Figure 2.1b. This is known as total internal reflection (TIR).

A dielectric optical waveguide is a physical structure that confines and guides electromagnetic waves by total internal reflection (TIR) as shown in Figure 2.2. In the simplest form, it consists of three layers of refractive indices n_1, n_2 and n_3 where $n_2 > n_3 \geq n_1$. In the present work Silicon-on-Insulator (SOI) structures will be considered with $n_3 > n_1$. If the refractive index contrast is sufficiently large, and the waveguide dimensions are suitably chosen, light at a given wavelength will be guided through the core by total internal reflection [2.1].

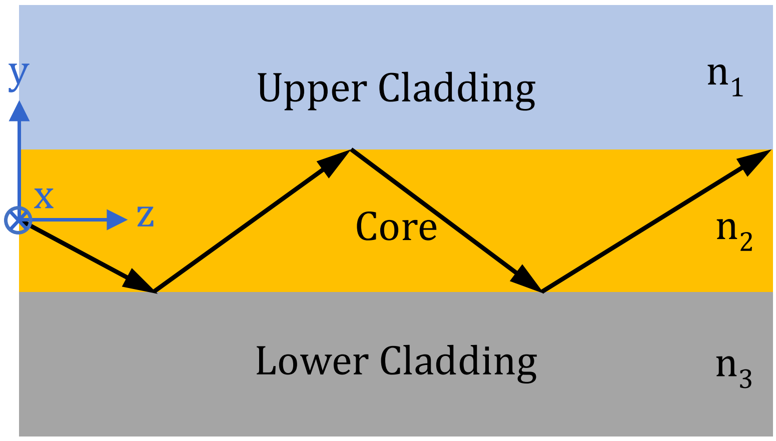

Figure 2.2: Light guided and confined by total internal reflection.

One such guided mode is represented as a vector diagram as shown in Figure 2.3, in which the geometric relationship of the propagation constant, β, which is used to characterize waveguide modes is explained.

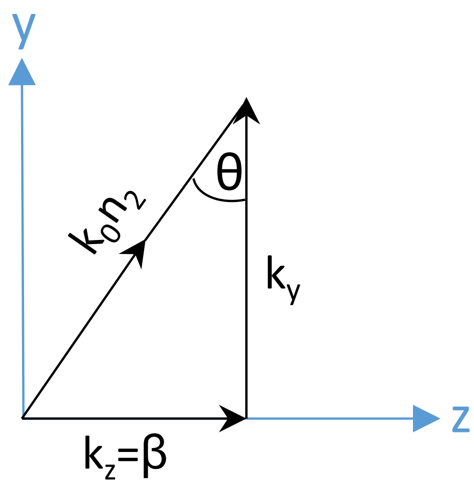

Figure 2.3: Vector diagram for wave propagation constant.

In Figure 2.3 the plane wave (ray) propagation constant is k_0n_2 where k_0 is known as the free space wavevector given by $k_0=2\pi/\lambda_0$ and λ_0 is the wavelength of light in free space. Therefore, the corresponding propagation constants along the y and z directions are:

$$k_y = k_0n_2cos\theta \tag{2.3}$$

$$k_z = k_0n_2sin\theta = \beta \tag{2.4}$$

It is useful to describe the z-directed propagation of a guided wave in an optical waveguide in terms of an effective refractive index [2.2]. From equation 2.4 the effective refractive index, N_{eff} can be written as:

$$N_{eff} = n_2sin\theta \tag{2.5}$$

and it follows that

$$\beta = k_0N_{eff} \tag{2.6}$$

Since the highest value for θ will be 90˚ (by Snell's law), $\beta \leq k_0n_2$.

Since it is assumed that $n_3>n_1$, it follows from equation 2.2 that the critical angle is

$$sin\theta = \frac{n_3}{n_2} \tag{2.7}$$

Substituting this into equation 2.5 shows that

$$N_{eff} \geq n_2 \cdot \frac{n_3}{n_2} = n_3 \qquad (2.8)$$

Hence

$$k_0 n_3 \leq \beta \leq k_0 n_2 \qquad (2.9)$$

and,

$$n_3 \leq N_{eff} \leq n_2 \qquad (2.10)$$

A slab waveguide can support Transverse Electric (TE) and Transverse Magnetic (TM) modes. TE polarisation is where the electric field E of the wave is tangential to the interface as shown in Figure 2.4a. TM polarisation is where the magnetic field of the wave is tangential to the interface as shown in Figure 2.4b. This will be discussed further in section 2.4.

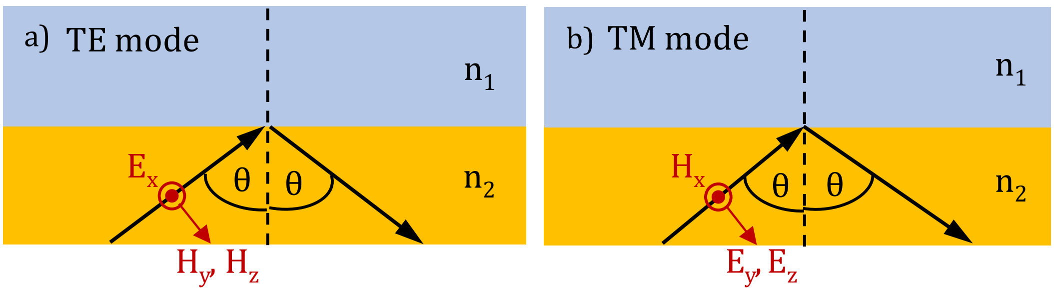

Figure 2.4: a) TE mode and b) TM mode wave propagation in the z direction.

Light guided through an optical fibre or waveguide can be described as a set of guided electromagnetic waves with time varying electric, $\underline{E}$, and magnetic, $\underline{H}$, fields. A loss free wave propagating along the *z* direction can be represented using the equations below:

$$\underline{E}(x, y, z, t) = \underline{E}(x, y)e^{j(\omega t - \beta z)} \qquad (2.11)$$

$$\underline{H}(x, y, z, t) = \underline{H}(x, y)e^{j(\omega t - \beta z)} \qquad (2.12)$$

where the angular frequency, ω is defined as:

$$\omega = \frac{2\pi c}{\lambda_0} \tag{2.13}$$

and c is the velocity of light in free space. Light will propagate when the frequency is above the cut off frequency of the lowest order mode, see section 2.2, and a finite number or discrete set of guided modes will be present at a given frequency. The cut off frequency is the lowest frequency for which a given mode will propagate. The cut-off condition will be discussed in more detail in section 2.8.

2.2 ELECTROMAGNETIC THEORY

Light propagation may also be described starting from Maxwell's equations as shown below:

$$\nabla \times \underline{E} = -\frac{\partial \underline{B}}{\partial t} \tag{2.14}$$

$$\nabla \times \underline{H} = \frac{\partial \underline{D}}{\partial t} \tag{2.15}$$

$$\nabla \cdot \underline{B} = 0 \tag{2.16}$$

$$\nabla \cdot \underline{D} = 0 \tag{2.17}$$

where $\underline{E}$, $\underline{H}$, $\underline{B}$, $\underline{D}$ and t are the electric field amplitude, magnetic field amplitude, magnetic flux density, electric flux density and time respectively. In a linear isotropic medium, the following equations are true:

$$\underline{D} = \varepsilon \underline{E} \tag{2.18}$$

$$\underline{B} = \mu \underline{H} \tag{2.19}$$

Here ε and μ are the permittivity and permeability which are defined as the following:

$$\varepsilon = \varepsilon_0 \varepsilon_r \tag{2.20}$$

$$\mu = \mu_0 \mu_r \tag{2.21}$$

where ε_0 and μ_0 are the permittivity and permeability in a vacuum and ε_r and μ_r are the relative permittivity and permeability of the material. In this project μ_r is assumed to be 1 as only non-magnetic materials are used.

As previously shown light propagating in the z direction can also be expressed by equations 2.11 and 2.12. If an oscillating wave is expressed by equation 2.22 then a partial differentiation with respect to time can be expressed by equation 2.23:

$$\underline{A}(x, y, z, t) = \underline{A}(x, y, z)e^{(j\omega t)} \tag{2.22}$$

$$\frac{\partial \underline{A}}{\partial t} = j\omega\underline{A} \tag{2.23}$$

and Maxwell's equations 2.14-2.17 can be rewritten as equations 2.24-2.27:

$$\nabla \times \underline{E} = -\frac{\partial \underline{B}}{\partial t} = -j\omega\underline{B} = -j\omega\mu_0\underline{H} \tag{2.24}$$

$$\nabla \times \underline{H} = j\omega\underline{D} = j\omega\varepsilon\underline{E} \tag{2.25}$$

$$\nabla \cdot \underline{H} = 0 \tag{2.26}$$

$$\nabla \cdot (\varepsilon_r\underline{E}) = 0 \tag{2.27}$$

Applying the curl operator, $\nabla \times$, to equation 2.24 and substituting from equation 2.25 yields:

$$\nabla \cdot (\nabla \times \underline{E}) = -j\omega\mu_0\nabla \times \underline{H} = -j\omega\mu_0 j\omega\varepsilon\underline{E} = \mu_0\varepsilon\omega^2\underline{E} \tag{2.28}$$

Any vector satisfies the following equation:

$$\nabla \cdot (\nabla \times \underline{E}) = \nabla(\nabla \cdot \underline{E}) - \nabla^2\underline{E} \tag{2.29}$$

where the Laplacian, ∇^2, is expressed in Cartesian coordinates as:

$$\nabla^2 = \frac{\partial^2}{\partial x^2} + \frac{\partial^2}{\partial y^2} + \frac{\partial^2}{\partial z^2} \tag{2.30}$$

For the case where ε_r is a function of position, equation 2.27 can be rewritten as:

$$\nabla \cdot \left(\varepsilon_r \underline{E}\right) = \nabla \varepsilon_r \cdot \underline{E} + \varepsilon_r \nabla \cdot \underline{E} = 0 \tag{2.31}$$

giving

$$\nabla \cdot \underline{E} = -\frac{\nabla \varepsilon_r}{\varepsilon_r} \cdot \underline{E} \tag{2.32}$$

Substituting equations 2.28 and 2.32 into equation 2.29 gives:

$$\nabla^2 \underline{E} + \nabla \left(\frac{\nabla \varepsilon_r}{\varepsilon_r} \cdot \underline{E}\right) + \mu_0 \varepsilon \omega^2 \underline{E} = 0 \tag{2.33}$$

The wave vector k is defined as:

$$k = \omega \sqrt{\mu_0 \varepsilon} \tag{2.34}$$

such that substituting equation 2.34 into equation 2.33 gives the wave equation for the electric field:

$$\nabla^2 \underline{E} + \nabla \left(\frac{\nabla \varepsilon_r}{\varepsilon_r} \cdot \underline{E}\right) + k^2 \underline{E} = 0 \tag{2.35}$$

When ε_r is constant in a medium, equation 2.35 can be reduced to give the Helmholtz equation:

$$\nabla^2 \underline{E} + k^2 \underline{E} = 0 \tag{2.36}$$

and equation 2.32 reduces to

$$\nabla \cdot \underline{E} = 0 \tag{2.37}$$

The wave equation for the magnetic field can be derived similarly to give:

$$\nabla^2 \underline{H} + k^2 \underline{H} = 0 \tag{2.38}$$

where it is noted from equation 2.26 that $\nabla \cdot \underline{H} = 0$.

When the waveguide structure is uniform in the z direction, the derivative of the electromagnetic field with respect to the z coordinate is constant. In a loss free medium, the following equation is true from equations 2.11 and 2.12

$$\frac{\partial}{\partial z} = -j\beta \tag{2.39}$$

where β is the phase constant in the z direction as given by equation 2.6. When ε_r is constant the Helmholtz equations 2.36 and 2.38 can be rewritten as:

$$\nabla_\perp^2 \underline{E} + (k^2 - \beta^2)\underline{E} = 0 \tag{2.40}$$

$$\nabla_\perp^2 \underline{H} + (k^2 - \beta^2)\underline{H} = 0 \tag{2.41}$$

where $\nabla_\perp^2 = \frac{\partial^2}{\partial x^2} + \frac{\partial^2}{\partial y^2}$

For waveguides uniform in the z direction:

$$\frac{\partial \varepsilon_r}{\partial z} = 0 \tag{2.42}$$

Therefore, the second term in equation 2.35 can be rewritten as:

$$\nabla\left(\frac{\nabla\varepsilon_r}{\varepsilon_r} \cdot \underline{E}\right) = \nabla\left(\frac{1}{\varepsilon_r}\frac{\partial\varepsilon_r}{\partial x} \cdot E_x + \frac{1}{\varepsilon_r}\frac{\partial\varepsilon_r}{\partial y} \cdot E_y\right) \tag{2.43}$$

Substituting equation 2.43 into equation 2.33 gives the vector wave equations for the E_x and E_y components as equations 2.44 and 2.45 respectively.

$$\frac{\partial^2 E_x}{\partial y^2} + \frac{\partial}{\partial x}\left(\frac{1}{\varepsilon_r}\frac{\partial\varepsilon_r}{\partial x} \cdot E_x\right) + \frac{\partial}{\partial x}\left(\frac{1}{\varepsilon_r}\frac{\partial\varepsilon_r}{\partial y} \cdot E_y\right) + (k_0^2\varepsilon_r - \beta^2)E_x = 0 \tag{2.44}$$

$$\frac{\partial^2 E_y}{\partial x^2} + \frac{\partial}{\partial y}\left(\frac{1}{\varepsilon_r}\frac{\partial\varepsilon_r}{\partial y} \cdot E_y\right) + \frac{\partial}{\partial y}\left(\frac{1}{\varepsilon_r}\frac{\partial\varepsilon_r}{\partial x} \cdot E_x\right) + (k_0^2\varepsilon_r - \beta^2)E_y = 0 \tag{2.45}$$

Similarly, the vector wave equations for the H_x and H_y components can be derived as equation 2.46 and 2.47 respectively.

$$\frac{\partial^2 H_x}{\partial y^2}+\frac{\partial}{\partial x}\left(\frac{1}{\varepsilon_r}\frac{\partial \varepsilon_r}{\partial x}\cdot H_x\right)+\frac{\partial}{\partial x}\left(\frac{1}{\varepsilon_r}\frac{\partial \varepsilon_r}{\partial y}\cdot H_y\right)+(k_0^2\varepsilon_r-\beta^2)H_x=0 \qquad (2.46)$$

$$\frac{\partial^2 H_y}{\partial x^2}+\frac{\partial}{\partial y}\left(\frac{1}{\varepsilon_r}\frac{\partial \varepsilon_r}{\partial y}\cdot H_y\right)+\frac{\partial}{\partial y}\left(\frac{1}{\varepsilon_r}\frac{\partial \varepsilon_r}{\partial x}\cdot H_x\right)+(k_0^2\varepsilon_r-\beta^2)H_y=0 \qquad (2.47)$$

The terms $\frac{\partial}{\partial x}\left(\frac{1}{\varepsilon_r}\frac{\partial \varepsilon_r}{\partial y}\cdot E_y\right)$ and $\frac{\partial}{\partial y}\left(\frac{1}{\varepsilon_r}\frac{\partial \varepsilon_r}{\partial x}\cdot E_x\right)$ in equations 2.44 and 2.45 respectively are often small and ignoring them gives the semi-vector equations for the E_x and E_y components as equations 2.48 and 2.49 respectively.

$$\frac{\partial^2 E_x}{\partial y^2}+\frac{\partial}{\partial x}\left(\frac{1}{\varepsilon_r}\frac{\partial \varepsilon_r}{\partial x}\cdot E_x\right)+(k_0^2\varepsilon_r-\beta^2)E_x=0 \qquad (2.48)$$

$$\frac{\partial^2 E_y}{\partial x^2}+\frac{\partial}{\partial y}\left(\frac{1}{\varepsilon_r}\frac{\partial \varepsilon_r}{\partial y}\cdot E_y\right)+(k_0^2\varepsilon_r-\beta^2)E_y=0 \qquad (2.49)$$

Similarly, the semi-vector equations for H_x and H_y components can be derived from equations 2.46 and 2.47 as equations 2.50 and 2.51.

$$\frac{\partial^2 H_x}{\partial y^2}+\frac{\partial}{\partial x}\left(\frac{1}{\varepsilon_r}\frac{\partial \varepsilon_r}{\partial x}\cdot H_x\right)+(k_0^2\varepsilon_r-\beta^2)H_x=0 \qquad (2.50)$$

$$\frac{\partial^2 H_y}{\partial x^2}+\frac{\partial}{\partial y}\left(\frac{1}{\varepsilon_r}\frac{\partial \varepsilon_r}{\partial y}\cdot H_y\right)++(k_0^2\varepsilon_r-\beta^2)H_y=0 \qquad (2.51)$$

2.3 TYPES OF WAVEGUIDES

Optical waveguides were originally developed for applications in the telecommunication field due to their mechanical stability, flexible geometry, noise immunity and efficient light-conducting over long distances. Depending on the use, waveguides have different architecture. The common forms of optical waveguides are slab waveguides (as discussed in section 2.1), optical fibres, buried waveguides, rib waveguides, ridge and slot waveguides as illustrated in Figure 2.5. They are fabricated with dielectric materials such as semiconductors [2.3, 4], glasses [2.5, 6], and polymers [2.7-9].

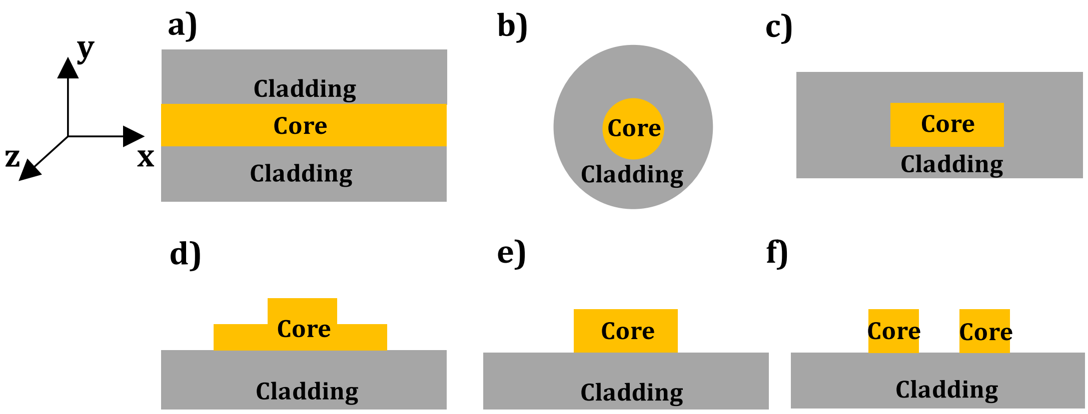

Figure 2.5: Cross-section of waveguide geometry: a) slab waveguide; b) optical fibre; c) buried waveguide; d) Rib waveguide; e) Ridge waveguide and f) slot waveguides.

In this project, the ridge waveguide structure of Figure 2.5e is used as it reduces the steps in fabrication and because the surface of the core needs to remain open to the environment for biological attachments. Slot waveguide designs are also examined in section 3.1.6.

The following section will show how guided waves propagate in slab waveguides and ridge waveguides. This chapter concentrates on slab waveguides and optimises the core height of the slab waveguide to give maximum sensor sensitivity. This gives an idea of the wafer dimensions needed for the simulations of a ridge waveguide structure shown in chapter 3.

2.4 MODES IN DIELECTRIC OPTICAL WAVEGUIDES

In section 2.2, vector and semi-vector equations were derived for the electric and magnetic fields. In this section TE and TM guided modes supported by slab waveguide and the TE-like or quasi-TE and the TM-like or quasi-TM modes of a ridge waveguide are explained.

In free space, the electric and magnetic field exist at 90° to each other and the direction of propagation as shown in Figure 2.6; the wave can be described as *polarised* and *transverse electromagnetic*.

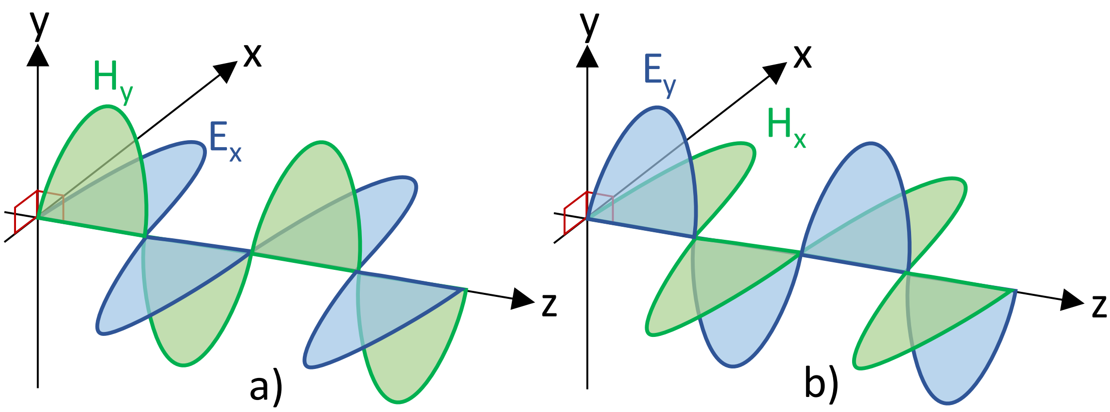

Figure 2.6: Sinusoidal plane wave showing the electric and magnetic fields in free space for a) x-polarisation b) y-polarisation.

Maxwell's equations 2.14 and 2.15 are repeated as:

$$\nabla \times \underline{E} = -\mu \frac{\partial \underline{H}}{\partial t} \tag{2.52}$$

$$\nabla \times \underline{H} = \frac{\partial \underline{E}}{\partial t} \tag{2.53}$$

Equation 2.52 and 2.53 can be expanded and manipulated to describe $\underline{E}$ and $\underline{H}$ in terms of the longitudinal components E_z and H_z to get equations 2.54-2.57 [2.10]:

$$H_x = \frac{j}{{k_c}^2}\left(\omega\mu \frac{\partial E_z}{\partial y} - \beta \frac{\partial H_z}{\partial x}\right) \tag{2.54}$$

$$H_y = -\frac{j}{{k_c}^2}\left(\omega\mu\frac{\partial E_z}{\partial x} - \beta\frac{\partial H_z}{\partial y}\right) \tag{2.55}$$

$$E_x = -\frac{j}{{k_c}^2}\left(\beta\frac{\partial E_z}{\partial x} + \omega\mu\frac{\partial H_z}{\partial y}\right) \tag{2.56}$$

$$E_y = \frac{j}{{k_c}^2}\left(-\beta\frac{\partial E_z}{\partial y} + \omega\mu\frac{\partial H_z}{\partial x}\right) \tag{2.57}$$

where ${k_c}^2 = k^2 - \beta^2$.

For a planar slab waveguide the waveguide is uniform in the z and y directions. Therefore $\frac{\partial \varepsilon_r}{\partial z} = 0$ and $\frac{\partial}{\partial y} = 0$, and in the lossless case $\frac{\partial}{\partial z} = -j\beta$. Equations 2.54-2.57 are reduced to equations 2.58-2.61:

$$H_x = \frac{j}{{k_c}^2}\left(\omega\mu\frac{\partial E_z}{\partial y}\right) \tag{2.58}$$

$$H_y = \frac{j}{{k_c}^2}\left(\beta\frac{\partial H_z}{\partial y}\right) \tag{2.59}$$

$$E_x = \frac{j}{{k_c}^2}\left(\omega\mu\frac{\partial H_z}{\partial y}\right) \tag{2.60}$$

$$E_y = \frac{j}{{k_c}^2}\left(-\beta\frac{\partial E_z}{\partial y}\right) \tag{2.61}$$

For the TE modes E_z=0, H_z≠0 and it follows that $E_y = H_x = 0$. For the TM modes H_z=0, E_z≠0 and it follows that $H_y = E_x = 0$.

Three levels of approximation can be made when evaluating the modes of a dielectric optical waveguide invariant in the z (propagation direction) but confining in the *x* and *y* directions. They are vector mode (no approximation mode), semi-vector mode and scalar mode [2.10].

The vector mode considers all six electromagnetic field components. Calculations are performed using either the $\underline{E}$ field or $\underline{H}$ field. Vector TE-like mode is a notation given when the dominant $\underline{E}$ field component is horizontal in Figure 2.5a; this would be the TE mode of the slab waveguide formed if the core width were infinite in extent. A vector TM-like mode is annotation given when the principal $\underline{H}$ field is assumed to be horizontal in Figure 2.5b by similar reasoning. For narrower ridge waveguides, all six electromagnetic field components must be considered, even though the categorisation is TE-like and TM-like vector modes.

In the semi-vector mode approximation [2.10] one of the transverse components of either the $\underline{E}$ field or the $\underline{H}$ field is assumed to have a negligible magnitude. Referring to Figure 2.5, for semi-vector TE-like mode the E_x (and H_y) components are non-zero and for semi-vector TM-like mode the E_y (and H_x) are non-zero.

The scalar mode is also known as the Transverse Electric and Magnetic (TEM) mode and it assumes $\underline{E}$ and $\underline{H}$ field continuity at all dielectric interfaces. The solution can be obtained from the scalar Helmholtz equations:

$$\left(\frac{\partial^2}{\partial x^2}+\frac{\partial^2}{\partial y^2}+\frac{\partial^2}{\partial z^2}\right)\underline{E}+k^2\underline{E}=0 \qquad (2.62a)$$

$$\left(\frac{\partial^2}{\partial x^2}+\frac{\partial^2}{\partial y^2}+\frac{\partial^2}{\partial z^2}\right)\underline{H}+k^2\underline{H}=0 \qquad (2.62b)$$

In this project, vector TE-like and vector TM-like modes are used for all simulations as they provide the most accurate result.

The planar slab waveguide equations 2.62a and b, can have one or more guided solutions depending on the values of n_1, n_2, n_3 and the operating wavelength. The first three TE modes of a symmetric slab waveguide (i.e. one for which n_1=n_3) are illustrated graphically in Figure 2.7.

The lowest mode is known as the fundamental mode (*m*=0). The fundamental mode has one maxima and in the symmetric waveguide case (n_1=n_3), has its maximum intensity at the centre of the waveguide. The integer '*m*' identifies the mode and (*m*+1) indicates the number of field maxima in the *y* direction.

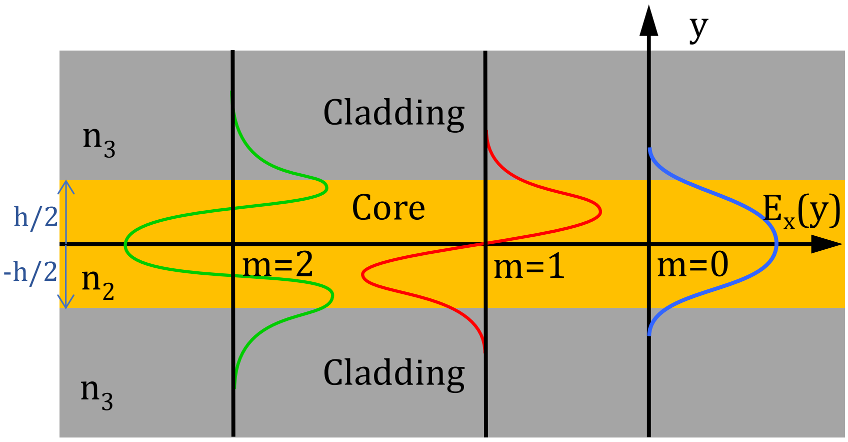

Figure 2.7: Electric field amplitude distributions over the transverse plane for the first three TE modes in a symmetric slab guide (n_1=n_3).

In higher order modes, the electric and magnetic fields are distributed more towards the outer edges of the core and penetrate further into the cladding as seen in Figure 2.7. To ensure a well-defined phase constant and field profile, structures supporting only a single (fundamental) TE and TM mode are preferred.

The guided-mode fields in a slab waveguide do not reach zero at the core-cladding boundaries but decay exponentially above and below the slab; these are known as evanescent fields and are explained in more detail in section 2.5 because of the relevance to the sensing applications explored in the present project.

2.5 Power and Confinement Factor

The power of a propagating wave is described by the Poynting vector, *P*, measured in W/m^2. For a guided TE mode in a planar slab waveguide [2.11],

$$P = \frac{\beta}{2\omega\mu}\int_{-\infty}^{\infty} E_x^2 dy \qquad (2.63a)$$

where *P* is the power carried by the mode, E_x is the electric field, ω is the angular frequency and μ is the permeability of the waveguide. Here, $\mu = \mu_0$ as μ_r is assumed to be 1 as mentioned previously in section 2.2.

For a guided TM mode the equivalent expression is [2.11],

$$P = \frac{\beta}{2\omega\varepsilon_0}\int_{-\infty}^{\infty}\frac{1}{n^2(y)}H_x^2 dy \qquad (2.63b)$$

where $n(y)$ is the refractive index and ε_0 is the permittivity of free space.

In the previous section, it was illustrated that not all of the power propagating in a waveguide mode is confined to the core of the waveguide. The confinement can be quantified by the confinement factor, Γ, as defined below for a TE mode:

$$\Gamma = \frac{\int_{-h/2}^{h/2} E_x^2(y)dy}{\int_{-\infty}^{\infty} E_x^2(y)dy} \qquad (2.64)$$

An equivalent expression with H_x replacing E_x holds for a TM mode.

The field outside the core is known as the evanescent field and is used for biosensing in this project as will be explained in more detail in the next section.

2.6 EVANESCENT WAVE SENSOR

By definition evanescence is 'the event of fading and gradually vanishing from sight' [2.12]. Light is guided in a high core-cladding refractive index optical waveguide by total internal reflection. During this some of the light travels in the cladding of the waveguide with an amplitude that decays exponentially outwards from the core. Previously in Figure 2.7, the fundamental TE mode (E_x field) in a symmetric slab waveguide was graphically illustrated where the field has maximum intensity at the centre and some of the field penetrates the upper and lower cladding regions. The field that penetrates into the upper cladding is the evanescent field that is the basis on which the device operates as a biosensor as illustrated in Figure 2.8.

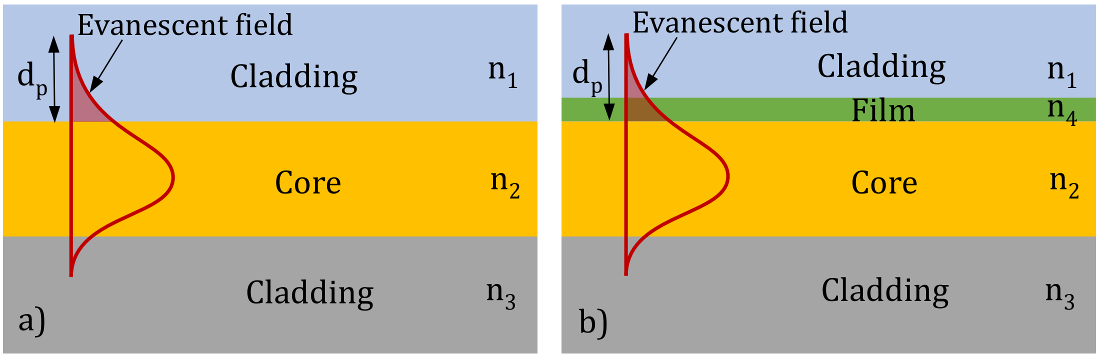

Figure 2.8: TE Evanescent field in waveguide: a) Homogenous or bulk EF sensor and b) Surface or adsorbed molecule layer EF sensor.

In Figure 2.8a the evanescent field is exposed to the upper cladding which can be a solution of refractive index n_1 and this type of sensing is referred to as homogenous sensing or bulk sensing.

In Figure 2.8b the evanescent field is exposed to a thin film also known as the adsorbed layer attached to the surface of the waveguide with a refractive index n_4. This thin film can be composed of antibodies and/or chemical linkers that attach the antibody to the surface of the waveguide. This type of sensing is referred to heterogeneous sensing or surface sensing and is used when the target molecules bind to the antibodies by a chemical reaction as explained in more detail in Chapter 5.

The sensitivity of an Evanescent Field (EF) sensor is defined as the change in effective index of the waveguide mode (ΔN_{eff}), relative to ambient refractive index change (in homogenous sensing) or relative to the index change of an adsorbed layer (in heterogeneous sensing) [2.13].

Homogenous sensing considers the whole evanescent tail whereas in heterogeneous sensing the evanescent field could penetrate beyond the thickness of the adsorbed layer.

If the adsorbed layer is thick enough to almost cover the EF tail then the thickness of the adsorbed layer will no longer affect the sensitivity and therefore any unbounded molecules above this surface will also not affect the sensitivity of the device. The EF tail or the penetration depth, d_p, for the homogenous case can be found using the following equation:

$$EF = E_0 e^{\frac{-y}{d_p}} \tag{2.65}$$

where d_p is the penetration depth and y is the distance from the surface. In the case of heterogeneous sensing, the decay rate is different in the thin film and the upper cladding. The extent of the evanescent field extending into the sample can be optimised by the material and structure of the waveguide.

Later in section 3.1.5 it is calculated that according the specification of this project, a minimum adsorbed layer thickness of 0.4µm and 0.7µm for the vector TE-like and vector TM-like modes respectively will make a ridge waveguide sensor based on Silicon-on-Insulator material to start behaving like a homogenous sensor.

This project will consider heterogenous sensing, and assume that the adsorbed layer is thick enough to act like a homogenous sensor and that other unbounded free molecules in the analyte will not affect the sensitivity of the device.

Figure 2.9 shows the proposed side view of a sensing channel in an evanescent field biosensor.

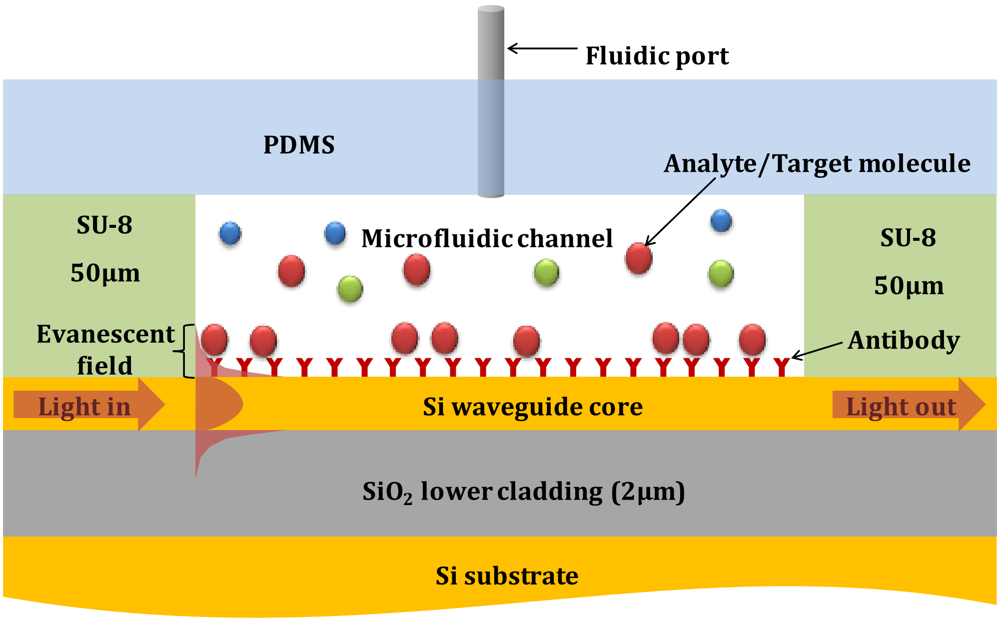

Figure 2.9: Schematic diagram showing the side of sensor window showing target molecules that binds with antibodies coated on the waveguide causing a change in refractive index on the surface of the waveguide.

At the sensing window of the sensor the waveguide surface is functionalised with antibodies that are specific to the binding of the target molecule. When an analyte is inserted to the cladding at the sensor window, target molecules bind with the receptor molecules changing the refractive index on the surface of the waveguide in the cladding. This result in a change in the effective index of the waveguide (ΔN_{eff}) causing a phase change in the propagating light due to the presence of an evanescent field.

The phase change in propagating distance L is,

$$\Delta\varphi = \Delta N_{eff} \cdot k_0 \cdot L \tag{2.66}$$

where k_0 is the phase constant ($2\pi/\lambda_0$). This is the fundamental principle upon which the evanescent field sensor is based. This is explained in more detail in section 3.2.

Note that the sensor shown in Figure 2.9 supports a TM-polarised wave. Because the silicon waveguide core has a much higher refractive index (n≈3.5) than the surrounding regions, this enhances the amplitude of the evanescent optical electric field at the surface since the boundary condition requires the tangential component of Displacement ($\varepsilon_0 n^2 \underline{E}$) to be continuous. This is discussed further in sections 3.1.3 and 3.1.4.

Figure 2.9 also illustrates a microfluidic channel. Microfluidics refers to mechanical flow control devices on the sub-millimetre scale and consists of components such as channels, pipes, valves, membranes and reservoirs. As microfluidic structures become miniaturised, fluid control becomes more dependent on diffusion, surface tension and viscosity and less dependent on gravity or inertia [2.14]. The precise control of fluids therefore can be achieved by pressure gradients, electrokinetics, magnetic fields, capillarity, rotation, sound and many more techniques and is a vast research area in itself that has made the “Lab on a Chip” concept possible [2.15].

In this project, simple microfluidic channels and reservoirs were successfully made of SU-8 by photolithography and sealed with polydimethylsiloxane (PDMS) as will be explained in section 4.8.

2.7 WAVEGUIDE MATERIALS

When deciding on the waveguide materials many factors such as the sensitivity of the biosensor, biocompatibility of the material, the ability to create nano-structures (fabrication limitations) and to integrate with existing technology for mass production need to be considered.

To obtain high sensitivity of detection a high ΔN_{eff} is required for a small change in index in the cladding (Δn_1). Therefore, the sensitivity of the waveguide can be expressed as:

$$S = \frac{\Delta N_{eff}}{\Delta n_1} \tag{2.67}$$

To increase the evanescent field, and hence ΔN_{eff}, the waveguide core thickness must be suitably chosen and high index contrast (HIC) waveguides supporting a TM polarised mode should be used. This is explained and shown with simulations in the following subsections and in chapter 3. HIC is when the refractive index difference between the core and the cladding is high, such as in SOI (Silicon-on-Insulator) waveguides where the silicon core refractive index is around 3.5 [2.16] and the SiO_2 cladding refractive index is around 1.45 [2.17] at a wavelength of 1.55µm. In the following design sections, it will be shown that SOI slab waveguides operating with a TM mode provide the highest sensitivity and allow better scaling, resulting in a smaller chip area.

Silicon based waveguides have been widely researched for biocompatibility and biomedical applications [2.18-20] and this is described in more detail in chapter 5. The present focus is on optical waveguiding properties.

SOI also has well established fabrication procedures and provides easy integration with different materials and with CMOS (complementary metal-oxide semiconductor) technology designed for the telecom wavelength of 1.55µm [2.21, 22]. Considering all these factors, SOI proves to be the logical choice of material for the fabrication of an optical biosensor.

2.8 WAVEGUIDE GEOMETRY

In section 2.3 it was indicated that the ridge waveguide structure is a suitable candidate waveguide type because the surface of the core is open to the environment and because it would have one waveguide fabrication step. From section 2.7, SOI is a good material in terms of sensitivity, biocompatibility, fabrication and integration.

In this section, a SOI planar slab waveguide is optimised for maximum sensitivity and compared with other materials. The optimum silicon core height is found for a SOI slab waveguide structure. In chapter 3, detailed simulations will be performed to optimise the height (section 3.1.3) and width (section 3.1.4) of an SOI ridge waveguide structure for the vector TE-like and vector TM-like modes.

2.8.1 Modes and cut-off heights of SOI

The first step in the design stage is to determine the height of the core that will only allow the propagation of the fundamental mode. Although higher order modes have a greater evanescent field, as illustrated in Figure 2.7, single mode waveguides are preferred due to their lower losses and because higher modes will interact with the external medium with different penetration depths resulting in different effective refractive indices.

The cut-off height is the smallest height at which a mode will propagate. The cut-off height for the m^{th} TE mode of a SOI slab waveguide was calculated using [2.10]:

$$\tan(q_2 h_{cut} - m\pi) = \frac{p_1}{q_2} \tag{2.68}$$

and the cut-off height for the m^{th} TM mode was calculated using:

$$\tan(q_2 h_{cut} - m\pi) = \frac{n_2^2}{n_1^2} \cdot \frac{p_1}{q_2} \tag{2.69}$$

where h_{cut} is the cut-off height, m is the mode number and q_2 and p_1 are:

$$q_2 = \sqrt{k_0^2(n_2^2 - n_3^2)} \tag{2.70}$$

$$p_1 = \sqrt{k_0^2(n_3^2 - n_1^2)} \tag{2.71}$$

Figure 2.10 shows the cut-off heights of an SOI waveguide for TE and TM modes at a wavelength of 1.55µm. The upper cladding is water in this case and this has a refractive index, n_1 of 1.33 [2.23]. n_2 and n_3 are taken to be 3.5 and 1.45 respectively.

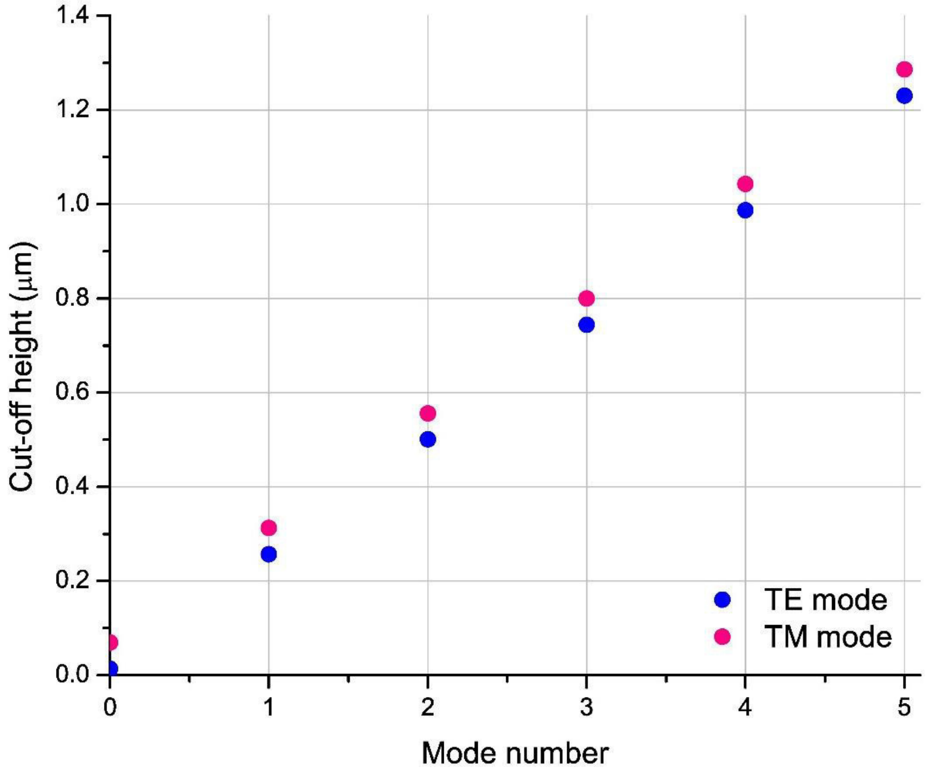

Figure 2.10: Cut-off heights of an SOI slab waveguide for TE and TM modes at a wavelength of 1.55µm.

From Figure 2.10, to maintain fundamental mode propagation the height of the waveguide should be between 0.013µm and 0.257µm for the TE mode and 0.07µm and 0.312µm for the TM mode at 1.55µm wavelength. As the height of the slab waveguide increases, more guided modes will propagate.

SOI waveguides can be designed to operate towards mid-infrared wavelengths [2.24]. However, the absorption of the buried oxide layer provides a limiting factor. Equations 2.68 and 2.69 were also used to calculate the minimum and maximum silicon core height for exclusively fundamental mode propagation for the TE and TM mode at wavelengths ranging from 1-10µm as shown in Figure 2.11. It is assumed for this illustrative calculation that the refractive indices of silicon and silicon dioxide are not dispersive which is not the case in practice [2.16].

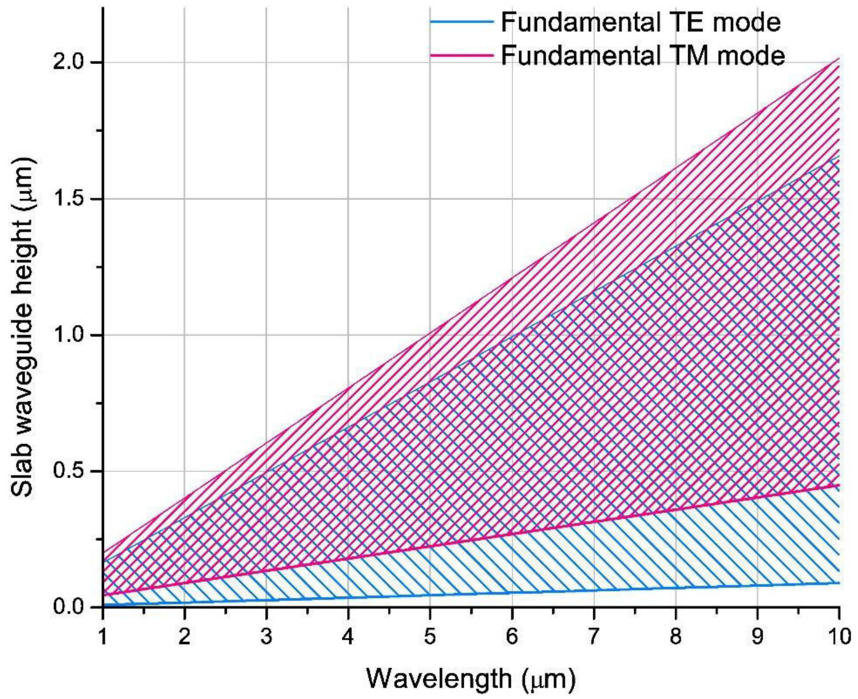

Figure 2.11: Slab waveguide height range for fundamental mode propagation in an SOI slab waveguide for wavelengths 1-10µm.

From Figure 2.11, as the wavelength increases the height range of the slab waveguide required for fundamental mode propagation increases. The area of overlap shows the slab waveguide heights at which fundamental mode propagation for both TE and TM modes will be possible.

In this project, the operating wavelength was fixed at 1.55µm.

2.8.2 Calculating sensitivity of an SOI slab waveguide

In this section, the sensitivity of an SOI slab waveguide is calculated for varying silicon core heights. In section 3.1.3 the same will be done with silicon ridge waveguides using commercial software.

As mentioned in sections 2.5 and 2.7 the sensitivity of the waveguide is governed by the change in the effective index (N_{eff}) relative to the change in the index of the upper cladding (n_1). This was expressed by equation 2.67 reproduced here as equation 2.72:

$$S = \frac{\Delta N_{eff}}{\Delta n_1} \tag{2.72}$$

The N_{eff} was introduced in section 2.1 expressed by equation 2.5 reproduced here as equation 2.73:

$$N_{eff} = n_2 sin\theta \tag{2.73}$$

For the asymmetric TE slab mode the following equation was used [2.2]:

$$k_0 n_2 hcos\theta - m\pi$$
$$= tan^{-1}\left[\frac{\sqrt{sin^2\theta - \left({}^{n_3}/_{n_2}\right)^2}}{cos\theta}\right] + tan^{-1}\left[\frac{\sqrt{sin^2\theta - ({}^{n_1}/_{n_2})^2}}{cos\theta}\right] \tag{2.74}$$

For the asymmetric TM slab mode the following equation was used:

$$k_0 n_2 hcos\theta - m\pi$$
$$= tan^{-1}\left[\frac{\sqrt{\left({}^{n_3}/_{n_2}\right)^2 sin^2\theta - 1}}{\left({}^{n_3}/_{n_2}\right)cos\theta}\right]$$
$$+ tan^{-1}\left[\frac{\sqrt{\left({}^{n_1}/_{n_2}\right)^2 sin^2\theta - 1}}{\left({}^{n_1}/_{n_2}\right)cos\theta}\right] \tag{2.75}$$

where h is the height of the core and m is equal to zero.

Solving equations 2.74 and 2.75 gives the value for ϑ. Once ϑ is known, N_{eff} can be calculated using equation 2.73.

Based on the equations above, a 1-D multilayer waveguide slab solver that is accessible online [2.25] was used to find the N_{eff} of TE and TM modes of the SOI slab waveguide. N_{eff} was found for TE and TM mode slab waveguides for varying core heights for n_1=1.33 and 1.32 (Δn_1 of 0.01) and then the sensitivity was calculated using equation 2.72 as is illustrated in Figure 2.12. n_2 and n_3 were fixed at 3.5 and 1.45 respectively. The wavelength used for the calculation was 1.55µm.

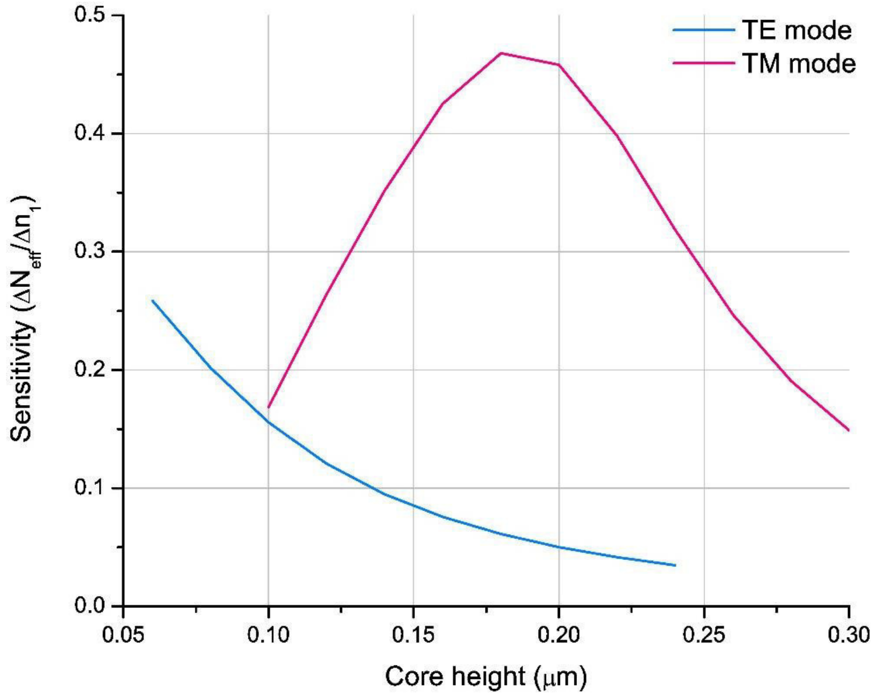

Figure 2.12: TE and TM mode sensitivity of an SOI slab waveguide calculated for varying silicon core heights.

From Figure 2.12 the TM mode is observed to be more sensitive towards a change in the index in the upper cladding, suggesting that the waveguides in the biosensor should operate in the TM mode. This is because the electric field is normal to the sensing surface as later illustrated in sections 3.1.3 and 3.1.4 for silicon ridge waveguides. Therefore, the rest of the simulation results in this chapter will be shown for the TM mode only.

Although from Figure 2.12 it is apparent that the optimum silicon core height is 0.18µm, in this project silicon core heights of 0.22µm, 0.25µm and 0.32µm are used due to the availability of wafers. Standard industrial silicon wafers have 0.22µm silicon core and 2µm oxide thickness on top of a silicon substrate [2.22].

A similar analysis was undertaken by Densmore *et al*. [2.26] where the ΔN_{eff} of slab waveguides was quantitatively evaluated with SOI, silicon nitride (Si_3N_4), polymer and silica cores (with index contrast of 2.03, 0.54, 0.05 and 0.01 respectively) to a Δn_1 of 0.01 for varying core thickness and a fixed oxide substrate (n_3=n_s=1.444) at wavelength of 1.55µm. Results from [2.26] are shown in Figure 2.13.

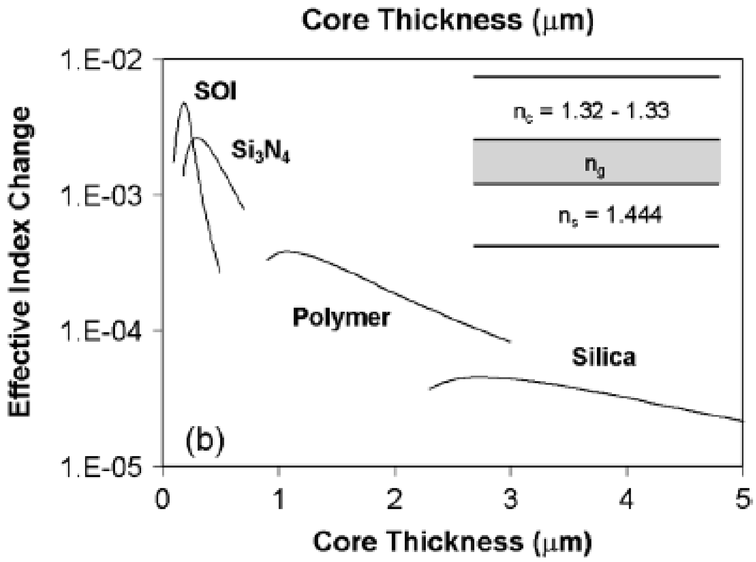

Figure 2.13: Change in effective index (ΔN_{eff}) of the TM mode for a change in 0.01 index in the cladding (Δn_c) for varying core thickness of SOI, Si_3N_4, polymer and silica [2.26]

Figure 2.13 shows that SOI has the highest sensitivity compared to Si_3N_4, polymer and silica concluding that a high index contrast material is crucial for obtaining a high sensitivity. Figure 2.13 also shows that as the index contrast decreases the core thickness at which highest sensitivity occurs increases.

2.8.3 Exploring the mid-infrared.

According to the ISO 20473 standard [2.27], the infrared wavelengths 0.7µm-1000µm can be subdivided as shown in Table 2.1.

Table 2.1: Spectral band designation for the infrared.

Designation of the radiation	Wavelength (µm)
Near infra-red (NIR)	0.78-3
Mid infra-red (MIR)	3-50
Far infra-red (FIR)	50-1000

Even though the 1.53-1.56μm range is designated to the NIR, it is known as the telecom wavelength as it is used for long-distance communication. This project uses the wavelength 1.55μm as SOI devices are designed for this operating wavelength. Silicon is transparent up to 8μm but SiO_2 absorbs heavily at wavelengths greater than 3.7μm [2.28] limiting the use of SOI at these longer wavelengths.

Analyte species are generally organic and absorb with distinct spectral "fingerprints" in the mid-infrared [2.6, 29] and therefore, sensing in the mid-infrared would not require surface functionalisation.

Chalcogenide glasses are amorphous semiconductors containing one or more of the following elements; sulfur (S), selenium (Se) and tellurium (Te) covalently bonded to elements such as arsenic (As), germanium (Ge), antimony (Sb) or gallium (Ga) [2.6]. Depending on the glass composition the refractive index of the glass would vary. Chalcogenide glasses have a wide transmission window of 0.4-20μm [2.6] and have been explored for evanescent wave sensing in the mid-infrared [2.30].

In this project, the sensitivity of evanescent sensors based on chalcogenide glasses is explored using the method introduced in section 2.8.2. A similar analysis to Figure 2.13 is performed for SOI and chalcogenide glass-based waveguides for the various refractive indices and wavelengths shown in Table 2.2. The sensitivity for varying core heights is illustrated in Figure 2.14.

The upper cladding, n_1, is water in this case with a refractive index of around 1.33 [2.23]. The chalcogenide glass indices are for the molecular structures $Ge_{15}As_{15}Se_{11}Te_{59}$ and $Ge_{17}As_{18}Se_{62}S_3$ and their corresponding indices are 3.359 and 2.53282 at a wavelength of 2.1μm [2.31]. Refractive index dispersion [2.32], though important for many applications, has been ignored in the present illustrative calculations.

Table 2.2: Values used for the sensitivity calculation of SOI and chalcogenide at varying wavelengths.

Material	n_1	n_2	n_3	Wavelength (μm)
SOI	1.33	3.5	1.45	1.55
SOI	1.33	3.5	1.45	3.8
Chalcogenide	1.33	3.359	2.53282	3
Chalcogenide	1.33	3.359	2.53282	6
Chalcogenide	1.33	3.359	2.53282	10

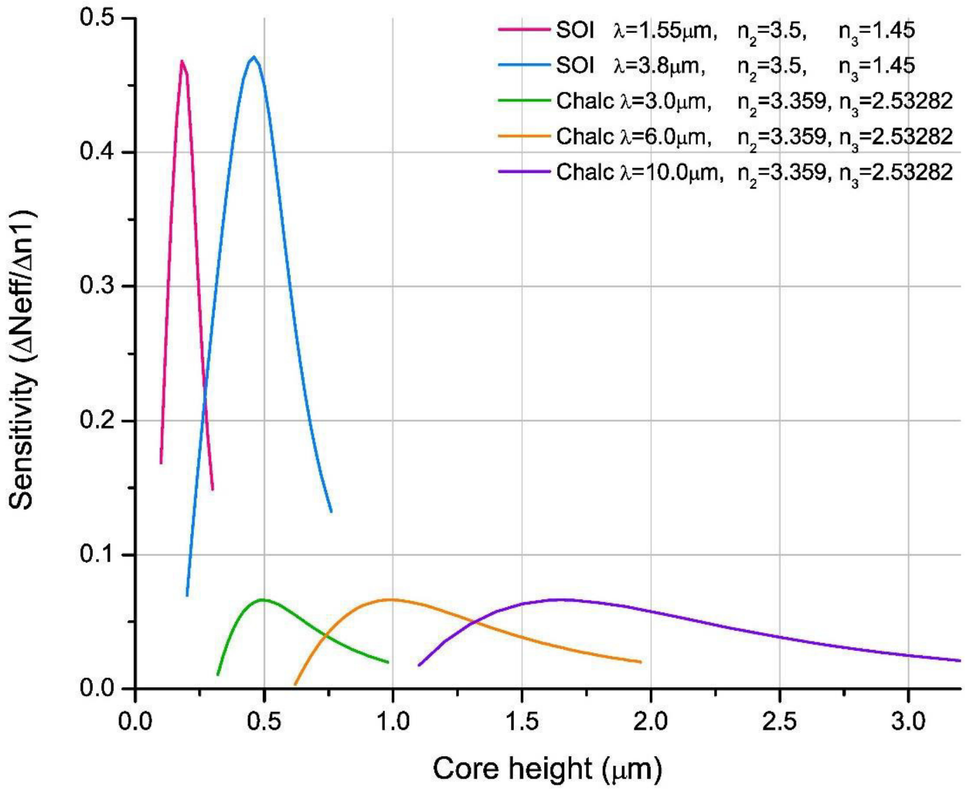

Figure 2.14: TM mode sensitivity for SOI and chalcogenide slab waveguide structures for varying core height at near and mid infrared wavelengths.

From Figure 2.14 sensitivity is higher for high index contrast material and vice versa regardless of the wavelength. As the wavelength increases the core height at which maximum sensitivity occurs increases.

Note from Figure 2.14 that all eight curves are similar in shape. In the next subsection, a method to normalise with regards to wavelength, refractive index and material thickness is described.

2.8.4 Asymmetry factor

In an attempt to present the results shown in Figure 2.14 on a universal sensitivity curve, a normalised film thickness, refractive index and frequency was considered. First, the frequency and heights of the upper cladding, core, lower cladding with refractive index n_1, n_2 and n_3 respectively were normalized using the following equation [2.33, 34]:

$$V = kh\sqrt{(n_2^2 - n_3^2)} \qquad (2.76)$$

where $k = 2\pi/\lambda$. V is defined as normalised frequency in the literature [2.33, 34] but in reality, equation 2.76 normalises both the frequency and the height of the waveguide.

The plots in Figure 2.14 can be replotted using V as shown in Figure 2.15.

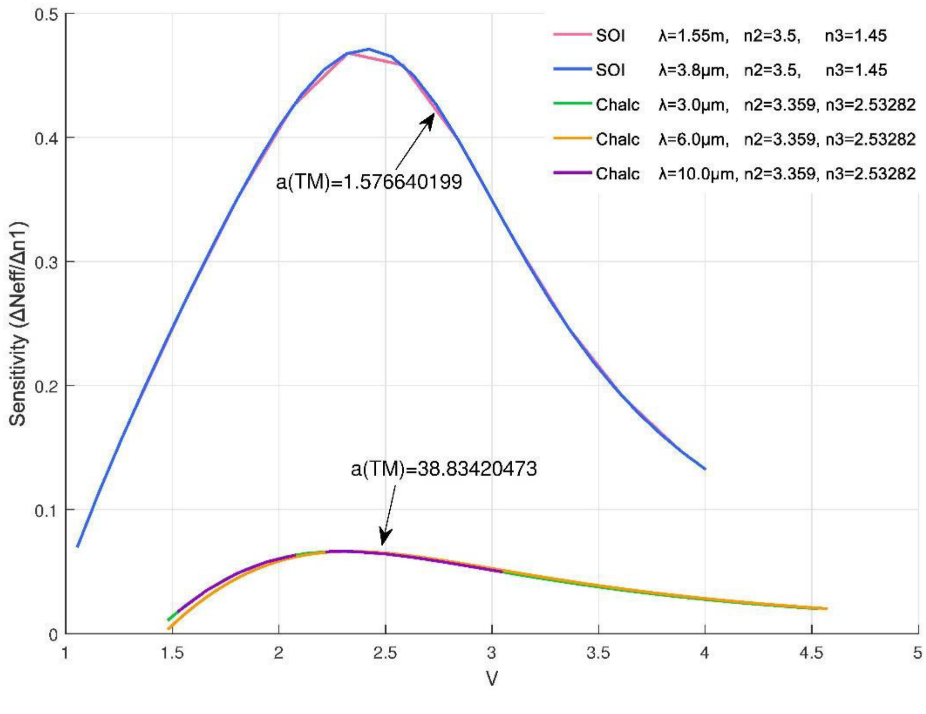

Figure 2.15: Normalised frequency and height vs sensitivity for various structures and wavelengths.

From Figure 2.15 slab waveguides with the same refractive index contrast follow the same curve. Slab waveguides with higher index contrast are more sensitive than the slab waveguides with smaller index contrast. So, it can be concluded that if the index contrast is known the sensitivity of the waveguide structure can be found using Figure 2.15. To facilitate this the refractive index of the slab can be normalised by the asymmetry factor, a, [2.33, 34]. The asymmetry factor for a TE mode in a slab waveguide is given by:

$$a(TE) = \frac{(n_3^2 - n_1^2)}{(n_2^2 - n_3^2)} \qquad (2.77)$$

and for TM mode it is given by:

$$a(TM) = \frac{n_2^4}{n_1^4} \cdot \frac{(n_3^2 - n_1^2)}{(n_2^2 - n_3^2)} \qquad (2.78)$$

Table 2.3 shows the TE mode and TM mode asymmetry factor calculated for the slab waveguide structures discussed in section 2.8.3. Slab waveguides with a lower a have a higher sensitivity. Therefore, if a is known for a slab waveguide then the sensitivity can be found using Figure 2.15.

Table 2.3: TE mode and TM mode asymmetry factor for SOI and chalcogenide slab waveguide structure.

Material	n_1	n_2	n_3	a (TE)	a (TM)
SOI	1.33	3.5	1.45	0.032875092	1.576640199
Chalcogenide	1.33	3.359	2.53282	0.954511059	38.83420473

The normalised plot of Figure 2.15 suggests that a chalcogenide-glass based slab waveguide structure with n_2=3.359 and n_1=1.457 would be comparable to the SOI slab waveguide structure in terms of sensitivity. Whilst waveguides comprised of a chalcogenide glass (AsSe) guiding layer deposited on a silicon dioxide layer have been demonstrated in [2.35] the absorption of the oxide layer would again restrict operation to the NIR. Nevertheless given that the molecular species exhibit absorption bands at higher wavelengths in the mid-infrared range [2.29], the use of chalcogenide waveguides is worth exploring in future work. In spite of this, given the scope of this project, the rest of the thesis will focus on SOI waveguides at an operating wavelength of 1.55µm.

2.9 Coupling light into the waveguide

In chapter 3, ridge waveguide dimensions will be reduced to 500nm × 220nm to enhance the performance of the sensor and increase packaging density. This makes coupling light in and out of the circuit difficult. Coupling light from a laser to the waveguide and coupling light out of the waveguide to a power meter or camera is an important function of the device that must be incorporated into the design.

In chapter 4, light from a tunable laser is coupled into the circuit through a tapered fibre and at the output the light is imaged by an infrared sensitive camera. Light from a tapered fibre can be coupled to the waveguide by one of the methods explained below. In this project both butt coupling and grating coupling were used. The theory is discussed in this section; numerical simulation and fabrication will be discussed in sections 3.5 and 4.5 respectively.

2.9.1 Butt coupling and end-fire coupling

Butt coupling and end-fire coupling techniques are quite similar in that light is incident on the end facet of the waveguide. In butt coupling the light is focused on to the waveguide using a tapered fibre and for end-fire coupling the light is focused using a lens as illustrated in figures 2.17a and 2.17b respectively.

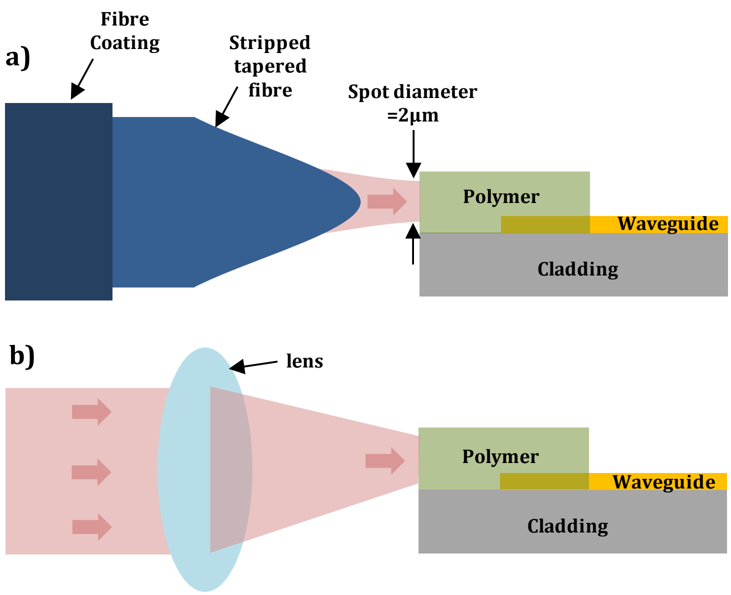

Figure 2.16: Illustration of a) Butt coupling and b) End-fire coupling.

The cross-section of the waveguide is too small to efficiently couple light directly. Therefore, in both cases, a tapered structure was fabricated above the waveguide using a polymer to enlarge the cross-section of the input waveguide to enable better coupling. The light travels through the polymer and couples into the waveguide. This will be explained in more detail in section 3.5.1.

2.9.2 Grating coupling

This method is gaining popularity rapidly as aligning the input beam to the waveguide is easier compared to the previous method, even though the input must be at a certain angle as shown in Figure 2.17. Another advantage is that only a specific mode can be excited which is a requirement for this project.

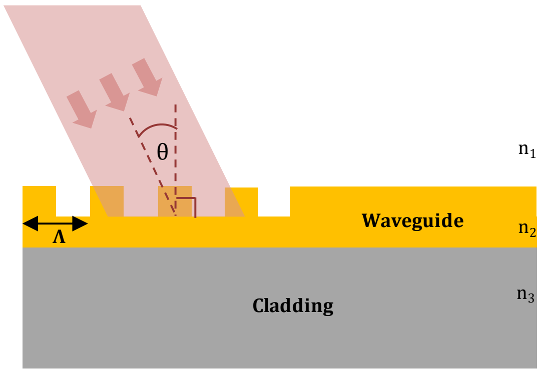

Figure 2.17: Illustration of grating coupling.

In order to couple light into the waveguide the phase matching condition must be met. This means the propagation constant in the z direction must be the same. This is given by the equation below:

$$\beta \ = k_z = k_0 n_1 sin\theta \tag{2.79}$$

Since $\beta \geq k_0 n_1$, gratings are required to couple light into the waveguide. The period, Λ, of the grating is given by the following equation [2.2]:

$$\Lambda = \frac{\lambda_0}{N_{eff} n_1 sin\theta} \tag{2.80}$$

More details on the design and coupling efficiency of a grating coupler will be presented in section 3.5.2.

2.10 Chapter summary

This chapter introduced basic waveguide theory and the concept on which the optical sensor is based. Material and height of the base planar slab waveguide was optimized. In Chapter 3, these waveguides will be used to design a Mach-Zehnder interferometer (MZI) which is the sensing element of the biosensor. Commercial software based on Beam propagation method (BPM) and Eigenmode expansion (EME) method numerical analysis will be used for the design and simulations as will be explained in chapter 3.

References

[2.1] R. J. Bozeat, "Thin Film Optical Waveguides on Silicon," PhD, University of Nottingham, 1993.

[2.2] G. T. Reed and A. P. Knights, *Silicon photonics: An introduction*. West Sussex: John Wiley & Sons, 2004.

[2.3] R. J. Deri and E. Kapon, "Low-loss III-V semiconductor optical waveguides," *IEEE Journal of Quantum Electronics,* vol. 27, pp. 626-640, 1991.

[2.4] L. Vivien and L. Pavesi, *Handbook of Silicon Photonics*. Boca Raton: Taylor & Francis, 2013.

[2.5] M. L. Anne, J. Keirsse, V. Nazabal, K. Hyodo, S. Inoue, C. Boussard-Pledel, H. Lhermite, J. Charrier, K. Yanakata, O. Loreal, J. Le Person, F. Colas, C. Compere, and B. Bureau, "Chalcogenide glass optical waveguides for infrared biosensing," *Sensors (Basel),* vol. 9, pp. 7398-7411, 2009.

[2.6] B. J. Eggleton, B. Luther-Davies, and K. Richardson, "Chalcogenide photonics," *Nat. Photon,* vol. 5, pp. 141-148, 2011.

[2.7] H. Ma, A. K.-Y. Jen, and L. R. Dalton, "Polymer-based optical waveguides: Materials, processing, and devices," *Advanced Materials,* vol. 14, pp. 1339-1365, 2002.

[2.8] A. Yeniay, R. Gao, K. Takayama, R. Gao, and A. F. Garito, "Ultra-Low-Loss Polymer Waveguides," *Journal of Lightwave Technology,* vol. 22, pp. 154-158, 2004.

[2.9] G. Fischbeck, R. Moosburger, C. Kostrzewa, A. Achen, and K. Petermann, "Singlemode optical waveguides using a high temperature stable poylmer with low losses in the 1.55 µm range," *Electronics letters,* vol. 33, pp. 518-519, 1997.

[2.10] F. A. Benson and T. M. Benson, *Fields, Waves and Transmission Lines. London*: Chapman & Hall, 1991.

[2.11] M. Noureddine, "Fourier variational methods for the analysis of optical waveguides and lasers," PhD, The University of Nottingham, 1998.

[2.12] F. I. Princeton University, "TheFreeDictionary," vol. WordNet 3.0, Farlex Clipart Collection, ed. Huntington Valley, USA, 2003-2008.

[2.13] G. J. Veldhuis, O. Parriaux, H. J. W. M. Hoekstra, and P. V. Lambeck, "Sensitivity enhancement in evanescent optical waveguide sensors," *Journal of Lightwave Technology,* vol. 18, pp. 677-682, 2000.

[2.14] J. Atencia and D. J. Beebe, "Controlled microfluidic interfaces," *Nature,* vol. 437, pp. 648-655, 2004.

[2.15] H. A. Stone, A. D. Stroock, and A. Ajdari, "Engineering Flows in Small Devices: Microfluidics Toward a Lab-on-a-Chip," *Annual Review of Fluid Mechanics,* vol. 36, pp. 381-411, 2004.

[2.16] H. Li, "Refractive index of silicon and germanium and its wavelength and temperature derivatives," *Journal of Physical and Chemical Reference Data,* vol. 9, pp. 561-658, 1980.

[2.17] I. Malitson, "Interspecimen comparison of the refractive index of fused silica," *Journal of the Optical Society of America,* vol. 55, pp. 1205-1209, 1965.

[2.18] J. L. Coffer, *Semiconducting silicon nanowires for biomedical applications*. Cambridge: Elsevier, 2014.

[2.19] M.-J. Bañuls, R. Puchades, and Á. Maquieira, "Chemical surface modifications for the development of silicon-based label-free integrated optical (IO) biosensors: A review," *Anal. Chimica Acta,* vol. 777, pp. 1-16, 2013.

[2.20] S. Ciampi, J. B. Harper, and J. J. Gooding, "Wet chemical routes to the assembly of organic monolayers on silicon surfaces via the formation of Si–C bonds: Surface preparation, passivation and functionalization," *Chemical Society Reviews,* vol. 39, pp. 2158-2183, 2010.

[2.21] O. Kononchuk and B.-Y. Nguyen, *Silicon-on-insulator (SOI) technology: Manufacture and Applications*. Cambridge: Elsevier, 2014.

[2.22] A. E.-J. Lim, J. Song, Q. Fang, C. Li, X. Tu, N. Duan, K. K. Chen, R. P.-C. Tern, and T.-Y. Liow, "Review of silicon photonics foundry efforts," *IEEE Journal of Selected Topics in Quantum Electronics,* vol. 20, pp. 405-416, 2014.

[2.23] D. J. Segelstein, "The complex refractive index of water," M. S. Thesis, Department of Physics, University of Missouri--Kansas City, 1981.

[2.24] G. Z. Mashanovich, M. M. Milosevic, M. Nedeljkovic, N. Owens, B. Xiong, E. J. Teo, and Y. Hu, "Low loss silicon waveguides for the mid-infrared," *Opt. Express,* vol. 19, pp. 7112-7119, 2011.

[2.25] (Accessed 15 Apr 2017). *1-D multilayer slab waveguide mode solver*. Available: http://www.computational-photonics.eu/oms.html

[2.26] A. Densmore, D. X. Xu, P. Waldron, S. Janz, P. Cheben, J. Lapointe, A. Delage, B. Lamontagne, J. H. Schmid, and E. Post, "A silicon-on-insulator photonic wire based evanescent field sensor," *Photonics Technology Letters, IEEE,* vol. 18, pp. 2520-2522, 2006.

[2.27] I. O. f. Standardization, "ISO 20473," ed. Switzerland, 2007.

[2.28] R. A. Soref, S. J. Emelett, and W. R. Buchwald, "Silicon waveguided components for the long-wave infrared region," *Journal of optics A: pure and applied optics,* vol. 8, p. 840, 2006.

[2.29] A. B. Seddon, "A prospective for new mid-infrared medical endoscopy using chalcogenide glasses," *International Journal of Applied Glass Science,* vol. 2, pp. 177-191, 2011.

[2.30] J. Charrier, M.-L. Brandily, H. Lhermite, K. Michel, B. Bureau, F. Verger, and V. Nazabal, "Evanescent wave optical micro-sensor based on chalcogenide glass," *Sensors and Actuators B: Chemical,* vol. 173, pp. 468-476, 2012.

[2.31] W. Pan, "Development of hot embossing for fabricating optical waveguides based on chalcogenide glasses," PhD, University of Nottingham, 2008.

[2.32] H. G. Dantanarayana, N. Abdel-Moneim, Z. Tang, L. Sojka, S. Sujecki, D. Furniss, A. B. Seddon, I. Kubat, O. Bang, and T. M. Benson, "Refractive index dispersion of chalcogenide glasses for ultra-high numerical-aperture fiber for mid-infrared supercontinuum generation," *Optical Materials Express,* vol. 4, pp. 1444-1455, 2014.

[2.33] H. Kogelnik and V. Ramaswamy, "Scaling rules for thin-film optical waveguides," *Applied Optics,* vol. 13, pp. 1857-1862, 1974.

[2.34] R. C. Alferness, W. Burns, J. Donelly, I. Kaminow, H. Kogelnik, F. Leonberger, A. Milton, T. Tamir, R. Tucker, and T. Tamir, *Guided-wave optoelectronics* vol. 26. Berlin: Springer Science & Business Media, 2013.

[2.35] M. D. Pelusi, V. G. Ta'eed, L. Fu, E. Magi, M. R. Lamont, S. Madden, D.-Y. Choi, D. A. Bulla, B. Luther-Davies, and B. J. Eggleton, "Applications of highly-nonlinear chalcogenide glass devices tailored for high-speed all-optical signal processing," *IEEE Journal of Selected Topics in Quantum Electronics,* vol. 14, pp. 529-539, 2008.

Chapter 3

3 DESIGN

In Chapter 2 an introduction to electromagnetic theory and the principles of an evanescent field sensor was presented. Furthermore, the waveguide material and geometry used in the sensor work described in this thesis were discussed. In this chapter, commercial software is used to investigate waveguide geometry to give maximum sensitivity while keeping ease and cost of fabrication in mind. Subsequently the components of the sensor (straight waveguide, curved waveguide, Y-splitters, Mach-Zehnder interferometer, plasmonic interferometer, multimode interferometer, tapers and grating couplers) will be modelled, compared with literature and then designed individually.

3.1 MODELLING WAVEGUIDES

Mainly two commercial software were used in the modelling of this project; RSoft BeamPROP and FIMMPROP which rely on the numerical methods Beam propagation method (BPM) and Eigenmode expansion (EME) method respectively for simulating propagation in optical waveguides. FIMMPROP is an integrated propagation module in the software FIMMWAVE which is a fully vectorial mode solver for 2D+Z waveguides. A brief introduction to BPM and EME is given below and subsequently the waveguides are designed and characterised.

3.1.1 Beam propagation (BPM) method

The Beam propagation method (BPM) is the most widely used technique for modelling light propagation in integrated and fibre-optic waveguide devices and circuits [3.1]. It was developed for the analysis of light propagation in slowly varying non-uniform guiding structures such as tapers, bends and couplers. BPM can solve in scalar, semi-vector or vector form (as mentioned in section 2.4), solve for paraxial or wide-angle beams [3.2], include different numerical implementations (such as the finite-difference FD-BPM [3.3], fast Fourier transform FFT-BPM [3.4] and the finite-element FE-BPM) and boundary conditions, handle reflections and perform mode solving. The BPM method is straightforward, efficient and flexible which allows for a large range of applications [3.5]. In the FFT-BPM the electromagnetic field is calculated by a superposition of plane waves propagating in a homogenous medium. The electromagnetic field propagating in an inhomogeneous waveguide configuration is calculated by integrating the fields in the spectral domain and applying phase correction in the spatial domain at each Δz [3.6].

3.1.2 Eigenmode expansion (EME) method

The Eigenmode expansion (EME) method computes in the frequency domain. As shown in section 2.3 a typical waveguide has a few guided modes and an infinite number of radiation modes which can be calculated using Maxwell's equations. The decomposition of a general excitation into a summation of these modes at each cross-section gives the Eigenmode expansion of the field supported by the device at each Δz.

In theory, an exact solution can be obtain using an infinite number of modes but in practice the number of modes is limited and can be solved by considering a modest number of them. The EME propagation algorithm is bi-directional, solves for wide angle, can solve in semi-vector and vector forms and uses a scattering matrix (S-matrix) technique to join different sections of a device [3.7].

3.1.3 Finding optimum height

In section 2.8.2 the effective index method was used to estimate the sensing performance of a Silicon-on-Insulator (SOI) slab waveguide as a function of core height. The sensitivity is calculated by the following equation as stated in section 2.7:

$$S = \frac{\Delta N_{eff}}{\Delta n_1} \tag{3.1}$$

where N_{eff} and n_1 are the effective index and cover index respectively.

In this section, the sensitivity is found for a waveguide of 2D cross-section (longitudinally invariant). The core height was varied for ridge waveguides of widths 0.5µm and 1µm as illustrated in Figure 3.1. A width of 0.5µm was used as the waveguide is single mode at this width which is a common width used in literature [3.8]. Additionally, the sensitivity does not change much for widths in the range of 0.25-0.6µm, as shown in section 3.1.4 where it is concluded that a width of 0.5µm should be used to reduce fabrication errors. A width of 1µm is used so that the waveguide can be compared to a laterally multi-mode slab waveguide structure as in section 2.8.2. A 2µm oxide (SiO_2) thickness was used for this project due to wafer availability as mentioned in section 2.8.2. The standard industrial oxide thickness is between 1-3µm [3.9] and in section 3.1.6 it is shown that an oxide thickness in this range presents low substrate leakage at an operating wavelength around 1.55µm resulting in an acceptably low propagation loss.

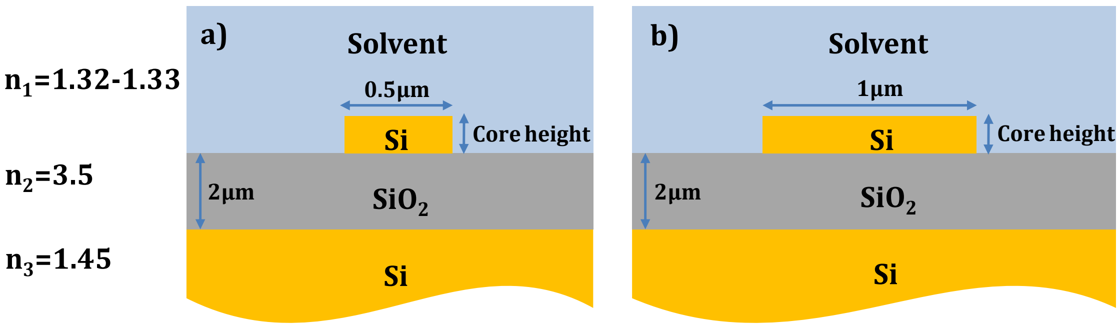

Figure 3.1: Ridge waveguide with width a) 0.5µm and b) 1µm for varying core heights.

The core height was varied from 0.14-0.34µm to ensure the waveguide is vertically single mode. The change in cover index, Δn_1, is 1.32-1.33 which assumes the solvent is water based [3.10]. The sensitivity was calculated for an operating wavelength of 1.55µm using the software FIMMWAVE mode solver [3.11] for vectorial and semi-vectorial TE-like and TM-like fundamental modes. Results are presented in Figure 3.2.

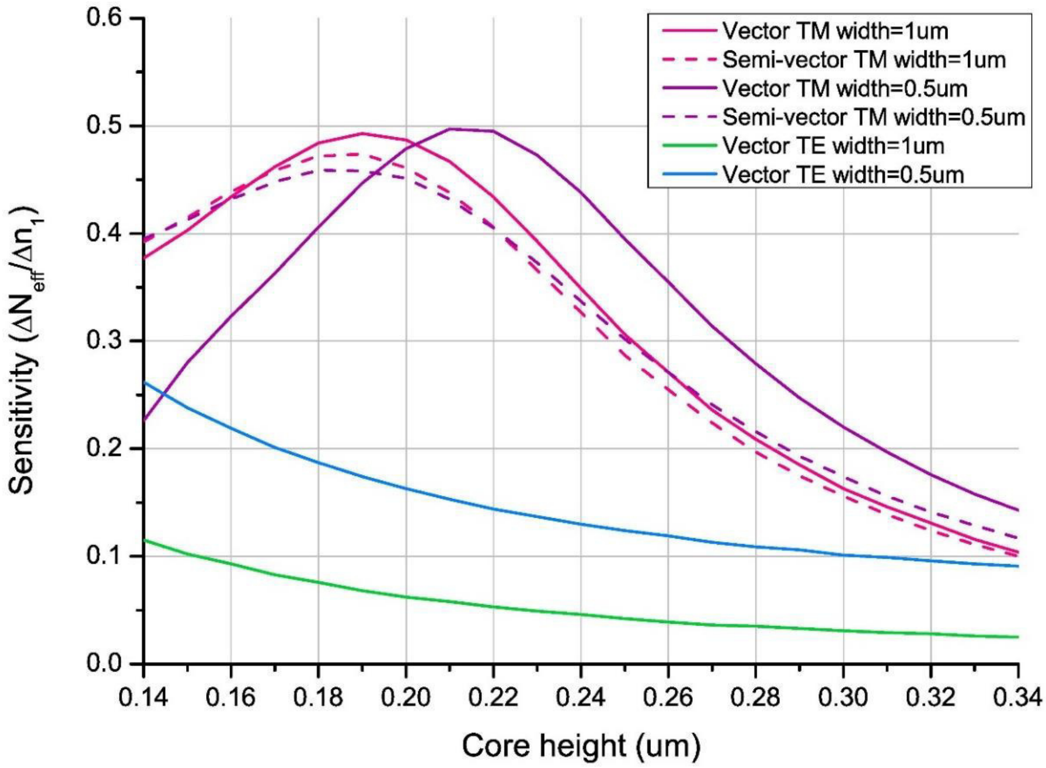

Figure 3.2: Silicon ridge waveguide sensitivity for Vector and Semi-vector TE-like and TM-like modes for varying core heights.

From Figure 3.2 it is shown that the sensitivity obtained for a SOI ridge waveguide is like that of SOI slab waveguide, as was shown in figure 2.12. Although in both figure 2.12 and Figure 3.2 the highest sensitivity is obtained when the core height is in the range of 0.18-0.22µm, a core height of 0.22µm is preferred in order to take advantage of standard industrial SOI fabrication processes [3.9].

Figure 3.3 illustrates the fundamental vector TM-like mode distribution (E_y component) at an operating wavelength of 1.55µm in a 0.5µm wide waveguide for varying core heights. In Figure 3.3a the core height is 0.14µm where the silicon core is weakly guiding and most of the model field resides in the silicon dioxide substrate. In Figure 3.3b and c the core height is 0.18µm and 0.22µm respectively and the mode can be seen to penetrate significantly into the upper cladding region which is a solution of refractive index 1.33 in this case. In Figure 3.3d the core height is 0.32µm and at this core height the mode is well confined to the core.

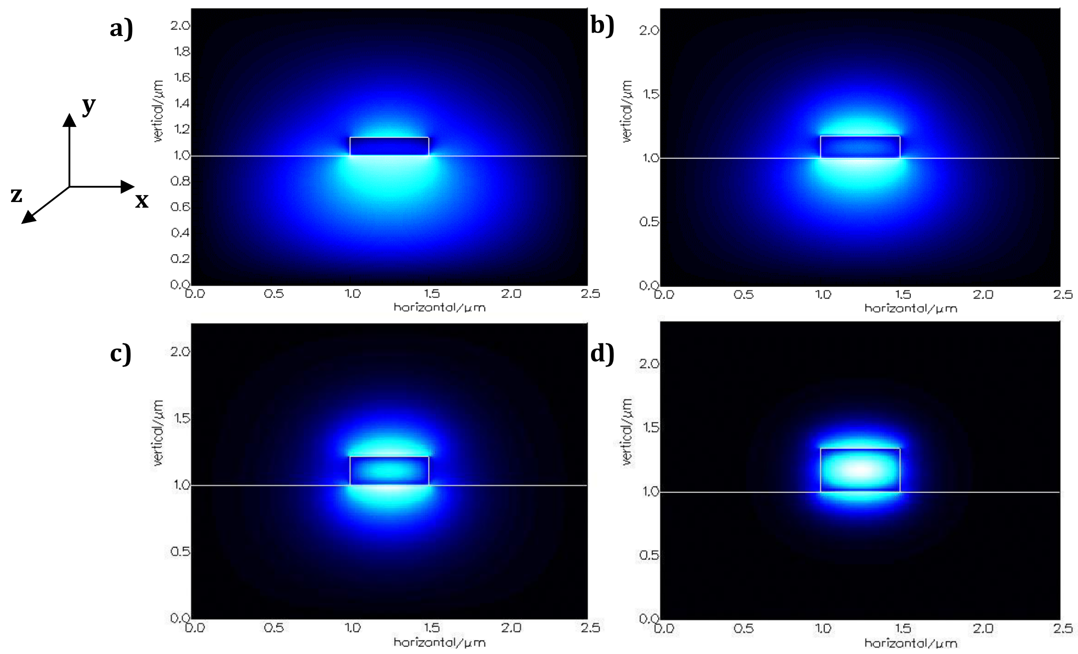

Figure 3.3: Distribution of the principal electric field component (E_y) for the fundamental Vector TM-like mode in a silicon ridge waveguide of width 5µm and core height a) 0.14µm, b) 0.18µm, c) 0.22µm and d) 0.32µm.

3.1.4 Finding optimum width

In the previous section the optimum core height was found to be in the range of 0.18-0.22µm. In this section, the core width was varied for a fixed core height of 0.22µm as illustrated in Figure 3.4.

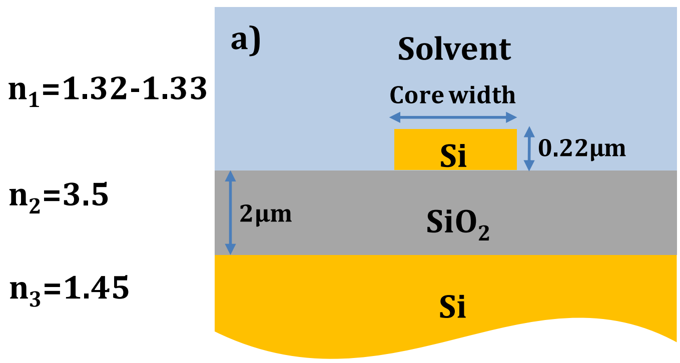

Figure 3.4: Ridge waveguide with core height 0.22µm for varying core widths.

The core width was varied from 0.16-0.60µm for vector TE-like mode and 0.25-0.60 for the vector TM-like mode to ensure single mode operation of the waveguide. As previously discussed the change in cover index, Δn_1, is 1.32-1.33. As in the previous sub-section, the sensitivity was calculated for an operating wavelength of 1.55µm using the software FIMMWAVE mode solver [3.11] for vectorial and semi-vectorial TE-like and TM-like fundamental modes. Results are presented in Figure 3.5.

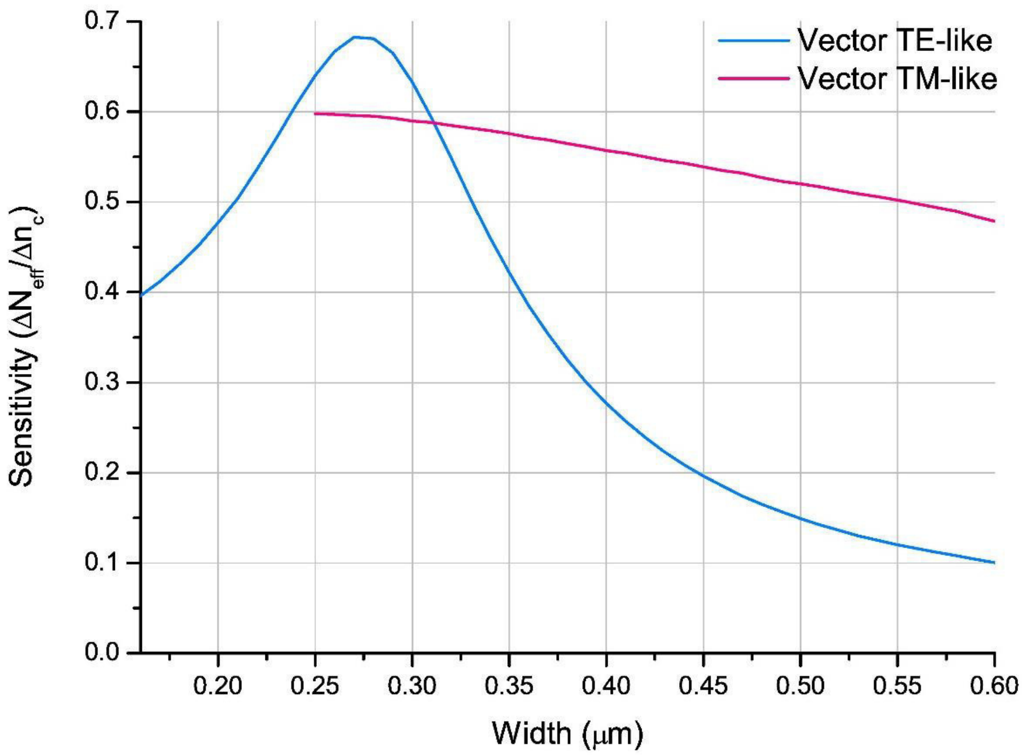

Figure 3.5: Silicon ridge waveguide sensitivity for Vector TE-like and Vector TM-like fundamental modes for varying waveguide widths.

In Figure 3.5, when the width of the waveguide is varied the sensitivity of the waveguide changes significantly for the vector TE-like mode whereas the sensitivity is not affected considerably for the vector TM-like mode. Keeping ease, cost and tolerance of fabrication in mind the waveguides in this project will have a fixed core height of 0.22µm and a width of 0.5µm and will operate in the vector TM-like mode with a high sensitivity of ≈0.5.

3.1.5. Evanescent field and heterogeneous sensing

In section 2.3 it was shown that the guided-mode fields in a slab waveguide decay exponentially above and below the slab and this field is known as the evanescent field (EF). The same is true for the guided-mode fields in (2D) ridge waveguides. Figure 3.6 and Figure 3.7 show the fundamental vector TE-like and vector TM-like field distribution in a 0.5 × 0.22µm SOI waveguide respectively.

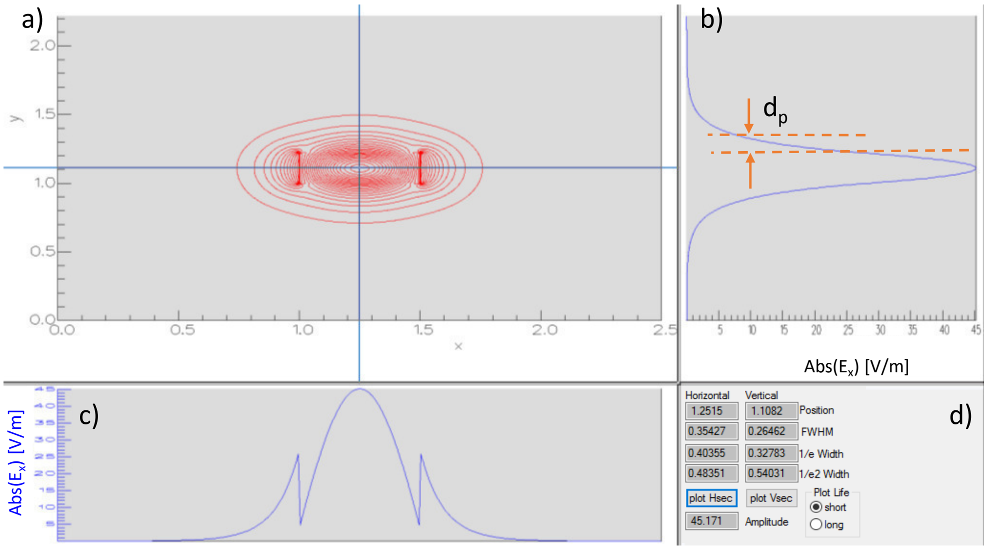

Figure 3.6: a) Contour graph, b) vertical cross-section of principal E_x field component, c) horizontal cross-section of principle E_x field component and d) axis properties at which E_x field distribution is imaged for a vector TE-like field distribution in a 0.5 × 0.22µm SOI waveguide at a wavelength of 1.55µm.

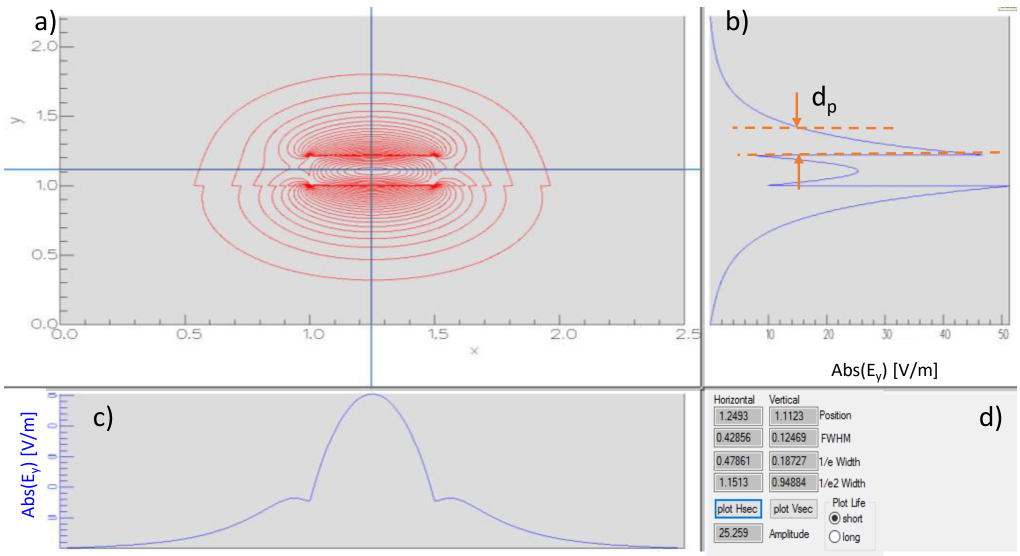

Figure 3.7: a) Contour graph, b) vertical cross-section of principal E_y field component, c) horizontal cross-section of principle E_y field component and d) axis properties at which E_y field distribution is imaged for a vector TM-like field distribution in a 0.5 × 0.22µm SOI waveguide at a wavelength of 1.55µm.

From Figure 3.6 and Figure 3.7 both vector TE-like and TM-like modes have evanescent fields that decay exponentially outwards from the silicon surfaces of the waveguide. For the vector TE-like mode the evanescent field is stronger on either side of the waveguide whereas for the vector TM-like mode the evanescent field is stronger on top and below the waveguide. The height of the evanescent field tail which interacts with the solvent is known as the penetration depth, d_p as illustrated in Figure 3.6b and Figure 3.7b.

The penetration depth can be found using equation 3.2:

$$EF = E_0 e^{\frac{-y}{d_p}} \tag{3.2}$$

Where d_p is the penetration depth and y is the distance from the silicon core surface as explained in section 2.5.

Using equation 3.2 the d_p for the vector TE-like and vector TM-like mode in Figure 3.6 and Figure 3.7 are calculated to be 0.104µm and 0.178µm respectively. From this it can be concluded that d_p is 58% greater for TM-like mode compared to the TE-like mode. It is worth mentioning that d_p from equation 3.2 does not consider the complete EF as illustrated in Figure 3.6b and Figure 3.7b.

As explained in section 2.5, homogeneous sensing is when the entire upper cladding (n_1) index changes, causing an effective index change (ΔN_{eff}) in the waveguide. In an immunosensor the waveguides in the sensing window are covered in antibodies which bind to receptor molecules changing the refractive index at the surface of the waveguide. The region that undergoes a change in refractive index is known as the adsorbed layer or adlayer and is illustrated in Figure 3.8.

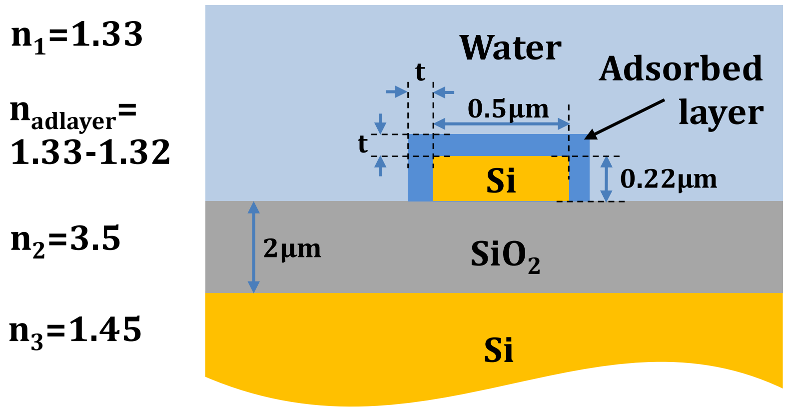

Figure 3.8: Ridge waveguide with adsorbed layer of thickness, t.

The thickness, *t* of the adsorbed layer was varied from 0 to 1µm and the sensitivity at a wavelength of 1.55µm was calculated using equation 3.1 as illustrated in Figure 3.9.

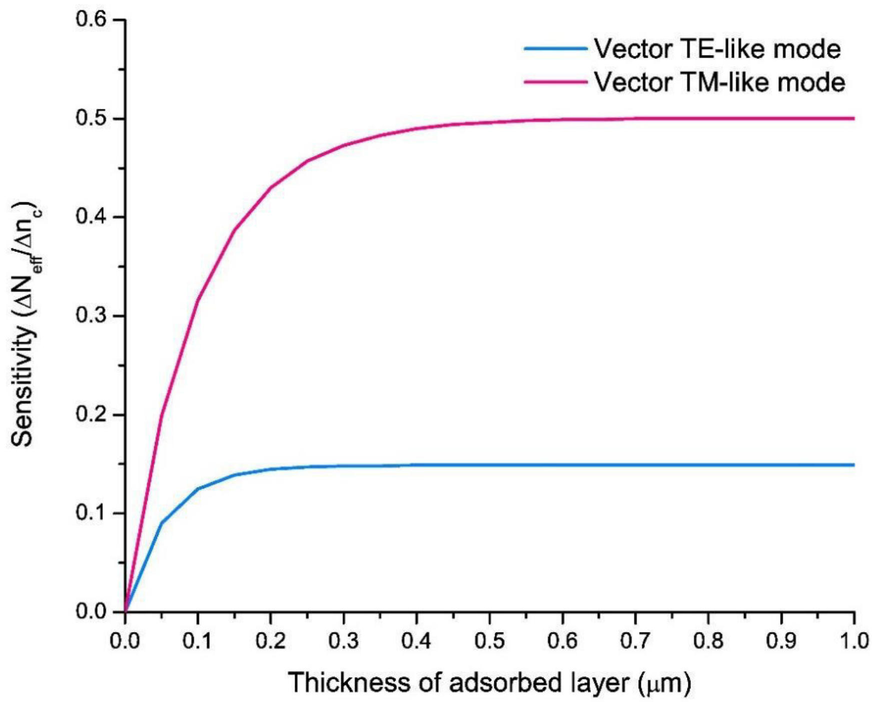

Figure 3.9: Sensitivity as a function of adsorbed layer thickness for vector TE-like and TM-like modes for a silicon waveguide of height 0.22µm, width 0.5µm and an operating wavelength of 1.55µm.

From Figure 3.9 it is shown that the sensitivity has no change when the adsorbed layer thickness is zero. As the thickness increases the sensitivity increases until it reaches its maximum sensitivity of 0.149 and 0.5 for the fundamental vector TE-like and TM-like modes respectively. The thickness of adsorbed layer at maximum sensitivity is 0.4µm and 0.7µm respectively which means after this point the waveguide would behave like a homogenous sensor.

3.1.6. Slot waveguides

Slot waveguides, as illustrated schematically in Figure 3.10, were introduced by Almeida *et al.* [3.12] and experimentally demonstrated by Xu *et al*. [3.13] in 2004. Light is guided and strongly confined inside a nano-metre scale region of low refractive index. It is caused by the large discontinuity of the electric field at high index contrast (HIC) interfaces and guided by external reflection and therefore the modes in this structure are inherently leaky modes [3.12].

While slot waveguides have been mainly used in microring resonators for biosensing applications [3.14, 15] more recently they have also been explored as planar slot waveguides for fluorescence or absorption based optical sensing [3.16-18] and Francesco Dell'Olio and Vittorio M. N. Passaro [3.17] perfomed a detailed analysis of this.

In this section the results published in [3.17] for slot waveguides and silicon wires are reproduced with FIMMWAVE in order to compare of the two approaches and to validate the simulation data used in this project. The published paper investigated modal behaviour by a full-vectorial 2D finite element method FEM using the commercial software COSMOL Multiphysics [3.19] whereas in this project a full-vectorial 2D FEM is used by FIMMWAVE mode solver.

Figure 3.10 illustrates the slot waveguide structure and the key parameters used. The wavelength is fixed at 1.545µm as in [3.17]. The cover medium index, n_c is varied from 1.333 to 1.335 to calculate sensitivity from equation 3.1. The refractive index of silicon is not specified in the published paper therefore an index of 3.476 is used as pre-defined by FIMMWAVE. The silicon core height is 0.25µm and the index of silicon dioxide is taken as 1.444 as stated in the paper.

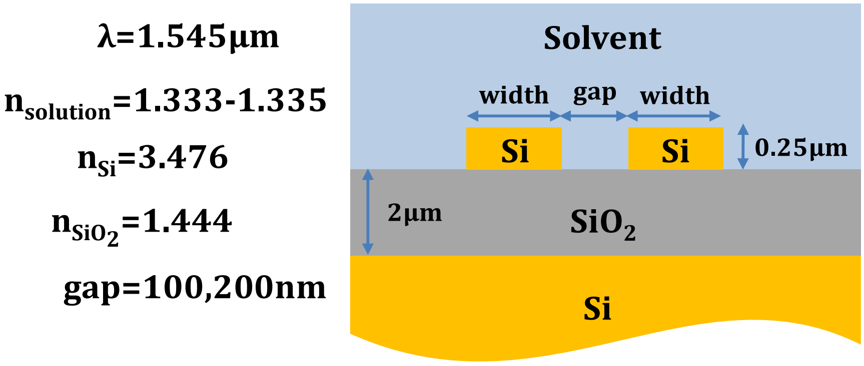

Figure 3.10: Schematic illustration of an SOI slot waveguide structure and parameters.

The slot waveguide sensitivity dependence on Si-wire width, *w* has been investigated for a gap width *g* of 100nm and 200nm for the fundamental vector TE-like and TM-like modes (also referred to as quasi-TE and quasi-TM modes respectively) as illustrated in Figure 3.11. In Figure 3.11 the width was varied from 0.16μm-0.28μm to allow easier comparison with results published in [3.17], and to view the sensitivity dependence over a wider width; also see Figure 3.16 and Figure 3.18 where a larger range of widths is considered.

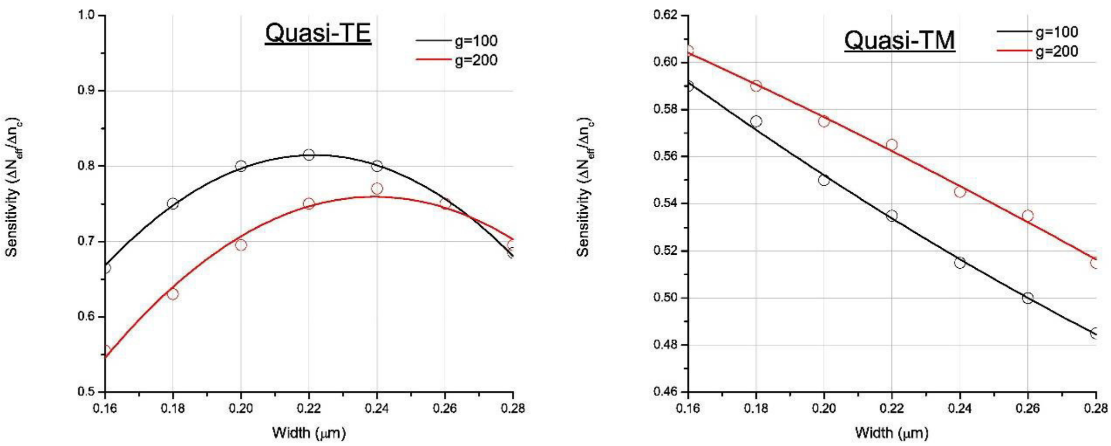

Figure 3.11: SOI slot waveguide dependence on waveguide width for g=100nm and g=200nm simulated with FIMMWAVE for an operating wavelength of 1.545μm.

In Figure 3.11, the quasi TE sensitivity increases first and then decreases as *w* increases for both g=100 and 200nm. Quasi-TM sensitivity decreases as *w* increases for both *g* values. Both trends are in general agreement with results published in [3.17]. Convergence has been checked by varying mesh size. Changing the wavelength slightly or changing the refractive index of silicon slightly does not affect the sensitivity graph significantly. Changing the silicon core height from 250nm to 220nm reduces the sensitivity slightly but the general trend with waveguide width stays the same. From both graphs in Figure 3.11, the quasi-TE mode has a higher sensitivity than quasi-TM mode to a change in refractive index of the cover medium. This is because of the strong optical confinement in the cover medium of the quasi-TE mode compared to the quasi-TM mode as visualised in Figure 3.12 for slot waveguides of *g*=100nm and *w*=0.22μm at an operating wavelength of 1.545μm.

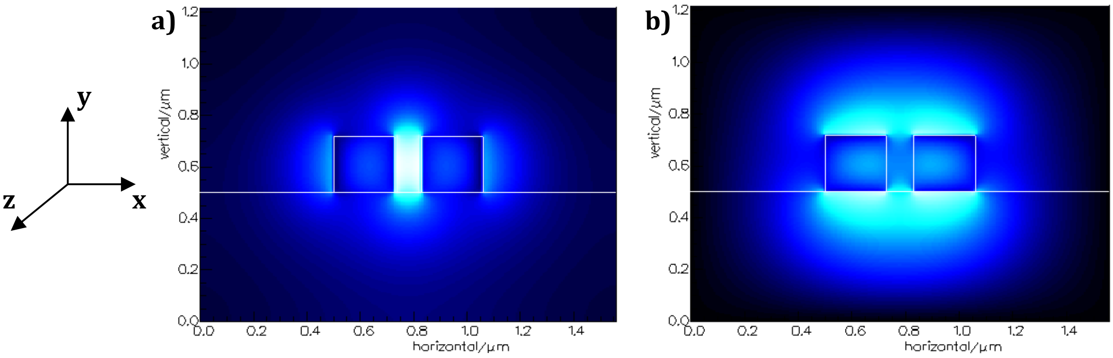

Figure 3.12: a) Principal electric field distribution for the fundamental Quasi-TE and b) Quasi-TM mode for SOI slot waveguide structure of g=100nm and w=0.22μm at wavelength of 1.55μm.

Note that the optical confinement for operating wavelength of 1.55μm looks the same as the optical confinement for operating wavelength of 1.545μm as seen in Figure 3.12.

Figure 3.13 is a schematic illustration of SOI rib and ridge (also referred to as a photonic wire) waveguide and used in [3.17].

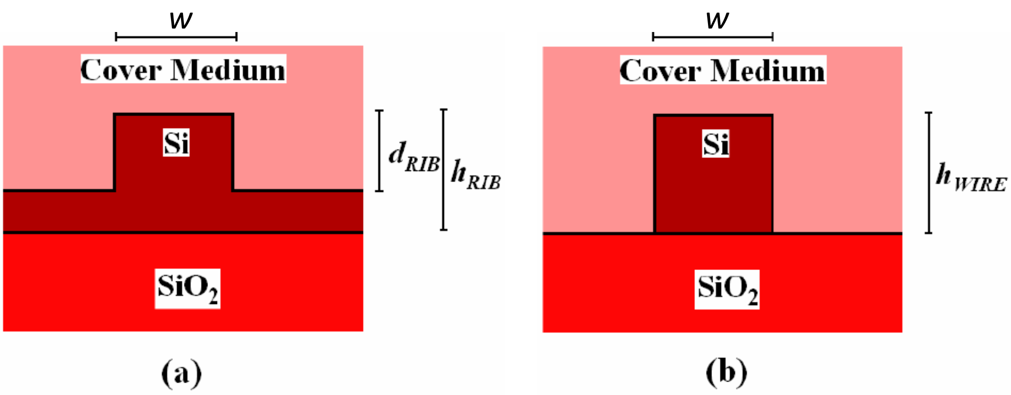

Figure 3.13: Schematic illustration of SOI a) rib and b) wire/ridge waveguide structure as given in [3.17].

For comparison with sensitivity of slot waveguides, the sensitivity of a Si-wire and a silicon rib waveguide was investigated as a function of width as presented in Figure

3.14 taken from [3.17]. Figure 3.14 was reproduced as shown in Figure 3.15 using FIMMWAVE to compare the two approaches and validate the simulation data. The core height of the Si-wire is fixed at 0.25µm and all other parameters are fixed at the same values as for the slot waveguide. The paper [3.17] also investigates rib waveguides but in Figure 3.14 it is evident that rib waveguides have a lower sensitivity compared to Si-wires. They also add an extra step in the fabrication process and therefore are not investigated further in this thesis.

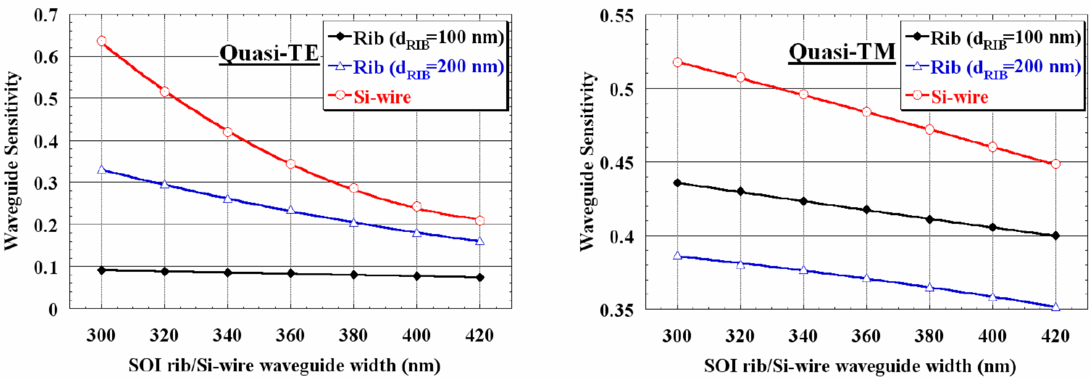

Figure 3.14: SOI rib waveguide and Si-wire waveguide sensitivity as a function of waveguide width for quasi-TE and quasi-TM published in [3.17] at a wavelength of 1.545µm.

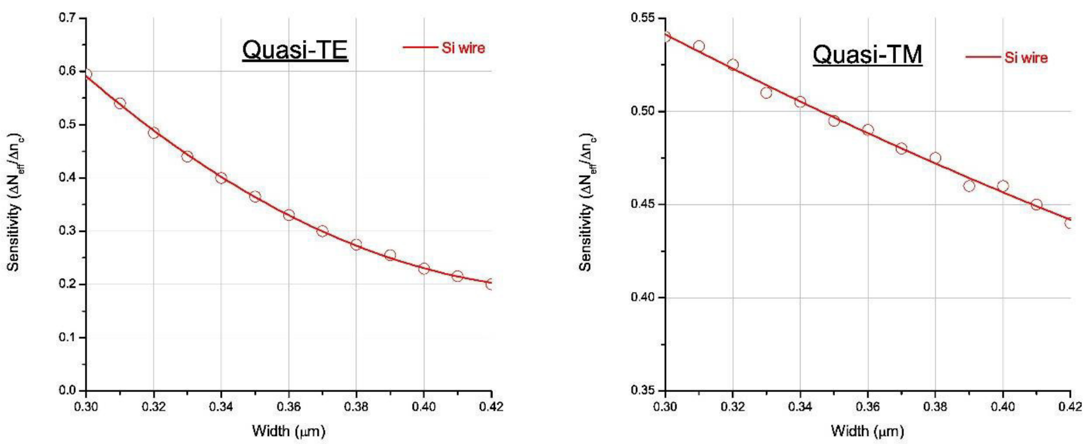

Figure 3.15: SOI Si-wire waveguide sensitivity as a function of waveguide width for quasi-TE and quasi-TM simulated with FIMMWAVE at a wavelength of 1.545µm.

The data in Figure 3.15 are very similar to the data reported in Figure 3.14. In both Figure 3.14 and Figure 3.15 the sensitivity decreases as waveguide width increases for both the quasi-TE and quasi-TM modes. The quasi-TM mode is more sensitive than the quasi-TE mode only for w>320nm.

The two *w* ranges investigated for the sensitivity of the slot waveguide and Si-wire are from 0.16-0.28µm and 0.30-0.42µm respectively. To facilitate a more precise comparison the Si-wire and slot waveguides sensitivity dependence was studied for a width range of 0.16-0.42µm and is presented in Figure 3.16.

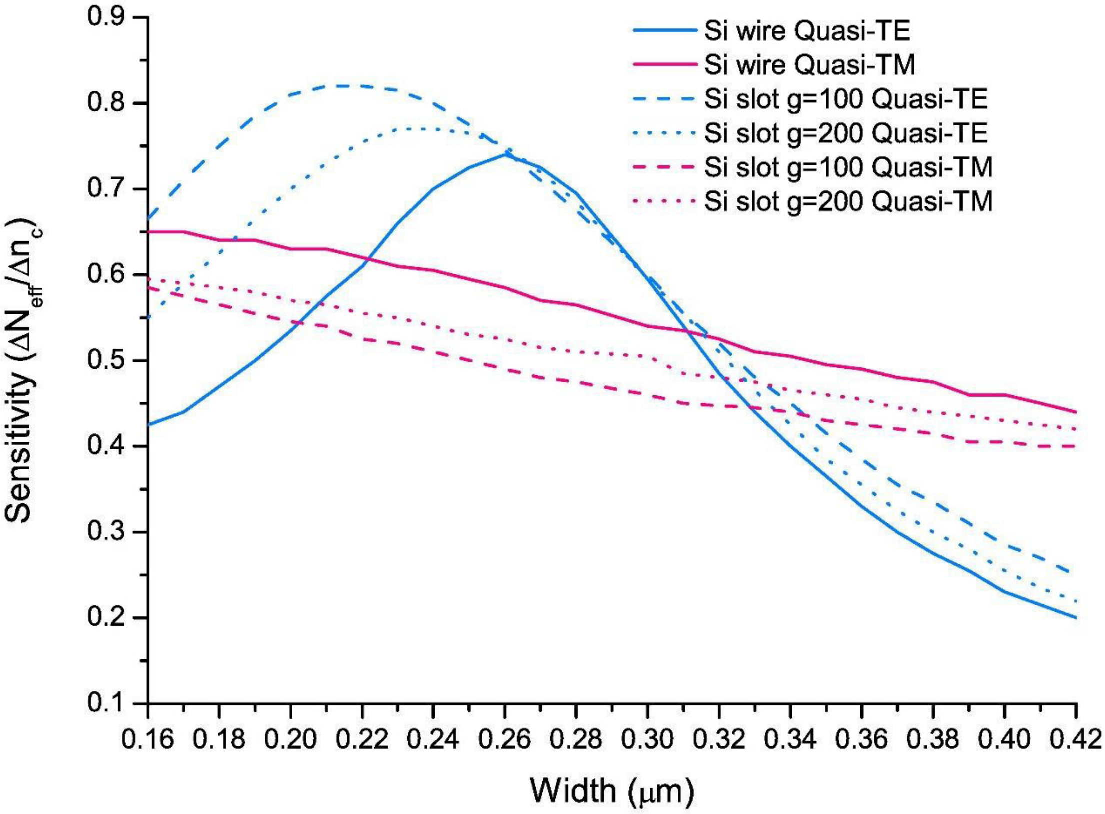

Figure 3.16: SOI Si-wire and slot waveguide (g=100nm and g=200nm) sensitivity as a function of waveguide width for fundamental quasi-TE and quasi-TM modes simulated with FIMMWAVE at a wavelength of 1.545µm.

From Figure 3.16 the sensitivity for the quasi-TE modes in a Si wire and both slot waveguides increases and then decreases as width increases whereas for the quasi-TM mode Si-wire and both slot waveguides the sensitivity decreases as *w* increases. The Si-wire for the quasi-TM mode is more sensitive when *w*<0.22µm or when *w*>0.32µm whereas the quasi-TM mode slot waveguides are more sensitive than the quasi-TE mode when *w*>0.34µm. In general slot waveguides are more sensitive than Si-wires for the quasi-TE mode of propagation whereas the opposite is true for the quasi-TM mode. To achieve the highest sensitivity of 0.82 the device would need to operate in a quasi-TE mode with a slot waveguide of g=100nm and *w*=0.22µm.

The above investigation was repeated, this time with the parameters that are chosen for use in this project, as illustrated in Figure 3.17. The core height was changed from 0.25µm to 0.22µm and the cover index, n_c was varied from 1.32-1.33 instead of 1.332-1.333. The operating wavelength was changed from 1.545µm to 1.55µm.

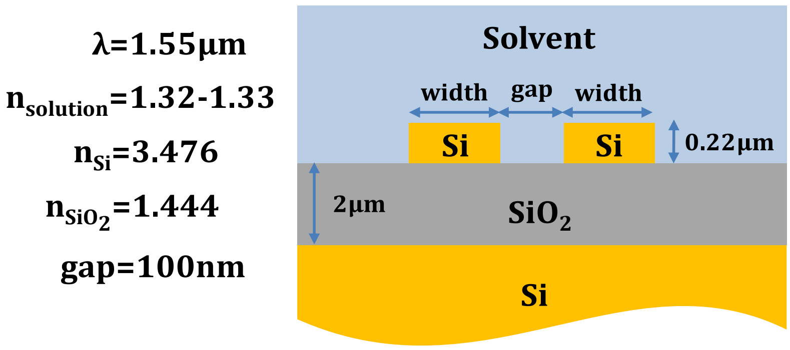

Figure 3.17: SOI slot waveguide structure and parameters.

The range of *w* examined was from 0.16-0.60µm to ensure a wide range was explored while ensuring single mode operation for each polarisation in the waveguides. The results are illustrated in Figure 3.18.

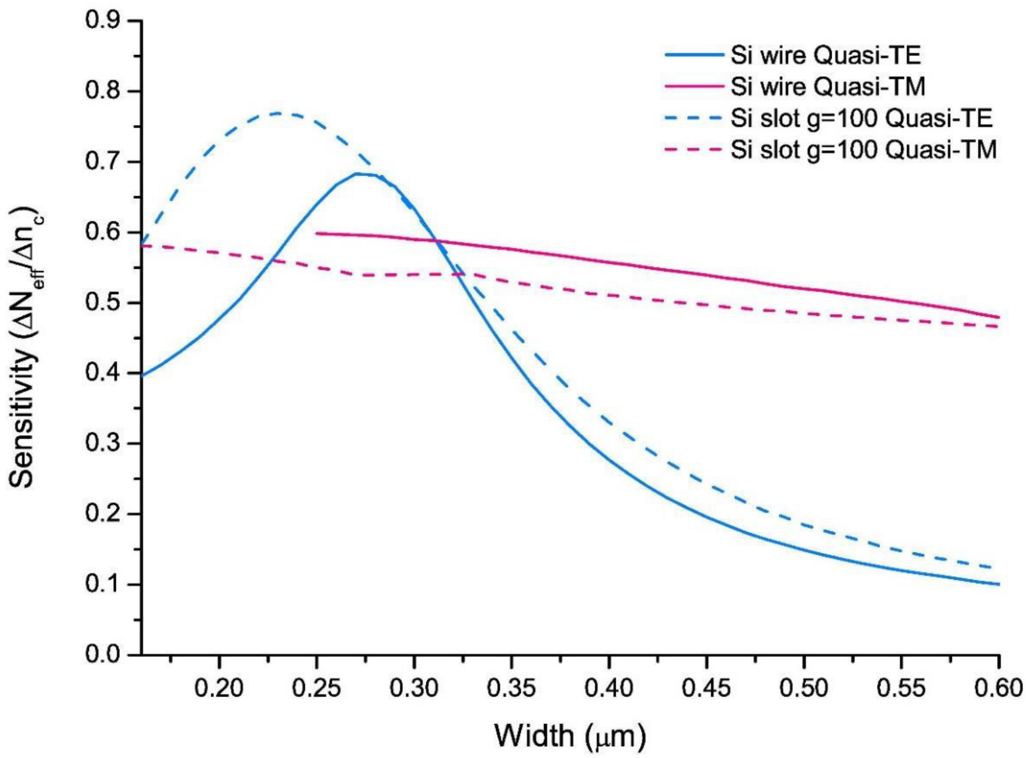

Figure 3.18: SOI Si-wire and slot waveguide (g=100nm) sensitivity as a function of waveguide width for quasi-TE and quasi-TM simulated with FIMMWAVE at a wavelength of 1.55µm.

The data in Figure 3.18 are very similar to the data in Figure 3.16. The quasi-TM Si-wire is more sensitive than the quasi-TE Si-wire when *w*>0.31µm and the quasi-TM slot waveguide is more sensitive than the quasi-TE slot waveguide when *w*>0.33µm. Slot waveguide is more sensitive than the Si-wire for the quasi-TE mode but less sensitive for the quasi-TM mode. To achieve the highest sensitivity of 0.77 the device would have to be designed with slot waveguides with g=100nm and w=0.23µm and operate in the quasi-TE mode.

However, the slot waveguides must be integrated into the ridge waveguide system to make use of its highly sensitivity in the quasi TE-mode. The problem of coupling light into a slot waveguide is addressed in the literature [3.20-23] by designing efficient strip-slot mode couplers/converters for SOI devices. Figure 3.19-Figure 3.22 show some of the structures designed to couple light from a silicon wire to a slot waveguide with high efficiency [3.20-23].

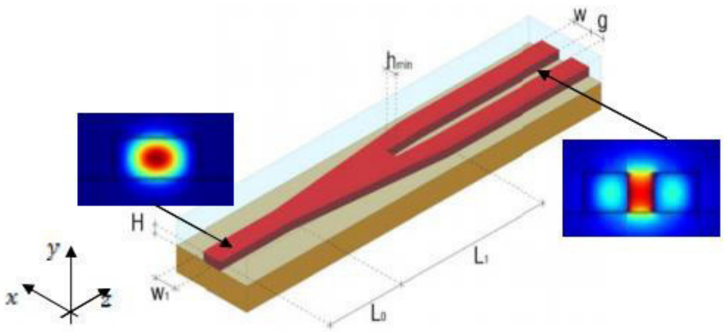

Figure 3.19: Schematic illustration of a Strip-slot coupler for the fundamental TE-like mode [3.20].

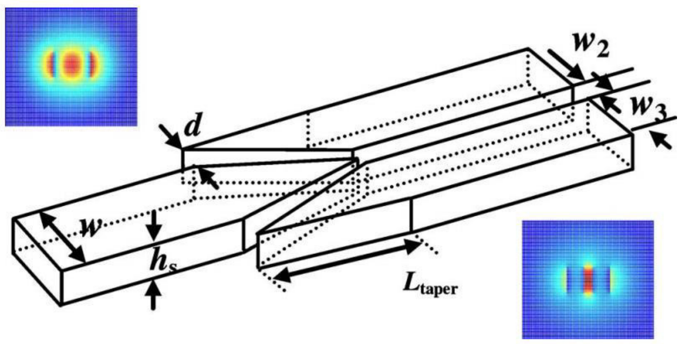

Figure 3.20: Schematic illustration of a Strip-slot coupler for the fundamental TE-like mode [3.21].

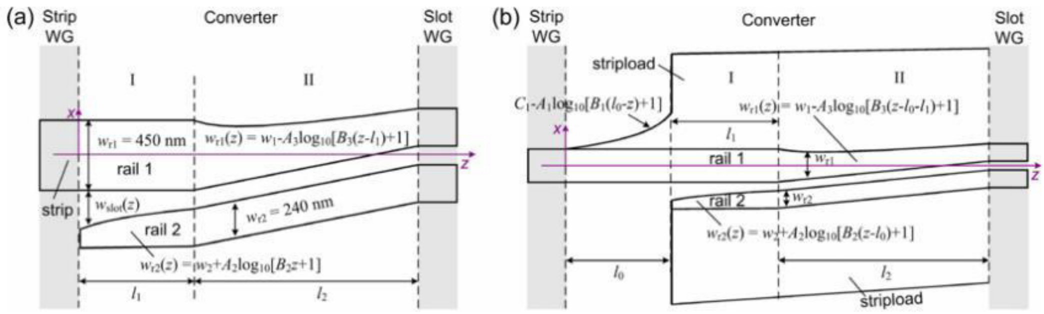

Figure 3.21: Schematic illustration of a Strip-slot coupler for the fundamental TE-like mode based on logarithmic tapers [3.22]

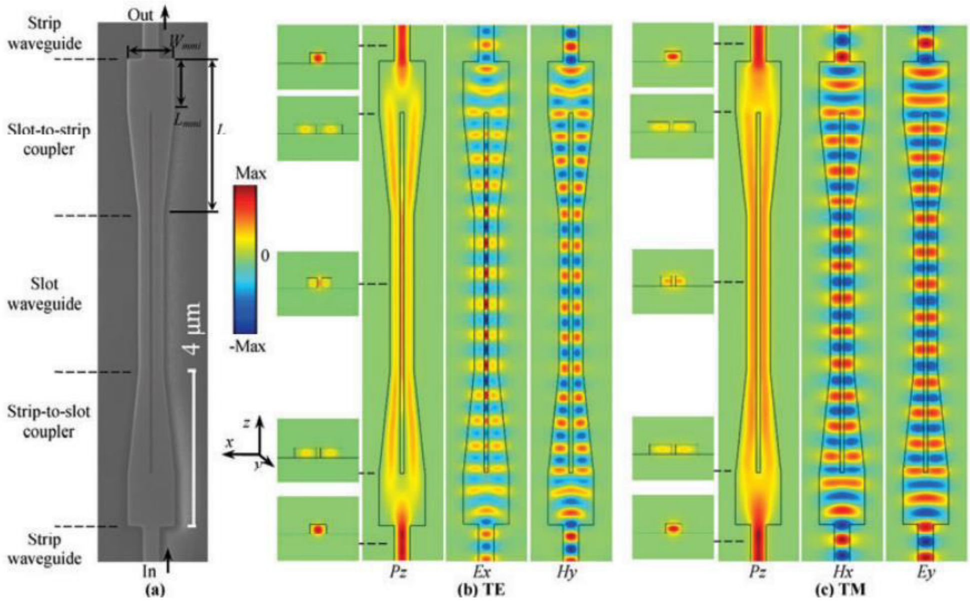

Figure 3.22: Schematic illustration of a Strip-slot coupler the for fundamental TE-like and TM-like modes based on multimode interferometer (MMI) [3.23].

Table 3.1 is a summary of the operating wavelength, dimensions of strip and slot waveguides and the efficiency of the strip-slot couplers presented above.

Table 3.1: Summary of strip to slot coupler efficiencies.

Strip-slot coupler	Operating wavelength (nm)	Strip waveguide height × width (nm)	Slot waveguide height × width (nm)	Gap (nm)	Efficiency for fundamental TE-like mode (%)
Figure 3.18 [3.20]	1550	220 × 510	220 × 220	120	≈100
Figure 3.19 [3.21]	1200-1800	250 × 400	250 × 260	100	≈100
Figure 3.20 [3.22]	1480-1580	220 × 450	220 × 240	100	≈100
Figure 3.21 [3.23]	1550	250 × 400	250 × 260	100	94.9 (94.6 for TM-like mode)

The optimum strip and slot waveguide height and width for this project would be 220 × 500 nm and 220 × 230 nm respectively for the fundamental TE-like mode at operating wavelength of 1550nm. The dimensions presented in Table 3.1 are almost similar to the dimensions needed for this project. Therefore, in theory a strip-slot coupler can be designed with near 100% efficiency which would allow an increase in sensitivity by 48% for the fundamental TE-like mode, but experimentally there would be some loss caused by strip-slot coupler.

Incorporating slot waveguides would not only require an addition strip to slot coupler but polarisation sensitive components such as the MMI coupler would have to be redesigned and optimised for the TE-like mode. Long and narrow waveguides slot waveguides would require more sophisticated and expensive fabrication techniques. Therefore, considering mass production and high reproducibility, working with silicon wire waveguides is preferable.

3.1.7. Propagation loss

As light propagates through the waveguide some loss would be caused even though SOI wires have good confinement. This loss is called the propagation loss and is caused by substrate leakage, scattering at sidewall roughness and material absorption.

Figure 3.23 presented by Pieter Dumon *et al.* [3.24], shows the substrate leakage of a SOI Si-wire as a function of buffer thickness (silicon dioxide) for varying core widths, *w* for the vector TE-like mode only. The core height and operating wavelength are fixed at 0.22µm and 1.55µm respectively. The loss was modelled using the eigen mode expansion (EME) method implemented in an in-house built software [3.25].

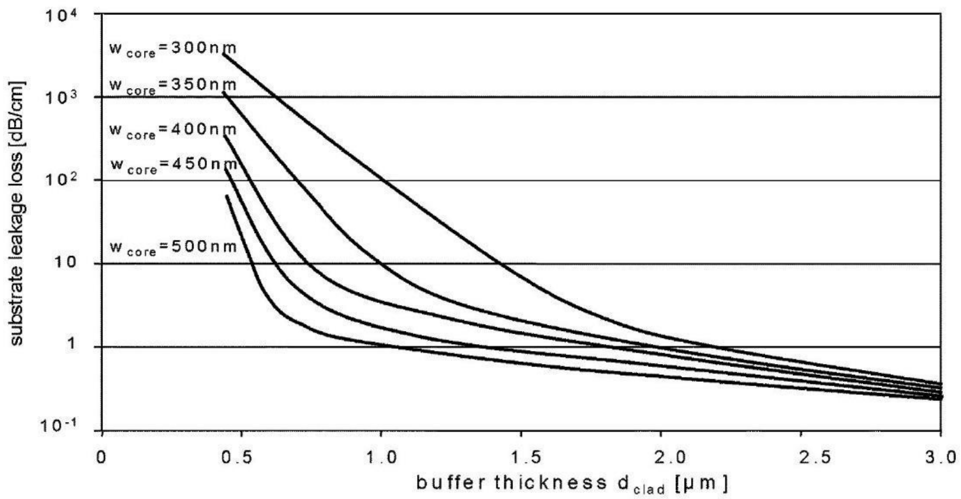

Figure 3.23: Substrate leakage of SOI waveguides for varying oxide thickness, for several widths, for vector TE-like mode. Image reproduced from [3.24].

Figure 3.23 shows that substrate leakage decreases exponentially with increasing oxide thickness. It is also shown that the loss decreases as the core width (w) increases.

Figure 3.24 shows a similar plot to Figure 3.23 and was reproduced using FIMMWAVE, which uses the EME method to calculate the substrate leakage loss of a silicon wire waveguide for the fundamental vector TE-like and TM-like modes as a function of buffer thickness. The core width was fixed at 500nm and the operating wavelength is 1.55µm.

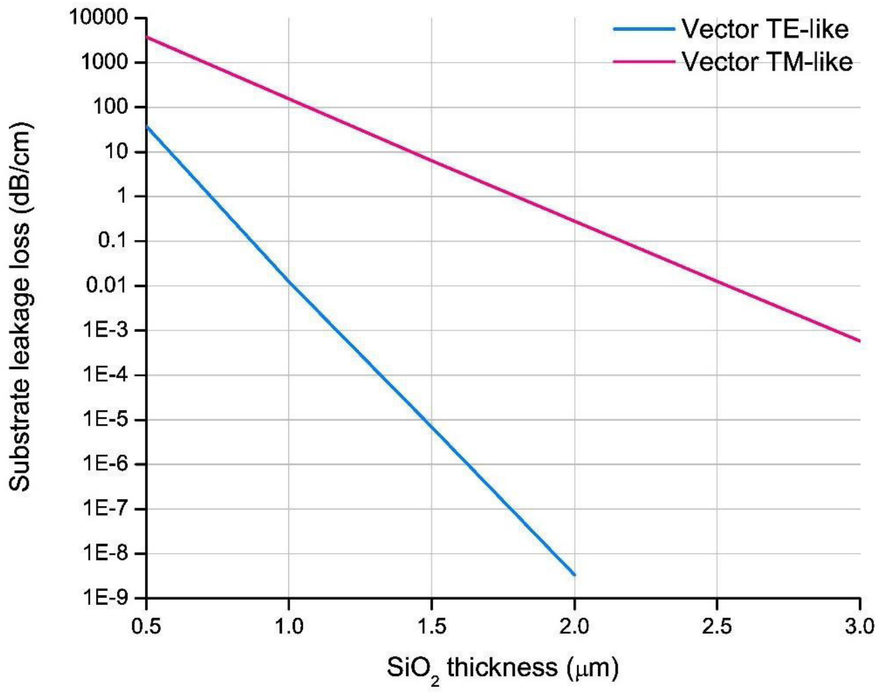

Figure 3.24: Substrate leakage loss as a function of buffer (SiO_2) thickness for the fundamental vector TE-like and TM-like modes at an operating wavelength of 1.55μm.

From Figure 3.24 it can be observed that the substrate leakage is larger for the vector TM-like mode and for both modes the loss decreases with buffer thickness.

Comparing results with literature is difficult as losses depend strongly on the cross-section of the waveguide core and the operating wavelength. Pieter Dumon *et al.* [3.24] measured a propagation loss of 2.4dB/cm for a 500×220nm SOI ridge waveguide with an oxide thickness of 1µm for the vector TE-like mode at wavelength of 1550nm. Yurii Vlasov *et al.* [3.26] measured a 3.6±0.1dB/cm propagation loss for a 445×220nm SOI waveguide with 2µm oxide layer for the vector TE-like mode at a wavelength of 1500nm.

Sidewall roughness can be greatly reduced by improving the fabrication process. Kevin Lee *et al*. [3.27] showed that by reducing the surface roughness from 10nm to 5 nm the propagation loss for a 300nm square core SOI strip waveguide for a vector TE-like mode at a wavelength of 1550nm can be reduced from 60dB/cm to 13dB/cm. Tai Tsuchizawa *et al*. [3.28] have further reduced the surface roughness to less than 2nm to obtain a very low propagation loss of 7.8dB/cm for a 300nm square core SOI strip waveguide and 2.8dB/cm for a 400×200nm core.

3.1.8. Curvature loss

As shown in the device layout in Figure 1.7 of chapter 1, the proposed biosensor device consists of S-bends[1], Y-splitters and S-function[1] waveguides all of which require bent waveguides with the smallest possible radius of curvature to achieve a compact device. Light propagating in a bend will be subject to radiation loss [3.26, 28, 29] and therefore it is important to determine bending loss as a function of bend radius and hence define the minimum allowable bending radius.

Figure 3.25 and Figure 3.26 show the bending loss of a Si-wire as a function of bend radius for the fundamental vector TE and TM-like modes respectively. Results were obtained from the FIMMWAVE 3D mode solver for when the Si-wire is exposed to air and solution.

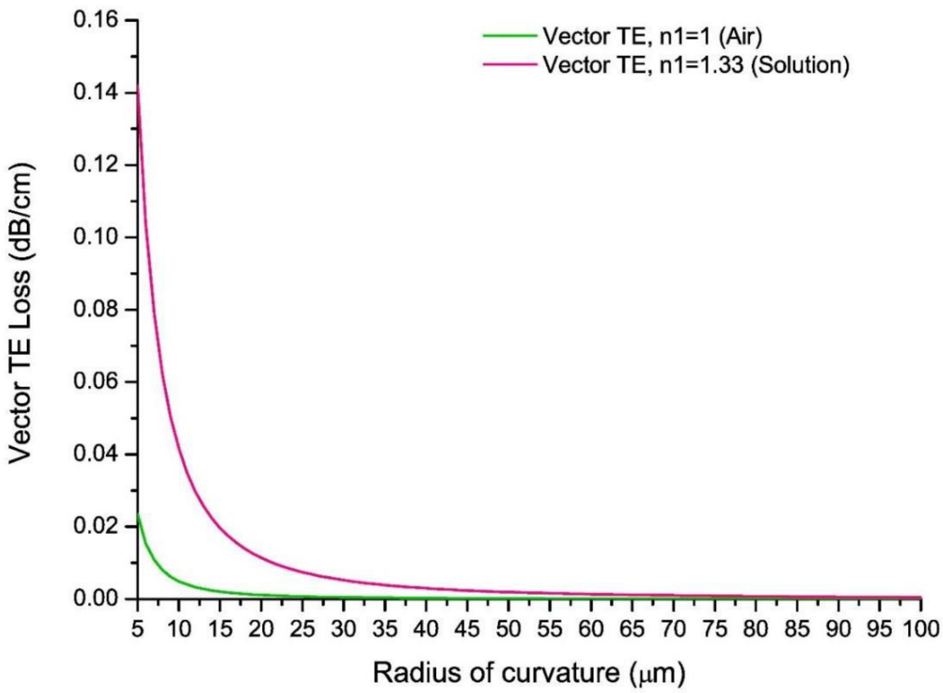

Figure 3.25: Vector-TE mode bending loss as a function of bend radius, R for when a 500×220nm waveguide is exposed to air and solution of refractive index of 1.33 at an operating wavelength of 1.55μm.

[1] The distinction between S-bends and S-function waveguides is made in section 3.1.9.

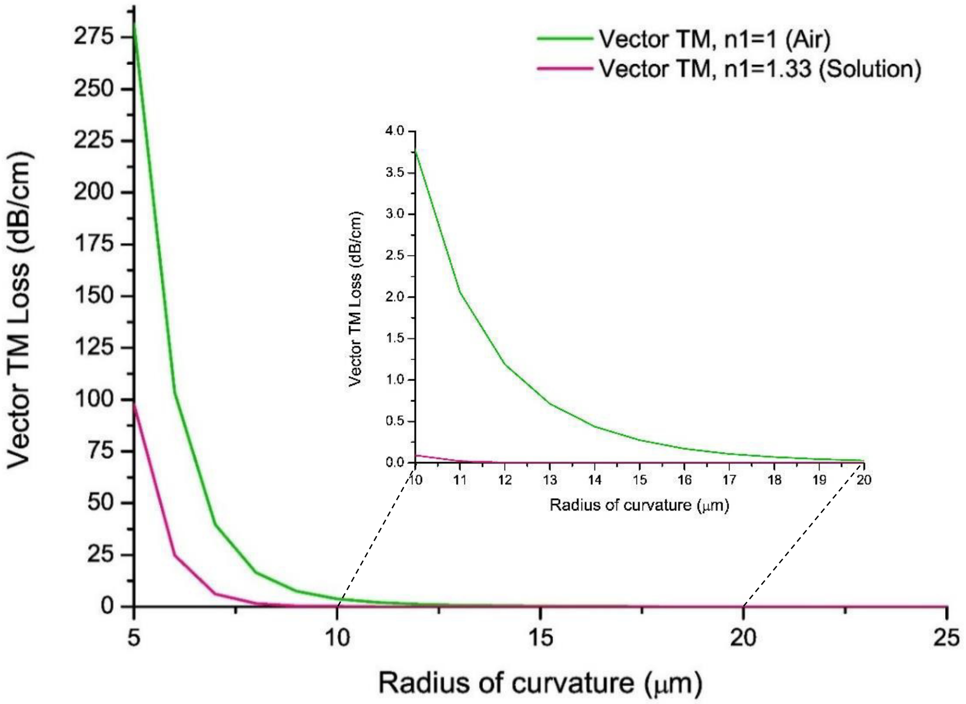

Figure 3.26: Vector TM-like mode bending loss as a function of bend radius, R for when a 500×220nm waveguide is exposed to air and solution of refractive index of 1.33 at an operating wavelength of 1.55μm.

From Figure 3.25 and Figure 3.26 for the vector TE-like mode the bending loss increases as the index of the cover increases from 1 to 1.33 whereas the opposite is true for the vector TM-like mode. For both vector TE and TM-like modes the bending loss decreases exponentially as the bend radius increases. For the quasi-TE mode, at R=5μm the bending loss is 0.024dB/cm and 0.142dB/cm for n_c=1 and n_c=1.33 respectively which is well below the straight waveguide propagation losses discussed in section 3.1.7. The curved waveguides in this project will have a cover index of n_c=1.33 or greater and from Figure 3.26 for bend radius greater than 11μm the loss is negligibly small when n_c=1.33. Therefore, for the vector TM-like mode operation, the minimum bend radius was fixed at 15μm.

In the literature the minimum bend radius for an SOI waveguide at 1550nm for the quasi-TE mode is said to be 2μm where the loss is 0.15dB for a core of 400×200nm core and 0.6dB for a 300nm square core and there is no bend related loss when the radius is 5μm or more [3.28]. Yurii Vlasov *et al*. [3.26] and Zhen Shen *et al*. [3.29] studied the bending loss for the vector TE and TM-like modes for a wavelength ranging from 1200nm to 1700nm for radii of 1, 2 and 5µm as shown in Figure 3.27 and Figure 3.28.

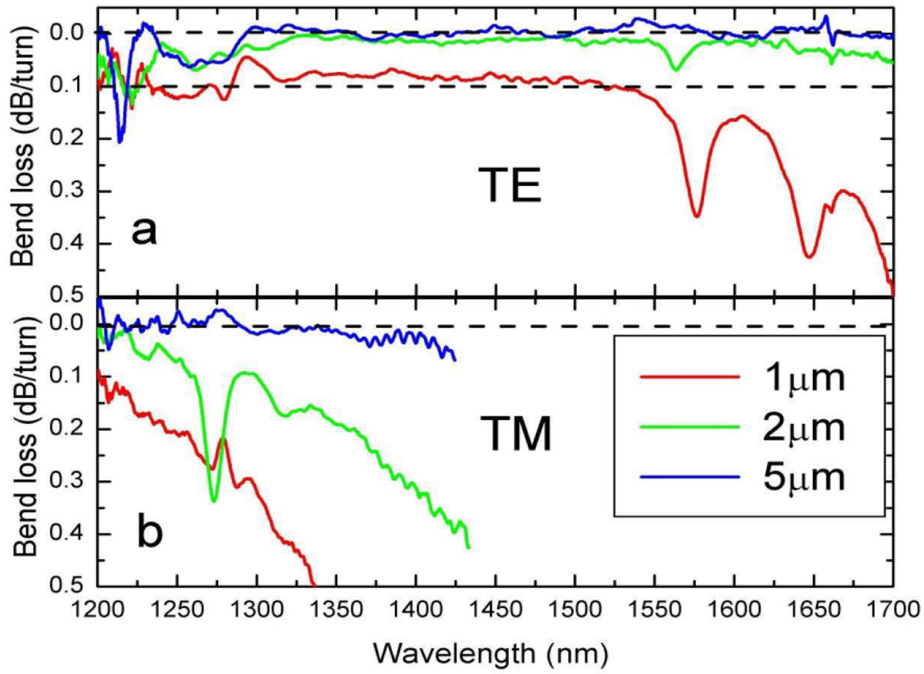

Figure 3.27: Bending loss for a) TE mode and b) TM mode SOI waveguides of core 445×220nm for radius 1, 2 and 5µm for varying wavelengths. Image reproduced from [3.26].

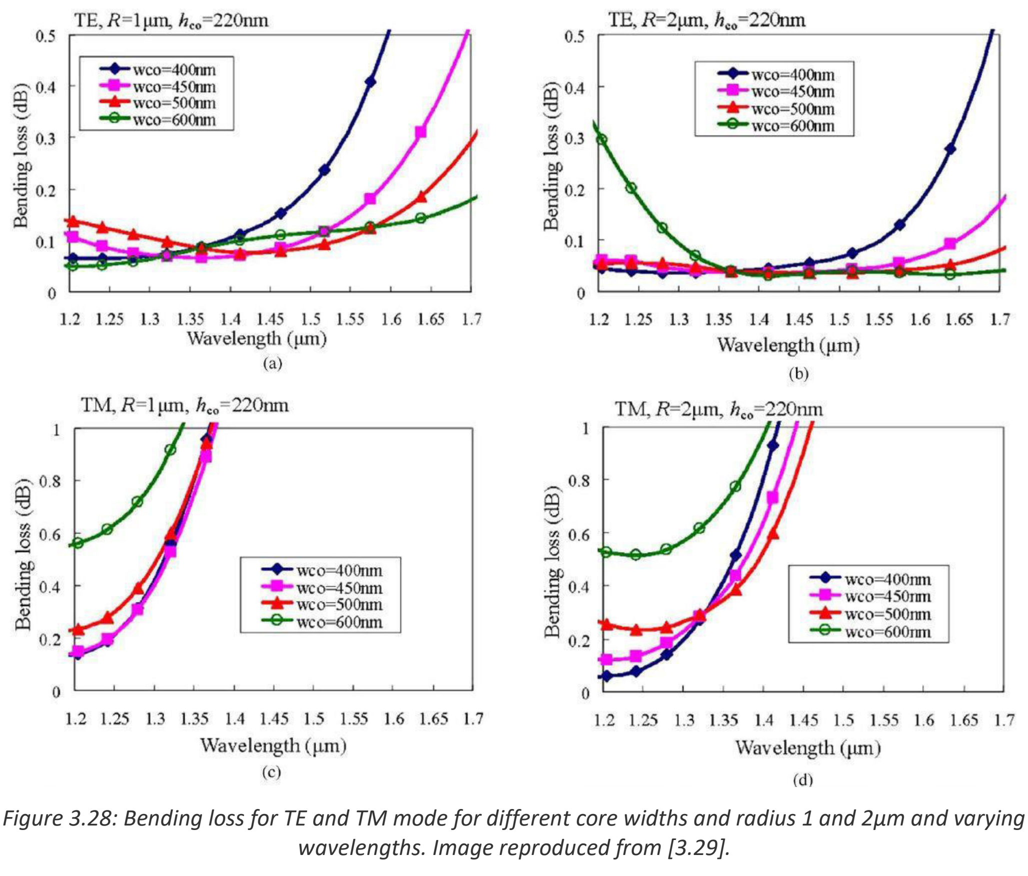

Figure 3.28: Bending loss for TE and TM mode for different core widths and radius 1 and 2µm and varying wavelengths. Image reproduced from [3.29].

In Figure 3.27a when R=5µm, the bend loss is ≈0dB/turn at a wavelength of 1550nm which is similar to the 0.02dB/cm obtained in Figure 3.25 for the vector TE-like mode. In Figure 3.27b and Figure 3.28c and d the losses for the vector TM-like mode are not recorded for a wavelength greater than 1450nm as the loss increases exponentially for such narrow radii as also shown in Figure 3.26.

Figure 3.29 graphically illustrates the spatial distribution of the principal electric field component E_y for the fundamental vector TM-like mode supported by a 500×220nm waveguide at a wavelength of 1.55µm for radii, R of a) 5µm and b) 15µm. For both radii the mode is slightly shifted to the right which is the outer edge of the curve but is still confined to the core. The smaller the radius the more the mode would shift to the edge as is seen in Figure 3.29a for R=5µm where the mode is shifted to right more than in Figure 3.29b for R=15µm.

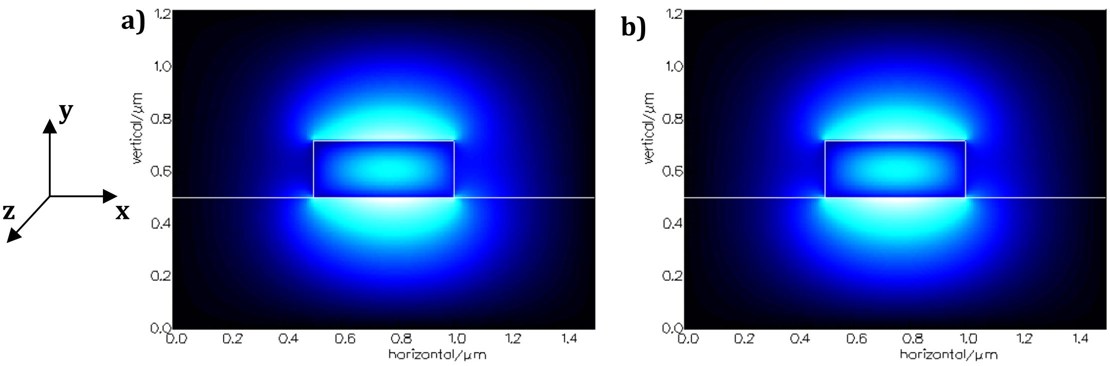

Figure 3.29: Spatial distribution of the principal electric field E_y component for the fundamental quasi-TM mode in a Si-wire of core height=0.22µm and width=0.5µm for a) R=5µm and b) R=15µm.

Based on these results the minimum radius of curvature used in the design of silicon-wire-based components for the present project is fixed at 15µm.

3.1.9. S-bends and S-function waveguides

In the first set of devices fabricated the outputs of the multimode interferometers (MMIs) were spaced 15µm apart and the Mach-Zehnder interferometers (MZIs) were spaced 250µm apart, as will be explained in more detail in sections 3.2 and 3.4. In order to connect these two devices a curved waveguide such as an S-bend or S-function waveguide is utilised as shown in Figure 1.7 in the device layout in chapter 1.

S-bends are constructed of two arcs designed in RSoft BeamProp. Figure 3.30 shows the RSoft CAD layout of the S-bends designed for a 1×8 MMI splitter.

To avoid bend related loss the S-bend were designed such that the radius *R* of both arcs are above the minimum bend radius. The minimum and maximum *R* for the layout shown in Figure 3.30 are 1724µm and 12069µm respectively and the bend has a footprint of 6800µm × 1750µm.

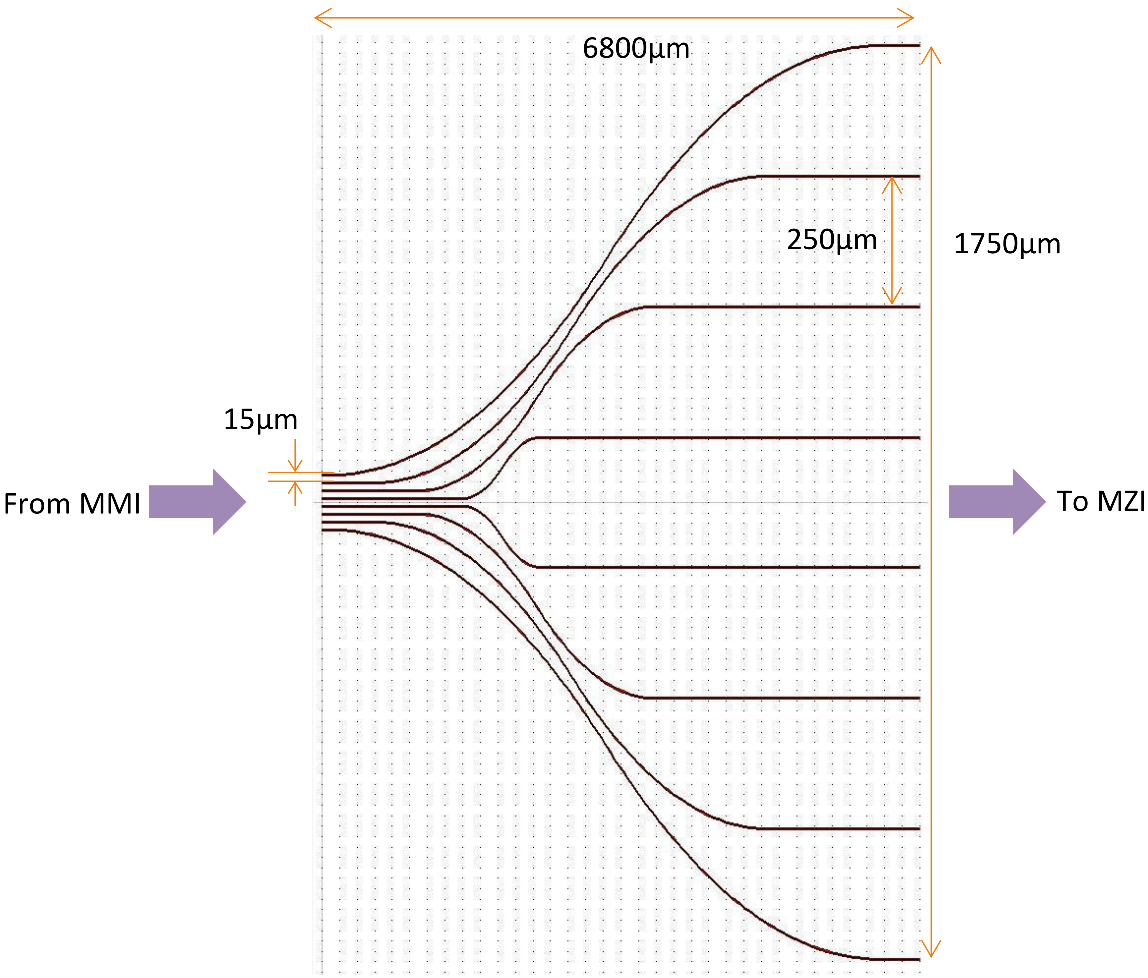

Figure 3.30: RSoft CAD layout of S-bends for separating the 8 outputs from a 1x8 MMI splitter.

In the final design the device contains MMIs with outputs spaced 5µm apart and the MZIs spaced by 127µm and these were simulated in FIMMPROP as shown in sections 3.2 and 3.4. RSoft BeamPROP uses S-bends to construct the MZI whereas in FIMMPROP an S-Function is used as shown in Figure 3.31 and expressed in equation 3.2.

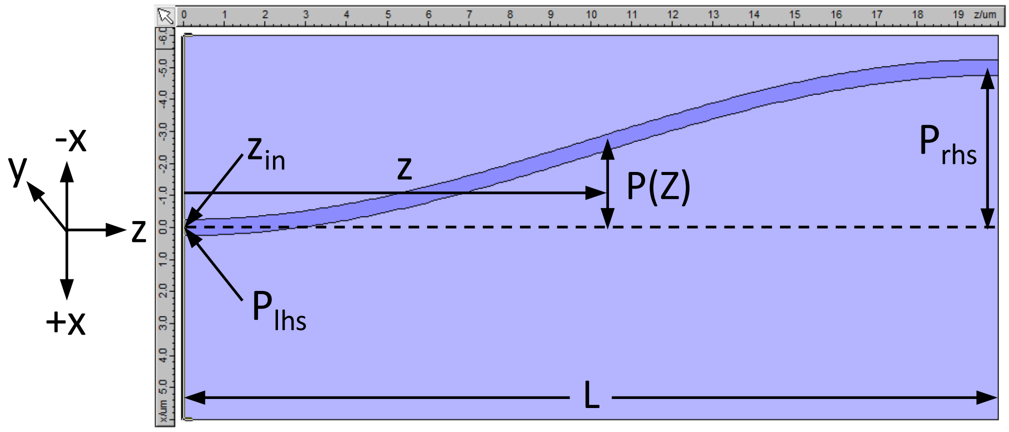

Figure 3.31:FIMMPROP CAD layout of a S-function waveguide.

As shown in Figure 3.31 the software lets the user input P_{lhs} and P_{rhs} may be the left-hand side and right-hand side offset from the z axis. Then the user can input the length, *L* of the waveguide structure. The path of the S-function curve is defined by equation 3.2 [3.30]:

$$P(Z) = P_{lhs}\left(1 - sin^2\left(\frac{\pi Z}{2}\right)\right) + P_{rhs}sin^2\left(\frac{\pi Z}{2}\right) \tag{3.2}$$

where $Z = (z - z_{in})/L$; z_{in} is the initial z position.

However, from equation 3.2 it is not possible to directly calculate the radius of curvature and therefore equation 3.3 [3.31] was used to calculate the radius of curvature at each position along of the curve.

$$R = \frac{\left[1 + \left(\frac{dP}{dz}\right)^2\right]^{\frac{3}{2}}}{\left(\frac{d^2P}{dz^2}\right)} \tag{3.3}$$

where

$$\frac{dP}{dz} = (P_{rhs} - P_{lhs})\frac{\pi}{2L}\sin\left(\frac{\pi z}{L}\right) \tag{3.4}$$

$$\frac{d^2P}{dz^2} = (P_{rhs} - P_{lhs})\frac{\pi^2}{2L^2}\cos\left(\frac{\pi z}{L}\right) \tag{3.5}$$

Figure 3.32 shows an S-function curve plotted on MATLAB using equation 3.2. The corresponding radius of curvature, R was plotted using equations 3.3-5 on MATLAB as shown in figure 3.32. P_{lhs} and P_{rhs} were fixed at 0 and 5um respectively. L was fixed at 20µm. See Appendix A for the MATLAB code.

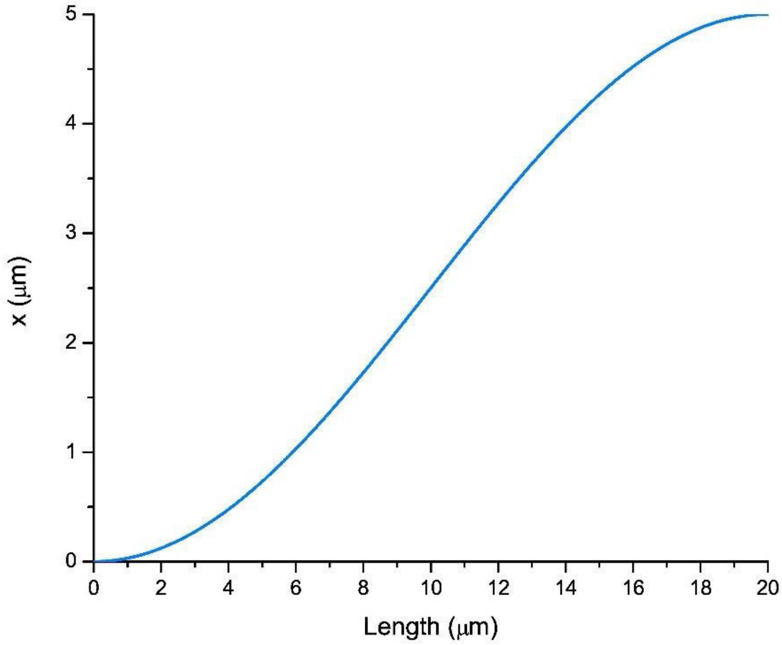

Figure 3.32: S-function waveguide plotted on MATLAB.

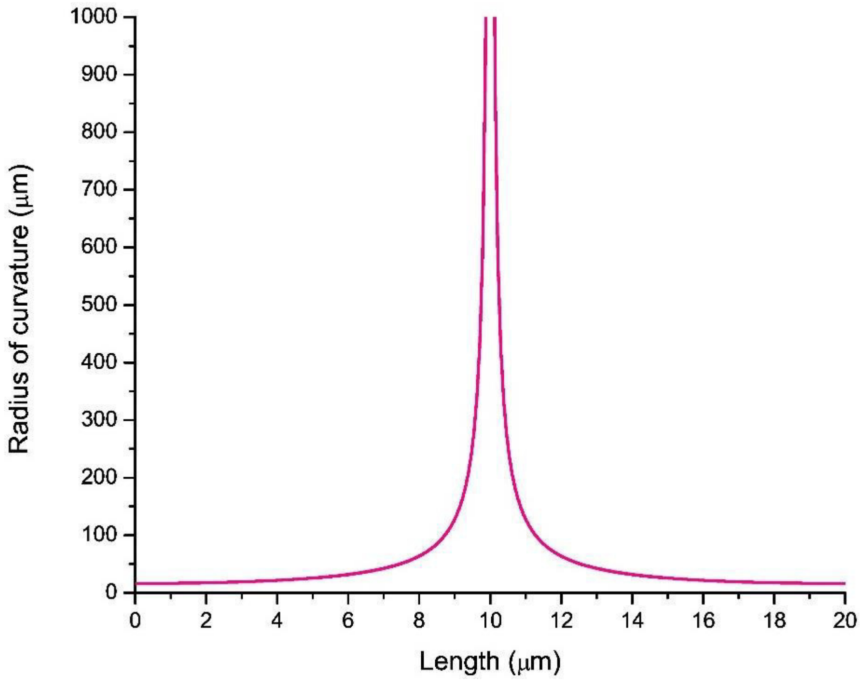

Figure 3.33: Radius of curvature for S-function waveguide of L=20µm, P_{lhs}=0 and P_{rhs}=5.

From Figure 3.32 an S-function curve can be seen that starts at *x*=0 (*Z*=0 and *L*=0µm at this point) and ends at *x*=5. Figure 3.33 shows the corresponding radius at each *L* of the curve. The radius of curvature increases exponentially up to halfway through the curve and then reduces exponentially. At the centre of the S-function the curve changes direction and so the radius of curvature tends to infinity as expected.

At *Z*=0 the minimum radius of curvature can be obtained which is 16.2µm and above the required 15µm minimum bend radius for TM mode SOI waveguides exposed to air as demonstrated in section 3.1.8. The S-function designed in this section will be exposed to SU-8 of refractive index 1.575 and so according to Figure 3.26 a bend radius lower 15µm could in theory be used, but to standardise the design parameters the minimum radius of curvature is fixed at 15µm. If P_{lhs} and P_{rhs} were fixed then *R* and *L* are variable. The minimum radius of curvature, R_{min} can be expressed by equation 3.6:

$$R_{min} = \frac{2L^2}{\pi^2(P_{rhs} - P_{lhs})} \tag{3.6}$$

This is useful as when P_{lhs}, P_{rhs} and L become larger the simulation window becomes larger making it time consuming, and sometimes impossible, to simulate the transmission loss in the bend using the software. Therefore, using equation 3.6 the minimum length, L_{min} can be calculated to give $R_{min} = 15\mu m$.

Figure 3.34 shows the FIMMPROP CAD layout of S-function bends designed for the outputs of a 1x8 MMI coupler. The waveguides on the left are spaced 5µm apart and on the right 127µm apart. To obtain an $R_{min} = 15\mu m$ for the outer S-function bends a L_{min} of 177.8µm is required. So, the length of the 8 S-function bends was set to 180µm which gives R_{min} of 15.4µm, 21.5µm, 35.9µm and 107.6µm from the outer to inner S-function bends respectively. S-bends designed for a 1x20 MMI with $R_{min} = 15\mu m$ correspond to $L_{min} = 293\mu m$.

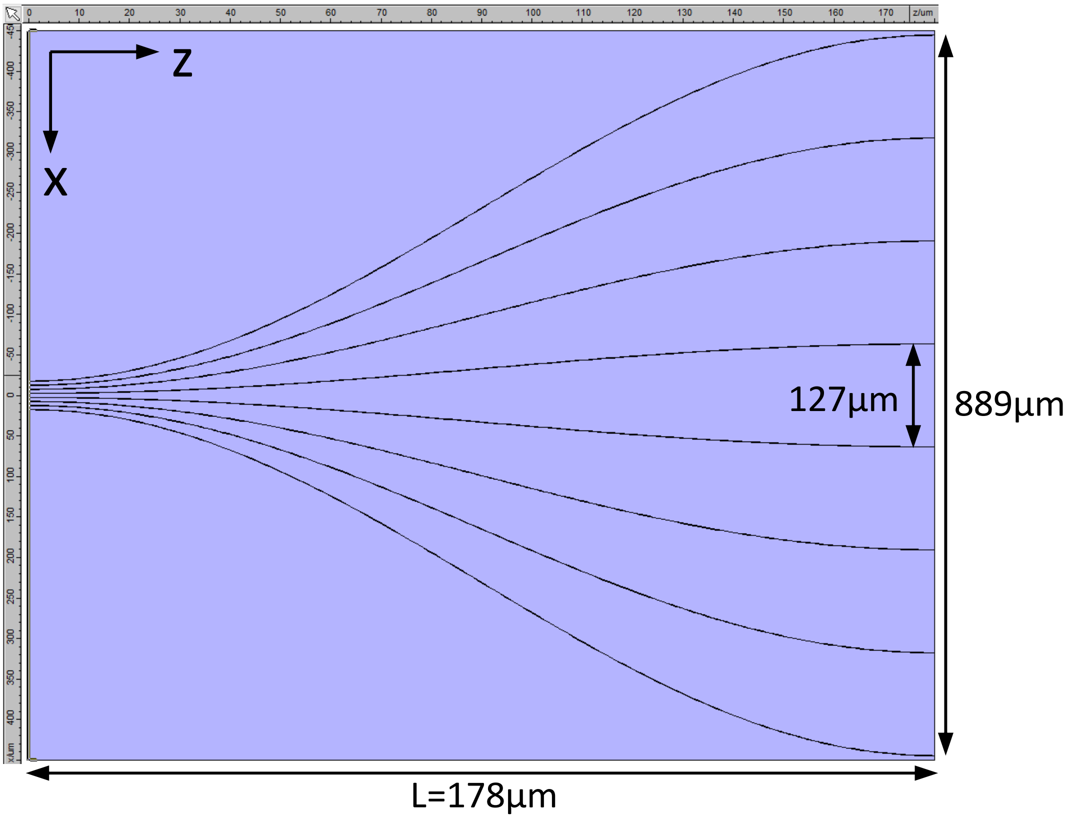

Figure 3.34: FIMMPROP CAD layout of S-bends for separating the 8 outputs from a 1x8 MMI splitter.

3.2. Mach-Zehnder interferometers

Evanescent field sensors based on effective refractive index changes generally operate in interference based systems such as Mach-Zehnder interferometers [3.32], Young interferometers [3.33, 34] and ring resonators [3.35]. These devices use different techniques of superposition to extract information about the propagating waves. Grating couplers [3.36] and photonic crystal [3.37] waveguide sensors also operate on refractive index based sensing but are not interference based systems.

The most commonly used interference sensor is the Mach Zehnder interferometer (MZI) which is used in this project and is schematically illustrated in Figure 3.35.

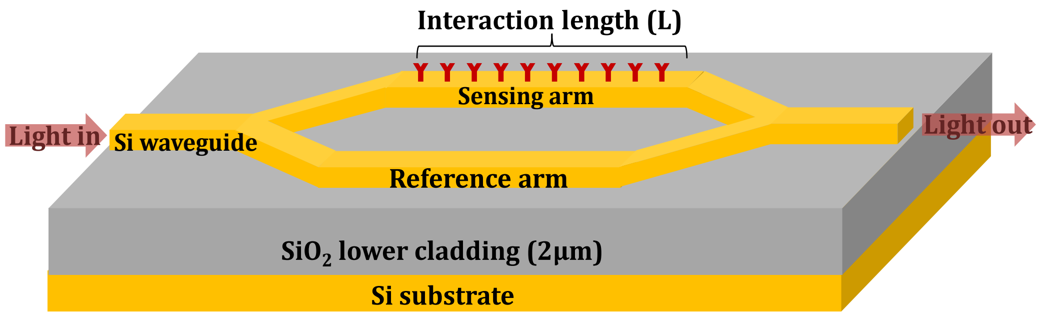

Figure 3.35: Schematic illustration of a Mach-Zehnder interferometer (MZI).

The incident light is divided into two equal parts that propagate to the sensing arm and the reference branch respectively.

As explained in section 2.5, a change in the effective index of the waveguide (ΔN_{eff}) at the sensing window, caused by the binding of the target molecule to the antibody, gives a phase change $\Delta\varphi$ in the interaction length, L, as expressed in equation 3.7.

$$\Delta\varphi = \Delta N_{eff} \cdot k_0 \cdot L \tag{3.7}$$

where k_0 is the free space wave number or the phase constant ($2\pi/\lambda_0$).

The reference branch is used to reduce ambiguity due to external factors such as input power fluctuations, temperature changes in the environment and non-specific adsorption. Non-specific adsorption is when other molecules that are not the target molecule bind with the antibody and cause a phase change. But for this the reference arm should also be functionalised with the same antibody as the sensing arm and a similar analyte without the target molecule will have to flow over the reference arm.

When the light from the sensing and reference arms recombines, constructive or destructive interference occurs which in turn modulates the light intensity at a single mode output. Therefore, the phase change can be calculated using equation 3.8 [3.38].

$$I = \frac{1}{2} I_0 [1 + \cos(\Delta\varphi)] \tag{3.8}$$

where I_0 is the input intensity. The cosinusoidal variation of the interference pattern can be directly related to the concentration of the analyte to be measured via the change in effective refractive index as described in equation 3.1. The simulated results are presented in section 3.2.3.

3.2.1 Design

Initial MZI structures for this project were designed using RSoft BeamPROP CAD software [3.39]. Due to wafer availability and fabrication limitations the first set of devices was designed for a silicon core height of 0.32µm and a waveguide width of 4µm. Even though in section 3.1.4 the waveguide width was fixed at 0.5µm, a waveguide width of 0.8µm was used for the second set of devices as it proved less difficult to simulate with RSoft BeamPROP while maintaining single mode operation.

Figure 3.36a and Figure 3.37a show the CAD layout of MZI devices with a 0.32µm x 4µm Si wire, which is multi moded, and 0.25µm x 0.8µm, which is single moded respectively. The MZI is constructed with two Y-junctions joined via two straight waveguides as shown in Figure 3.36a. Each Y-junction is made from two S-bends.

Figure 3.36b and Figure 3.37b show the BPM simulation of the waveguide power of the respective MZI devices for a vector TM-like mode at an operating wavelength of 1.55µm. Since the TM-like mode gives the higher sensor sensitivity, as shown in sections 3.1.3-3.1.5, all simulations shown are for the vector TM-like mode.

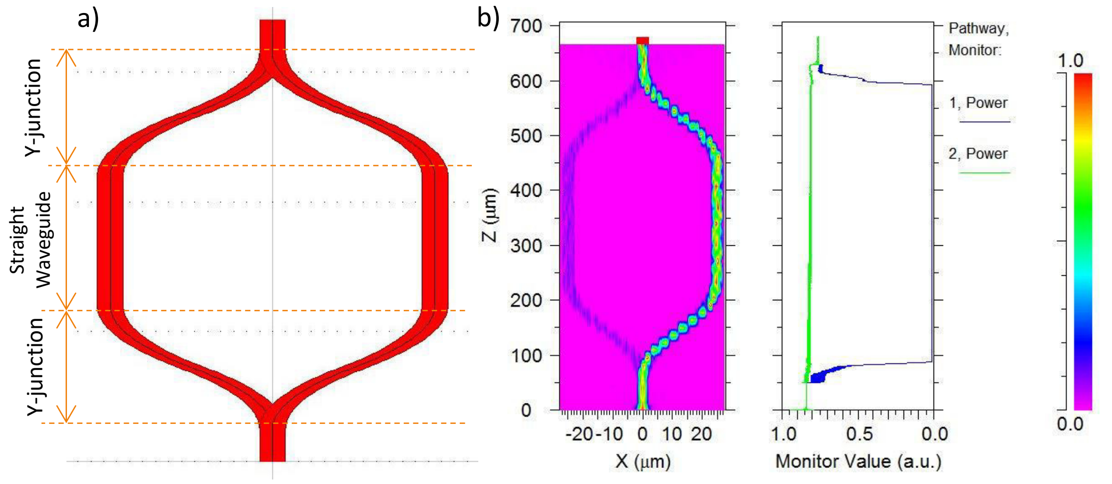

Figure 3.36: a) MZI layout for 0.32µm x 4µm Si wire (Multi mode waveguide) and b) Waveguide power in sensing and reference arm for 0.32µm x 4µm Si wire MZI.

From Figure 3.36b it can be seen that the light does not split evenly at the Y-junction. This is because in the presence of higher order modes the input field is not distributed symmetrically at the start of the Y-junction as illustrated previously in Figure 2.6. Figure 3.36b serves to show that the input and output waveguides must be single mode to function properly as an MZI. Figure 3.37a and 3.37b show a single mode MZI device where the power of the waveguide splits evenly into the two branches and recombines at the end.

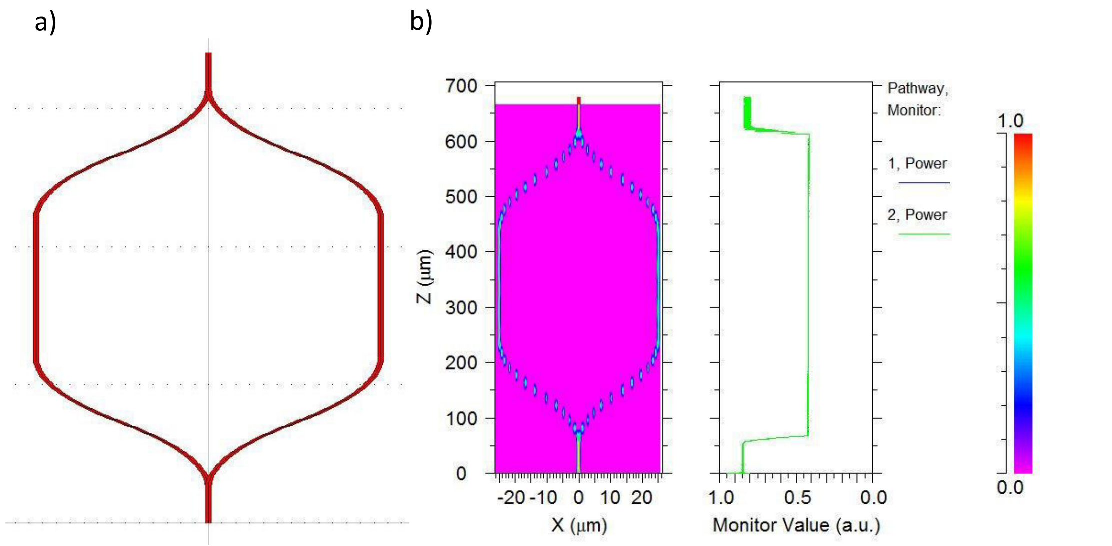

Figure 3.37: a) MZI layout for 0.25µm x 0.8µm Si wire (Single mode waveguide) and b) Waveguide power in sensing and reference arm for 0.25µm x 0.8µm Si wire MZI.

Even though the 0.32µm x 4µm Si wire MZI will not function properly it was fabricated (for varying interaction lengths) with the first set of test devices and tested as will be described in Chapter 6. The first set of fabricated devices enabled initial experimental data to be obtained, albeit with the MZI not functioning as intended.

As discussed in section 3.1.3 and 3.1.4 the height and the width of the silicon core were fixed at 220nm and 500nm respectively. The accuracy decreases when simulating narrower high index contrast waveguides in RSoft BeamPROP as demonstrated in section 3.4.3, therefore the following simulations were performed with Photon Design's FIMMPROP software which uses the Eigenmode expansion (EME) method for simulating optical waveguides in 2D and 3D.

As discussed earlier in this section RSoft BeamPROP uses S-bends to construct the Y-junction, whereas as discussed in section 3.1.8, FIMMPROP uses an S-Function to design curved waveguides. Two S-function waveguides are used to construct a Y-splitter.

The Y-junction must be optimised for minimum insertion loss and non-uniformity. The minimum length was calculated using equation 3.6 for a minimum radius of curvature of 15µm. Table 3.2 shows the distance between the two outputs of the Y-splitter, ρ which is twice the P_{rhs}, length, insertion loss and non-uniformity of the optimised Y-junction splitters.

Table 3.2: Insertion loss and non-uniformity of optimised Y-junction splitters.

ρ (µm)	Length (µm)	Insertion loss (dB)	Non-uniformity (dB)
5	14	0.26	0.00
10	20	0.31	0.00
20	28	0.44	0.00

From Table 3.2 the length and insertion loss increases as ρ is increased. Non-uniformity remains at 0.00dB. The results in table 3.2 were confirmed by simulating the Y-junctions as a function of length. Figure 3.38 shows the insertion loss of Y-junctions for ρ=5, 10 and 20µm when their length is varied from 1-100µm.

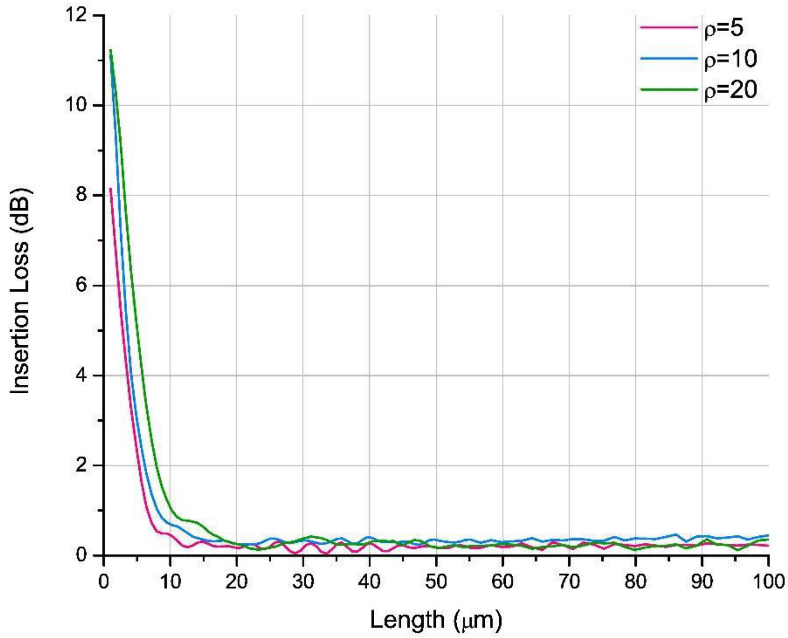

Figure 3.38: Insertion loss in Y-junctions of output separation 5µm, 10µm, 20µm and 25µm as a function of length in the propagating direction.

ρ=25µm is not shown as the computational memory available for the simulation was insufficient. In FIMMPROP the bend is modelled as a series of straight sections. When the length of the Y-junction is too small the bend angle is very large. Figure 3.38 shows initially a transient region where loss is increasing inversely to length squared. As the length increases the transmission increases and then oscillates [3.30]. These oscillations are due to the reflections off the boundary. Plotting Figure 3.38 indicates the minimum length required to obtain a valid insertion loss of the Y-junction splitter.

From Table 3.2 and Figure 3.38 it is clear that ρ=5µm at length=14µm should be used but this would pose a fabrication challenge for the microfluidic channel layer which needs to be aligned on top of the sensing arm of the MZI. To make aligning of the microfluidics channel easier the outputs of the Y-junction are instead fixed to be 25µm apart at a length of 31µm. Figure 3.39 shows the vector TM-like mode simulation of the optimised Y-junction using FIMMPROP.

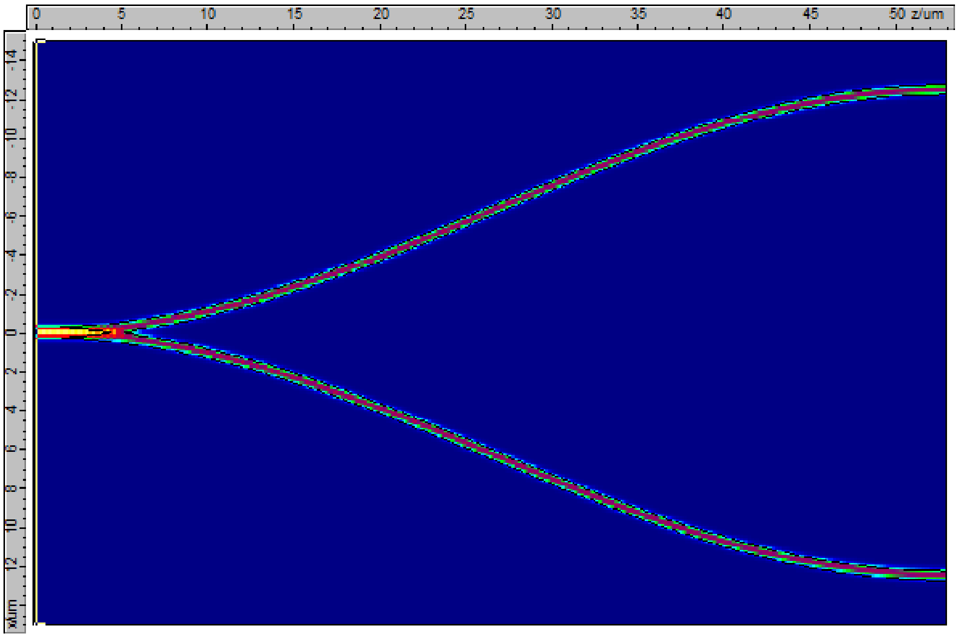

Figure 3.39: Optimised Y-junction splitter for TM-like mode at ρ=25µm and Z=53µm.

Once the Y-junction is designed using two S-function waveguides as shown above, the MZI was designed next. Figure 3.40 shows the FIMMPROP CAD layout of a MZI for a 220nm × 500nm Si-wire.

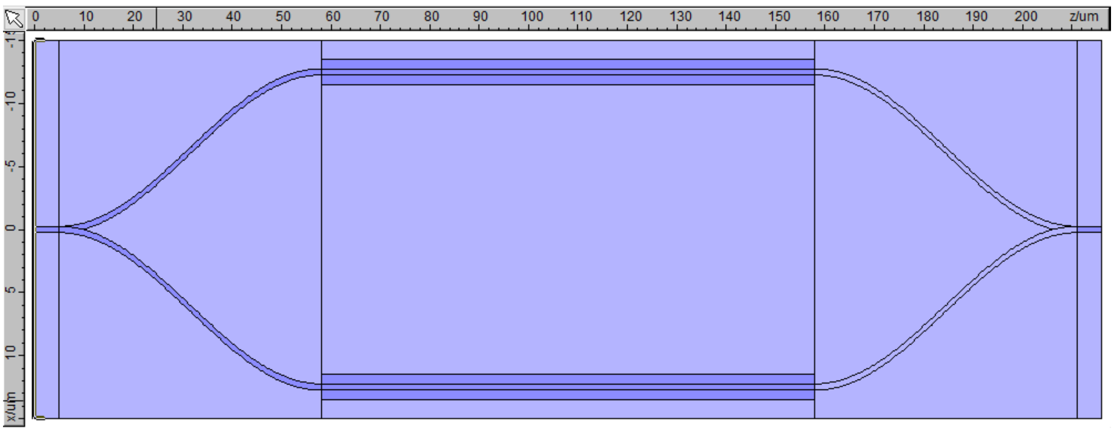

Figure 3.40: CAD layout for a MZI for 220nm × 500nm Si-wire.

In Figure 3.40 the MZI is constructed from left to right in this order: a straight waveguide, a Y-junction, two straight waveguides, an inverted Y-junction and finally another straight waveguide. The length of the sensing and reference arms is 100µm in this case and each waveguide is open to a 2µm fluid channel.

In this section, the MZI designed uses straight waveguides for the sensing and reference arm and in the next section the two straight waveguides are replaced with spiral waveguides. Further simulation results, for MZIs with straight waveguides and spiral waveguides, will be presented in section 3.2.3.

3.2.2 MZI with spirals

As presented in equation 3.3 the sensitivity increases as the sensing length increases but in the configuration shown in Figure 3.40 as the length increases the overall length of the device increases. To counter this problem spiral waveguides are used. Spiral waveguides are increasingly gaining popularity and have recently been used for many applications such as spectrometers [3.40, 41], ring resonators [3.42, 43], filters [3.42, 44], chirpers [3.45] and Bragg gratings [3.46]. The most common type of spiral used is the Archimedean spiral which can be expressed in parametric form as equation 3.9 and 3.10.

$$x = R.cos(\theta) \tag{3.9}$$

$$y = R.sin(\theta) \tag{3.10}$$

where R and ϑ are the radius and angle respectively. In this project, R is set equal to ϑ, therefore equations 3.9 and 3.10 can be re-written as equations 3.11 and 3.12.

$$x = R.cos(R) \tag{3.11}$$

$$y = R.sin(R) \tag{3.12}$$

The Archimedean spiral waveguide was designed in MATLAB as shown in Figure 3.41 before converting it to a format recognised by a mask design software. The mask design software used for this project is WaveMaker 5.004 BASIC which recognises files in GDS format. Therefore, MZIs designed on MATLAB were saved in CSV format and converted to GDS format using another software known as LayoutEditor.

Figure 3.41a shows one Archimedean spiral with one complete turn designed on MATLAB. R and ϑ are both increased from 0 to 2π. Next an Archimedean spiral with 6.5 turns was designed as shown in Figure 3.41b where R goes from 0 to 13π μm.

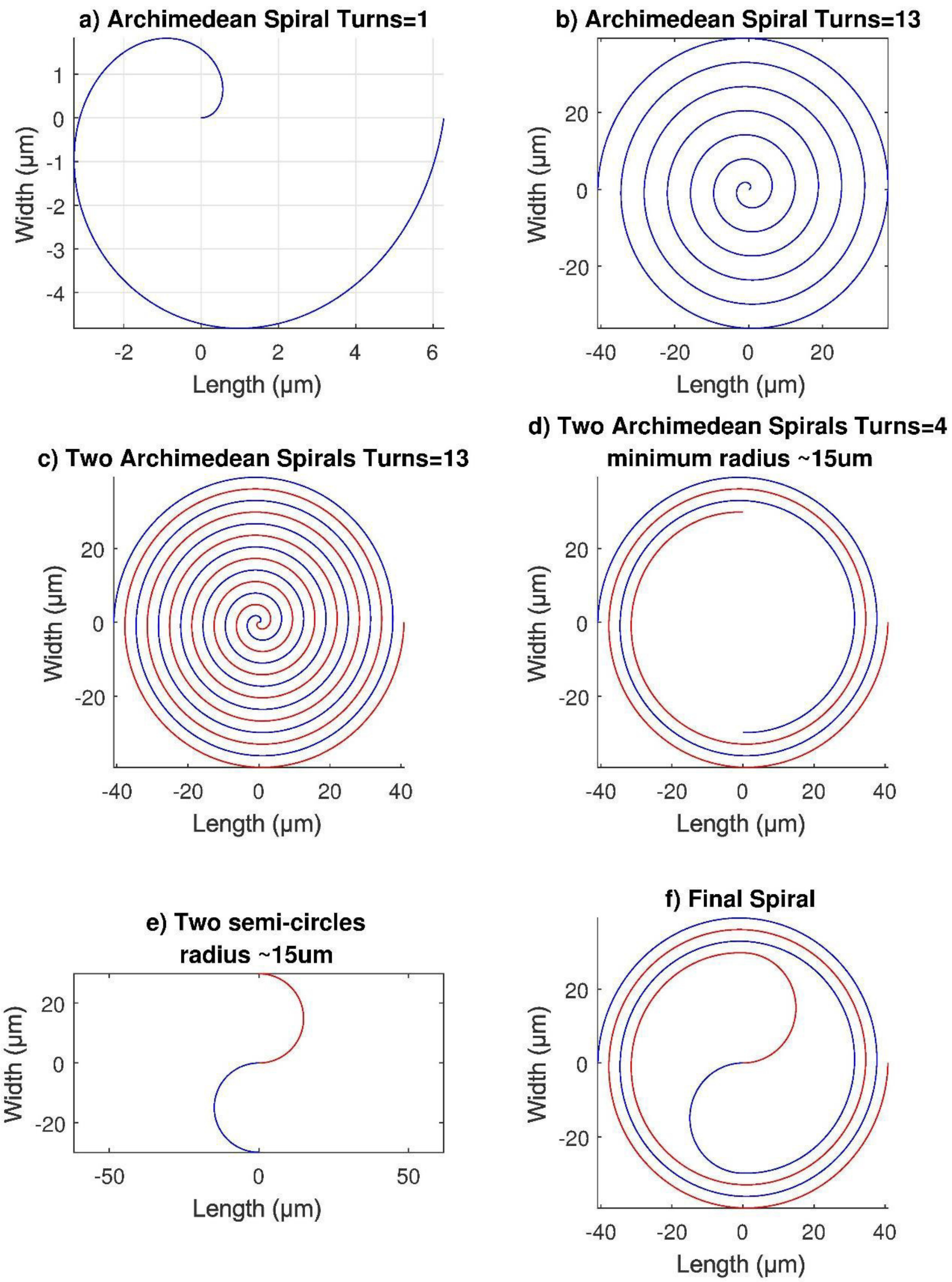

Figure 3.41: Design of spiral waveguides on MATLAB.

Then a second Archimedean spiral was added with a negative R as shown in Figure 3.41c. The second spiral is presented in red so the two spirals can be clearly identified. Now the total number of turns is 13 and R goes from 0 to 13π. The distance between each waveguide is π μm.

In section 3.1.7 the minimum radius of curvature for a vector TM-like mode for an operating wavelength of 1.55µm was found to be 15µm. So, the minimum *R* was fixed to 9.5π (≈30µm) as shown in Figure 3.41d. Now the number of turns is 4. Next two semi circles of radius 4.75π (≈15µm) were designed as shown in Figure 3.41e. Finally, the Archimedean spirals and the semi-circles were placed together to create a spiral waveguide as shown in Figure 3.41f.

Two spiral waveguides connected to straight waveguides were used to construct the sensing and reference arms of a MZI as shown in Figure 3.42. The two arms are spaced apart by a vertical and horizontal offset. For the design in Figure 3.42 the vertical offset was fixed at 25µm so that the Y-junction designed in the previous section can be used to connect the two arms to create a MZI. The minimum horizontal offset is set at 4 times the maximum R which in this case is 163µm, therefore the horizontal offset was fixed at 175µm.

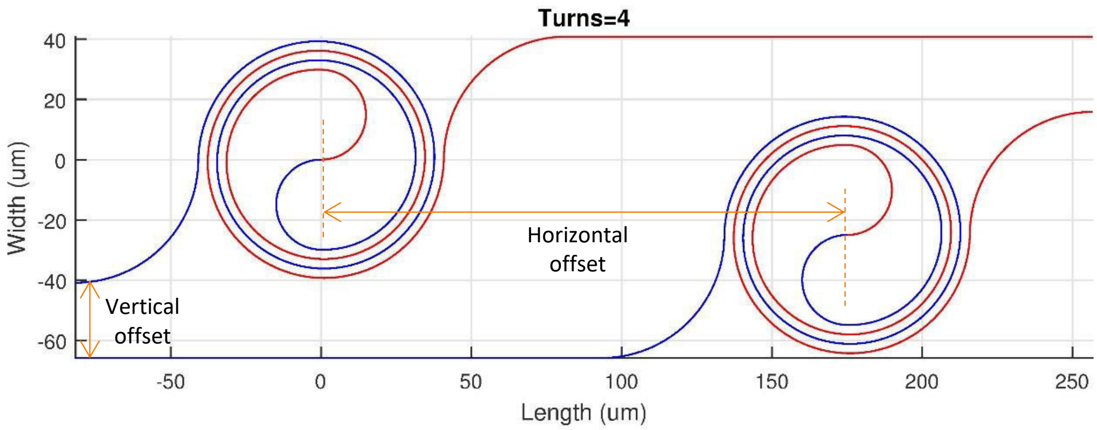

Figure 3.42: MATLAB design of the sensing and reference arm of the MZI designed with spiral waveguides where each spiral has 4 turns.

The length of one spiral is given by the equation 3.13 [3.47].

$$length\ of\ spiral = \int_{R_{min}}^{R_{max}} \sqrt{\left(\frac{dx}{dR}\right)^2 + \left(\frac{dy}{dR}\right)^2} \qquad (3.13)$$

The total length of one arm of the MZI shown in Figure 3.42 is 1174.6µm. The length can be increased within the same footprint by increasing the number of turns. See appendix B for the complete MATLAB code used to construct Figure 3.42, save in CSV format and calculate the length of each arm of the MZI.

Figure 3.43 shows the sensing and reference arms constructed with spirals of 10, 25 and 40 turns.

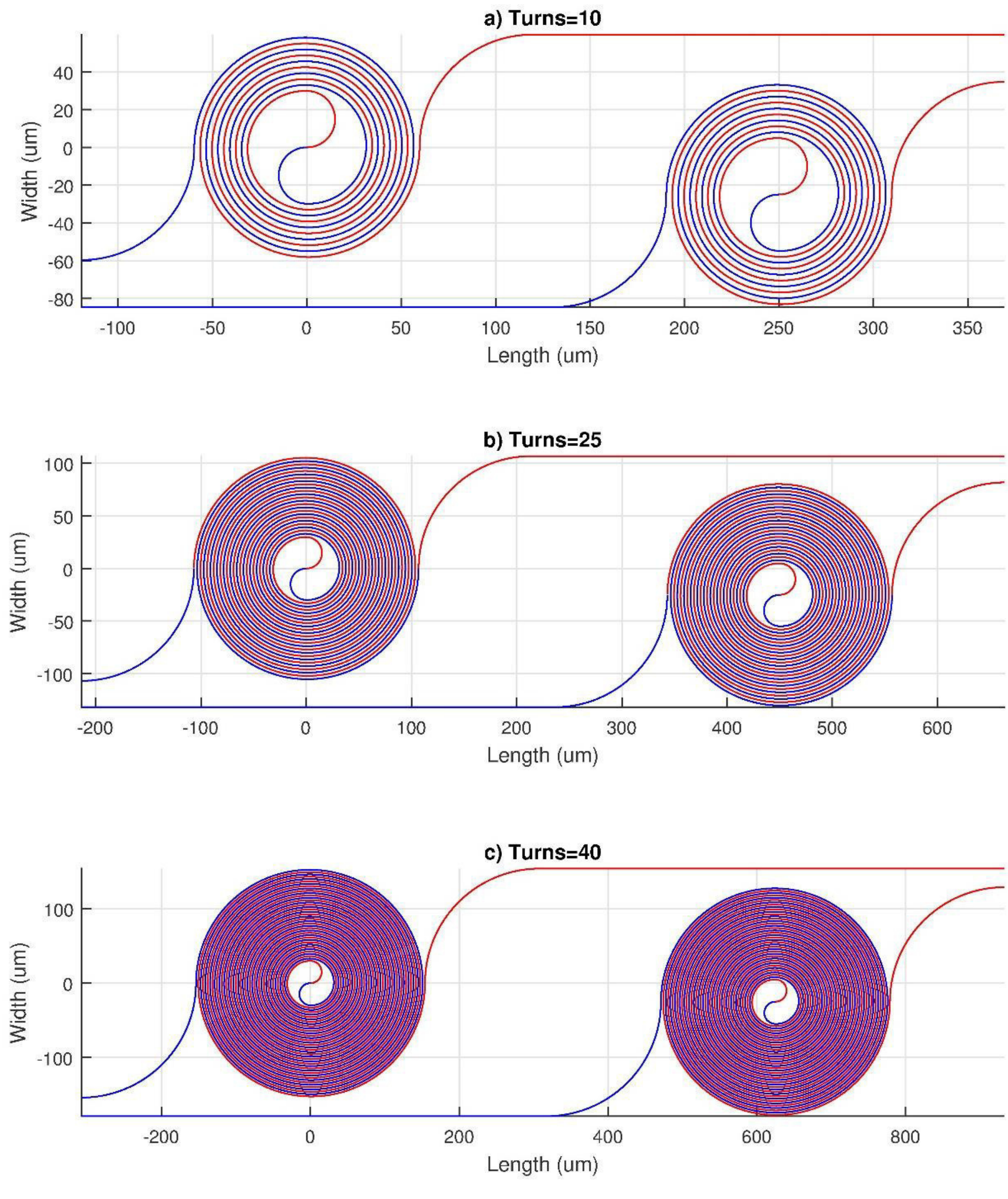

Figure 3.43: MATLAB design of the sensing and reference arm of the MZI designed with spiral waveguides where the number of turns in the spiral are a)10, b)25 and c)40.

Table 3.3 presents the maximum radius, minimum horizontal offset, horizontal offset used, area of MZI and the length of each arm of spiral MZI for 4, 10, 25 and 40 turns. From Table 3.3 the footprint or area of the MZI is small compared to the length of each arm achieved thus enabling the device to be as compact as possible while achieving the highest possible sensitivity which will be discussed in the following section.

Table 3.3: Maximum radius, Minimum horizontal offset, horizontal offset used, area and length of arm of spiral MZI for turns=4, 10, 25 and 40.

Turns	Maximum Radius (µm)	Minimum horizontal offset (µm)	Horizontal offset used (µm)	Area (Length × width) (µm × µm)	Length of arm (µm)
4	40.84	163.3	175	0.03mm^2 (338.4 × 81.7)	1 175
10	59.69	238.7	250	0.06mm^2 (488.8 × 119.4)	3 145
25	106.81	427.3	450	0.19mm^2 (877.2 × 213.6)	11 192
40	153.94	615.8	625	0.38mm^2 (1,239.2 × 307.8)	23 655

3.2.3 Simulated results

In this section, the sensitivity for a change in cover index was simulated using FIMMWAVE and the results for a perfect MZI are presented. For a perfect MZI it is assumed that the light is split equally into each arm and that there is no phase difference, both arms of exactly the same length and are are subjected to the same environment.

As explained previously in section 3.2, the binding of the target molecule with the antibody causes a change in the effective refractive index of the sensing arm which in turn causes a phase change, $\Delta\varphi$ expressed by equation 3.7 over the interaction length, L.

$$\Delta\varphi = \Delta N_{eff} \cdot k_0 \cdot L \tag{3.7}$$

where k_0 is the free space wave number or the phase constant ($2\pi/\lambda_0$).

Figure 3.44 shows the $\Delta\varphi$ when the cover index n_c was varied from 1.32 to 1.34 over an SOI waveguide of cross-section 0.5 × 0.22 µm and L of 1000µm. From Figure 3.44 it can be seen that a Δn_c of 0.0031 causes a 2π phase change in the propagating light.

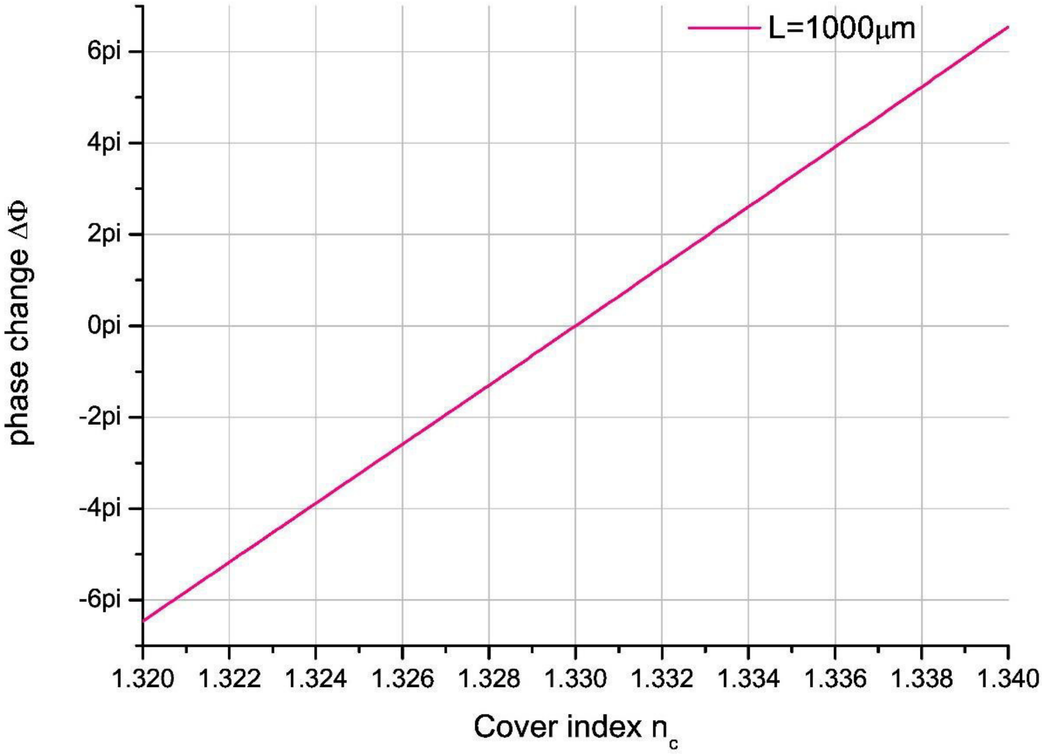

Figure 3.44: Phase change, Δϕ for varying cover index, n_c when L=1000µm.

As explained in section 3.2 the sensing and reference arms recombine and the phase change translates to a change in intensity which can be calculated using equation 3.8.

$$I = \frac{1}{2} I_0[1 + \cos(\Delta\varphi)] \tag{3.8}$$

where I_0 is the input intensity. The cosinusoidal variation of the simulated intensity is illustrated in Figure 3.45.

In a completed and working device it is the light intensity that is measured. Using the input and output light intensity and equations 3.7 and 3.8 the change in $\Delta\varphi$ and ΔN_{eff} can be calculated respectively. From Figure 3.5 a waveguide geometry operating in the vector TM-like mode for which $\Delta N_{eff}/\Delta n_c = 0.5$, Δn_c was chosen. For a homogenous sensor (see section 2.6), the device needs to be calibrated to know how the Δn_c corresponds to the change in concentration of the analyte solution. For a heterogeneous sensor (see section 2.6), the device needs to be calibrated to know how the Δn_c corresponds to the concentration of receptor molecules binding to the antibodies on the surface of the waveguide.

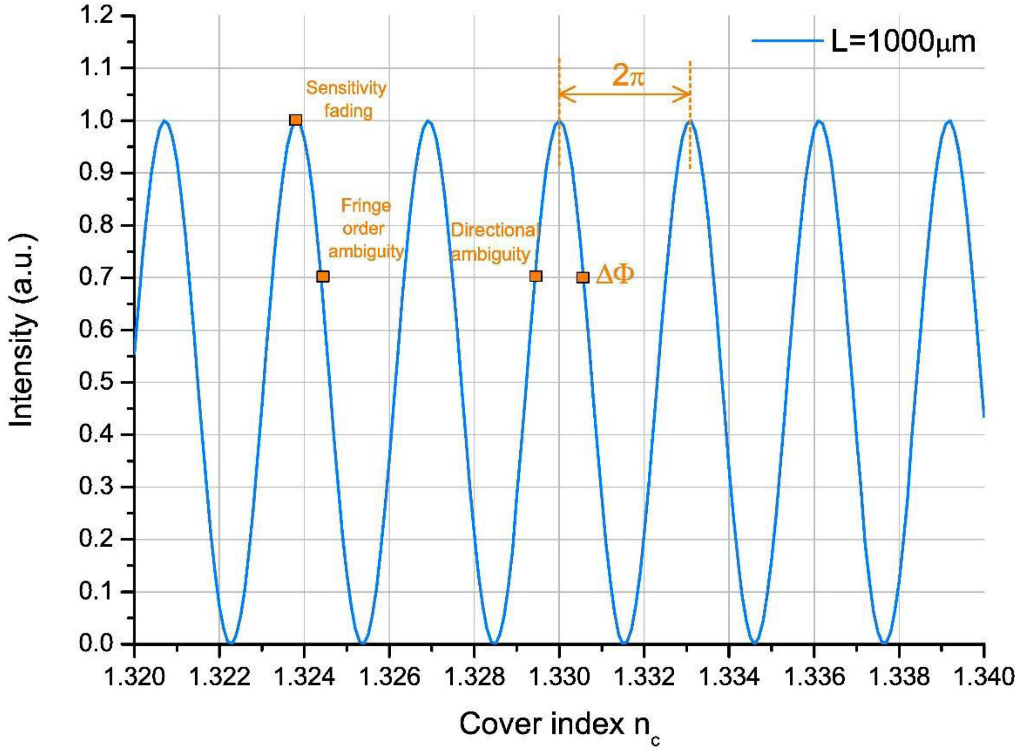

Figure 3.45: Change in Intensity for varying cover index, n_c *when L=1000μm and its intrinsic problems.*

Figure 3.45 also illustrates three intrinsic problems related to the MZI principle.

- The fringe order ambiguity – Occurs when $\Delta\varphi$ could be mistaken for a point on another fringe.
- Directional ambiguity – Occurs when $\Delta\varphi$ could be mistaken for a point on the same fringe.
- Sensitivity fading – Occurs when $\Delta\varphi$ is at the top or bottom if the fringe and is at risk of becoming zero.

These intrinsic problems have been addressed by R.G.Heideman and P.V.Lambeck [3.38] by applying additional active phase modulation but it is not currently applied in the work described in this thesis.

Another way to avoid these three instrinsic problems is to design the MZI with unequal sensor and reference arm lengths in such a way that *Δφ* is always located on one arm of the fringe.

If *L* was increased then the Δn_c needed to cause the same phase change will be smaller as given by equation 3.7 and illustrated in Figure 3.46 making the MZI more sensitive to a change in the cladding refractive index.

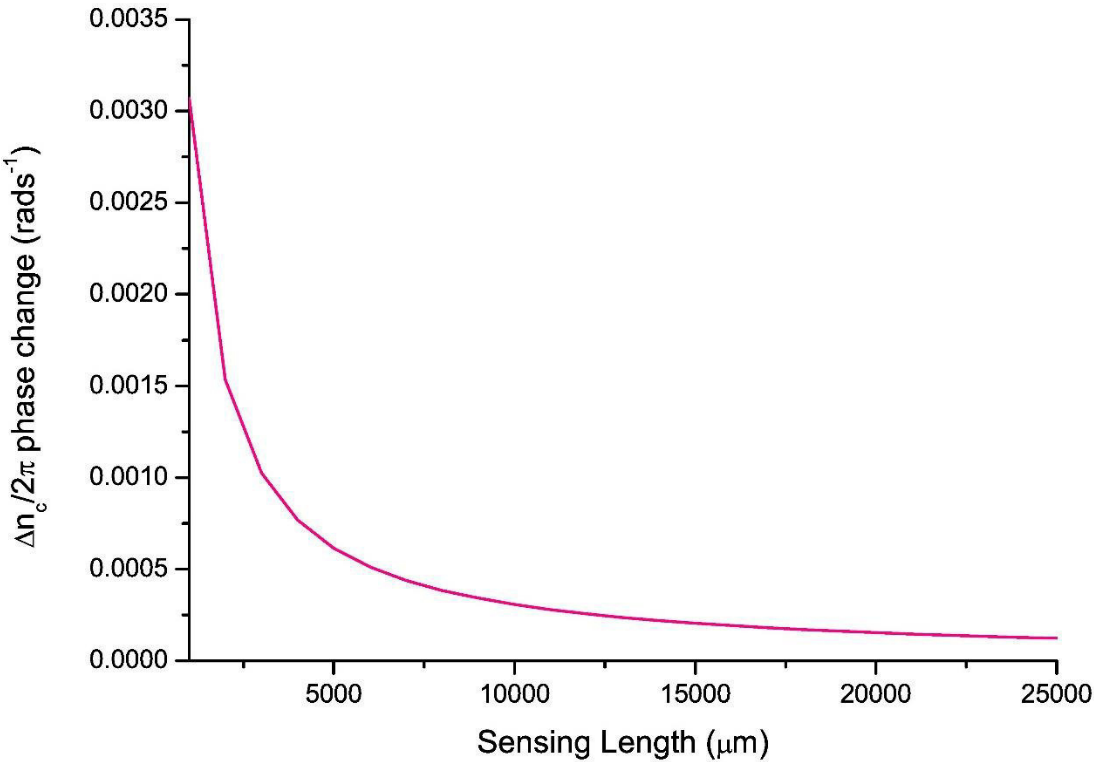

Figure 3.46: Sensitivity for varying L.

L was varied from 1000 to 25,000μm and the Δn_c needed for a 2π phase change was calculated, as shown in Figure 3.46. This graph is useful as in section 3.2.2 spiral MZIs were designed where the L could be between 1 175 to 23 655μm as shown in Table 3.3. The sensitivity increases as length increases.

For *L*=1000μm the $\Delta n_c/2\pi = 0.0031$ rads^{-1} (assuming $\Delta N_{eff}/\Delta n_c = 0.5$). If a phase resolution of 2π × 10^{-4} rads is assumed [3.38] it gives the device a sensitivity of 3.1 × 10^{-7} RIUs.

Using spirals can increase the interaction length, *L* within a given device footprint. Table 3.4 shows the calculated sensitivity for each spiral MZI design proposed in Table 3.3. However, as the length of the arm increases the device becomes more vulnerable to fabrication errors. The increase in sensitivity must be weighed against the complexity and yield of fabrication.

Table 3.4: Sensitivity calculation for spiral MZIs based on the spiral geometries summarised in Table 3.3.

Turns	Length of arm (µm)	Sensitivity (RIUs)
4	1 175	2.6×10^{-7}
10	3 145	9.9×10^{-8}
25	11 192	2.8×10^{-8}
40	23 655	1.3×10^{-8}

In the literature MZIs have been demonstrated with high sensitivity, down to 10^{-6} to 10^{-7} refractive index units (RIUs) [3.32, 38].

However, if the MZI is to be designed in a way that $\Delta\varphi$ is always located on one arm of the fringe as illustrated in Figure 3.45, then increasing the sensitivity is not always optimal due to the intrinsic problems of a MZI.

3.3 PLASMONIC INTERFEROMETERS

In addition to the MZI interferometer, another optical sensor considered based on Silicon-on-Insulator (SOI) material is a plasmonic interferometer. In this section, the plasmonic interferometer is discussed in detail.

3.3.1 Plasmonic waveguide theory

Metals can concentrate a mode's power at the surface of the waveguide to form Surface plasmon polaritons (SPP). A Surface plasmon (SP) is the quantum of oscillation at the surfaces of metals at optical frequencies. Surface plasmon polaritons (SPP) occur when the incident light (a photon) at infrared or visible frequency couples with the SP to create a self-sustaining and propagating electromagnetic wave at the surface of the plasmonic material. Plasmonic materials are metals or metal-like materials that exhibit negative real permittivity at a particular wavelength. A thin metal layer cannot be simply added on top of the waveguide as the phase matching condition must be met for the guided mode to excite the plasmon mode. The phase matching condition [3.48] can be expressed as $k_p = \beta$ where β is the propagation constant of the guided mode and k_p is the wavevector of the plasmon mode given by [3.48]

$$k_p = k_0 \cdot \sqrt{\frac{\varepsilon_m \cdot \varepsilon_d}{\varepsilon_m + \varepsilon_d}} \tag{3.14}$$

where k_0 is the free space vector, ε_m and ε_d are complex dielectric constants of the metal film and dielectric. It is also worth noting that only the electric field components E_y and E_z light can excite the plasmon mode and therefore only TM polarised light can be used for plasmonic sensing [3.48].

For a high index contrast material system such as SOI the phase matching condition is difficult to meet as the wavevectors of the metal and the dielectric differ too much [3.49]. Therefore, the guided wave is coupled to the plasmonic mode with the use of Bragg gratings [3.50, 51] or by end-fire coupling into an embedded metal with TM polarised light and using the interference between the two surface plasmon modes as first explained by Debarckere *et al*. [3.52] and illustrated in Figure 3.47.

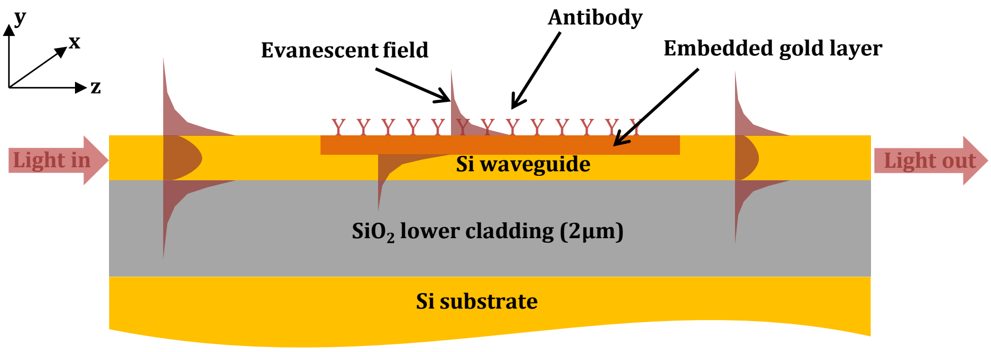

Figure 3.47: Illustration of a plasmonic interferometer.

At the embedded gold layer on the waveguide, the guided mode launches two plasmon modes, one above and one below the gold layer. These two plasmon modes will have different phase velocities depending on the refractive index of the dielectric above and below the gold layer respectively. At the end of the gold layer the plasmon modes will couple back to the guided mode with constructive or destructive interference (caused by the phase difference between the two plasmon modes) similar to an MZI. The intensity variation at the output can be used to find the change in refractive index of the sensing medium. From literature, a theoretical detection limit of 10^{-6} RIU has been presented [3.52] which is comparable to the sensitivities presented in section 3.2.3.

3.3.2 Design

CAMFER, an Eigen mode solver [3.53] was used to simulate a plasmonic interferometer comprised of a 0.32µm x 4µm silicon photonic wire. The embedded gold thickness and length were optimised to get 0.23µm and 13µm respectively to obtain maximum sensitivity for the current silicon wire dimensions. The refractive index used for gold is 0.556 with an extinction coefficient of 9.936 [3.54]. A Δn_c of 0.01 (1.34-1.33) shifts the resonant condition by 5nm as shown by the solid lines in Figure 3.48 giving a predicted system wavelength shift responsivity of 500nm/RIU.

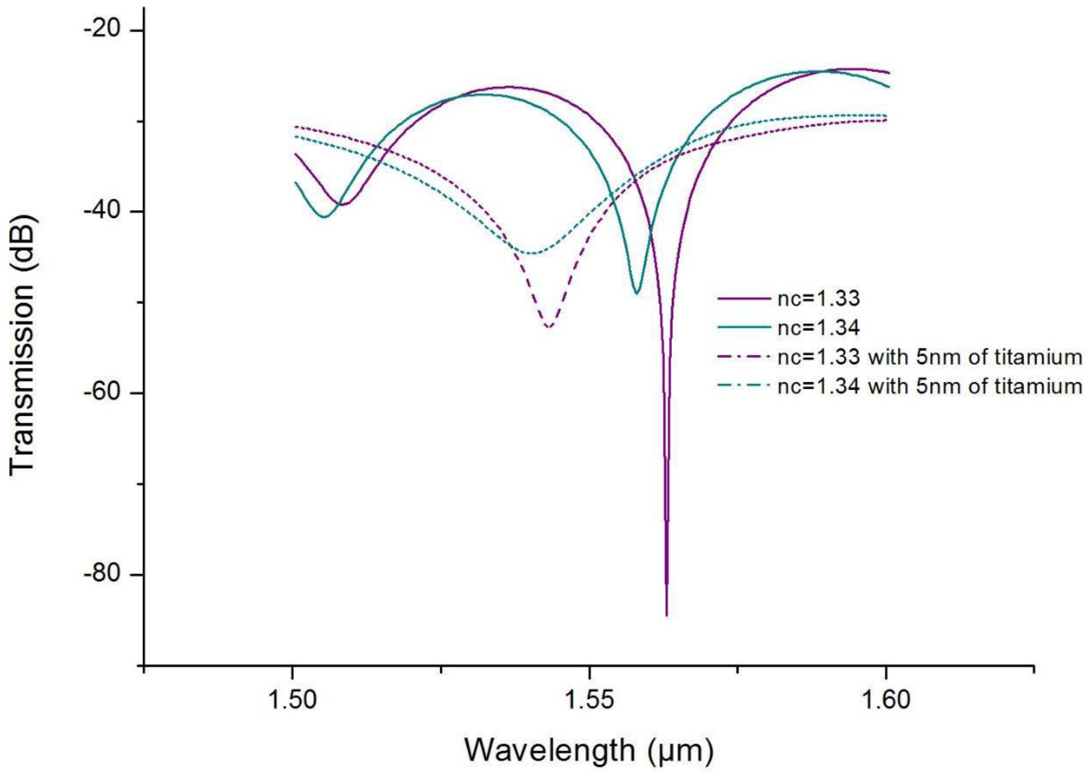

Figure 3.48: Simulated transmission (with and without a thin titanium layer) of the plasmonic interferometer as a function of wavelength.

Due to the high insertion loss, detection is very difficult even with an isolated device. Although a plasmonic interferometer offers advantages of compactness, its high insertion loss mitigates against the desired parallel detection in the present project. Nevertheless, a plasmonic interferometer was fabricated as described in chapter 4 and some initial results are shown in chapter 6.

A 5nm layer of titanium was deposited by thermal evaporation to improve adhesion between gold and silicon in practice. The dotted curves in Figure 3.48 shows that the 5nm thick titanium layer reduces the sensitivity to 250nm/RIU when the refractive index of titanium is 3.685 and the extinction coefficient is 4.618 [3.55]. In the experimental realisation of the structure (see section 4.3.4) a 5nm layer of titanium was deposited. See section 6.2 for optical results of the plasmonic interferometer fabricated.

3.4 MULTIMODE INTERFERENCE (MMI) COUPLER

In 1973 Olof Brynghal used Fresnel image planes as shown in Figure 3.49, and a pinhole array as shown in Figure 3.50 to demonstrate the formation of multiple images of an object based on self-imaging techniques [3.56]. In 1975 R. Ulrich reviewed this phenomenon on multimode planar dielectric slab waveguides [3.57, 58] which was explained in more detail by Heaton *et al*. [3.59] in 1992. In 1995 Soldano and Pennings [3.60] stated the principle as "*Self-imaging is a property of multimode waveguides by which an input field profile is reproduced in single or multiple images at periodic intervals along the propagation direction of the guide*".

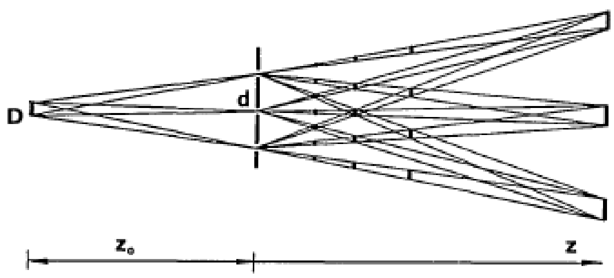

Figure 3.49: Illustration of how Fresnel images are formed in a self-imaging situation [3.56].

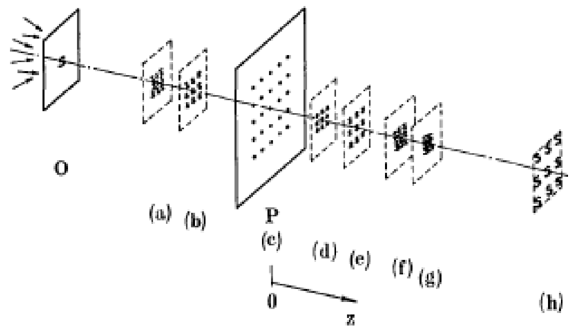

Figure 3.50: Schematic representation of the imaging system. Arrays of images of spatial incoherently illuminated object in O appear in several planes behind and in front of the pinhole array P [3.56].

Multimode Interference (MMI) devices are based this self-imaging principle where the input image is reproduced into multiple images at the output with high uniformity [3.60]. Compared to Y-branches, MMI couplers can be made very compact and sharply increase tolerance to fabrication errors as sharp edges near the branching points are avoided. MMI devices also have wide optical bandwidths (in the context of telecommunication systems), low cross talk and polarisation independence and are widely used in integrated optics as power splitters [3.61, 62], modulators [3.63], multiplexers [3.64], switches [3.65] and in Mach-Zehnder interferometers [3.62].

For present purposes, a wide bandwidth is not required as the biosensor operates at a fixed wavelength of 1.55µm. However, for completeness the bandwidth is studied in section 3.4.2.3. On the other hand, polarisation dependence is important for the designed biosensor as the device needs to operate in a vector TM-like mode. In section 3.4.2.1 it is shown that the MMI couplers are polarisation sensitive.

1×*N* MMI couplers (where *N* is the number of outputs) have been theoretically and experimentally investigated widely especially for SOI based devices because of their compactness due to high index contrast, low losses and compatibility with silicon electronics and biological samples [3.66-71]. The highest number of outputs presented theoretically is 64 [3.72] and experimentally is 12 [3.68] whereas this project has experimentally achieved 20 outputs.

In this project, parallel sensing of biological fluid is achieved by connecting Mach-Zehnder interferometers (as explained in section 3.2) to the outputs of an MMI coupler. This chapter will focus on the theory, design and optimisation of the MMI couplers.

3.4.1 Design of MMI couplers

Inside the MMI cavity the beam is split into numerous modes and the symmetric intensity pattern is repeated periodically at the intervals of Λ along the guide:

$$\Lambda = \frac{n_{eff} {W_{MMI}}^2}{\lambda_0} \tag{3.15}$$

where n_{eff} is the effective refractive index of the MMI cavity, W_{MMI} the width of the MMI cavity and λ_0 is the operational wavelength [3.59]. Figure 3.51 shows the theoretical light intensity patterns of a self-imaging waveguide where the symmetric pattern is repeated periodically and *N* images of the input guide are formed in the plane $z = \Lambda/N$.

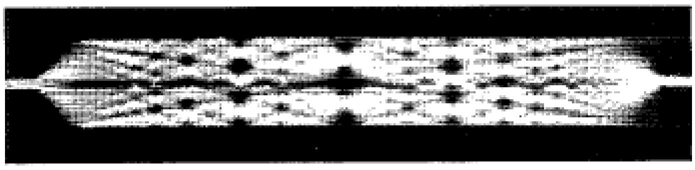

Figure 3.51: Theoretical light intensity patterns in a 20µm wide self-imaging waveguide [3.59].

The N images formed are equally spaced across the multimode guide. The transverse distance between the images is known as the 'Pitch', $\rho = W_{MMI}/N$. In this section, the MMIs were designed for SOI core height 0.32µm due to the initial availability of wafer and the width of input and output waveguides was 4µm as illustrated in Figure 3.52. In section 3.4.3 the MMIs are redesigned for the preferred SOI waveguide dimension of 0.22µm × 0.5µm.

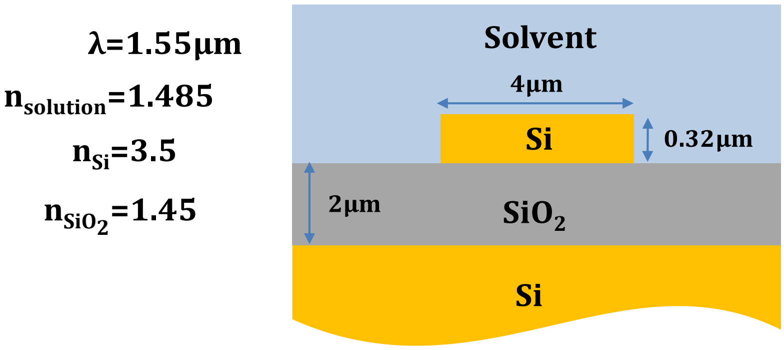

Figure 3.52: Schematic illustration of a cross-section of the Input/output waveguide for the MMI.

The pitch was fixed at 15µm to prevent interference between the output waveguides. W_{MMI} is determined by the number of output waveguides, N, where $W_{MMI}=N\rho$. Figure 3.53 is a schematic diagram of a 1x2 MMI with its design parameters shown.

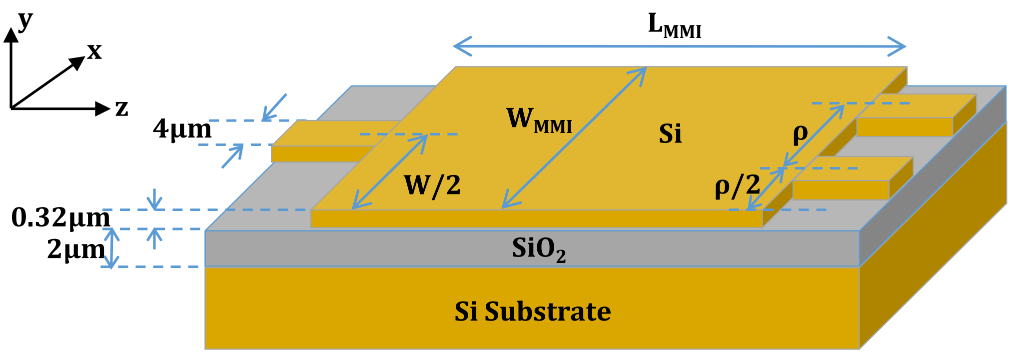

Figure 3.53: Schematic diagram of a 1x2 MMI structure.

Using these values the approximate MMI length, L_{MMI} is calculated by Equation 3.16 [3.59]:

$$L_{MMI} = \frac{\Lambda}{N} = \frac{n_{eff} {W_{MMI}}^2}{N\lambda_0} \tag{3.16}$$

Equation 3.16 gives only an approximate length as the modes are not strictly confined to the multimode MMI region [3.70] as is assumed in the derivation of the equation. Propagation in the structure was simulated using a 3D BPM (RSoft Beam Prop). Figure 3.54 shows the CAD layout for a 1x2 MMI coupler. Input and output waveguide width and height were kept at 4µm and 0.32µm respectively and the operating wavelength was 1.55µm.

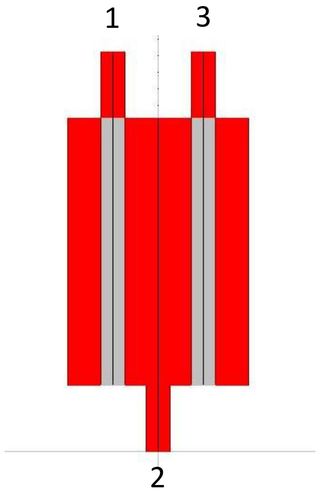

Figure 3.54: CAD layout of a 1x2 MMI coupler and the power paths.

The two grey strips in Figure 3.54 are inactive structures included to monitor the power in their pathways within the BPM as shown in Figure 3.55.

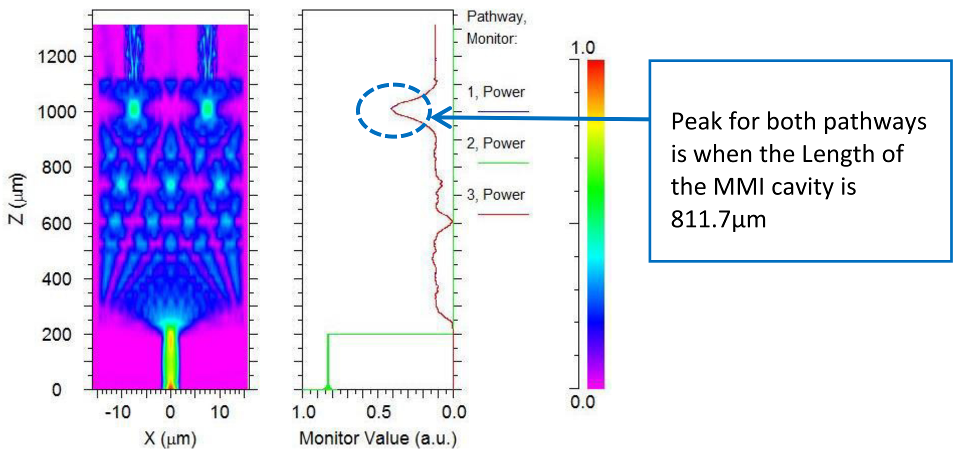

Figure 3.55: Illustrating TE-like mode BPM simulation of a 1x2 MMI coupler for an operating wavelength of 1.55µm and input/output waveguide cross-section of 0.32µm × 4µm.

Optimum cavity length is when the power of all the outputs is equal or almost the same. At optimum length, the device will have its lowest insertion loss and highest uniformity, which is discussed in more detail in section 3.4.2.2. The structure was simulated again with the optimum L_{MMI} to confirm the MMI cavity length as shown in Figure 3.56.

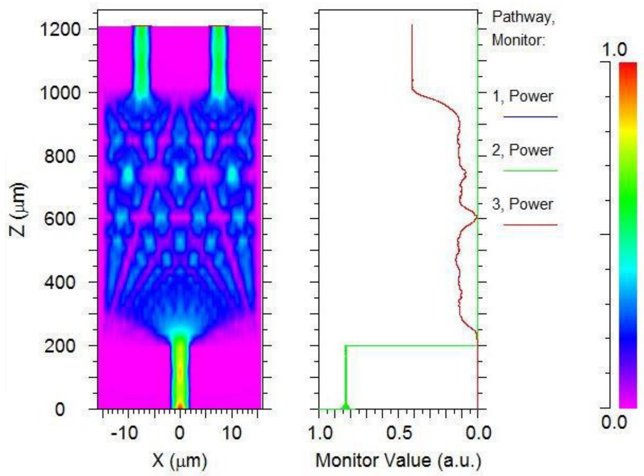

Figure 3.56: Optimised 1x2 MMI splitter for the TE-like mode at an operating wavelength of 1.55μm and input/output waveguide cross-section of 0.32μm × 4μm.

The same technique was used to design a 1x20 MMI as illustrated in Figure 3.57.

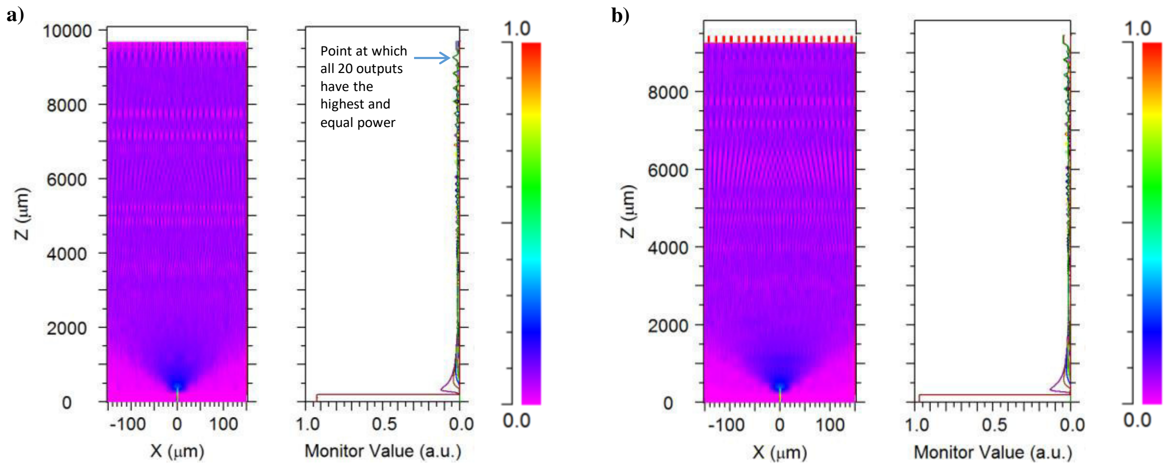

Figure 3.57: Illustrating TE-like mode simulation for 1x2 MMI with a) longer cavity length and b) optimum cavity length for an operating wavelength of 1.55μm and input/output waveguide cross-section of 0.32μm × 4μm.

3.4.2 Simulation evaluation

There are some key factors to consider when designing an MMI such as polarization dependence, insertion loss, non-uniformity, tolerance to wafer core thickness variations and fabrication tolerance. In the following subsections, the MMI devices are characterized to explore these conditions.

3.4.2.1 Polarisation dependence

Table 3.5 shows the calculated width and length of the MMI cavity for 2, 3, 5, 8, 12, 15, and 20 outputs. The simulated optimum length for vector TE-like and TM-like modes are presented for these MMI couplers.

Table 3.5: Optimum 1×N MMI cavity length for TE-like and TM-like modes for an operating wavelength of 1.55μm and input/output waveguide cross-section of 0.32μm × 4μm.

N	W_{MMI} (μm)	L_{MMI} calculated (μm)	L_{MMI} Optimum (μm)	
			TE-like mode	TM-like mode
2	30	889.7	910.1	802.6
3	45	1334.5	1361.2	1200.4
5	75	2224.3	2269.7	2008.3
8	120	3558.9	3630.4	3205.1
12	180	5338.3	5443.4	4804.2
15	225	6672.9	6803.0	6006.2
20	300	8897.2	9063.5	8012.2

From the table, it can be observed that the optimum lengths for TM-like mode are significantly shorter than those for the TE-like mode making the device polarization sensitive. This is an advantage for evanescent field based biosensors which operate in a TM-like mode to obtain high sensitivity and for which only one light polarisation is required since the other polarisation is not efficiently coupled into the MZI sections.

3.4.2.2 *Insertion loss and uniformity*

Insertion loss and uniformity are the two most commonly used Figures of Merits to compare the efficiency of MMI devices [3.73, 74]. Insertion loss is defined as:

$$Loss\ insertion(dB) = -10log_{10}\left(\sum_{n=1}^{N}\frac{P_n}{P_{in}}\right) \tag{3.17}$$

where P_{in} is the input power and P_n is the power of the n^{th} port.

The Non-uniformity is defined as:

$$Non\text{–}uniformity(dB) = -10log_{10}\left(\frac{P_{min}}{P_{max}}\right) \tag{3.18}$$

where P_{min} and P_{max} are the maximum and minimum power observed in the *N* ports.

Insertion loss and uniformity calculated for (1×N) MMI couplers up to 1×20 are presented in Table 3.6.

Table 3.6: Insertion loss and Non-uniformity for 1×N MMIs for an operating wavelength of 1.55µm and input/output waveguide cross-section of 0.32µm × 4µm.

N	Insertion Loss (dB)		Non-uniformity (dB)	
	TE-like mode	TM-like mode	TE-like mode	TM-like mode
2	0.11	0.07	0.00	0.00
3	0.12	0.12	0.00	0.00
5	0.16	0.17	0.01	0.01
8	0.19	0.28	0.02	0.01
12	0.21	0.40	0.04	0.03
15	0.23	0.49	0.04	0.03
20	0.23	0.73	0.06	0.08

It is assumed in [3.59] that all guided waves are confined to the MMI cavity whereas in reality there will also be leaky modes and radiation modes present [3.59]. Therefore, losses increase as the MMI length increases when N increases [3.71].

3.4.2.3 Optical bandwidth and fabrication tolerance for 1xN MMIs

The wavelength dependence or optical bandwidth is evaluated on the basis of the cost of a maximum additional loss of 1dB. Theoretically the optical bandwidth is inversely proportional to the number of outputs [3.75]. Fabrication tolerance is defined as the 1×N MMI cavity width (W_{MMI}) variation that produces an additional loss of 1dB. Table 3.7 shows that the bandwidth reduces as the number of outputs increases, however, the fabrication tolerance stays the same.

Table 3.7: Bandwidth and Fabrication Tolerance for 1xN MMIs for an operating wavelength of 1.55µm and input/output waveguide cross-section of 0.32µm × 4µm.

N	Optical Bandwidth (nm)		Fabrication Tolerance (µm)
	TE-like mode	TM-like mode	
2	81	63	±1
3	60	41	±1
5	36	26	±1
8	23	16	±1
12	15	12	±1
15	12	9	±1
20	9	8	±1

3.4.2.4 Wafer core thickness and tolerance

The core height of the SOI devices depends on the wafer purchased. The wafer used for initial experiments on MMI couplers had a standard deviation of 19.8 nm on a silicon core thickness of 320nm and a buried oxide of 2µm. Therefore, MMIs were designed to have +/- 20nm of silicon core height tolerance.

Figure 3.58 presents the optimum cavity length for a +/- 20nm of silicon core height tolerance for the vector TM-like mode calculated from simulations using RSoft BeamPROP.

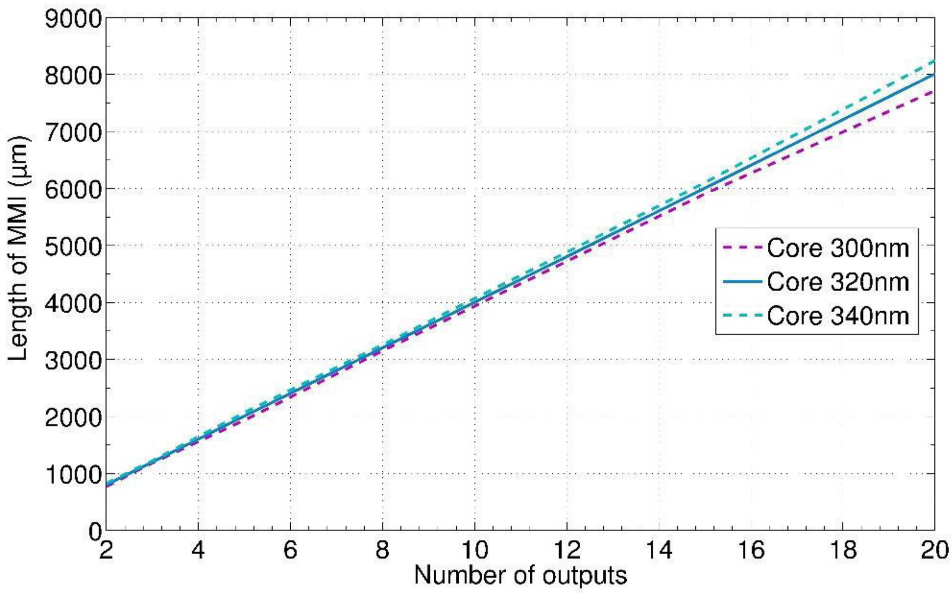

Figure 3.58: Optimum MMI cavity length for silicon core thickness 0.32µm and +/-20nm for 1xN MMI for the vector TM-like mode at an operating wavelength of 1.55µm and input/output waveguide cross-section of 0.32µm × 4µm.

The results presented in Figure 3.58 show that the length of the MMI cavity increases linearly as the number of outputs increases. As the number of outputs increases, the tolerance to core thickness variation decreases.

3.4.3 MMI with single mode input/output waveguide

The input and output waveguides in the MMI designs in section 3.4.2 are multimoded at a wavelength of 1.55µm as the width and height of waveguides are 4µm and 0.32µm respectively. As explained in section 3.2.2 the waveguides must be single mode for the MZI to be functional as splitter with high uniformity. In this section, the MMI is further improved by reducing the height and width of the input and output waveguides to 0.5µm and 0.22µm respectively as illustrated in Figure 3.59. Further the pitch is reduced from 15µm to 5µm thus greatly reducing the footprint of the MMI device.

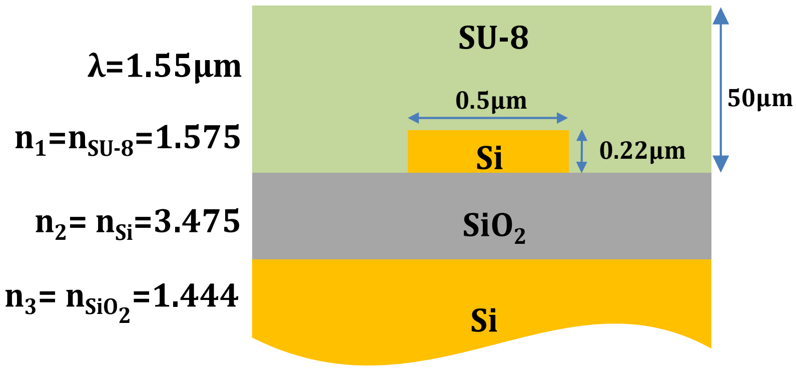

Figure 3.59: Cross-section of input/output waveguide

The MMI will be covered with the polymer SU-8 therefore upper cladding index, n_1 is set to 1.575 [3.76] and the core and lower cladding, n_2 and n_3 are set to 3.475 and 1.444 respectively as these are the default index values given in the FIMMWAVE software at the operating wavelength of 1.55µm. These values are used throughout the remainder of these chapter; therefore, the simulations in section 3.4.3.1 and 3.4.3.2 are directly comparable.

3.4.3.1 Simulation evaluation for MMI with single mode input/output waveguides using RSoft BeamProp

The 1x2 MMI described in the previous section was simulated using RSoft BeamProp software as shown in Figure 3.60 for a TM-like mode at an operating wavelength of 1.55µm. The width of the input/output waveguides in Figure 3.60a is 2µm which is multi-moded and the input/output waveguides in Figure 3.60b is 0.5µm which is single-moded. The width of the MMI cavity was fixed at 10µm in both cases.

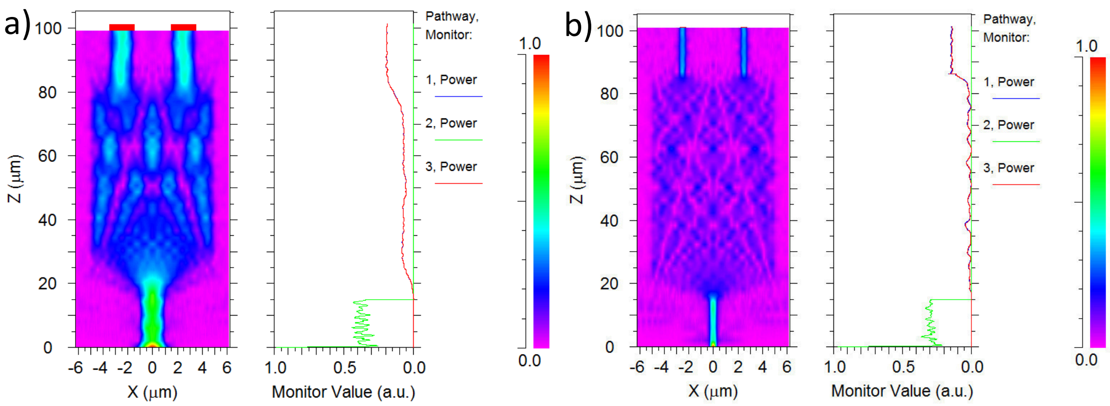

Figure 3.60: Optimised 1x2 MMI splitter for TM-like mode with input/output waveguide width a) 2µm and b) 0.5µm simulated with RSoft BeamPROP for an operating wavelength of 1.55µm and MMI cavity width of 10µm.

The length of the MMI cavity is 71.2µm and 71.4µm for input/output waveguide width 0.5µm and 2µm respectively. From both simulations in figure 3.56 a sharp drop in power over the first 15nm of propagating can be seen and the power continues to fluctuate throughout the input waveguide and the output waveguide. As a result, it is impossible to calculate an accurate insertion loss for this device. The RSoft BeamProp software becomes unreliable when simulating vector TM-like mode propagation in these narrow high index contrast (HIC) structures. The same device was therefore simulated using another commercial software FIMMWAVE [3.11] using the Eigenmode expansion (EME) method as shown in the following subsections.

3.4.2.2 Simulation evaluation for MMI with single mode input/output waveguides using FIMMPROP

The 1x2 MMIs from subsection 3.4.2.1, with input/output width of 0.5µm and 2µm were simulated using FIMMPROP as shown in Figure 3.61.

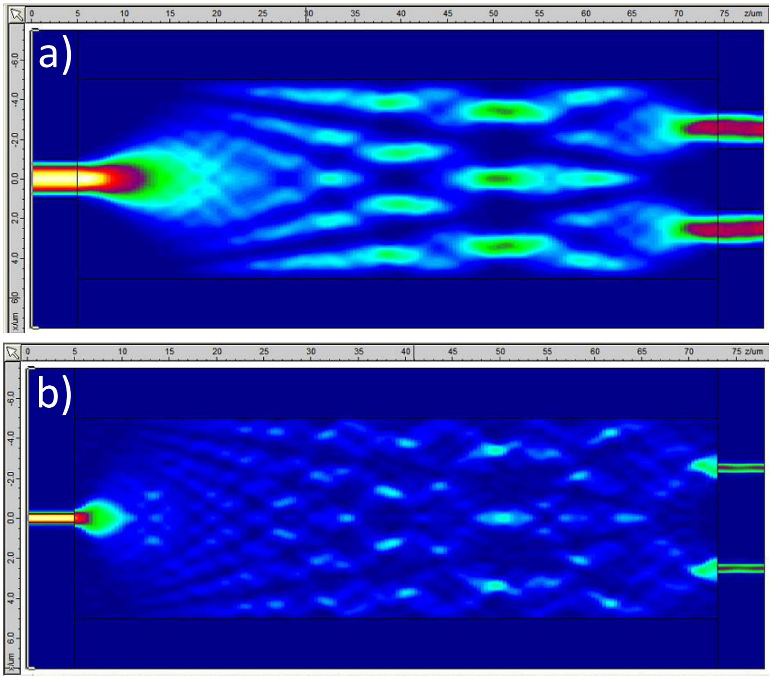

Figure 3.61: Optimised 1x2 MMI splitter for TM-like mode with input/output waveguide width a) 2µm and b) 0.5µm simulated with FIMMPROP for an operating wavelength of 1.55µm and MMI cavity width of 10µm.

Compared to Figure 3.60 the power in the input and output waveguides are much more stable in Figure 3.61. The optimal length of the MMI cavity is found to be 68µm and 69.3µm for input/output waveguide width 0.5µm and 2µm respectively. The optimum length of the MMI cavity obtained from RSoft Beam Prop was 71.2µm and 71.4µm respectively as compared in Table 3.8.

For the same wavelength and refractive indices, the two softwares give an L_{MMI} with ≈3µm difference. Since RSoft BeamPROP show unstable behaviour for narrow HIC waveguides the results obtained using FIMMPROP are viewed as more credible and therefore the rest of the MMIs presented in this chapter were designed using FIMMPROP.

Table 3.8: Comparison of L_{MMI} for input/output waveguide width using RSoft BeamPROP and FIMMPROP for the vector TM-like mode at an operating wavelength of 1.55µm.

Input/output waveguide width (µm)	W_{MMI} (µm)	RSoft BeamPROP TM-like mode L_{MMI} (µm)	FIMMWAVE TM-like mode L_{MMI} (µm)
0.5	10	71.2	68.9
2.0	10	71.4	69.7

The optimum length of the MMI cavity studied in subsection 3.4.2.1 with the larger dimension was 802.6µm. By reducing the core height from 0.32µm to 0.22µm, narrowing the input/output waveguide width from 4µm to 0.5µm and reducing the pitch from 15µm to 5µm the MMI cavity length has been reduced by a factor of 12.

Table 3.9 shows the insertion loss and non-uniformity, calculated from simulation results using equations 3.17 and 3.18 respectively, for varying widths of input/output waveguides for a 1x2 MMI. Simulations were undertaken using FIMMPROP for an operating wavelength of 1.55µm and W_{MMI} of 10µm.

Table 3.9: Insertion loss and non-uniformity for 1x2 MMIs for varying input/output waveguide widths for an operating wavelength of 1.55µm and W_{MMI} of 10µm.

Input/output width (µm)	L_{MMI} (µm)	Insertion loss (dB)	Non-uniformity (dB)
0.5	68.9	3.003	0.000
1.0	68.4	1.275	0.000
1.5	68.0	0.455	0.000
2.0	69.7	0.146	0.000

Table 3.9 shows that as the input/output waveguide width increases the insertion loss decreases significantly. The non-uniformity remains 0dB as the simulated output in each waveguide is the same. From section 3.1.3 the waveguide widths were fixed at 0.5µm for optimum sensitivity whereas from Table 3.9 it is apparent that the width of the input and output waveguides should be 2µm to reduce the insertion loss. To overcome this a taper is introduced as described in the following sections.

Table 3.10 shows the insertion loss and non-uniformity calculated for MMI splitters up to 20. The width of the input and output waveguides were fixed at 0.5µm. Insertion loss and non-uniformity were calculated from simulation results using equations 3.17 and 3.18 respectively. All simulations were undertaken for the vector TM-like mode at a wavelength of 1.55µm using FIMMPROP.

From Table 3.10 it can be seen that the L_{MMI}, insertion loss and non-uniformity increases as the number of outputs, N increases.

Table 3.10: Insertion loss and non-uniformity for single mode waveguide MMI splitters the vector TM-like mode at a wavelength of 1.55µm.

N	W_{MMI} (µm)	L_{MMI} (µm)	Insertion Loss (dB)	Non-uniformity (dB)
2	10	68.9	1.35	0
4	20	134.5	1.66	0.01
8	40	268.0	2.30	1.11
12	60	401.8	2.91	1.01
16	80	537.4	2.97	1.70

3.4.4 Tapered MMI

In this section techniques to reduce insertion loss observed to occur for narrow input/output waveguide widths in section 3.4.3 by tapering the input and output waveguides are discussed.

Tapers are used to couple light into devices with different cross-sections and are also used as spot size converters to couple light in and out of fibres from waveguides as will be described in section 3.5.1. To couple light with high efficiency the taper structure must operate adiabatically where the fundamental mode of the waveguide should propagate through the taper while undergoing relatively little mode conversion to higher-order modes or radiation modes [3.77]. This is achieved by changing the taper cross-section very slowly. The cross-section of the taper can be changed linearly [3.78], exponentially [3.79] or parabolically [3.78]. In this section, linear tapers combined with MMIs are considered.

Robert Halir *et al*. [3.80], D. J. Thompson *et al.* [3.81] and Zhang Sheng *et al*. [3.82] have designed 1x2 MMIs with tapered input and output waveguides with insertion losses of 0.1dB, 1dB and 0.039dB respectively; their designs are illustrated in Figure 3.62. Note that these values cannot be directly compared to the MMI splitters designed in this chapter as the structure specifications are not the same but the literature designs provide suggested avenues for further study.

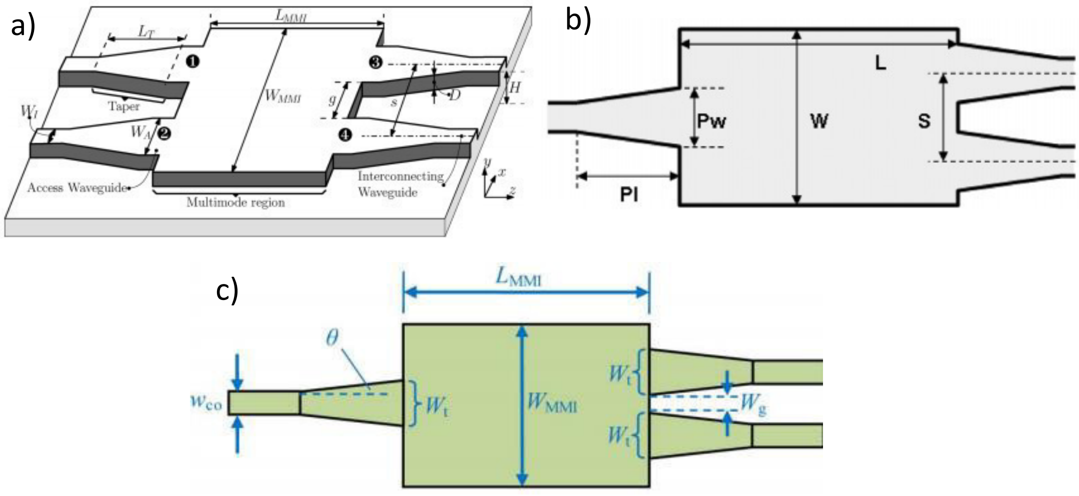

Figure 3.62: Tapered MMI structures designed by a) Robert Halir et al. [3.80], b) D. J. Thompson et al [3.81] and c) Zhang Sheng et al. [3.82].

3.4.4.3 Designing tapered MMI with FIMMWAVE

In section 3.4.2.2 it was shown that for an MMI with input and output waveguide width of 0.5µm the insertion loss is 3dB. In an attempt to reduce this loss effect of tapering the input and output waveguides is studied in this section, as illustrated in figure 3.64. The *w* and taper width, T_w is fixed at 0.5µm and 2µm respectively. The L_{MMI} is optimised for input/output waveguide width of 2µm and a taper of optimum T_L is designed separately and then combined to save computational time.

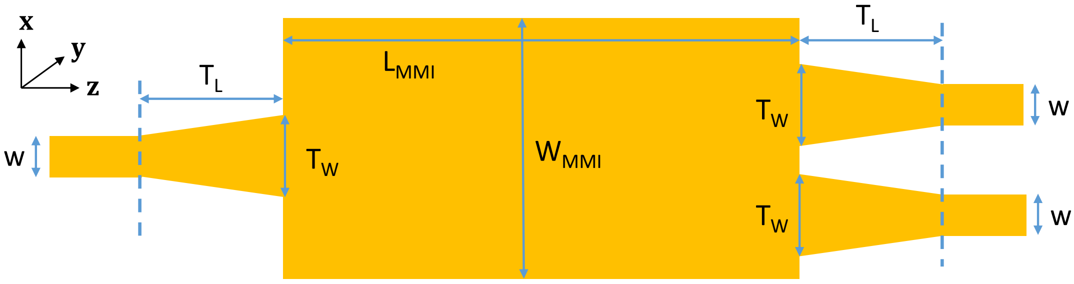

Figure 3.63: Illustration of a 1x2 MMI with tapered input and output waveguides.

In this section, a linear taper length, T_L, of 50µm is considered where the taper length is long enough to be adiabatic and the insertion loss caused by the taper is assumed negligible.

3.4.4.2. Simulation evaluation of tapered MMIs with FIMMWAVE

In this section 1xN MMIs were simulated for input and output waveguide widths of 2µm without the taper structure to save computational time. Table 3.11 shows the L_{MMI}, Insertion loss and non-uniformity of MMI splitters with input and output waveguide width of 2µm.

Table 3.11: Insertion loss and non-uniformity for MMI splitters with input/output waveguide width of 2µm.

N	WMMI (µm)	LMMI (µm)	Insertion Loss (dB)	Non-uniformity (dB)
2	10	69.7	0.076	0
4	20	136.5	0.19	0.06
8	40	270	0.44	0.44
12	60	405.6	0.57	0.12

From Table 3.11 the L_{MMI}, insertion loss and non-uniformity increases as expected as the number of outputs, N increases. However, the insertion loss and non-uniformity has significantly reduced compared to Table 3.10 where MMIs were designed to have input/output waveguide of width 0.5µm.

3.4.5 Y-junction splitters and Directional Couplers (DCs)

Directional couplers (DCs) are constructed from two propagating waveguides set close enough together such that energy passing through one is coupled to the other [3.83]. A DC designed to split power equally between two waveguides is called a hybrid coupler. DCs are power dividers and when used in reverse they can be used as power combiners.

Cascaded Y-splitters and directional couplers (DCs) can be used instead of MMIs to split light, and a DC can be used to replace the Y-splitters used in the MZI studied in section 3.2.1. In this section, optimum Y-splitters and DCs are designed to suit the design parameters of the MZI and MMIs. In section 3.2.1, Y-junctions for MZIs were designed where the output separation, ρ was 5,10, 20 and 25µm.

3.1.4.1 Comparing directional couplers to Y-junction splitters

In this section, optimum DCs were designed and compared with the equivalent Y-junction splitters in terms of insertion loss and length.

Few detailed studies of DC designed with SOI waveguides have been reported in the literature [3.84, 85]. Figure 3.64 shows a DC designed for an SOI waveguide of cross-section 0.3µm × 0.3µm and an edge to edge coupling distance, *d*, between the coupling (waveguide connected to light source) and isolated waveguides (waveguide not connected to light source) of 0.3µm and 0.2µm.

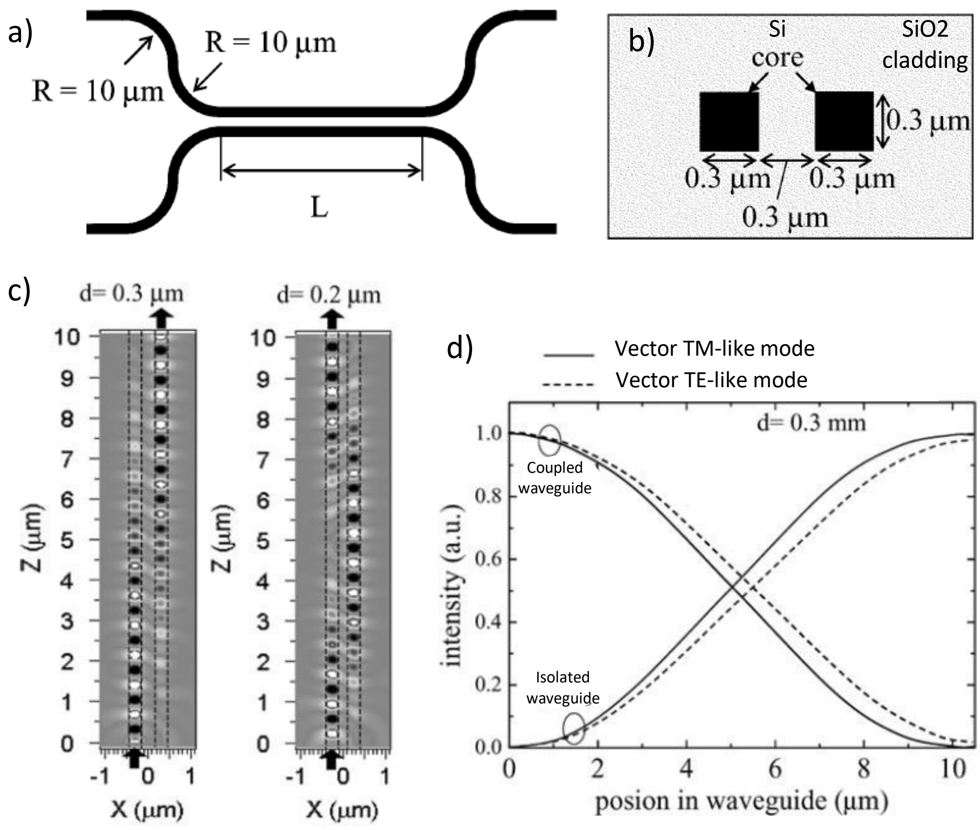

Figure 3.64: a) Top view of a directional coupler b) Cross-sectional views of the silicon wire waveguides, c) Vector TM-like mode profiles of directional coupler for d=0.3µm and d=0.2µm and d) Optical intensity profile for vector TM-like and TE-like modes [3.84].

From Figure 3.64 the coupling length for the vector TM-like mode is about 10µm and 4.9µm for *d*=0.3µm and *d*=0.2µm respectively at an operational wavelength of 1.55µm [3.84].

DCs are sensitive to wavelength and polarization as the coupling length, L_c for complete power transfer is expressed by equation 3.19 [3.85].

$$L_c = \frac{\pi}{(n_e - n_o)k_o} \tag{3.19}$$

where n_e and n_o are the effective refractive indices of the even and odd supermodes supported by the structure and k_o is the free space wavevector. $L_c/2$ is the length required for a 3dB power splitting as needed for this project.

To suit the design parameters of the biosensor an SOI DC for vector TM-like mode was designed using FIMMWAVE. The SOI waveguide cross-section was kept at 0.5µm × 0.22µm. Figure 3.65 shows the vector TM-like mode profile and Figure 3.66 shows the optical intensity for a DC of length 1000µm and d=0.2µm at an operating wavelength of 1.55µm.

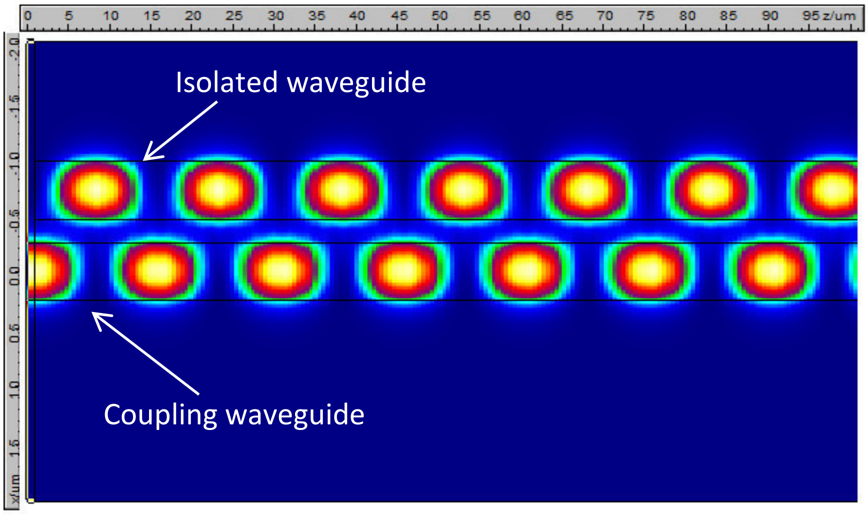

Figure 3.65: FIMMPROP simulation of the vector TM-mode profile of a DC of length 1000µm and d=0.2µm at an operating wavelength of 1.55µm.

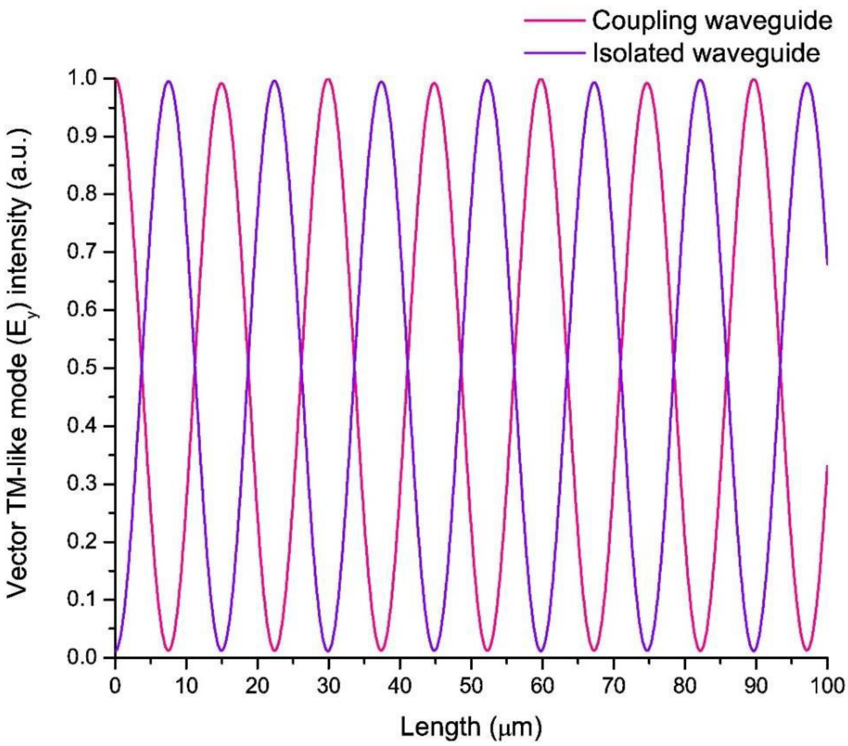

Figure 3.66: Optical intensity of principal E_y field for vector TM-like mode directional coupler of length 1000µm and gap of 0.2µm at an operating wavelength of 1.55µm.

From Figure 3.65 and Figure 3.66, the TM-mode is coupled into the isolated waveguide and once the field is in theory completely transferred to the isolated waveguide the field is then transferred back to the coupling waveguide. This continues to happen if the waveguides are close enough to couple light and no loss occurs.

For this project, a hybrid DC coupler is sought which can replace the Y-junction designed in section 3.2.1. First the optimum coupling length for equal mode intensity was found as *d* was varied as shown in Figure 3.67a and the corresponding insertion loss was calculated as shown in Figure 3.67b.

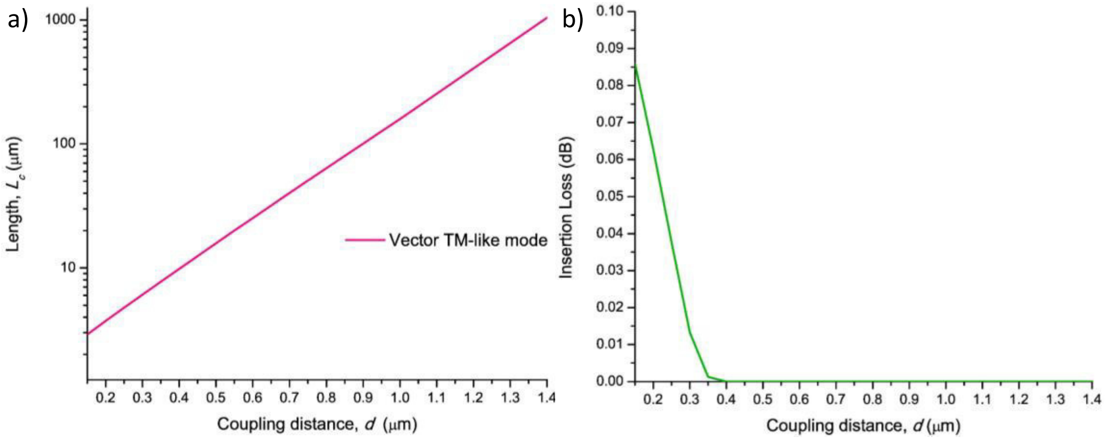

Figure 3.67: Vector TM-like mode (E_y) results for DC a) coupling length as d is varied and b) insertion loss as gap is varied for an operating wavelength of 1.55µm.

From Figure 3.67a the length increases logarithmically as the edge to edge coupling distance, *d*, between the coupling and isolated waveguide is increased. Therefore, to obtain a shorter device a smaller *d* is preferred. From Figure 3.67b the insertion loss reduces to ≈0 dB as d ≥ 0.4µm. Therefore, *d* was fixed to 0.45µm and the coupling length was fixed at 12.46µm for the following simulations.

For the DC to be compared to a Y-junction splitter, S-function waveguides were added to the end of the DC as illustrated in Figure 3.68 in order to physically separate the outputs of the DC.

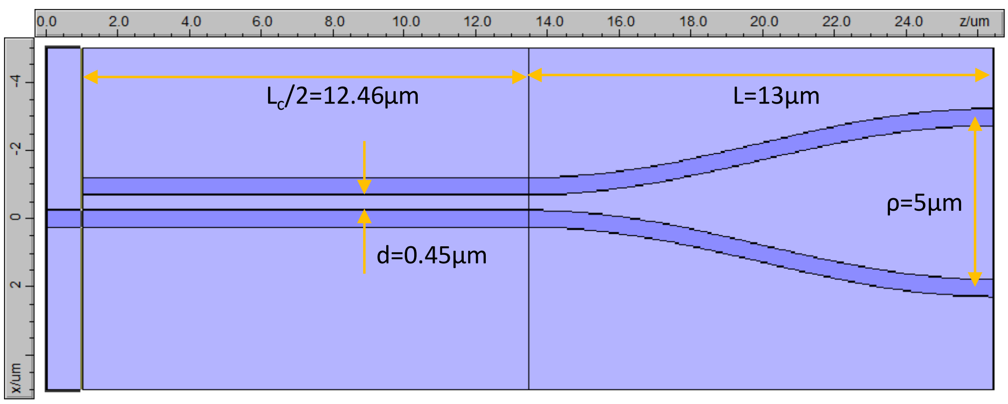

Figure 3.68: FIMMPROP CAD layout of a directional coupler with S-function waveguides.

The distance between the output waveguides, ρ in Figure 3.68 was fixed at 5µm. The length of the S-function was calculated by equation 3.6 to maintain a radius of curvature below 15µm.

Once the S-function waveguides are included, $L_c/2$ reduces as light continues to couple to a short distance through the two S-function waveguides as well. Therefore, $L_c/2$ must be optimised again along with the S-function waveguides present. Figure 3.69 shows a FIMMPROP vector TM-like mode simulation of an optimised DC for ρ=5µm.

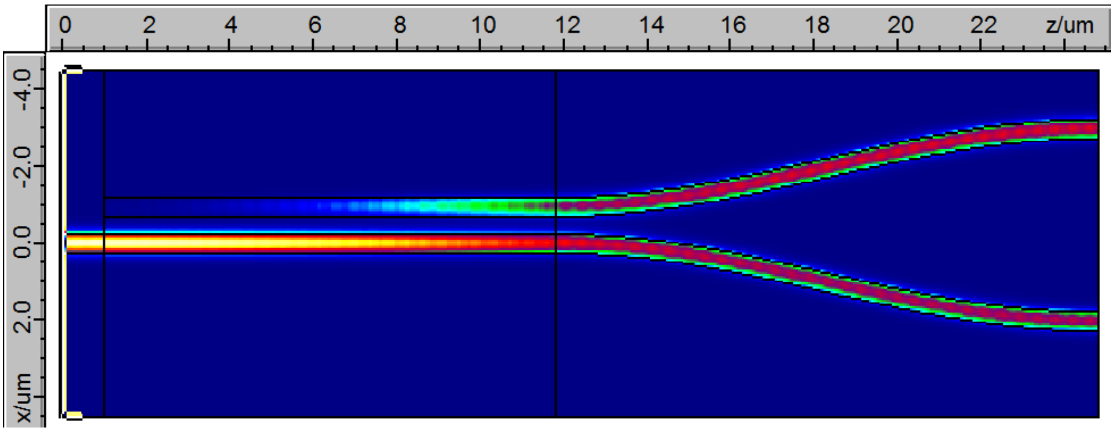

Figure 3.69: DC coupler designed for the vector TM-like mode where d=0.45µm, coupling length=11.4µm, ρ=5µm, length of S-function waveguides=13µm and the operating wavelength=1.55µm.

Figure 3.69 shows a slightly shorter $L_c/2$ of 11.4µm making the total length of the device 24.4µm. Table 3.12 compares the Y-junction splitters and Directional coupler splitters in terms of device length, insertion loss and non-uniformity for ρ=5, 10, 20 and 25µm.

From Table 3.12 it can be seen that Y-junctions have a shorter length but have a significantly higher insertion loss compared to the DC+S-function waveguides. The non-uniformity remains 0dB for both cases. Considering the higher insertion loss and lower fabrication tolerances of Y-junctions (owing to the sharp splitting), DC+S-function waveguides are better for the replacement of MMIs.

Table 3.12: Comparison of Y-junction and DC splitters in terms of length, insertion loss and non-uniformity designed for the vector TM-like mode for an operating wavelength of 1.55µm.

ρ (µm)	Length (µm)		Insertion Loss (dB)		Non-uniformity (dB)	
	Y-Junction	DC+S-function waveguides	Y-Junction	DC+S-function waveguides	Y-Junction	DC+S-function waveguides
5	14	24.40	0.26	0.04	0.00	0.00
10	20	29.99	0.31	0.11	0.00	0.00
20	28	37.67	0.44	0.30	0.00	0.00

3.1.4.2 Comparing MMI to cascaded Y-junction splitters

In section 3.4.4 MMIs were designed to split light between up to 20 paths to enable parallel sensing which is achieved by connecting a MZI to each output of the MMI. To compare Y-junction splitters to MMIs, they must be cascaded as shown in Figure 3.70.

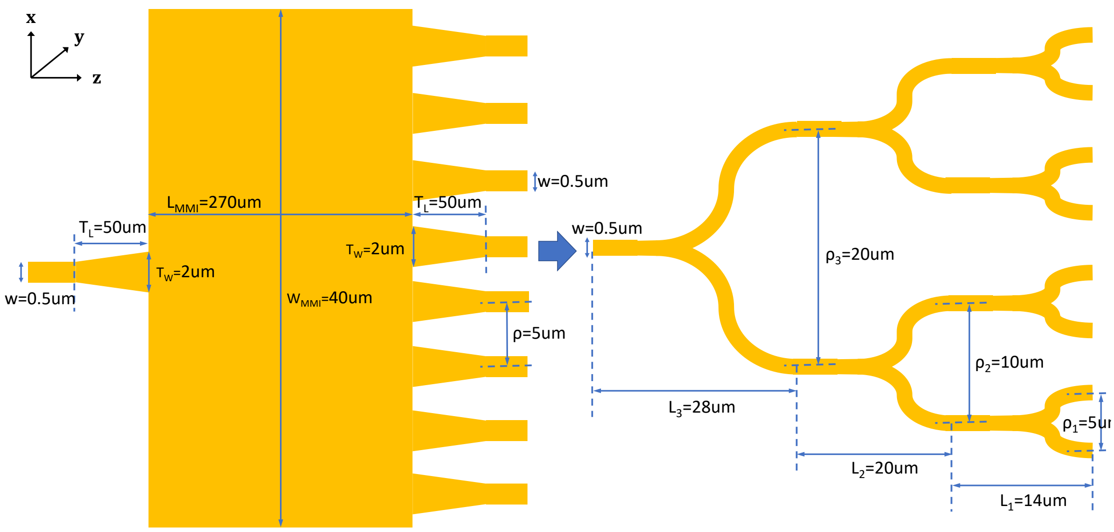

Figure 3.70: Schematic illustration of a 1x8 MMI coupler and a corresponding 1x8 splitter formed from 3 layers of cascaded Y-junction splitters.

Figure 3.70 illustrates a tapered 1x8 MMI splitter and three layers of cascaded Y-junction splitters which can split light into 8 outputs. The output waveguides of the MMI and the cascaded Y-junction splitter are 5µm apart. Therefore, the ρ was fixed at

5, 10 and 20µm for the Y-junctions which requires lengths of 20, 30 and 40µm to maintain a radius of curvature below 15µm.

Table 3.13 compares the tapered MMI to the cascaded Y-junction splitters in terms of length and insertion loss.

Table 3.13: Comparison of tapered 1xN MMI coupler and a corresponding 1xN splitter formed from 3 layers of cascaded Y-junction splitters in terms of length and insertion loss designed for the vector TM-like mode for an operating wavelength of 1.55µm.

N	Width (µm)	MMI + Tapers		Cascaded Y-Junctions		
		Total length (µm)	Total insertion loss (dB)	Total length (µm)	ρ (µm)	Total insertion loss (dB)
2	10	169.7	0.08	14	5	0.26
4	20	236.5	0.19	34	5, 10	0.57
8	40	370.0	0.44	62	5, 10, 20	1.01

From Figure 3.70 and Table 3.13, the total length of the MMI + tapers are multiple times larger than the corresponding cascaded Y-junctions. However, the insertion loss is much smaller for the MMI + tapers compared to the cascaded Y-junctions.

In section 3.1.9, S-function waveguides were designed to connect the outputs of the MMIs to the MZI which must be 127µm apart. The tapered MMI and the S-function waveguides can be compared to a larger cascaded Y-junction splitter as illustrated in Figure 3.71.

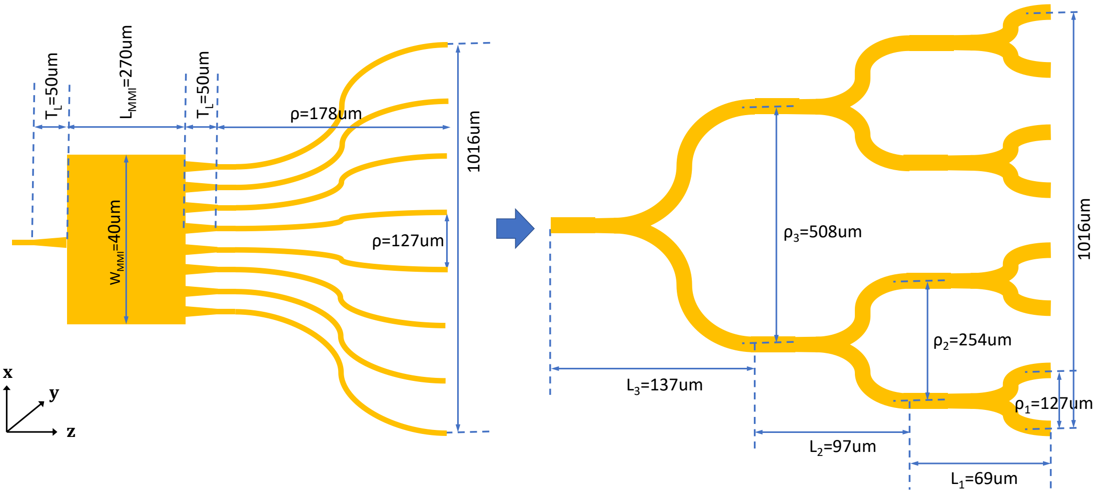

Figure 3.71: Schematic illustration of a 1x8 MMI splitter with S-function waveguides and a corresponding 1x8 splitter formed from 3 layers of cascaded Y-junction splitters.

To make the outputs of the cascaded Y-junction splitter 127µm apart, ρ was fixed to 127, 254 and 508µm which requires lengths of 100, 140 and 200µm respectively to maintain a radius of curvature less than 15µm. Table 3.14 compares tapered 1xN MMI + S-bends to the equivalent cascaded 1xN Y-junction splitter.

Table 3.14: Comparison of tapered 1xN MMI coupler and S-function waveguides and a corresponding 1xN splitter formed from 3 layers of cascaded Y-junction splitters in terms of length designed for the vector TM-like mode for an operating wavelength of 1.55µm.

N	Width (µm)	MMI + Tapers + S bends	Cascaded Y-Junctions	
		Total length (µm)	Total length (µm)	ρ (µm)
2	254	236.9	69	127
4	508	352.9	166	127, 254
8	1016	548.0	303	127, 254, 508

From Figure 3.71 and Table 3.14, the length of MMI + tapers + S bends are significantly larger than the lengths of the corresponding cascaded Y-junction splitters.

In this sub-section, simulations show that incorporating MMIs will increase the device footprint many times compared to Y-junction splitters and DCs. MMIs have a lower insertion loss compared to Y-junctions splitters but DCs have the lowest insertion loss and the smallest length. Y-junction splitters are prone to fabrication imperfection due to its sharp splitting of waveguides whereas MMIs and DCs do not have sharp edges. Therefore, DCs prove to be a better candidate for the splitting of light to 1 × N outputs as it has the advantage over length, insertion loss and fabrication tolerance.

3.4.4 Adaptable MMI designs for the future

In addition to tapered input/output waveguide several techniques have been proposed to improve the performance of MMI devices in terms of coupling and insertion losses, smaller cavity lengths and device sizes, tolerance to operating wavelengths, polarisation and fabrication imperfections. Some of the techniques used are discussed in this section.

A. Maese-Novo *et al*. proposed a sub wavelength grating (SWG) structure to increase the bandwidth by almost fivefold [3.69]. SWGs are periodic or aperiodic structures in which diffraction effects are supressed by using a grating pitch substantially smaller than the wavelength. A 2x2 MMI was presented with a bandwidth of 450nm as shown in Figure 3.72. The SWG calculations were carried out using Floquent-Bloch modes of the periodic structure [3.86] and designed using an in-house 2D simulation tool.

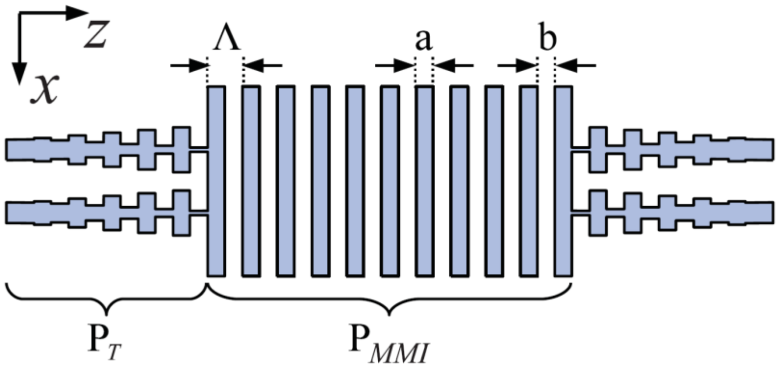

Figure 3.72: Schematic of a 2x2 MMI coupler with sub wavelength grating (SWG) structures [3.69].

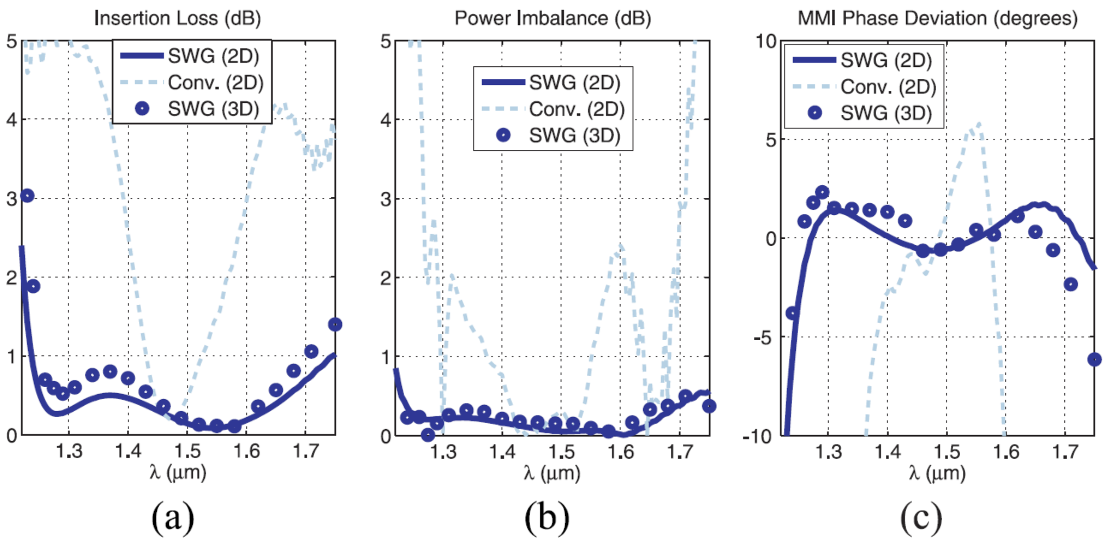

Figure 3.73: a) Insertion loss, b) power imbalance (non-uniformity) and c) Phase deviation as a function of wavelength for SWG MMI and conventional MMI for vector TE-like mode [3.69].

It was shown that the MMI bandwidth is solely limited by the wavelength dependence of the beat length, L_π ($L_\pi=4NL_{MMI}/3$) but could be made substantially independent by SWG dispersion on the MMI device for a wavelength range of 1260nm-1675nm as shown in Figure 3.73. The device had calculated insertion loss, power imbalance and MMI phase deviations of less than 1dB, 0.6dB and 3° respectively and the length of the device was reduced to half that of a conventional design. The main restriction for using this novel structure in the present work is the need for the fabrication of the SWG.

Similarly the MMI coupler shape can be rectangular or may vary linearly [3.87], exponentially [3.88], parabolically [3.89] or maybe tapered to have a butterfly like structure [3.90] as shown in Figure 3.74 and Figure 3.75 in order, to reduce its length and improve performance.

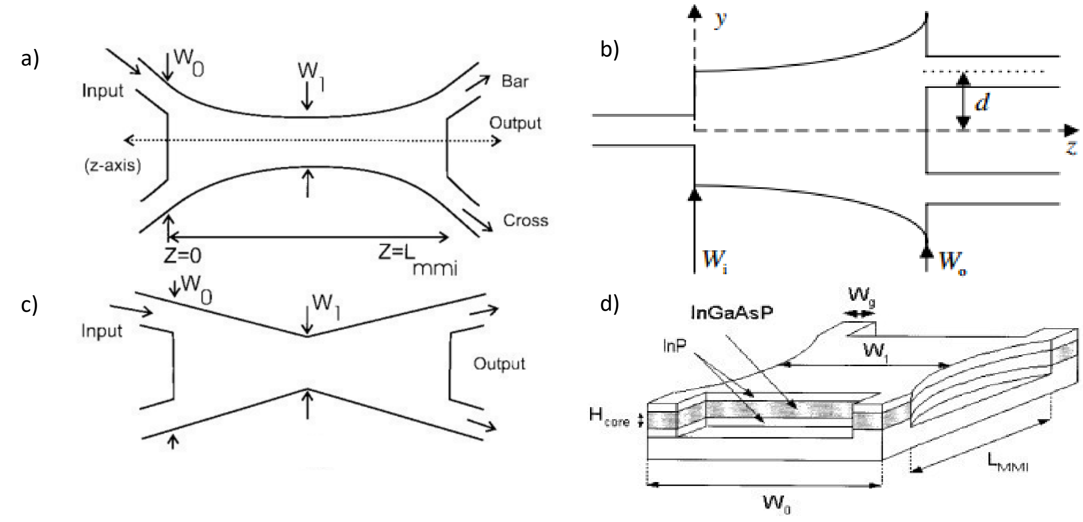

Figure 3.74: a) Parabolically tapered 2x2 MMI structure [3.87], b) exponentially tapered 1x2 MMI structure [3.88], c) linearly tapered 2x2 MMI structure [3.87] and d) parabolically tapered 2x2 MMI structure [3.89].

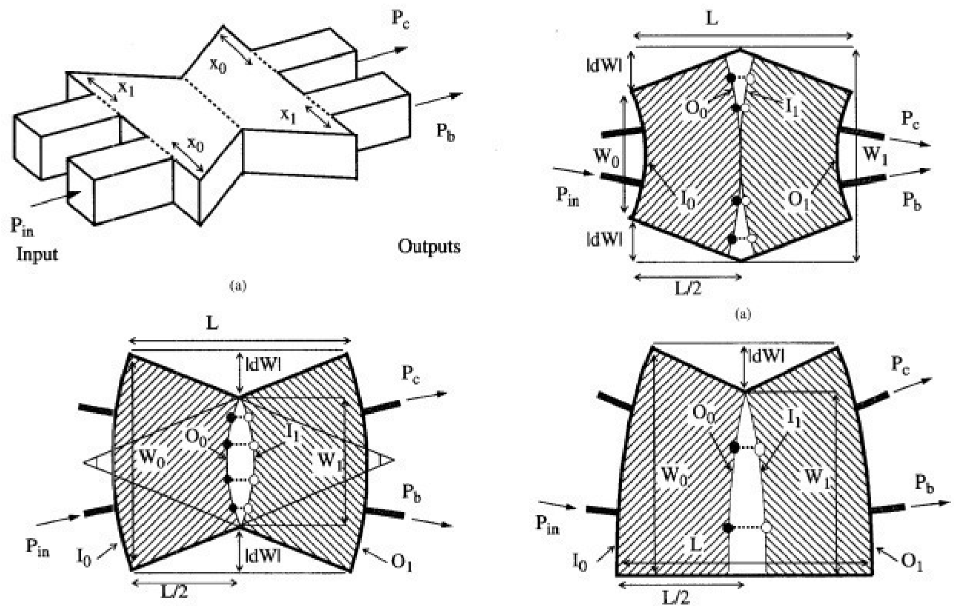

Figure 3.75: 'Butterfly' MMI couplers [3.90].

These concepts also provide opportunity for further design outside this project.

3.5 COUPLING LIGHT IN AND OUT OF WAVEGUIDES.

As introduced previously in section 2.9 light is usually coupled in and out of the waveguide by butt coupling or grating coupling. In this section parameters of tapered couplers for butt coupling are optimised to increase transmission and grating couplers are described. In both cases a tapered fibre with a spot size of 2±0.5um was used to focus the light into the waveguide or grating.

3.5.1 Butt coupling and end fire coupling

In this section, a spot size converter is designed to propagate a 2±0.5um diameter light beam at a wavelength of 1.55µm into a 0.5 × 0.22µm cross-section SOI waveguide with the help of an SU-8 taper as shown in Figure 3.76. The 2µm thick SU-8 taper sits on an inverted silicon waveguide taper.

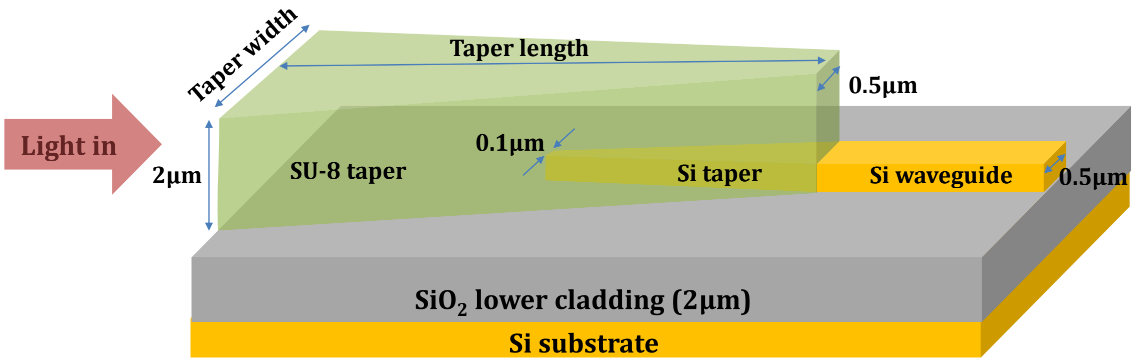

Figure 3.76: Spot size converter with a tapered SU-8 layer on top of an inverted tapered silicon waveguide.

Pu *et al*. [3.91] show that a smaller silicon taper tip width reduces loss; however, it is difficult to fabricate extremely narrow waveguides by etching. Therefore, the silicon taper tip was fixed to 100nm in this project.

The length of the SU-8 taper is twice the length of the inverted silicon taper for simulation convenience at this point. The width and length of the SU-8 taper were varied as shown in Figure 3.77 and Figure 3.78 to obtain maximum transmission. Calculations were performed using FIMMPROP for the vector TM-like mode at an operating wavelength of 1.55µm.

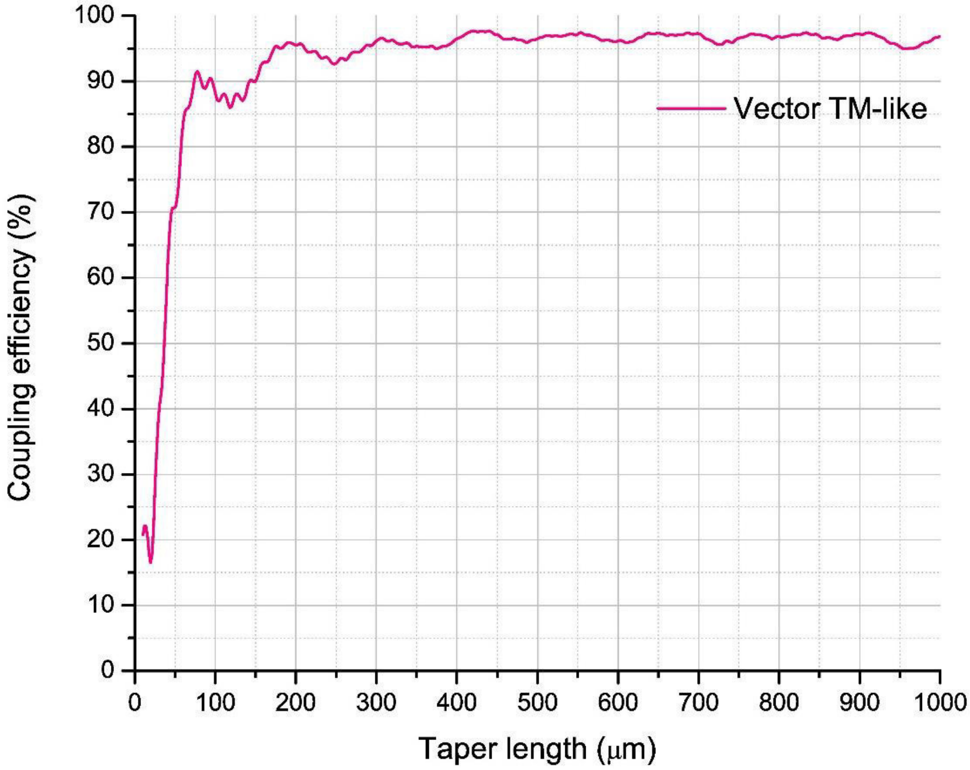

Figure 3.77: Spot size converter transmission a function of SU-8 taper length when taper width=10μm for the vector TM-like mode at an operating wavelength of 1.55μm.

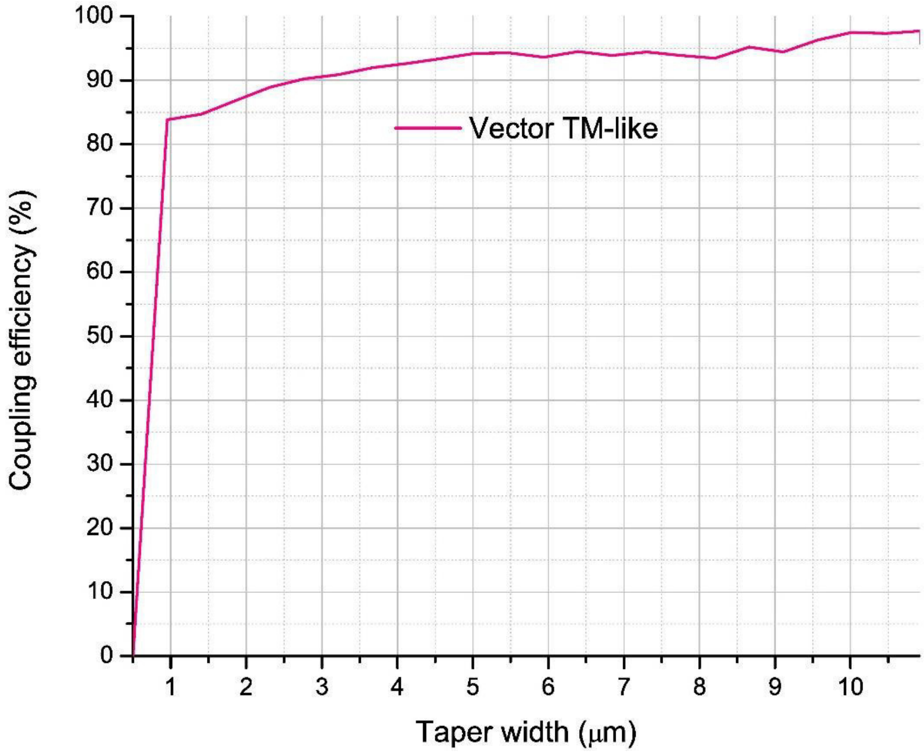

Figure 3.78: Spot size converter transmission a function of initial SU-8 taper width when taper length=600μm for the vector TM-like mode at an operating wavelength of 1.55μm.

From Figure 3.77 and Figure 3.78, to obtain a 97.7% transmission the taper length must be at least 400nm and width of 10µm. In this project, the taper length was set to 600µm to allow tolerance when cleaving as explained in section 4.6. The taper width was set to 10µm. In Figure 3.79 the TM-like mode optical field is visualised at beginning and end of the SU-8 taper simulated using FIMMWAVE.

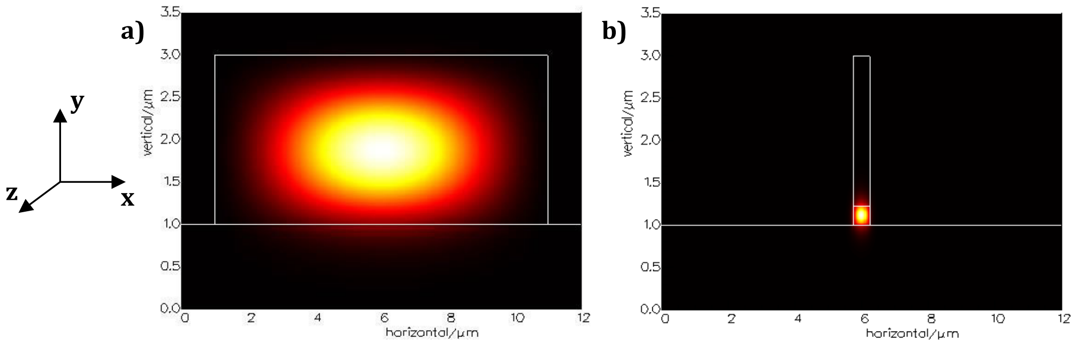

Figure 3.79: The vector TM-like mode (E_y) distribution for spot size converter at a) the beginning and b) the end.

In the literature spot size converters have been designed with a rectangular shaped polymer on top of an inverted tapered silicon waveguide. In the literature, the polymer structure is not tapered. The dimensions, insertion loss and experimental coupling efficiency are summarised in Table 3.15 along with the results obtained above for comparison.

Table 3.15: Experimental results for spot size converters from literature and theoretical results from this project

Paper	Silicon taper			Mode	Upper cladding		Insertion Loss (dB)	Coupling efficiency
	Height × width (nm)	Silicon tip (nm)	Length (µm)		material	Height × width (µm)		
[3.92]	220 × 450	75	150	TE	polymer	2 × 2	1	-
[3.93]	350 × 300	50	60	TE	SiO2	1.5 × 5	-	66%
[3.91]	250 × 480	40	300	TE	SiO_2+ Polymer	3.4 ×3.4	0.66	-
				TM			0.36	-
[3.94]	340 × -	40	200	TE	SU-8	3 × 5	-	60%
				TM			-	60%
This work	220 × 500	100	600	TM	SU-8	2 × tapered from 10 to 0.5	0.10	97.7%

From the literature, the lowest insertion loss for the TM-like mode was measured to be 0.36 dB [3.91]. By tapering the SU-8 polymer, the insertion loss can be reduced to 0.1dB and the coupling efficiency can be increased to 97.7%. The fabrication of the SU-8 taper is described in section 4.5 and experimental results are given in Chapter 5.

3.5.2 Grating coupling

A brief introduction to grating coupling was given in section 2.9.2. In this section, a few grating couplers from the literature are reviewed.

One-dimensional (1D) grating couplers are polarisation sensitive and operate in the vector TE-like mode [3.95, 96]. To operate in the vector TM-like mode, two-dimensional (2D) gratings are used [3.95, 97]. Once the grating patterns are optimised the coupling efficiency can be considerably improved further by focusing the gratings, apodization, or focused apodization.

Frederik Van Laere *et al*. [3.98] designed and fabricated a focused grating coupler as illustrated in Figure 3.80a for the vector TE-like mode with a theoretical efficiency of 37% for an operating wavelength of 1.55µm. Zhejiang University [3.99] designed a grating coupler with a similar pattern as shown in Figure 3.80b with a coupling loss of 3dB and 4dB for the vector TE-like mode and TM-like modes respectively for an operating wavelength of 1.55µm which will be used for this project. A grating coupler was not designed due to software and time constraints; instead a grating coupler designed by Zhejiang University was used for this project.

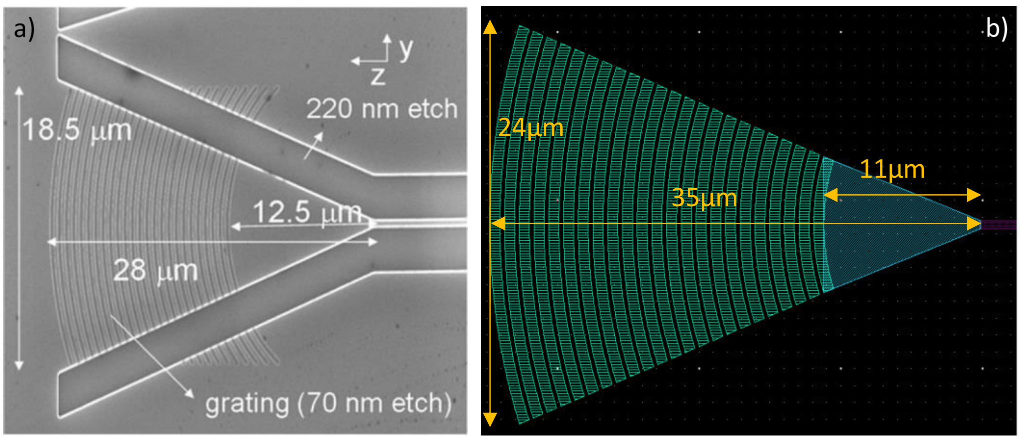

Figure 3.80: Focused grating coupler for a) vector TE-like mode [3.98] and b) vector TE-like and TM-like modes for an operating wavelength of 1.55µm.

Robert Halir *et al*. [3.100] designed an apodized grating coupler as shown in Figure 3.81a and Zhenzhou Chen *et al*. [3.101] designed a focused apodized grating coupler as shown in Figure 3.81b. Both grating couplers were designed for the vector TM-like mode with a couplinloss of 3.7dB and 3dB respectively.

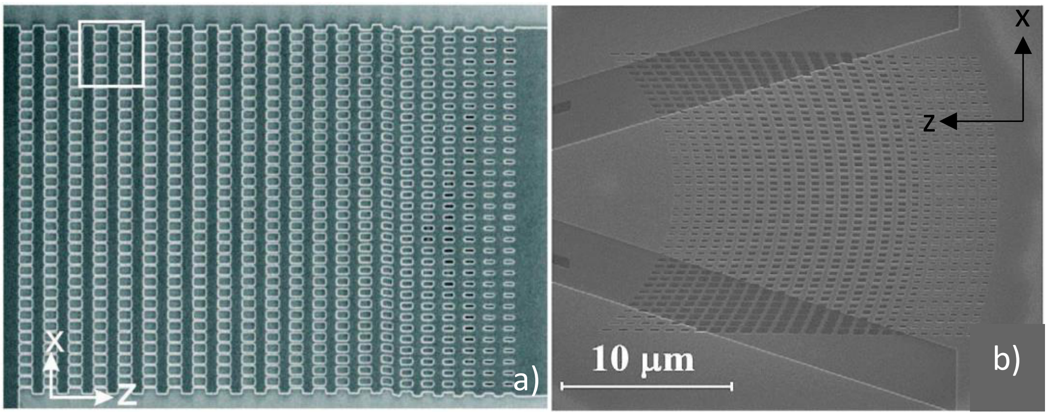

Figure 3.81: a) Apodized grating coupler [3.100] and b) focused apodised grating coupler [3.101] for the vector TM-like mode at an operating wavelength of 1.55μm.

Grating couplers are inefficient compared to spot size converters due to mode mismatch and they require an additional etch step; but they allow for compact and high-density integration of photonic devices which is important for the commercialisation of the sensor.

In this project, both the spot size coupler shown in Figure 3.76 and the focused grating coupler shown in Figure 3.80b were considered and optically tested as shown in chapter 6.

3.6 CHAPTER SUMMARY

This chapter introduced Beam propagation method (BPM) and Eigenmode expansion (EME) method for simulating propagation in optical waveguides. Both methods can be used to simulate the structures in the proposed multi-channel biosensing device but as the high index contrast waveguides became narrower, EME proved to give more stable results.

Various commonly used components for optical biosensors mentioned in the literature and illustrated in Figure 3.82 were reviewed in this chapter.

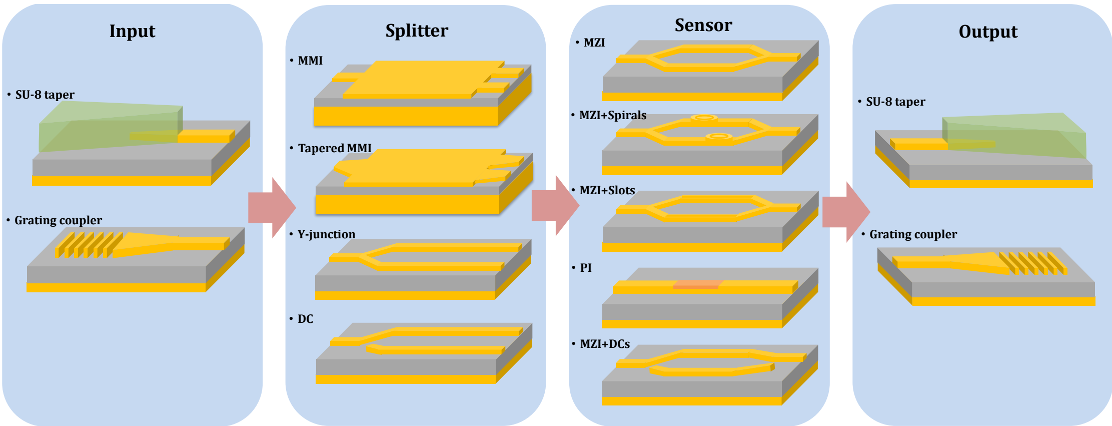

Figure 3.82: Possible structures considered for the construction of an evanescent wave optical biosensor.

Each component was simulated and optimised for maximum sensitivity and minimum loss for a vector TM-like mode. However, the structure with the best simulation result is not always the easiest or cheapest to fabricate. Therefore, considering all advantages and disadvantages each component was carefully selected for the final optical biosensor layouts as shown in Table 3.16.

Table 3.16: Summary of components selected for the biosensor at various stages of this project.

Device set number	Waveguide cross- section width × height (μm × μm)	Input/output method	Splitter	Bends	Sensor
1	4 × 0.32	SU-8 taper + inverted Si taper	1xN MMI	S-bends	MZI
2	4 × 0.32	SU-8 taper + inverted Si taper	1xN MMI	S-bends	PI
3	0.8 × 0.25	SU-8 taper + inverted Si taper	1xN MMI	S-bends	MZI
4	0.5 × 0.22	Grating coupler	Cascaded DC	S-bends	MZI + Spiral
5	0.5 × 0.22	Grating coupler	1xN tapered MMI	S-function waveguides	MZI + Spiral

To begin with, the SOI ridge waveguide height and width were optimised for a fundamental vector TM-like mode for maximum sensitivity given by equation 3.1. The optimum height and width obtained were 0.21μm and 0.25μm respectively for a sensitivity of 0.598. However, SOI wafers with core height of 0.22μm can be purchased off the shelf thereby improving the cost and availability of the initial wafer. Furthermore, using standard wafers and dimensions makes fabrication and integration easier and cheaper. A wavelength width of 0.25μm requires more precise lithography at the fabrication stage and is more vulnerable to fabrication imperfections; therefore the width is increased to 0.5μm in the present realisation.

From section 3.1.4 and Figure 3.5, SOI ridge waveguide of core height of 0.22μm and width of 0.5μm at a wavelength of 1.55μm operating with a fundamental vector TM-like mode gives a sensitivity of 0.52 which is only a 13% decrease of sensitivity from the optimum simulation result obtained for a width of 0.25μm.

Similarly, from section 3.1.4 and Figure 3.5, an SOI ridge waveguide of core height and width of 0.22μm and 0.27μm gives a sensitivity of 0.683 for the vector TE-like mode which is a 31% increase in sensitivity compared to the 0.52 sensitivity of the vector

TM-like mode. But fabricating ridge waveguides of width 0.27µm again gives rise to difficulty in fabrication as mentioned earlier and increasing the width to 0.5µm reduces the vector TE-like mode sensitivity drastically to 0.149.

Table 3.17 gives a summary of the various optimum ridge and slot waveguide dimensions discussed in this chapter along with their sensitivity to aid comparison.

Table 3.17: Summary of ridge and SOI waveguide dimensions and sensitivity.

	Core height (µm)	Core width (µm)	Sensitivity	Figure
Vector TM-like mode (wire)	0.21	0.25	0.598	Figure 3.5
Vector TE-like mode (wire)	0.22	0.27	0.683	Figure 3.5
Vector TM-like mode (wire selected)	0.22	0.5	0.520	Figure 3.5
Vector TM-like mode (slot waveguide)	0.22	0.16	0.581	Figure 3.18
Vector TE-like mode (slot waveguide)	0.22	0.23	0.769	Figure 3.18

In addition to ridge waveguides, slot waveguides were studied in this chapter as they are becoming increasingly popular for optical biosensing applications. As shown in section 3.1.6 and summarised in Table 3.17 using slot waveguides increased sensitivity by 48% and 12% for vector TE-like and TM-like mode respectively. However, to obtain such a high sensitivity the distance between the slots, *d*, needs to be 0.1µm, with a core height of 0.22µm and width of 0.23µm and 0.16µm for vector TE-like and TM-like modes respectively.

If slot waveguides were to be incorporated in this project then the MZI designs presented in section 3.2.1 indicate that the waveguides would have to be at least 1 mm in length. Fabricating waveguides with a cross-section of 220 × 230 nm and length of 1mm, and including a 0.1µm slot would be extremely difficult to fabricate. Slot waveguides in ring resonators described in the literature have a footprint of less than a 100µm × 100µm [3.15, 18] and sometimes much smaller [3.14] and so are relatively easier to fabricate.

However, incorporating long and narrow slot waveguides into the device gives rise to more complications than just the complexity of fabrication. Surface functionalisation is an important aspect to consider for slot waveguides and the antibodies would have to be attached to the inner walls of the slot waveguide which is only 220nm in width with the *d* between the slots only 100nm. Slot waveguides are generally used in ring resonators for homogenous sensing [3.13, 14, 18, 102, 103] where the change in analyte concentration causes a change in the effective refractive index and not the binding of the antibody. Very few literature papers demonstrate the surface functionalisation of an SOI slot waveguide [3.104]. Chapter 5 will discuss surface functionalisation and its challenges in more detail, surface functionalisation of such a small slot is of left for future work.

Therefore, considering the addition of a strip to slot converter, polarisation of light, surface functionalisation feasibility and complexity of fabrication, this project will not incorporate slot waveguides into the design of the optical biosensor.

Section 3.1.7 discusses propagation loss caused by substrate leakage and scattering by sidewall roughness. While sidewall roughness depends on fabrication techniques, substrate loss can be reduced using sufficiently large enough SiO_2 insulation layer as the lower cladding. According to the simulations presented in Figure 3.24 a 1um SiO_2 layer would give a loss of 0.01dB/cm for vector TE-like mode and a 2µm SiO_2 layer would give a loss of 0.26dB/cm for vector TM-like mode. Therefore, a 2µm SiO_2 insulation layer is selected for this project.

Curved waveguides are used to make the devices as compact as possible but if the bend radius is too small, light propagating will be subjected to radiation loss. In section 3.1.8 the minimum curvature loss was studied for a fundamental vector TE-like mode; at R=5µm the bending loss at a wavelength of 1.55µm is 0.024dB/cm and 0.142dB/cm for n_c=1 and n_c=1.33 respectively. For the vector TM-like mode the bend loss is 0dB/cm for n_c=1.33 and bend radius greater than 11µm. The curved waveguides in this project will have a cover index of $n_c \geq 1.33$ therefore the minimum bend radius was fixed at 15µm for all components designed with curved waveguides.

S-bends and S-function waveguides were designed in section 3.1.9 to connect the outputs of an MMI to the input of a MZI. The designs were optimised for the shortest length while maintaining the minimum radius of curvature less than 15µm. This was done using equation 3.6 which has not been reported before.

MZIs were first designed in RSoft BeamPROP using multimoded waveguides of cross-section 4µm × 0.32µm which were then found to split the fundamental mode asymmetrically. Therefore, it became critical that the waveguides designed in this project operated in a single mode for each polarisation. MZIs with an arm length of 1000µm were then designed using FIMMPROP, as shown in section 3.2.1. to increase the length of the arms of the MZI, spiral waveguides were designed in section 3.2.2.

Due to the intrinsic problems related to the MZI principle, a more sensitive MZI is not always the best option. The $\Delta\varphi$ caused by the Δn_c must be smaller than π and fall on one side of the fringe as illustrated in figure 3.45. Therefore, several MZIs with varying lengths should be fabricated and tested.

A MZI with arm length of 1000µm corresponds to a sensitivity of 3.1×10^{-7} RIUs and a MZI with a spiral of length 3145µm corresponds to a sensitivity of 9.9×10^{-8} RIUs. Longer spiral lengths would be difficult to fabricate and therefore should be considered when fabrication becomes more achievable.

Plasmonic interferometers were designed to give a sensitivity of 250nm/RIU but due to the high insertion loss it cannot be used for parallel detection which is a requirement of this project. However, a test device was fabricated and tested as described in chapters 4 and 6.

The light is split for parallel detection using MMIs. Initially MMIs were designed for input/output waveguide cross-section of 4µm × 0.32µm due to wafer availability. MMIs with single mode input/output waveguides with a cross-section 0.5µm × 0.22µm of were then designed which much shorter in length by a factor of 12. To reduce the insertion loss of these MMIs, a taper was designed for the inputs and outputs. Table 3.18 is a summary of the insertion loss of an MMI with and without tapered input/output waveguides for increasing number of outputs, *N*. From Table 3.18, it can be seen that the insertion loss is greatly reduced by including a taper to the input/output waveguides of an MMI.

Table 3.18: Summary of insertion loss of non-tapered MMI and tapered MMI for N=2, 4, 8 and 12 at an operating wavelength of 1.55μm.

N	Insertion Loss (dB) for an MMI without taper	Insertion Loss (dB) of an MMI with taper
2	1.35	0.08
4	1.66	0.19
8	2.30	0.44
12	2.91	0.57

Y-junction splitters and DCs were then designed and compared with MMIs as summarised in Table 3.19 for an output separation, ρ of 5μm. From Table 3.19 it can be seen that the Y-junction splitters has a much smaller length whereas DC + S bends have the smallest insertion loss. Y-junction splitters are prone to fabrication imperfections due to sharp splitting of waveguide which would give rise to a high non-uniformity. DCs have the lowest insertion loss and requires a fraction of the length taken by a tapered MMI.

Table 3.19: Comparison of length and insertion loss for tapered MMI, Y-junction splitter and DC + S bend with output separating of 5μm at an operating wavelength of 1.55μm.

Device with two outputs 5μm apart	Length (μm)	Insertion Loss (dB)
1×2 tapered MMI	169.70	0.08
Y-junction splitter	14.00	0.26
DC + S bend	29.99	0.04

Finally, a spot size converter was designed to couple light in and out of the silicon waveguide. A 2μm thick SU-8 was tapered from 10μm to 0.5μm in width which is placed on an inverted silicon taper. The 220nm thick silicon core is tapered from 100nm to 500nm. The SU-8 taper is 600µm long and the inverted silicon taper starts from the mid-point of the SU-8 taper. The simulated insertion loss is 0.1dB and coupling efficiency is 97.7% for this spot size converter.

Grating couplers were reviewed but not designed due to the limitation in software and time but existing grating couplers are considered as they allow for compact devices.

Based on the simulations performed in this chapter, the ideal evanescent biosensor with the lowest insertion loss, non-uniformity and parallel detection but also compromising against the complexity of fabrication and overall device area, is shown in Table 3.16 device set number 5.

Device sets 1-4 listed in Table 3.16, were fabricated as described in Chapter 4 and assessed optically in Chapter 6.

REFERENCES

[3.1] T. M. Benson, E. Bekker, A. Vukovic, and P. Sewell, "Challenges for integrated optics design and simulation," in *Photonics North 2007*, 2007, pp. 67963C-67969.

[3.2] G. R. Hadley, "Wide-angle beam propagation using Padé approximant operators," *Optics Letters,* vol. 17, pp. 1426-1428, 1992.

[3.3] Y. Chung and N. Dagli, "An assessment of finite difference beam propagation method," *IEEE Journal of Quantum Electronics,* vol. 26, pp. 1335-1339, 1990.

[3.4] J. Yamauchi, *Propagating beam analysis of optical waveguides,* Baldock: Research Studies Press, 2003.

[3.5] R. Scarmozzino, A. Gopinath, R. Pregla, and S. Helfert, "Numerical techniques for modeling guided-wave photonic devices," *IEEE Journal of Selected Topics in Quantum Electronics,* vol. 6, pp. 150-162, 2000.

[3.6] P. Lagasse and R. Baets, "Application of propagating beam methods to electromagnetic and acoustic wave propagation problems: A review," *Radio Science,* vol. 22, pp. 1225-1233, 1987.

[3.7] D. F. Gallagher and T. P. Felici, "Eigenmode expansion methods for simulation of optical propagation in photonics: pros and cons," in *Integrated Optoelectronics Devices*, 2003, pp. 69-82.

[3.8] P. Dumon, W. Bogaerts, V. Wiaux, J. Wouters, S. Beckx, J. Van Campenhout, D. Taillaert, B. Luyssaert, P. Bienstman, D. Van Thourhout, and R. Baets, "Low-loss SOI photonic wires and ring resonators fabricated with deep UV lithography," *Photonics Technology Letters, IEEE,* vol. 16, pp. 1328-1330, 2004.

[3.9] A. E.-J. Lim, J. Song, Q. Fang, C. Li, X. Tu, N. Duan, K. K. Chen, R. P.-C. Tern, and T.-Y. Liow, "Review of silicon photonics foundry efforts," *IEEE Journal of Selected Topics in Quantum Electronics,* vol. 20, pp. 405-416, 2014.

[3.10] D. J. Segelstein, "The complex refractive index of water," M. S. Thesis, Department of Physics, University of Missouri--Kansas City, 1981.

[3.11] (Accessed 26 Sep 2016). *FIMMWAVE*. Available: https://www.photond.com/products/fimmwave.htm

[3.12] V. R. Almeida, Q. Xu, C. A. Barrios, and M. Lipson, "Guiding and confining light in void nanostructure," *Optics Letters,* vol. 29, pp. 1209-1211, 2004.

[3.13] Q. Xu, V. R. Almeida, R. R. Panepucci, and M. Lipson, "Experimental demonstration of guiding and confining light in nanometer-size low-refractive-index material," *Optics Letters,* vol. 29, pp. 1626-1628, 2004.

[3.14] T. Claes, J. G. Molera, K. D. Vos, E. Schacht, R. Baets, and P. Bienstman, "Label-Free Biosensing With a Slot-Waveguide-Based Ring Resonator in Silicon on Insulator," *IEEE Photonics Journal,* vol. 1, pp. 197-204, 2009.

[3.15] T. Baehr-Jones, M. Hochberg, C. Walker, and A. Scherer, "High-Q optical resonators in silicon-on-insulator-based slot waveguides," *Applied Physics Letters,* vol. 86, p. 081101, 2005.

[3.16] R. Bernini, N. Cennamo, A. Minardo, and L. Zeni, "Planar Waveguides for Fluorescence-Based Biosensing: Optimization and Analysis," *IEEE Sensors Journal,* vol. 6, pp. 1218-1226, 2006.

[3.17] F. Dell'Olio and V. M. Passaro, "Optical sensing by optimized silicon slot waveguides," *Optics Express,* vol. 15, pp. 4977-4993, 2007.

[3.18] C. A. Barrios, "Optical slot-waveguide based biochemical sensors," *Sensors,* vol. 9, pp. 4751-4765, 2009.

[3.19] (Accessed 30 Sep 2016). *COMSOL*. Available: http://cn.comsol.com/

[3.20] V. M. N. Passaro and M. La Notte, "Optimizing SOI Slot Waveguide Fabrication Tolerances and Strip-Slot Coupling for Very Efficient Optical Sensing," *Sensors (Basel, Switzerland),* vol. 12, pp. 2436-2455, 2012.

[3.21] Z. Wang, N. Zhu, Y. Tang, L. Wosinski, D. Dai, and S. He, "Ultracompact low-loss coupler between strip and slot waveguides," *Optics Letters,* vol. 34, pp. 1498-1500, 2009.

[3.22] R. Palmer, L. Alloatti, D. Korn, W. Heni, P. C. Schindler, J. Bolten, M. Karl, M. Waldow, T. Wahlbrink, W. Freude, C. Koos, and J. Leuthold, "Low-Loss Silicon Strip-to-Slot Mode Converters," *IEEE Photonics Journal,* vol. 5, p. 2200409, 2013.

[3.23] Q. Deng, Q. Yan, L. Liu, X. Li, and Z. Zhou, "Highly compact polarization insensitive strip-slot waveguide mode converter," in *2015 Conference on Lasers and Electro-Optics (CLEO)*, 2015, pp. 1-2.

[3.24] P. Dumon, W. Bogaerts, V. Wiaux, J. Wouters, S. Beckx, J. Van Campenhout, D. Taillaert, B. Luyssaert, P. Bienstman, and D. Van Thourhout, "Low-loss SOI photonic wires and ring resonators fabricated with deep UV lithography," *IEEE Photonics Technology Letters,* vol. 16, pp. 1328-1330, 2004.

[3.25] P. Bienstman and R. Baets, "Optical modelling of photonic crystals and VCSELs using eigenmode expansion and perfectly matched layers," *Optical and Quantum Electronics,* vol. 33, pp. 327-341, 2001.

[3.26] Y. Vlasov and S. McNab, "Losses in single-mode silicon-on-insulator strip waveguides and bends," *Optics Express,* vol. 12, pp. 1622-1631, 2004.

[3.27] K. K. Lee, D. R. Lim, H.-C. Luan, A. Agarwal, J. Foresi, and L. C. Kimerling, "Effect of size and roughness on light transmission in a Si/SiO2 waveguide: Experiments and model," *Applied Physics Letters,* vol. 77, pp. 1617-1619, 2000.

[3.28] T. Tsuchizawa, K. Yamada, H. Fukuda, T. Watanabe, J.-i. Takahashi, M. Takahashi, T. Shoji, E. Tamechika, S.-i. Itabashi, and H. Morita, "Microphotonics devices based on silicon microfabrication technology," *IEEE Journal of Selected Topics in Quantum Electronics,* vol. 11, pp. 232-240, 2005.

[3.29] Z. Sheng, D. Dai, and S. He, "Comparative study of losses in ultrasharp silicon-on-insulator nanowire bends," *IEEE Journal of Selected Topics in Quantum Electronics,* vol. 15, pp. 1406-1412, 2009.

[3.30] P. Design, "FIMMPROP Version 5.4.1 Manual," 1997-2012.

[3.31] (Accessed 30 May 2017). *Curvature and Radius of Curvature* Available: https://www.math24.net/curvature-radius/

[3.32] B. Sepulveda, J. S. Del Rio, M. Moreno, F. Blanco, K. Mayora, C. Domínguez, and L. M. Lechuga, "Optical biosensor microsystems based on the integration of highly sensitive Mach–Zehnder interferometer devices," *Journal of optics A: Pure and Applied Optics,* vol. 8, p. S561, 2006.

[3.33] A. Ymeti, J. S. Kanger, R. Wijn, P. V. Lambeck, and J. Greve, "Development of a multichannel integrated interferometer immunosensor," *Sensors and Actuators B: Chemical,* vol. 83, pp. 1-7, 2002.

[3.34] A. Ymeti, J. S. Kanger, J. Greve, G. A. J. Besselink, P. V. Lambeck, R. Wijn, and R. G. Heideman, "Integration of microfluidics with a four-channel integrated optical Young interferometer immunosensor," *Biosensors and Bioelectronics,* vol. 20, pp. 1417-1421, 2005.

[3.35] D. X. Xu, A. Densmore, A. Delâge, P. Waldron, R. McKinnon, S. Janz, J. Lapointe, G. Lopinski, T. Mischki, E. Post, P. Cheben, and J. H. Schmid, "Folded cavity SOI microring sensors for highsensitivity and real time measurement of biomolecular binding," *Opt. Express,* vol. 16, pp. 15137-15148, 2008.

[3.36] J. Vörös, J. J. Ramsden, G. Csúcs, I. Szendrő, S. M. De Paul, M. Textor, and N. D. Spencer, "Optical grating coupler biosensors," *Biomaterials,* vol. 23, pp. 3699-3710, 2002.

[3.37] N. Skivesen, A. Têtu, M. Kristensen, J. Kjems, L. H. Frandsen, and P. I. Borel, "Photonic-crystal waveguide biosensor," *Opt. Express,* vol. 15, pp. 3169-3176, 2007.

[3.38] R. G. Heideman and P. V. Lambeck, "Remote opto-chemical sensing with extreme sensitivity: design, fabrication and performance of a pigtailed integrated optical phase-modulated Mach–Zehnder interferometer system," *Sensors and Actuators B: Chemical,* vol. 61, pp. 100-127, 1999.

[3.39] (Accessed 05 Oct 2016). *RSoft BeamPROP*. Available: https://optics.synopsys.com/rsoft/

[3.40] A. V. Velasco, P. Cheben, P. J. Bock, A. Delâge, J. H. Schmid, J. Lapointe, S. Janz, M. L. Calvo, D.-X. Xu, and M. Florjańczyk, "High-resolution Fourier-transform spectrometer chip with microphotonic silicon spiral waveguides," *Optics Letters,* vol. 38, pp. 706-708, 2013.

[3.41] B. Redding, S. F. Liew, Y. Bromberg, R. Sarma, and H. Cao, "Evanescently coupled multimode spiral spectrometer," *Optica,* vol. 3, pp. 956-962, 2016.

[3.42] D.-X. Xu, A. Delâge, R. McKinnon, M. Vachon, R. Ma, J. Lapointe, A. Densmore, P. Cheben, S. Janz, and J. H. Schmid, "Archimedean spiral cavity ring resonators in silicon as ultra-compact optical comb filters," *Optics Express,* vol. 18, pp. 1937-1945, 2010.

[3.43] N. Maleeva, M. Fistul, A. Karpov, A. Zhuravel, A. Averkin, P. Jung, and A. Ustinov, "Electrodynamics of a ring-shaped spiral resonator," *Journal of Applied Physics,* vol. 115, p. 064910, 2014.

[3.44] K. A. Bachman, J. J. Peltzer, P. D. Flammer, T. E. Furtak, R. T. Collins, and R. E. Hollingsworth, "Spiral plasmonic nanoantennas as circular polarization transmission filters," *Optics Express,* vol. 20, pp. 1308-1319, 2012.

[3.45] M. Peccianti, M. Ferrera, L. Razzari, R. Morandotti, B. E. Little, S. T. Chu, and D. J. Moss, "Subpicosecond optical pulse compression via an integrated nonlinear chirper," *Optics Express,* vol. 18, pp. 7625-7633, 2010.

[3.46] A. D. Simard, Y. Painchaud, and S. LaRochelle, "Integrated Bragg gratings in spiral waveguides," *Optics Express,* vol. 21, pp. 8953-8963, 2013.

[3.47] (Accessed 31 Feb 2017). *Arc Length of a Curve*. Available: www.mathwords.com/a/arc_length_of_a_curve.htm

[3.48] W. Tzyy-Jiann, T. Cheng-Wei, L. Fu-Kun, and C. Hsuen-Li, "Surface plasmon resonance waveguide biosensor by bipolarization wavelength interrogation," *Photonics Technology Letters, IEEE,* vol. 16, pp. 1715-1717, 2004.

[3.49] K. De Vos, P. De Backere, R. Baets, and P. Bienstman, "Label-free biosensors on silicon-on-insulator optical chips based on microring cavities and surface plasmon interferometry," in *Transparent Optical Networks, 2008. ICTON 2008. 10th Anniversary International Conference on*, 2008, pp. 88-91.

[3.50] R. Kashyap and G. Nemova, "Surface plasmon resonance-based fiber and planar waveguide sensors," *Journal of Sensors,* vol. 2009, 2009.

[3.51] J. ČtyrokÝ, F. Abdelmalek, W. Ecke, and K. Usbeck, "Modelling of the surface plasmon resonance waveguide sensor with Bragg grating," *Optical and Quantum Electronics,* vol. 31, pp. 927-941, 1999.

[3.52] P. Debackere, S. Scheerlinck, P. Bienstman, and R. Baets, "Surface plasmon interferometer in silicon-on-insulator: novel concept for an integrated biosensor," *Optics Express,* vol. 14, pp. 7063-7072, 2006.

[3.53] (Accessed 26 Oct 2016). *CAMFR*. Available: http://camfr.sourceforge.net/

[3.54] P. B. Johnson and R.-W. Christy, "Optical constants of the noble metals," *Physical Review B,* vol. 6, p. 4370, 1972.

[3.55] P. Johnson and R. Christy, "Optical constants of transition metals: Ti, v, cr, mn, fe, co, ni, and pd," *Physical Review B,* vol. 9, p. 5056, 1974.

[3.56] O. Bryngdahl, "Image formation using self-imaging techniques," *J. Opt. Soc. Am.,* vol. 63, pp. 416-419, 1973.

[3.57] R. Ulrich, "Light-propagation and imaging in planar optical waveguides," *Nouvelle Revue d'Optique,* vol. 6, p. 253, 1975.

[3.58] R. Ulrich, "Image formation by phase coincidences in optical waveguides," *Optics Communications,* vol. 13, pp. 259-264, 1975.

[3.59] J. Heaton, R. Jenkins, D. Wight, J. Parker, J. Birbeck, and K. Hilton, "Novel 1 - to - N way integrated optical beam splitters using symmetric mode mixing in GaAs/AlGaAs multimode waveguides," *Applied Physics Letters,* vol. 61, pp. 1754-1756, 1992.

[3.60] L. B. Soldano and E. C. M. Pennings, "Optical multi-mode interference devices based on self-imaging: principles and applications," *Lightwave Technology, Journal of,* vol. 13, pp. 615-627, 1995.

[3.61] D. S. Levy, P. Kyung Hyun, R. Scarmozzino, R. M. Osgood, C. Dries, P. Studenkov, and S. Forrest, "Fabrication of ultracompact 3-dB 2 x 2 MMI power splitters," *Photonics Technology Letters, IEEE,* vol. 11, pp. 1009-1011, 1999.

[3.62] L. Zhuang, P. Wang, Z. Cao, G. Cao, Z. Wang, and F. Qiu, "A novel MMI–MZ all-optical switch," *Optik - International Journal for Light and Electron Optics*.

[3.63] P. Yue, B. M. Mao, X. Yi, Q. N. Li, and Z. J. Liu, "A MMI-based ultra-linear high-gain modulator and its performance analysis," *Optics & Laser Technology,* vol. 53, pp. 33-39, 2013.

[3.64] M. R. Paiam and R. I. MacDonald, "A 12-channel phased-array wavelength multiplexer with multimode interference couplers," *Photonics Technology Letters, IEEE,* vol. 10, pp. 241-243, 1998.

[3.65] W. Fan, Y. Jianyi, C. Limei, J. Xiaoqing, and W. Minghua, "Optical switch based on multimode interference coupler," *Photonics Technology Letters, IEEE,* vol. 18, pp. 421-423, 2006.

[3.66] A. Z. Chowdhury, "Performance study of silica-on-silicon based multimode interference (MMI) optical coupler," *Photonic Sensors,* pp. 1-9, 2013.

[3.67] P. Trinh, S. Yegnanarayanan, F. Coppinger, and B. Jalali, "Compact multimode interference couplers in silicon-on-insulator technology," in *Lasers and Electro-Optics, 1997. CLEO'97., Summaries of Papers Presented at the Conference on*, pp. 441-441, 1997.

[3.68] D. Kwong, Y. Zhang, A. Hosseini, Y. Liu, and R. T. Chen, "Demonstration of Rib Waveguide Based 1x12 Multimode Interference Optical Beam Splitter on Silicon-on-Insulator," in *Photonics Society Summer Topical Meeting Series, 2010 IEEE*, 2010, pp. 221-222.

[3.69] A. Maese-Novo, R. Halir, S. Romero-García, D. Pérez-Galacho, L. Zavargo-Peche, A. Ortega-Moñux, I. Molina-Fernández, J. Wangüemert-Pérez, and P. Cheben, "Wavelength independent multimode interference coupler," *Optics Express,* vol. 21, pp. 7033-7040, 2013.

[3.70] A. Cleary, S. Garcia-Blanco, A. Glidle, J. S. Aitchison, P. Laybourn, and J. M. Cooper, "An integrated fluorescence array as a platform for lab-on-a-chip technology using multimode interference splitters," *Sensors Journal, IEEE,* vol. 5, pp. 1315-1320, 2005.

[3.71] Q. Lai, M. Bachmann, and H. Melchior, "Low-loss 1× N multimode interference couplers with homogeneous output power distributions realised in silica on Si material," *Electronics Letters,* vol. 33, pp. 1699-1700, 1997.

[3.72] T. Rasmussen, J. K. Rasmussen, and J. H. Povlsen, "Design and performance evaluation of 1-by-64 multimode interference power splitter for optical communications," *Lightwave Technology, Journal of,* vol. 13, pp. 2069-2074, 1995.

[3.73] R. Yin, J. Yang, X. Jiang, J. Li, and M. Wang, "Improved approach to low-loss and high-uniformity MMI devices," *Optics Communications,* vol. 181, pp. 317-321, 2000.

[3.74] Y. Shi, D. Dai, and S. He, "Improved performance of a silicon-on-insulator-based multimode interference coupler by using taper structures," *Optics Communications,* vol. 253, pp. 276-282, 2005.

[3.75] P. A. Besse, M. Bachmann, H. Melchior, L. B. Soldano, and M. K. Smit, "Optical bandwidth and fabrication tolerances of multimode interference couplers," *Lightwave Technology, Journal of,* vol. 12, pp. 1004-1009, 1994.

[3.76] T. Sum, A. Bettiol, J. Van Kan, F. Watt, E. Pun, and K. Tung, "Proton beam writing of low-loss polymer optical waveguides," *Applied Physics Letters,* vol. 83, pp. 1707-1709, 2003.

[3.77] Y. Fu, T. Ye, W. Tang, and T. Chu, "Efficient adiabatic silicon-on-insulator waveguide taper," *Photonics Research,* vol. 2, pp. A41-A44, 2014.

[3.78] S. J. Hettrick, J. Wang, C. Li, J. S. Wilkinson, and D. P. Shepherd, "An experimental comparison of linear and parabolic tapered waveguide lasers and a demonstration of broad-stripe diode pumping," *Journal of Lightwave Technology,* vol. 22, pp. 845-849, 2004.

[3.79] G. Ren, S. Chen, Y. Cheng, and Y. Zhai, "Study on inverse taper based mode transformer for low loss coupling between silicon wire waveguide and lensed fiber," *Optics Communications,* vol. 284, pp. 4782-4788, 2011.

[3.80] R. Halir, I. Molina-Fernández, A. Ortega-Moñux, J. Wangüemert-Pérez, D.-X. Xu, P. Cheben, and S. Janz, "A design procedure for high-performance, rib-waveguide-based multimode interference couplers in silicon-on-insulator," *Lightwave Technology, Journal of,* vol. 26, pp. 2928-2936, 2008.

[3.81] D. Thomson, Y. Hu, G. Reed, and J.-M. Fedeli, "Low loss MMI couplers for high performance MZI modulators," *Photonics Technology Letters, IEEE,* vol. 22, pp. 1485-1487, 2010.

[3.82] Z. Sheng, Z. Wang, C. Qiu, L. Li, A. Pang, A. Wu, X. Wang, S. Zou, and F. Gan, "A compact and low-loss MMI coupler fabricated with CMOS technology," *Photonics Journal, IEEE,* vol. 4, pp. 2272-2277, 2012.

[3.83] E. A. Marcatili, "Dielectric rectangular waveguide and directional coupler for integrated optics," *Bell Labs Technical Journal,* vol. 48, pp. 2071-2102, 1969.

[3.84] H. Yamada, C. Tao, S. Ishida, and Y. Arakawa, "Optical directional coupler based on Si-wire waveguides," *IEEE Photonics Technology Letters,* vol. 17, pp. 585-587, 2005.

[3.85] I. Kiyat, A. Aydinli, and N. Dagli, "A compact silicon-on-insulator polarization splitter," *IEEE Photonics Technology Letters,* vol. 17, pp. 100-102, 2005.

[3.86] L. Zavargo-Peche, A. Ortega-Monux, J. G. Wanguemert-Perez, and I. Molina-Fernandez, "Fourier based combined techniques to design novel sub-wavelength optical integrated devices," *Progress In Electromagnetics Research,* vol. 123, pp. 447-465, 2012.

[3.87] D. S. Levy, R. Scarmozzino, Y. M. Li, and R. M. Osgood Jr, "A new design for ultracompact multimode interference-based 2 x 2 couplers," *Photonics Technology Letters, IEEE,* vol. 10, pp. 96-98, 1998.

[3.88] J.-J. Wu, "A multimode interference coupler with exponentially tapered waveguide," *Progress In Electromagnetics Research C,* vol. 1, pp. 113-122, 2008.

[3.89] C. Themistos, M. Rajarajan, B. M. A. Rahman, S. S. A. Obayya, and K. T. V. Grattan, "Rigorous Comparison of Parabolically Tapered and Conventional Multimode-Interference-Based 3-dB Power Splitters in InGaAsP/InP Waveguides," *Appl. Opt.,* vol. 43, pp. 5228-5235, 2004.

[3.90] P. A. Besse, E. Gini, M. Bachmann, and H. Melchior, "New 2x2 and 1x3 multimode interference couplers with free selection of power splitting ratios," *Lightwave Technology, Journal of,* vol. 14, pp. 2286-2293, 1996.

[3.91] M. Pu, L. Liu, H. Ou, K. Yvind, and J. M. Hvam, "Ultra-low-loss inverted taper coupler for silicon-on-insulator ridge waveguide," *Optics Communications,* vol. 283, pp. 3678-3682, 2010.

[3.92] S. J. McNab, N. Moll, and Y. A. Vlasov, "Ultra-low loss photonic integrated circuit with membrane-type photonic crystal waveguides," *Optics Express,* vol. 11, pp. 2927-2939, 2003.

[3.93] Y. Liu, Y. Li, Z. Fan, B. Xing, Y. Yu, and J. Yu, "Fabrication and optical optimization of spot-size converters with strong cladding layers," *Journal of optics A: Pure and Applied Optics,* vol. 11, p. 085002, 2009.

[3.94] T. Wahlbrink, W. S. Tsai, M. Waldow, M. Först, J. Bolten, T. Mollenhauer, and H. Kurz, "Fabrication of high efficiency SOI taper structures," *Microelectronic Engineering,* vol. 86, pp. 1117-1119, 2009.

[3.95] L. C. Andreani, D. Gerace, M. Passoni, A. Bozzola, and L. Carroll, "Optimizing grating couplers for silicon photonics," in *Transparent Optical Networks (ICTON), 2016 18th International Conference on*, 2016, pp. 1-4.

[3.96] G. Roelkens, D. Van Thourhout, and R. Baets, "SOI grating structure for perfectly vertical fiber coupling," in *Proceedings of the European Conference on Integrated Optics (ECIO 2007)*, 2007, p. 4.

[3.97] D. Taillaert, H. Chong, P. I. Borel, L. H. Frandsen, R. M. De La Rue, and R. Baets, "A compact two-dimensional grating coupler used as a polarization splitter," *IEEE Photonics Technology Letters,* vol. 15, pp. 1249-1251, 2003.

[3.98] F. Van Laere, T. Claes, J. Schrauwen, S. Scheerlinck, W. Bogaerts, D. Taillaert, L. O'Faolain, D. Van Thourhout, and R. Baets, "Compact focusing grating couplers for silicon-on-insulator integrated circuits," *IEEE Photonics Technology Letters,* vol. 19, pp. 1919-1921, 2007.

[3.99] M. Z. Daoxing Dai, "Grating Coupler," ed. Zhejiang University, China, 2016.

[3.100] R. Halir, P. Cheben, J. Schmid, R. Ma, D. Bedard, S. Janz, D.-X. Xu, A. Densmore, J. Lapointe, and I. Molina-Fernández, "Continuously apodized fiber-to-chip surface grating coupler with refractive index engineered subwavelength structure," *Optics Letters,* vol. 35, pp. 3243-3245, 2010.

[3.101] Z. Cheng, X. Chen, C. Y. Wong, K. Xu, and H. K. Tsang, "Apodized focusing subwavelength grating couplers for suspended membrane waveguides," *Applied Physics Letters,* vol. 101, p. 101104, 2012.

[3.102] J. L. Coffer, *Semiconducting silicon nanowires for biomedical applications*. Cambridge: Elsevier, 2014.

[3.103] D. Taillaert, W. Bogaerts, P. Bienstman, T. F. Krauss, P. V. Daele, I. Moerman, S. Verstuyft, K. D. Mesel, and R. Baets, "An out-of-plane grating coupler for efficient butt-coupling between compact planar waveguides and single-mode fibers," *IEEE Journal of Quantum Electronics,* vol. 38, pp. 949-955, 2002.

[3.104] C. A. Barrios, M. J. Bañuls, V. González-Pedro, K. B. Gylfason, B. Sánchez, A. Griol, A. Maquieira, H. Sohlström, M. Holgado, and R. Casquel, "Label-free optical biosensing with slot-waveguides," *Optics Letters,* vol. 33, pp. 708-710, 2008.

Chapter 4

4 FABRICATION

In Chapter 3, the design of 5 sets of biosensor devices was discussed as summarised in Table 3.16. In this Chapter, the fabrication of the first 3 sets of biosensor devices are presented. The fabrication of set 4 and 5 is similar to that of set 3.

Although the optimum silicon core height as demonstrated in chapters 2 and 3 is 0.22µm, the first 3 sets of devices fabricated for this project have core heights of 0.32µm and 0.25µm due to wafer availability.

Set 1 and 2, had a silicon core height of 0.32µm and the waveguide width was fixed at 4µm due to fabrication limitations at The University of Nottingham. Narrower waveguides require the use of an electron beam writer in the photolithography stage. Set 3, had a silicon core height of 0.25µm and narrower waveguides of 0.8µm, where the photolithography was done at The University of Southampton. All other fabrication was done in the nanofabrication facility in the School of Physics and Astronomy at The Physics Department of The University of Nottingham, UK.

Set 4 was fabricated in Zhejiang University, China and another set of set 4 was fabricated at Glasgow University. Both sets of devices were fabricated on a wafer of core height 0.22µm and the waveguide width was fixed to 0.5µm.

In this chapter, the processing techniques used for these devices will be described in some detail.

4.1 MASK LAYOUT

For the fabrication, a mask containing the designs from chapter 3 was required. For set 3, 4 and 5 where the waveguide photolithography was done using an e-beam, a physical mask was not required as the mask layout was fed directly to the e-beam lithography software. The mask layout was designed on a commercial software, Wavemaker 5.004 BASIC. Figure 4.1 shows one device layout of set 3 as seen on the software interface. The waveguides can be seen in purple where there is one inverted tapered input, a 1x5 multimode interferometer (MMI), five S-bends connecting to five Mach-Zehnders (MZIs) and each MZI ending with an inverted tapered output waveguide. This is layer 1 of set 3. Layer 2 was comprised of the 2µm thick SU-8 input/output taper structures that can be seen in orange colour in Figure 4.1. And finally layer 3, which can be seen in blue in Figure 4.1, are the microfluidic channels which will be surrounded in 50µm thick SU-8. Further structures around the device were added to make aligning the three mask layers during the photolithography stage easier. See appendices E-H for the complete mask layout and description.

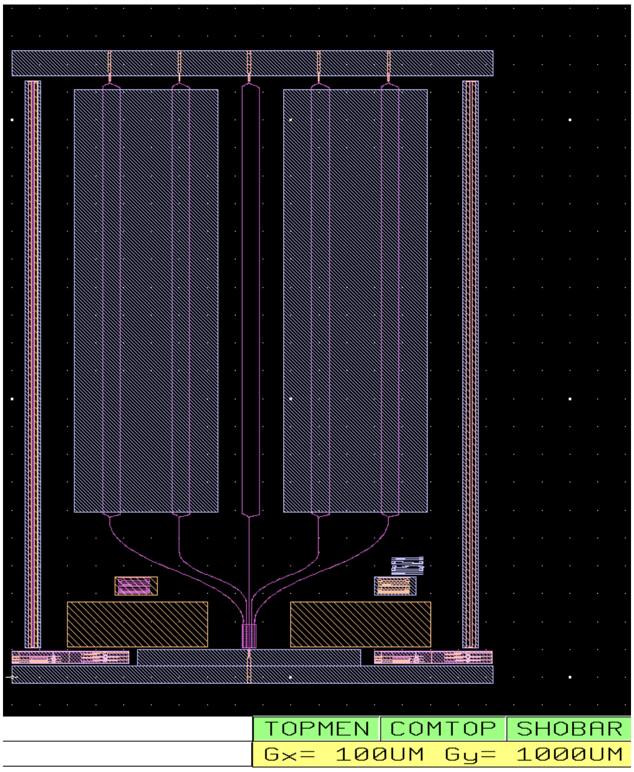

Figure 4.1: Device layout of a biosensor in set 3 comprised of a tapered input waveguide, 1x5 MMI, MZIs and tapered output waveguides as seen on Wavemaker 5.004 BASIC.

The mask layouts designed for sets 1, 2 and 3, were sent in GDS (graphic database system) format to Compugraphics Jena GmbH, Germany to be manufactured into masks as shown in Figure 4.2a and b. The mask was made from 3 x 3 inch glass covered with chrome metal-absorbing film containing the patterns shown in Figure 4.2. See Appendix I for images of all masks manufactured.

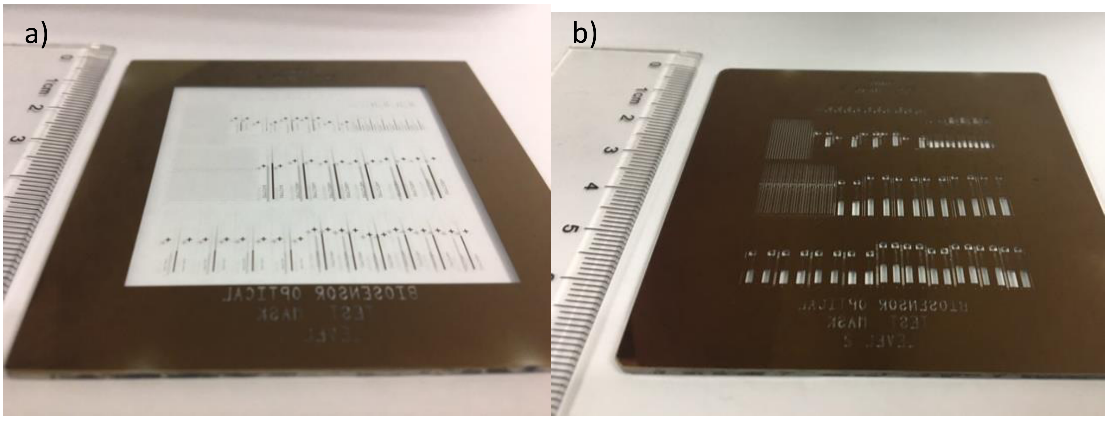

Figure 4.2: Set 1 Mask a) layer 1 and b) layer 2 (reverse chrome view).

4.2 Waveguide and Device Fabrication

The first stage of fabrication was to use a photolithography and etch process to etch down the silicon (Si) to the silicon dioxide (SiO_2) insulator layer and obtain the patterns of the devices designed previously on the silicon layer. The two 6-inch Silicon-on-Insulator (SOI) wafers purchased for this experiment had a Si layer of 0.32µm and 0.25µm and SiO_2 layer of 2µm on a silicon substrate as shown in Figure 4.3. The 6-inch wafer was first cleaved into samples of manageable size (3cm x 4cm) for fabrication. The first stage of processing was to etch down unmasked regions to the SiO_2 layer and this process involved several steps that are described below.

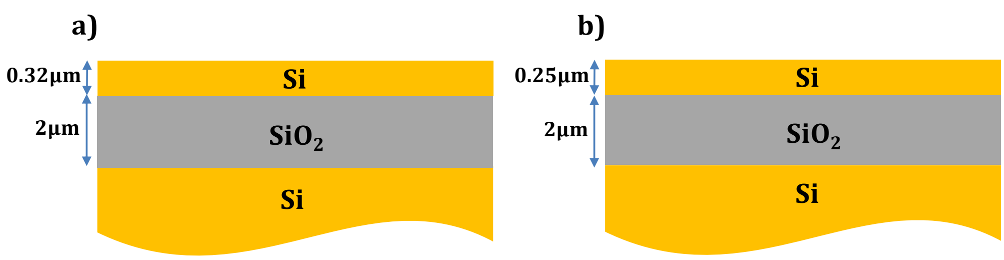

Figure 4.3: Schematic cross-section of SOI wafers with a) silicon core height 0.32µm and b) silicon core height 0.25µm.

4.3 SAMPLE CLEANING

The sample must be thoroughly cleaned before the process as any dust, dirt or oil particle will affect the Photolithography and hence the etched pattern. A basic solvent cleaning method was utilised to clean the sample. The sample was immersed in the following list of solvents and each time placed in an ultrasonic bath for 10 minutes at 25°C. The solvents' sequence used was ethyl lactate, acetone, methanol and isopropanol. Each time the sample was taken out of a solvent it was dried with nitrogen before placing it in the next solvent except when taken out of acetone as acetone leaves traces when dried. If any contamination was visible on the surface, the cleaning procedure was repeated until the surface was completely cleaned. The sample was then dehydrated in air in an oven at 150°C for 30 minutes to remove any surface moisture retained after cleaning.

4.4 PHOTOLITHOGRAPHY

Two types of photolithography were performed. The much wider waveguides of 4um (for set 1 and 2) used a mask aligner with UV light for patterning the designs whereas the narrower waveguides of 0.8µm (for set 3) were made using e-beam lithography where a physical mask is not required.

4.3.1 Photolithography using mask aligner at The University of Nottingham

This step was done according the standard procedure followed by the School of Physics and Astronomy at The University of Nottingham. Positive resist AZ6612 was spin coated at 4000rpm for 30 seconds to obtain a 1.2µm thick resist layer as shown in Figure 4.4a, and soft baked at 110°C for 50 seconds. The sample was then aligned to the mask shown in Figure 4.2a in a mask aligner (Karl Suss MJB-3) and ultraviolet (UV) light was exposed for 6 seconds at 9mJ/s as illustrated in Figure 4.4b. The exposed sample was developed for 30 seconds using AZ726MIF developer, rinsed with water and dried with nitrogen. Figure 4.4c shows a schematic cross-section of the developed photoresist and Figure 4.5 shows the developed photoresist patterns of a 1x20 MMI splitter with output waveguides as seen through a microscope.

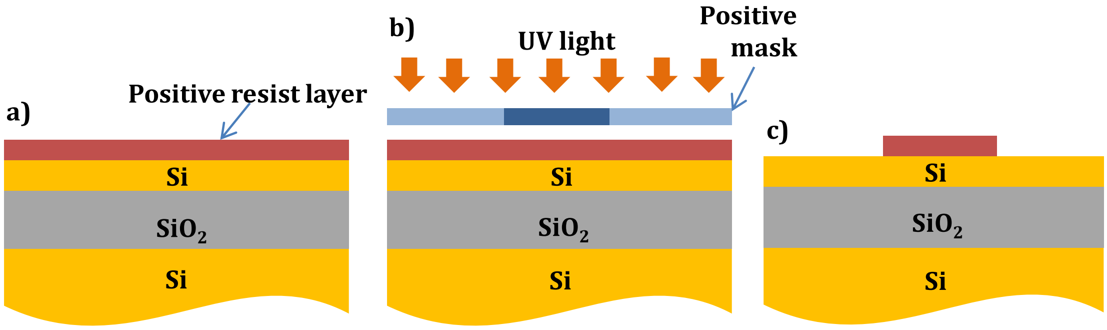

Figure 4.4: Schematic diagram of photolithography process; a) Spin coating positive resist, b) UV exposure through a mask and c) Developed photoresist patterns.

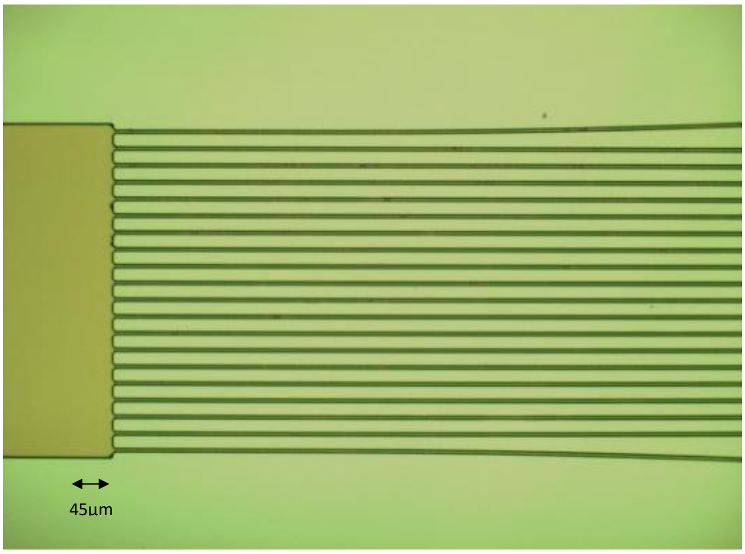

Figure 4.5: Developed photoresist patterns of a 1x20 MMI coupler output waveguides (View from microscope x50).

4.3.2 Photolithography using e-beam at The University of Southampton

This step was done according to the standard procedure in The University of Southampton. The designs for layer 1 of set 3 was changed slightly so that only a 2.5µm area around the waveguide/device was exposed and would be removed by the etching process. This is commonly known as “trench etching” as shown later in Figures 4.8 and 4.9. Etching a trench instead of all of the unwanted silicon layer saves time on the e-beam machine.

ZEP-520A, a non-chemically amplified high resolution positive resist from Nippon Zeon, was spin coated at 6000 rpm to get a thickness of 265 nm. The sample was then baked at 180 ^{0}C on a hot plate for 3 minutes. The samples were then exposed at 250 µC/cm^2 using a JEOL JBX 9300FS e-beam lithography tool. The exposed sample was then developed for 90 seconds in n-amyl-acetate and rinsed with isopropyl alcohol.

4.4 Plasma etching at The University of Nottingham

Once the photoresist develops nearly perfectly into the required patterns the sample is etched by inductively coupled plasma (ICP) etching. ICP etching is used instead of Reactive ion etch (RIE) to obtain good quality sidewalls and because RIE is not strong enough for this process. A CORIAL 200L plasma etcher was used with SF_6 and C_2H_4 (protects the resist layer) at 800W.

The sample was stuck by wax onto a spare silicon wafer and the spare wafer was then glued to the graphite stage of the etcher with a heat transfer grease (FOMBLIM per fluorinated grease from Solvary Solexis) that can withstand high pressure and is chemically unreactive. This helps the sample stay the same temperature as the graphite stage and failing to include this step will result in cooked resist. The grease was not directly applied to the sample as grease was not easy to remove from the sample compared to wax.

A small side build on the resist was observed as shown schematically in Figure 4.6a and was removed by a 'Descum' process by etching the resist for 120 seconds in the ICP. This improved the quality of the etched pattern in the next step. The silicon (0.32µm) was then etched for 110seconds which included an extra 20 seconds to compensate for different etch rates at different points on the sample. This may have resulted in slight etching of SiO_2 but would not have affected the function of the product. Then the resist was removed with oxygen plasma for 105 seconds which also included an extra 20 seconds. This left etched silicon patterns on SiO_2 as shown in Figures 4.6b and 4.9.

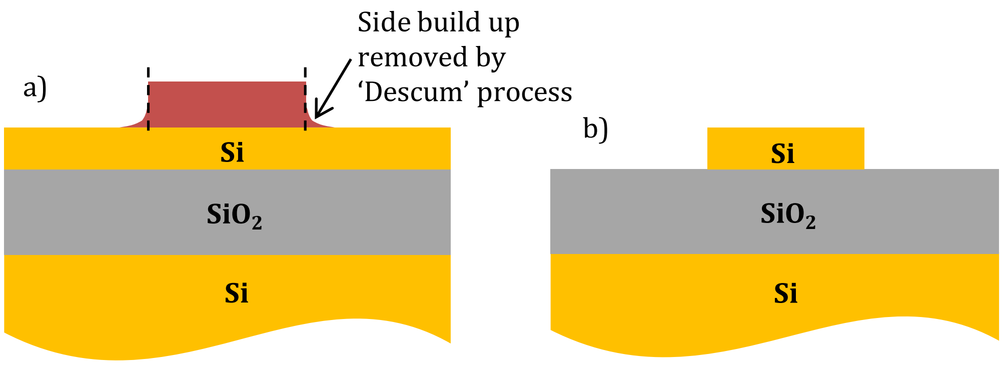

Figure 4.6: The etch process; a) Etching the side build-up of resist and b) etched waveguide.

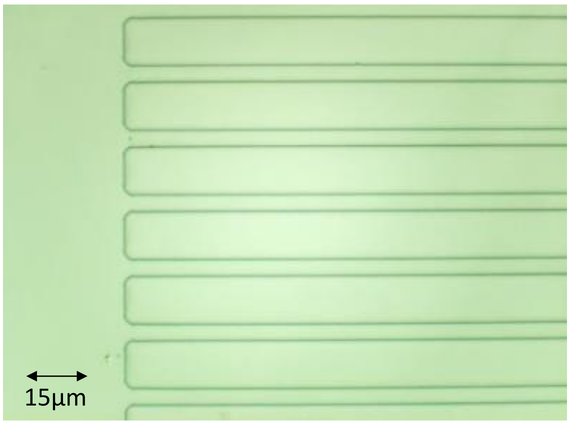

Figure 4.7: Etched silicon patterns of a 1x20 MMI coupler output waveguides for silicon core height of 0.32µm and waveguide width of 4µm (set 1). Photolithography using mask aligner and plasma etching done at The University of Nottingham. (View from microscope x100).

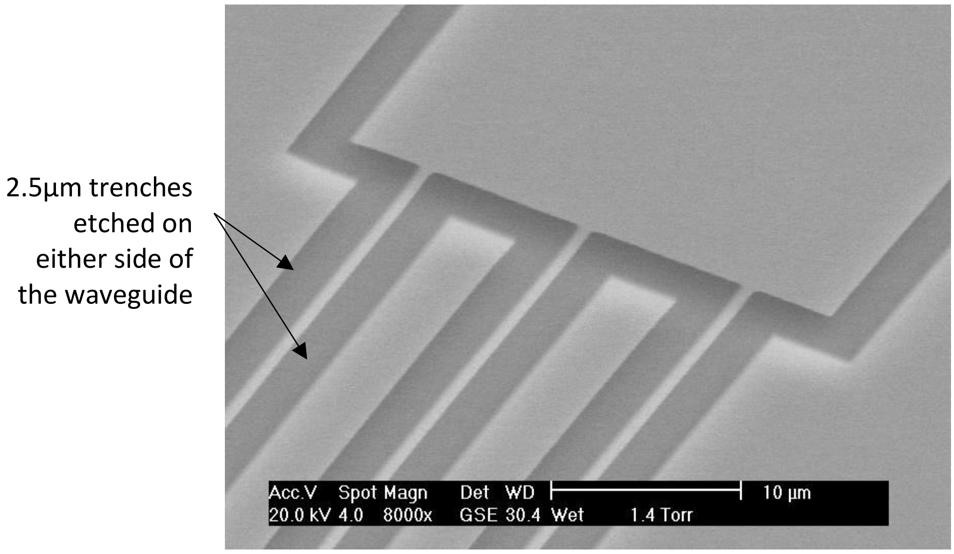

Figure 4.8: ESEM image of a 1x3 MMI output with silicon core height 0.25µm and waveguide width of 0.8µm (set 3). E-beam lithography done at The University of Southampton and plasma etching done at The University of Nottingham.

2.5µm trenches etched on either side of the waveguide

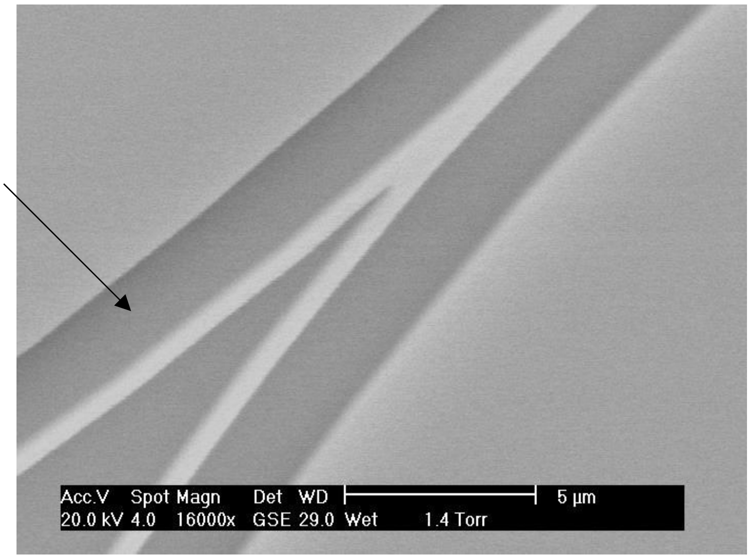

Figure 4.9: ESEM image of a Y-junction splitter of an MZI with silicon core height 0.25µm and waveguide width of 0.8µm (set 3). E-beam lithography done at The University of Southampton and plasma etching done at The University of Nottingham.

4.5 SU-8 TAPER FABRICATION

SU-8 resist was used to serve two purposes in this project. A 2µm thick tapered SU-8 structure was used to couple light in and out of the sample (see designs in section 3.5.2) and a 50µm thick layer was used to form the microfluidics structure which will be briefly described in section 4.8.

SU-8 has been used as optical waveguides in biosensing applications as it provides good transmission properties and low propagation loss [4.1-3]. The light is coupled into the input waveguide through a tapered fibre with a spot diameter of 2µm. Since the input waveguide has a cross-section of 4µm by 0.32µm the coupling loss from the tapered fibre to the silicon waveguide would be high. To minimise the coupling loss and more effectively couple light into the waveguide and out, a tapered SU-8 structure was used as shown in Figure 4.10.

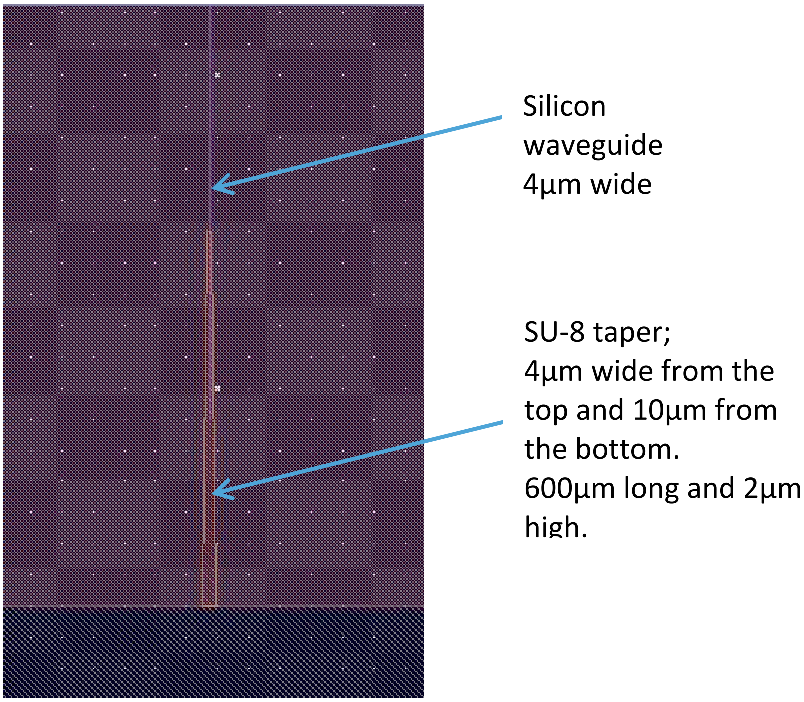

Figure 4.10: Tapered SU-8 Structure on silicon waveguide of core height of 0.32µm and width of 4µm (set 1 and 2) (Mask Layout View).

SU-8 is an epoxy-based negative photoresist that contains eight epoxy groups per molecule as illustrated in Figure 4.11, giving the polymer very high functionality. Regions exposed to UV light polymerise resulting in an extremely high crosslink density [4.4] and a high degree of thermal stability.

SU-8 exhibits high biocompatibility and stacking of several layers of SU-8 enables three-dimensional micro-fabrication. Another main reason for using SU-8 is its ability to make irreversible bonds with PDMS by generating amino groups on PDMS [4.5, 6] thus enabling sealing of the microfluidic channels to the waveguides.

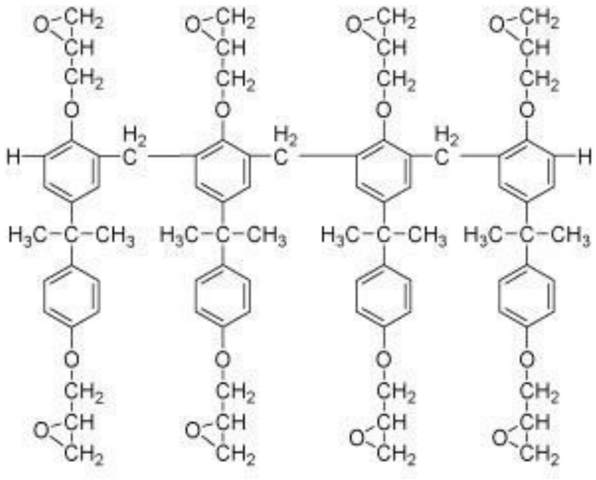

Figure 4.11: SU-8 (glycidyl-ether-bisphenol-A novolac) polymer structure [4.7].

The second stage of fabrication was to fabricate the tapered SU-8 structures on to the input and output waveguides of the etched sample. Commercially available SU-8 2002 from MicroChem Corp was used and the processing guidelines provided by MicroChem [4.8] were slightly altered as described in the next section, to overcome problems with adhesion, cracks forming and uneven edges forming which were all linked to exposure and cooling of the sample.

4.5.1 SU-8 photolithography at The University of Nottingham

SU-8 photoresist is a colourless, viscous liquid and the normal process of fabrication is to spin coat, soft bake, expose, post-exposure bake followed by development. However, this process needs to be optimised for specific applications. The photolithography of SU-8 is the same for devices in set 1-3 but different masks are used as the designs differ.

Figure 4.12 shows a sample placed on a spinner where the base of the spinner is covered in foil as the spinning process spreads the excess SU-8 all over the base and removing this viscous liquid can be difficult. 1ml of resist per 25mm of substrate diameter was dispensed on to the surface of the etched sample. To obtain 2µm thick layer the SU-8 had to be spread at 500rpm for 5 seconds and spun at 2000rpm for 30 seconds to get an evenly spread 2µm thick SU-8 resist layer as illustrated in Figure 4.13a. The spin speed determined the thickness [4.8].

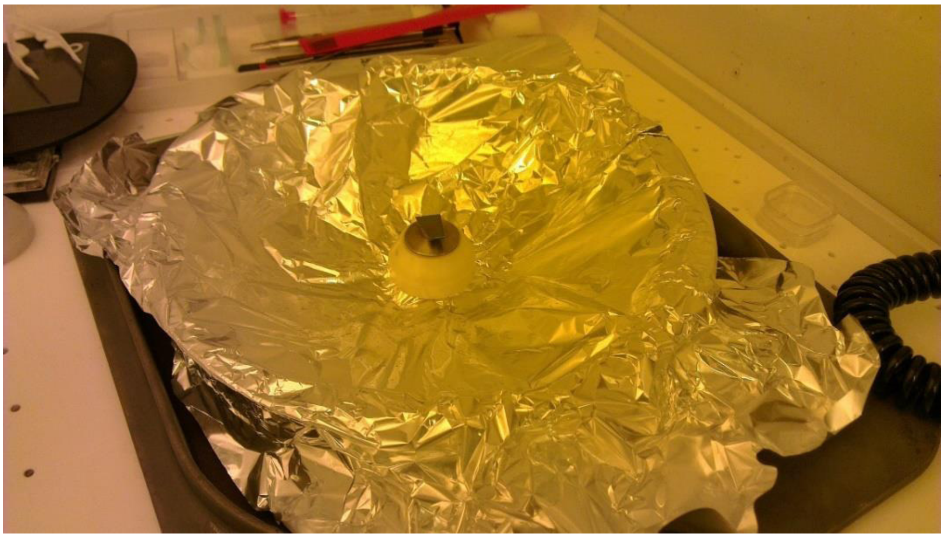

Figure 4.12: Sample placed on a spinner for SU-8 spinning. The foil made cleaning easier.

The sample was then soft baked at 65°C for 15 minutes and 95°C for 1 minute on two different hotplates. The sample had to be gradually heated and cooled to room temperature to reduce thermal shock which caused the formation of waves on the surface of the resist. Leaving the sample overnight at room temperature helped drive out solvents and reduced the tackiness for the next step which required the sample to come into contact with the mask.

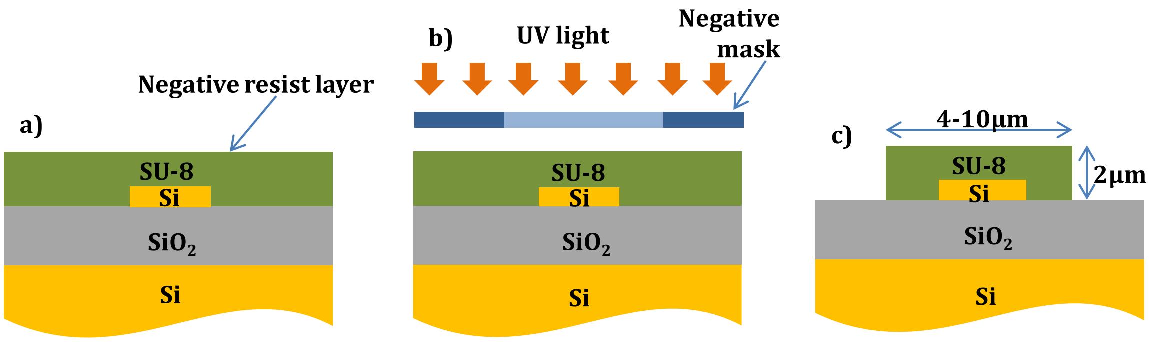

Figure 4.13: Schematic diagram of SU-8 photolithography process a) 2µm thick SU-8 resist later spin coated, b) UV exposure over negative mask and c) Final structure with SU-8 on silicon illustrated for set 1 and 2.

The sample was aligned to the negative mask in the mask aligner. Two different masks were used for sets 1-2 and 3. Aligning the negative mask to the etched waveguides was quite tricky and can take time. It is important that they are perfectly aligned to prevent coupling losses. Figure 4.14a shows an input waveguide not aligned accurately with the SU-8 taper and Figures 4.14b and 4.15 shows the input waveguide well aligned with the SU-8 taper.

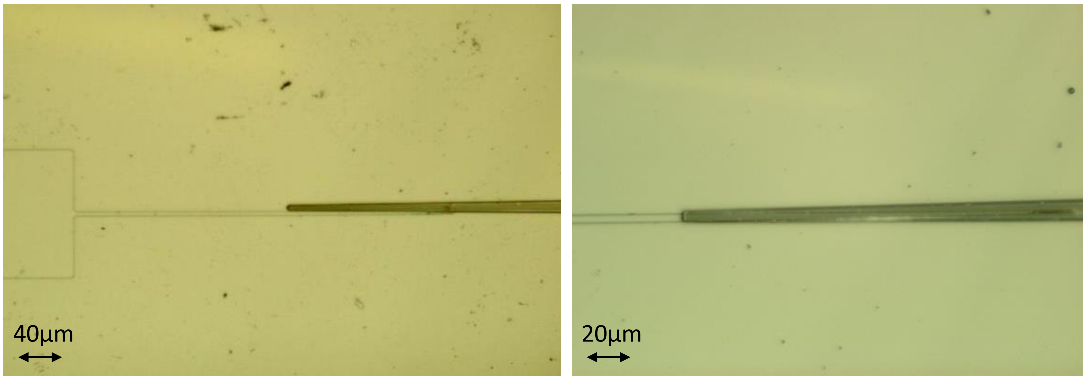

Figure 4.14: Set 1 input silicon waveguide of an MMI a) Not aligned well with SU-8 taper b) Well aligned with SU-8 taper (view from microscope x20).

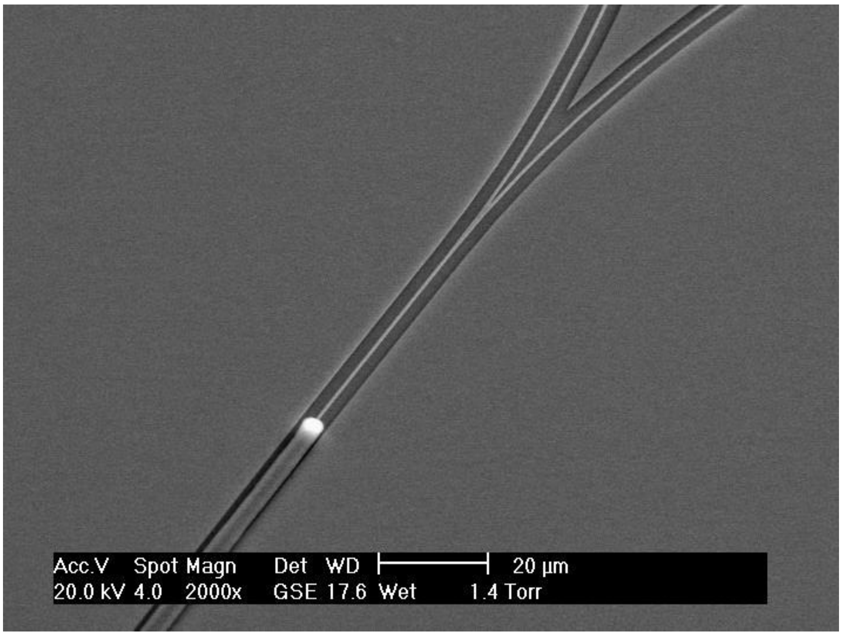

Figure 4.15: Set 3 ESEM image of an input waveguide perfectly aligned with the SU-8 taper.

Once the sample was perfectly aligned to the negative mask it was then exposed to UV light for 6 seconds at 9mJ/s as illustrated in Figure 4.13b. Over exposed resists left uneven patterns when developed later as shown in Figure 4.16. Figure 4.16 is a cross on the SU-8 mask (layer 2 of set 1 and 2) to help with the alignment to the fabricated silicon devices.

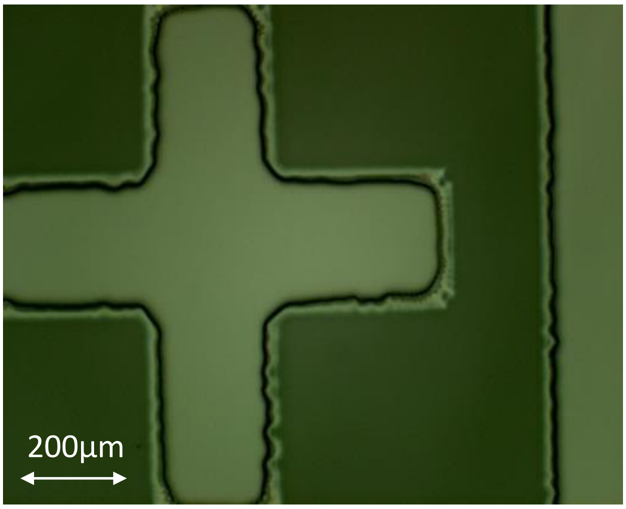

Figure 4.16: An over exposed and developed uneven SU-8 pattern used for the alignment of layer 2 to layer 1 in set 1. (view from microscope x100).

Post-exposure bake (PEB) should take place directly after exposure. The exposed resist cross-linked and hardened during the PEB. The sample was placed on a hotplate at 65°C and the temperature was gradually increased to 95°C during a time span of 20 minutes. The temperature of the hotplate was then gradually ramped down to 40°C in a time span of 4 minutes. The sample was then removed from the hotplate and allowed to cool to room temperature. Failure to gradually heat and cool in this manner, resulted in poor adhesion between the resist and silicon as shown in Figure 4.17a, and crack formation on the resist as shown in Figure 4.17b.

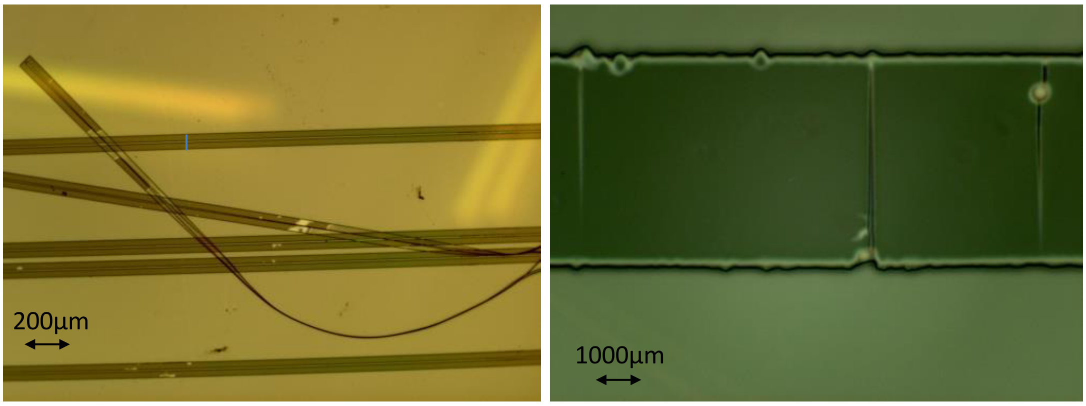

Figure 4.17: a) Poor adhesion between SU-8 and Silicon (View from microscope x20) and b) Cracks formed on SU-8 patterns (View from microscope x100).

Once the sample had cooled down to room temperature it was developed by placing it on a beaker with ethylene carbonate solvent for 40 seconds. The unexposed and uncross-linked SU-8 was washed away in this solution. A stirrer can be placed in the beaker to help with this process. The sample was then washed with isopropanol and dried with nitrogen to yield the structure illustrated schematically in Figure 4.13c.

To make the SU-8 mechanically and thermally stable a hard bake was incorporated into the process. The sample was placed in an oven at 60°C and the temperature was gradually ramped up to 175°C during a 35 minute time period and then allowed to cool naturally to room temperature. Figure 4.18 shows an ESEM image of a final SU-8 taper structure before the cleaving stage.

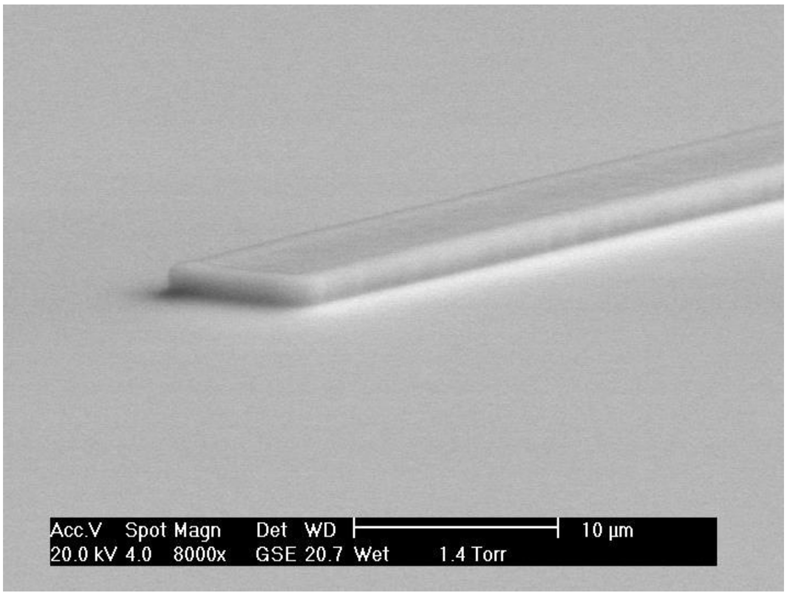

Figure 4.18: ESEM of a well cured SU-8 taper structure from set 2 ready for cleaving.

4.6 CLEAVING

After fabrication, the samples had to be cleaved perpendicular to the SU-8 tapers to obtain good quality end facets. The samples were cleaved with the help of a simple manual diamond scriber.

First a layer of positive resist was spin coated and soft baked for 30 seconds at 110°C in order to protect the device features. Two lines were scribed on either side of the tapered waveguide on a manual diamond scriber and then placed on a rubber mat with the sample features facing down. A small pressure was applied with a diamond pen just enough to crack the wafer. The wafer did not always crack on the scribed line, as shown in Figure 4.19a, if the sample was not perpendicular to the natural cleavage directions of the wafer. It was important to leave tolerance space for this.

Once the sample was cleaved the positive resist was washed off with acetone, isopropanol and dried with nitrogen gas. Figure 4.19b b shows an SEM image of the cleaved facet of an SU-8 tapered waveguide under high magnification. We can see that the cleaved facet is smooth. A smooth facet is needed to minimise light scatter and maximise the coupling efficiency.

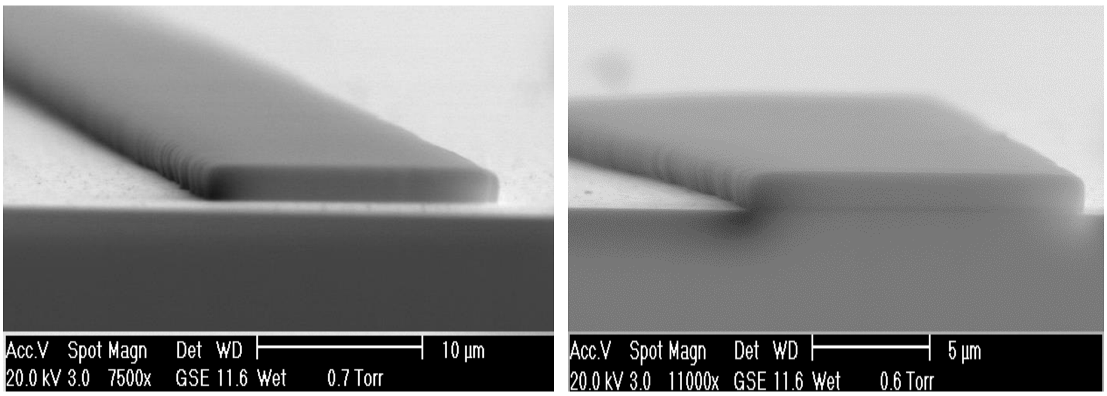

Figure 4.19: a) Wafer not cleaved through the SU-8 taper and b) wafer cleaved through the SU-8 taper (view from ESEM).

4.7 Fabrication of Plasmonic Interferometer (PI) - Set 2

Section 3.3 discussed the theory and design of plasmonic waveguides. The waveguides designed for set 1 with a silicon core height 0.32µm and width of 4µm were used for the fabrication of the plasmonic waveguides as described below. The complete fabrication was done at the School of Physics and Astronomy of The University of Nottingham, UK.

4.7.1 Waveguide fabrication

The wafer was thoroughly cleaned by sonicating in solvents as described in section 4.3, then dried with nitrogen and dehydrated at 150°C for 30 minutes. The photolithography was done as described in section 4.3.1 The positive resist AZ6612 was spin coated at 4000rpm for 30 seconds to obtain a 1.2µm thick resist layer and soft baked at 110°C for 50 seconds. The resist was then patterned by exposing UV light for 6 seconds at 9mJ/s in a mask aligner (Karl Suss MJB-3). The exposed sample was developed for 30 seconds using AZ726MIF developer, rinsed with water and dried with nitrogen.

The waveguide etching was performed as described in section 4.4 to give a waveguide schematically illustrated in Figure 4.20. The 'descum' formed by the resist was first etched for 120 seconds and the silcon was etched for 110 seconds by inductively coupled plasma (ICP) etching using a CORIAL 200L plasma etcher with SF_6 and C_2H_4 at 800W and finally the resist was removed with oxygen plasma for 105 seconds. In both processes the etching time included an extra 20 seconds to compensate for different etch rates at different point of the sample. This may result in etching in to the oxide layer slightly, but this will not affect the function of the product.

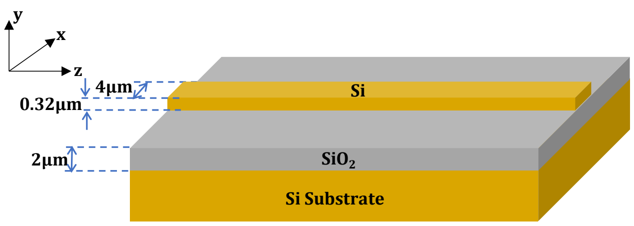

Figure 4.20: Schematic illustration of the fabricated waveguide used for the plasmonic interferometer.

4.7.2 Embedding a thin gold layer

The plasmonic interferometer was formed in pre-defined SOI waveguides 0.32µm x 4µm fabricated as explained above. Negative resist AZ5214E was spin coated at 4000rmp for 30 seconds and soft baked for 3 minutes at 90°C in a hotplate. The resist was then patterned by exposing UV light for 2 seconds at 9mJ/s in the same mask aligner. Post exposure bake was done at 120°C in a hotplate for 30 minutes. A flood exposure (UV exposure with no mask) was done for 20 seconds at 9mJ/s. The sample was then developed in AZ712MIF developer for 19 seconds, rinsed with water and dried with nitrogen.

The sample was etched by the same process as described above in section 4.7.1, for 54 seconds to obtain an etch depth of 230nm to get a structure illustrated in Figure 4.21a. The next step was to deposit gold but, in order to improve adhesion between gold and silicon, a 5nm layer of titanium was deposited by thermal evaporation using an EDWARD Auto 306 Thermal Evaporator at 24 Amps and deposition rate of 0.3nm/s. Then 225nm of gold was deposited via thermal evaporation at 40 Amps and deposition rate of 0.37nm/s.

The sample was developed with dimethyl sulfoxide (DMSO) at 80°C for 30 minutes and then at 55°C for 3 hours. Once the sample was developed it was rinsed with water and dried with nitrogen to get a PI illustrated in Figure 4.21b. Figure 4.22 shows two completed plasmonic interferometers with different gold lengths. See section 6.2 for optical results of the PIs.

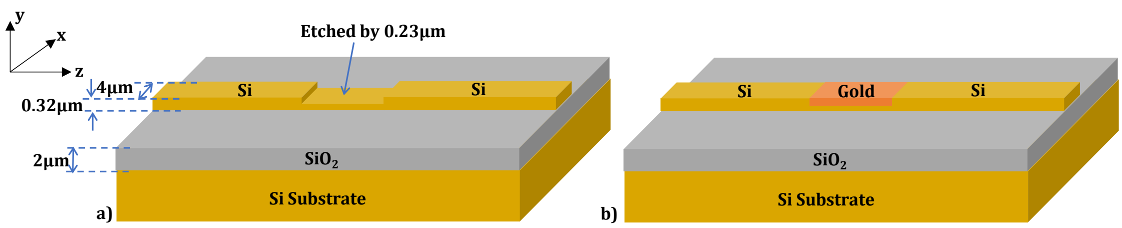

Figure 4.21: a) A window on the silicon waveguide etched down by 0.23µm and b) a gold layer thermally evaporated on to the etched window.

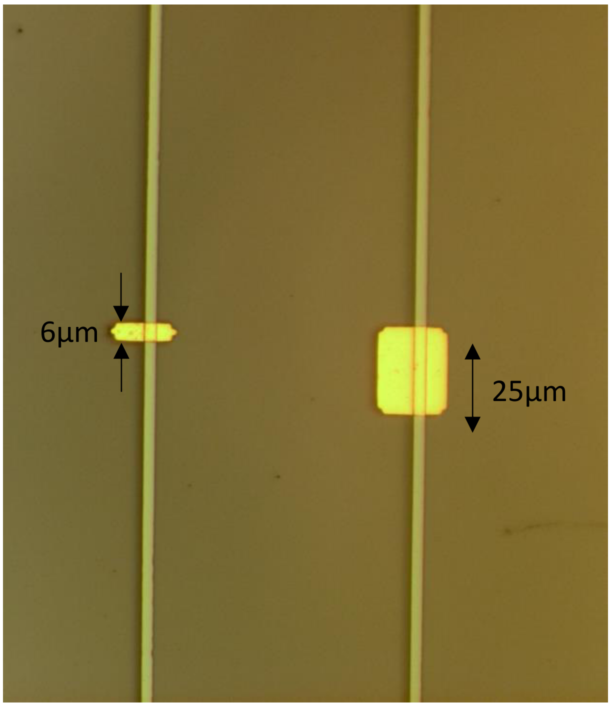

Figure 4.22: Completed plasmonic interferometer (x50 view from microscope).

4.8 Polydimethylsiloxane (PDMS) bonding to SU-8

In section 2.6, a brief introduction to microfluidics was given. In this project, the microfluidic channels were fabricated in 50µm thick SU-8 and sealed by a polydimethylsiloxane (PDMS) layer as shown in Figure 4.23.

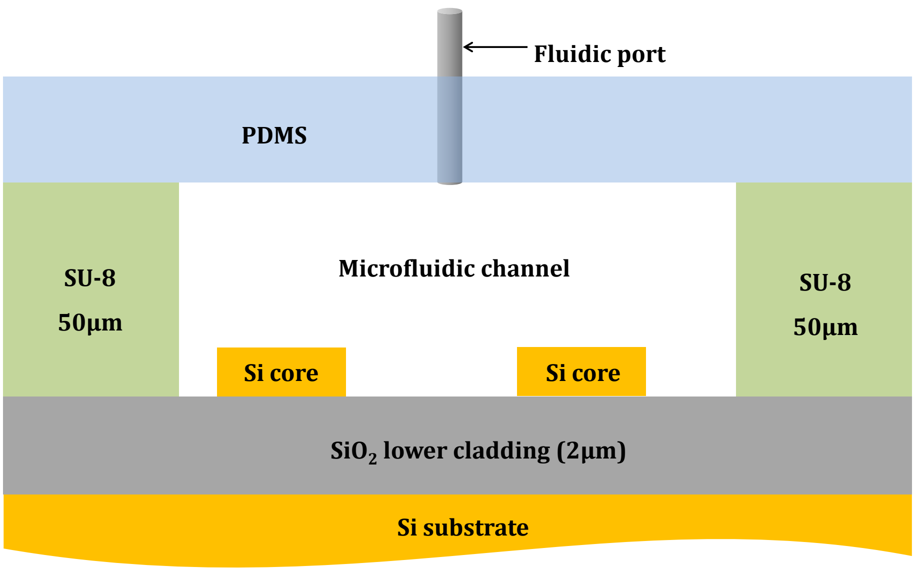

Figure 4.23: Schematic cross-section of a completed device with microfluidic channel and fluidic port.

SU-8 is normally used as the master for creating patterns on the PDMS layer as the cured layer of PDMS can be easily peeled off the SU-8 surface. Plasma treating the PDMS alters the surface chemistry of the PDMS allowing the formation for irreversible bonds between the PDMS and SU-8.

4.8.1 Polydimethylsiloxane (PDMS)

Early microfluidic devices used silicon and glass [4.9] but these were expensive, complex and required specialised fabricating facilities. On the other hand polymers are cheaper and channels can be formed by moulding or embossing rather than etching [4.10]. Cheaper devices make single use devices cost effectively; single use eliminates the potential for contamination between analyses.

PDMS is a silicon based organic polymer illustrated in Figure 4.24 and has been one of the most widely used polymers for microfluidics [4.10]. It is a transparent, nontoxic soft polymer with low permeability to water, low electrical conductivity, and flexible surface chemistry [4.11]. PDMS makes integrating components easier, allows multi-layer microfluidic systems to be fabricated and most importantly it can have features with 0.1µm fidelity [4.10].

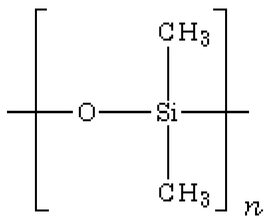

Figure 4.24: Chemical Structure of PDMS.

Although PDMS is compatible with micrometre scale features, only a thin sheet of PDMS is required to seal and connect fluidic ports to the microfluidic channels made by SU-8.

4.8.2 Preparing the PDMS

PDMS was prepared according to the 'Microfluidic Device Fabrication Protocol' (See Appendix J) in the School of Life Sciences at The University of Nottingham, UK. PDMS consists of two compounds, a Base and a Curing Agent (Sylgard 184 purchased from Dow Corning) which were mixed thoroughly in the ratio 10:1 respectively by weight. The quantity depended on the size and thickness of the layer required. The resulting mixture consisted of trapped air bubbles and therefore needs to be degassed. The PDMS was then poured in to a petri dish and cured in an oven at 60°C for 3 hours.

Microfluidic devices on the PDMS are made by pouring the PDMS over a patterned silicon wafer (master) before curing. However, this project only required a uniform layer of PDMS (as schematically illustrated in Figure 4.23) and therefore the mixture was poured into a petri dish and cured.

The required size of cured PDMS was cut out from the petri dish using a scalpel. Fluidic ports were created by punching holes on the PDMS from the channel side with a Biopsy punch. This was done under a dissection microscope. Distilled water was driven through the port to remove any debris and dried with nitrogen. Scotch tape was applied and removed three times on the bonding side to clean the surface.

4.8.3 Preparing the SU-8 2050

As can be observed from Figure 4.23 The microfluidic channel itself was not made of PDMS, as aligning it to the densely-packed sensor can be difficult. So, a second layer of 50µm thick SU-8 was spin coated on the waveguide device to form the microfluidic channel, as microstructures fabricated from SU-8 have good mechanical properties, thermal stability, chemically stable which makes it ideal for microfluidic and bioMEMS (Micro Electro Mechanical Systems) applications. SU-8 is also highly hydrophobic and has a low surface energy, but this would not have been a problem as active pumping was to have been used. However, a wet chemical or oxygen plasma can make the SU-8 surface hydrophilic and increase surface energy. A uniform PDMS layer containing fluidic ports was used to seal the top of the channels and hold fluidic ports (Figure 4.26). This concept was previously developed in [4.12].

Commercially available SU-8 2050 from Microchem Corp was used which is more viscous than the SU-8 2002 which was used for the fabrication of the taper structures, as described in section 4.5. The standard operating protocol provided by the company [4.13] was followed with some changes to the pre- and post-exposure bake times to prevent adhesion problems and the formation of cracks on SU-8. This processing was done in a clean room in the School of Physics and Astronomy at The University of Nottingham, UK, on the waveguide samples fabricated.

3ml of resist per 25mm of substrate diameter was dispensed on to the surface of the wafer for spin coating. This was spread at 500rpm for 5 seconds and spun at 3000rpm for 30 seconds on the biosensor device to obtain a 50µm thick resist layer. During this process, an edge build-up sometimes occured and this was removed with a cotton bud to so that the mask could be placed into close contact with the wafer after the soft bake.

The sample was then Soft Baked (Pre-Exposure Bake) at 65°C for 6 minutes on a pre-heated hotplate and immediately transferred to another hot plate pre-heated to 95°C for 12 minutes. The wafer was removed and allowed to cool naturally from room temperature, avoiding thermal shock. This step eliminates solvents from the photoresist. As SU-8 is tacky it was found helpful to leave the samples overnight before the exposure to reduce the chances of the sample sticking to the mask.

The sample was then carefully aligned to the mask on the MJB-3 mask aligner and exposed to UV light for 16.6 seconds at 9mJ/s and baked. The Post-Exposure Bake was the same as the Soft Bake described above. The exposed photoresist cross-linked and hardened during the Post Exposure Bake.

The unexposed resist was removed or developed with ethyl lactate on a spin coater. Enough ethyl lactate was pipetted onto the wafer to cover the photoresist and the whole sample spun at 2000rpm for 2 minutes. This was repeated 2-4 times until all the unexposed resist was removed. Then the wafer was covered with isopropanol and spun at 2000rpm for 2 minutes in order to wash away any remaining rest or ethyl lactate.

The sample was not Hard Baked in order to leave some free bonds on the surface for bonding with PDMS. The sample was then dried in a vacuum oven at room temperature for 5 hours to draw the solvents out.

4.8.4 Bonding PDMS to SU-8

In general, polymer substrates must be bonded to seal microfluidic channels and the adhesion between the substrates with adhesives maybe a problem as the adhesive may flow into the channels and deteriorate the performance of the device. A method to permanently bond PDMS to SU-8 without conventional adhesives was reported in [4.5, 6]. The method is based on nitrogen plasma treating the surface of PDMS to introduce amino groups that react and form covalent bonds with the residual epoxy groups on the surface of SU-8. Figure 4.25 schematically presents the process for sealing SU-8 channels using PDMS and Figure 4.26 shows the chemical bonding achieved between the PDMS and SU-8 layer [4.6].

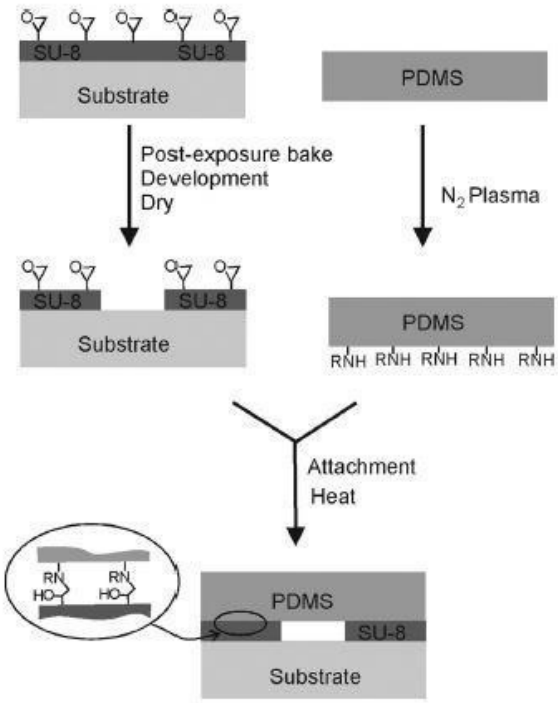

Figure 4.25: Process for sealing SU-8 channels using PDMS [4.6].

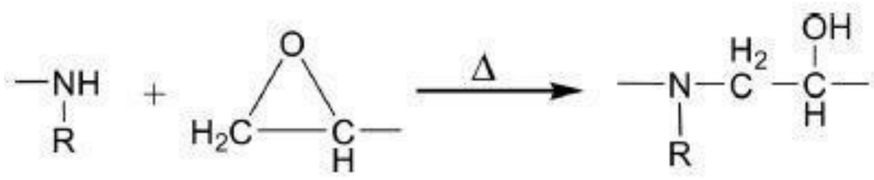

Figure 4.26: Chemical bonding achieved between PDMS and SU-8 [4.6].

Unfortunately in the present work, the exact experimental procedure presented in [4.6] did not form irreversible bonding between the SU-8 and PDMS. So, the experimental procedure had to be changed slightly until a procedure that worked was found. The following experiment was done in the School of Life Sciences at The University of Nottingham, UK.

A piece of PDMS including the microfluidic ports was cut and placed in a Plasma oven with the bonding side face up. The power of the oven was set to 45W and a vacuum applied. The chamber was degassed to the lowest pressure and nitrogen gas was purged into the chamber to maximum pressure. This step was repeated twice more to ensure the chamber consisted mostly of nitrogen and very little oxygen. The plasma was ignited for 1.5 minutes at 0.28mbar pressure. The vacuum pump was turned off and the ventilator turned on. The PDMS was taken out and place on top of the SU-8 as soon as possible and incubated at 100°C for 30 minutes in an oven to make the bonds stronger.

To assess the strength of the irreversible bond a pressure of up to 3 Bar (300kPa) was applied through the fluidic port and the bond did not give away. 3 Bars is the maximum pressure the fluidic port tubing can withstand which means that the sealed channels can nominally hold a larger fluidic pressure than the rest of the microfluidic device connectors.

4.9 CHAPTER SUMMARY

Processing techniques for device fabrication for device sets 1, 2 and 3 have been presented in this chapter. The photolithography for sets 1 and 2 was done using a mask aligner at The University of Nottingham, UK, whereas the photolithography for set 2 was done using an e-beam at the University of Southampton, UK. The rest of the fabrication was done at the University of Nottingham, UK. The devices in all three sets were etched using a plasma etcher, and photolithography using a mask aligner was used to fabricate the SU-tapers. The plasmonic interferometers in set 2 were fabricated by etching down 0.23µm of the waveguide using a plasma etcher and then thermally evaporating platinum and gold on to the etched area of the waveguide. Platinum was used to improve adhesion between the gold layer and the silicon waveguide.

Finally, microfluidic channels were fabricated with 50µm thick SU-8 and sealed with a uniform layer of PDMS. The PDMS was bonded covalently to the SU-8 using a nitrogen plasma. The devices were then cleaved to enable input/output coupling of light. These fabricated devices were then tested and characterised as will be described in Chapter 6.

REFERENCES

[4.1] D. Esinenco, S. Psoma, M. Kusko, A. Schneider, and R. Muller, "SU-8 micro-biosensor based on Mach-Zehnder interferometer," *Rev. Adv. Mater. Sci,* vol. 10, pp. 295-299, 2005.

[4.2] B. Shew, C. Kuo, Y. Huang, and Y. Tsai, "UV-LIGA interferometer biosensor based on the SU-8 optical waveguide," *Sensors and Actuators A: Physical,* vol. 120, pp. 383-389, 2005.

[4.3] B. Y. Shew, Y. C. Cheng, and Y. H. Tsai, "Monolithic SU-8 micro-interferometer for biochemical detections," *Sensors and Actuators A: Physical,* vol. 141, pp. 299-306, 2008.

[4.4] (Accessed 20 Jun 2015). Available: http://www.nanotech.dtu.dk

[4.5] Z. Zhang, P. Zhao, and G. Xiao, "The fabrication of polymer microfluidic devices using a solid-to-solid interfacial polyaddition," *Polymer,* vol. 50, pp. 5358-5361, 2009.

[4.6] Z. Zhang, P. Zhao, G. Xiao, B. R. Watts, and C. Xu, "Sealing SU-8 microfluidic channels using PDMS," *Biomicrofluidics,* vol. 5, pp. 1-8, 2011.

[4.7] J. M. Shaw, J. D. Gelorme, N. C. LaBianca, W. E. Conley, and S. J. Holmes, "Negative photoresists for optical lithography," *IBM Journal of Research and Development,* vol. 41, pp. 81-94, 1997.

[4.8] "Data Sheet- Processing Guidelines SU-8 2002," M. Corp., Ed., ed. www.microchem.com.

[4.9] S. Tuomikoski and S. Franssila, "Free-standing SU-8 microfluidic chips by adhesive bonding and release etching," *Sensors and Actuators A: Physical,* vol. 120, pp. 408-415, 2005.

[4.10] J. C. McDonald and G. M. Whitesides, "Poly (dimethylsiloxane) as a material for fabricating microfluidic devices," *Accounts of Chemical Research,* vol. 35, pp. 491-499, 2002.

[4.11] A. D. Stroock and G. M. Whitesides, "Components for integrated poly (dimethylsiloxane) microfluidic systems," *Electrophoresis,* vol. 23, pp. 3461-3473, 2002.

[4.12] A. Densmore, D. X. Xu, P. Cheben, M. Vachon, S. Janz, R. Ma, D. Bedard, Y. Li, G. Lopinski, Dela, x, A. ge, J. H. Schmid, R. Halir, and I. Molina-Fernandez, "Integration of vertical grating couplers and microfluidic channels with silicon photonic wire biosensor arrays," in *Sensors, 2010 IEEE*, 2010, pp. 1550-1553.

[4.13] "Data Sheet- Processing Guidelines SU-8 2050," M. Corp., Ed., ed. www.microchem.com.

Chapter 5

5 BIORECEPTORS

As explained in Chapter 1, a biosensor is made of a bioreceptor and a transducer. The design, fabrication and testing of the transducer component of the biosensor has been discussed in chapters 2-4. The transducer is just sensitive to environmental refractive index changes until a selective bioreceptor layer is added to the surface of the transducer. This chapter will discuss the possible bioreceptor layers that can be used for this project and some preliminary results of surface functionalisation experiments are presented.

The bioreceptor layer is the surface onto which the analyte is inserted, which can be an Enzyme, Antibody, Nucleic Acid, Tissue, Microbial or Polysaccharides [5.1]. In this case the bioreceptor layer consisted of antibodies that were specific to the binding of the target molecule/antigen. They provided a specific, sensitive response to the analyte of interest. Biosensors based on this transducer technology are known as an immunosensor [5.1, 2].

Immunosensors detect an antigen-antibody reaction directly or indirectly. Direct immunosensors, or homogenous immunoassay, detect the binding in the form of a change in electric potential, current, conductance, impedance, intensity and phase change of electromagnetic (EM) radiation, mass, temperature or viscosity. An indirect immunosensor or heterogeneous immunoassay uses separate labelled species such as a fluorescence or luminescence which are detected after the antigen-antibody binding [5.2].

This project focuses on direct immunosensors, homogenous immunoassay or henceforth referred to in this report as label-free detection for reasons described in the following section.

5.1 LABEL-FREE DETECTION

Generally, there are two protocols that can be implemented in optical biosensing; label based detection and label free-detection [5.2-4].

The early development of optical fibres based biosensors relied on methods of enhancing the signal by labelling the target molecule with an enzyme, fluorescent tags, radioisotopes etc. Fluorescence based detection uses a method of labelling the target molecules with fluorescent tags, which emit light (photons) at a particular wavelength when illuminated with a laser at the excitation wavelength. The intensity of the fluorescence increases with the analyte concentration and is extremely sensitive - with the detection limit down to a single molecule [5.5]. However, fluorescence based detection involves a laborious process of labelling the target molecule which can interfere with the function of the molecule [5.6], generally resulting in the death of specimens [5.7], and real time measurements cannot be obtained. Quantitative analysis and kinetic analysis is challenging as the number of tags cannot be precisely controlled. Multiple detections require multiple labels and additional reagents at an additional cost. Labels are prone to quenching and photobleaching which reduce efficiency. Radioactive labels require “hot labs” and contaminated reagents and labware must be properly disposed of [5.7].

Advances in optical transducers have led to increased sensitivities that allow direct measurements of the bonding between the target molecule and bioreceptors. In particular, label free optical detection has received a lot of interest [5.2-4]. In label-free detection, target molecules are not labelled or altered and are detected in their natural forms [5.6]. Label free detection is relatively less expensive and allows for quantitative and kinetic measurements of molecular interaction. The sensitivity is dependent on concentration or surface density and not on the total number of target molecules in the analyte [5.6]. Reagent use is maximized because of the reversibility of the antibody-antigen reaction thereby facilitating the regeneration of the immobilized component [5.2]. The most important advantage is probably the ability to make real time measurements.

5.2 Surface Functionalisation

The aim of the work described in this chapter is to attach or immobilize an antibody on to the surface of the silicon waveguide at the sensing window as shown in Figure 5.1a. This is done by surface functionalization or chemical modification of the silicon surface which introduces chemical functional groups to the surface that form covalent bonds with the antibody [5.8]. In other words, it is a chemical linker between the sensor and the antibody as shown in Figure 5.1b.

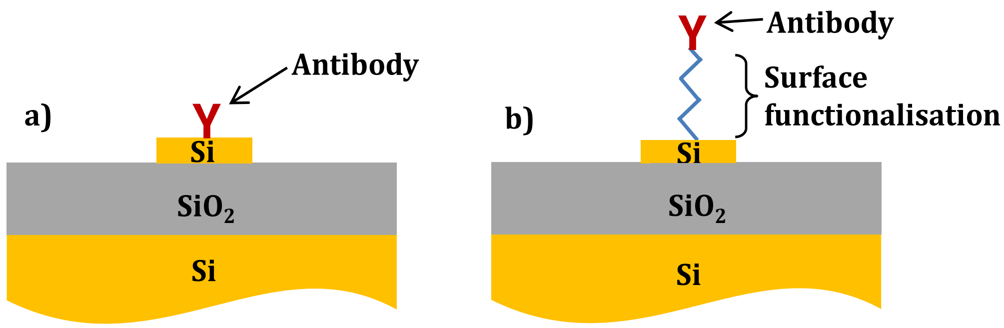

Figure 5.1: Illustration of a cross-section of a silicon waveguide with an a) Anti body attached to silicon waveguide directly and b) Antibody attached to silicon via a chemical linker

Surface functionalization of silicon is a well-researched and documented area and the most common form of silicon modification is accomplished by passivating the native oxide layer or a hydrogen-terminated silicon surface as explained in more detail in the following sections.

Silicon (100) is the most commonly used silicon crystal orientation for commercial microelectronic devices and is also what is used in this project. The surface of silicon is terminated with hydrogen bonds, as illustrated in Figure 5.2a, which are vulnerable to oxidization in air and form a native oxide layer approximately 5nm thick which characteristically possesses silanol (Si-OH) groups as illustrated in Figure 5.2b.

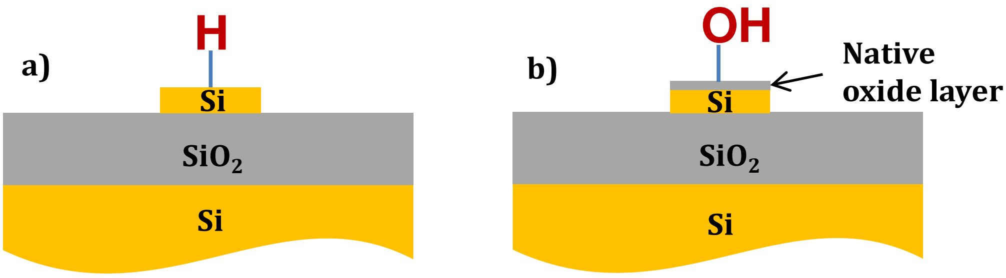

Figure 5.2: Illustration of a cross-section of a silicon ridge waveguide with an a) H-terminated and b) OH-terminated surface.

An H-terminated surface can be changed to an OH-terminated surface thermally or through ozonolysis [5.9] or by leaving it exposed to air over time[5.10]. To increase the OH bonds on the surface a hydroxylation procedure can be performed as explained in section 5.2.3. Similarly, an OH-terminated surface can be converted to an H-terminated surface using a piranha etch as explained in section 5.2.2.

The surface functionalization therefore would depend on the surface terminations of the waveguide. Figure 5.3 lists some common methods used for surface functionalization of silicon wires depending on their surface termination.

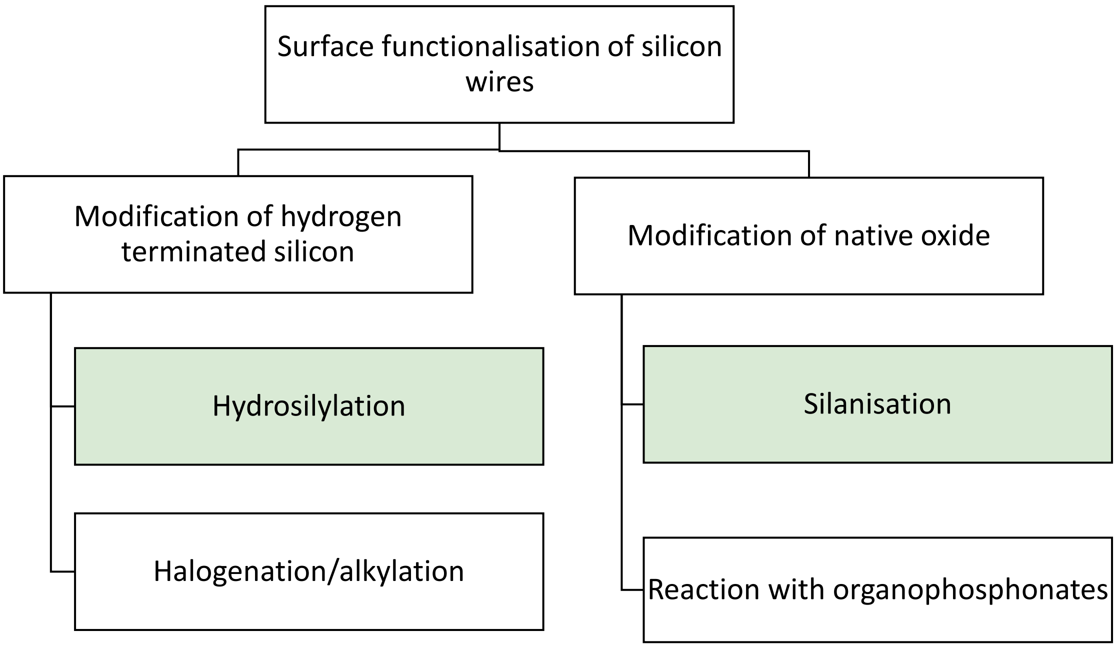

Figure 5.3: Methods of surface functionalization of silicon waveguides [5.11].

Most of the literature available on the surface functionalization of silicon is actually carried out on the native oxide layer or on a “clean” silicon surface.

For this project, hydrosilylation, and silanisation, was undertaken on H-terminated, and OH-terminated, silicon (100), respectively. Then amino terminated monolayers were attached to these surfaces. A fluorescent tag was then attached to the amine to image and assess the surface modification and selectivity.

Fluorescein isothiocyanate (FITC) as illustrated in Figure 5.4 is the fluorescent tag used as the isothiocynate group is reactive towards nucleophiles such as amine or thiol groups [5.8, 12]. FITC emits green light at a wavelength of 520nm when excited by blue light at a wavelength of 495nm. This emission is imaged using a microscope and filters.

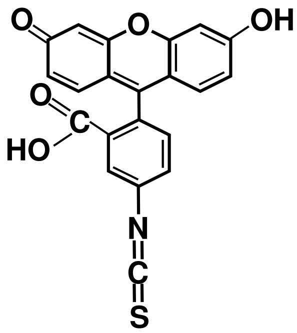

Figure 5.4: Chemical structure of a fluorescein isothiocyanate (FITC) molecule.

The following experiments were conducted in the School of Life Sciences and the School of Chemistry at the University of Nottingham, UK.

5.3 SURFACE FUNCTIONALISATION BY HYDROSILYLATION

In this section, a method of surface functionalisation of a silicon surface is described by hydrosilylation followed by the attachment of an amine functional group. FITC was then attached to the amine in order to image the surface modification through a microscope. Finally, some preliminary experiments and results are presented.

5.3.1 Surface passivation of H-terminated silicon

Surface functionalization of H-terminated silicon is preferred and the oxide layer presents an additional insulation layer between the waveguide and the antibody-antigen reaction. Since the silicon waveguide is covered in a native oxide layer, the surface functionalization starts with the wet chemical etching of the oxide layer which also forms an H-terminated silicon surface. This hydrosilylation was achieved by dipping the silicon (100) wafer into a solution of 2% hydrofluoric (HF) acid (200µl (µdm^3) of HF mixed in 10ml of distilled water) for 10 minutes at ambient temperature, yielding a silicon (100) dihydride surface [5.13-16]. The freshly etched silicon H-terminated surfaces are chemically homogenous (>99% H-termination) as illustrated in Figure 5.5 [5.13]

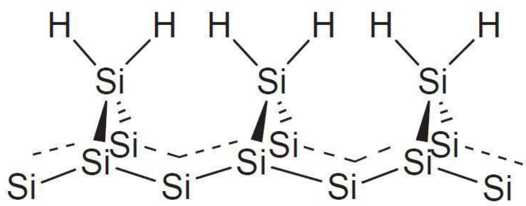

Figure 5.5: Chemical structure of Dyhydride terminated flat Si(100) [5.13].

Similarly, a silicon (111) surface can be H-terminated by dipping the wafer into 40% aqueous ammonium fluoride yielding a monohydride silicon (111) surface [5.13, 17, 18] as illustrated in Figure 5.6.

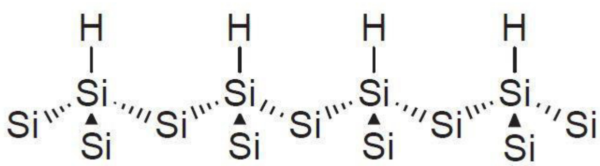

Figure 5.6: Chemical structure of Monohydride terminated flat Si(111) [5.13].

The H-terminated surface can be handled in air for tens of minutes before rapid oxidation to silicon dioxide takes place [5.13, 16]. Therefore, the next step was conducted immediately after the hydrosilylation step.

5.3.2 Amino termination on H-terminated silicon surface

Several different methods for the preparation of amino-functionalized surfaces have been investigated experimentally in the literature [5.18, 19].

In this project 10-N-boc-amino-dec-1-ene was used to form NH_2-terminated monolayers. The amine functional handle of this alkene chain is protected with t-butyoxycarbonyl (t-BOC) group because the amine can potentially react with the bare silicon surface [5.14]. Each process step was conducted at ambient temperature.

Immediately after the hydrosilylation, 100µl (µdm^3) of 10-N-boc-amino-dec-1-ene was pipetted on to the silicon sample covering the entire surface (10mm x 10mm) and illuminated with 254nm ultraviolet (UV) light for 2 hours at 2mW/cm^2 under a nitrogen atmosphere.

Deprotection was achieved by treating the surface with 25% trifluoroacetic acid (TFA) in water for 1 hour followed by a 5 minutes rinse in 10% NH_4OH.

The fluorescein isothiocynate (FITC) label, which was the fluorescent tag, was diluted with phosphate buffer solution (PBS) to a 1:1000 weight ratio and injected on to the sample and left for an hour at room temperature. The sample was then washed with PBS and dried with nitrogen.

This method is illustrated in Figure 5.7.

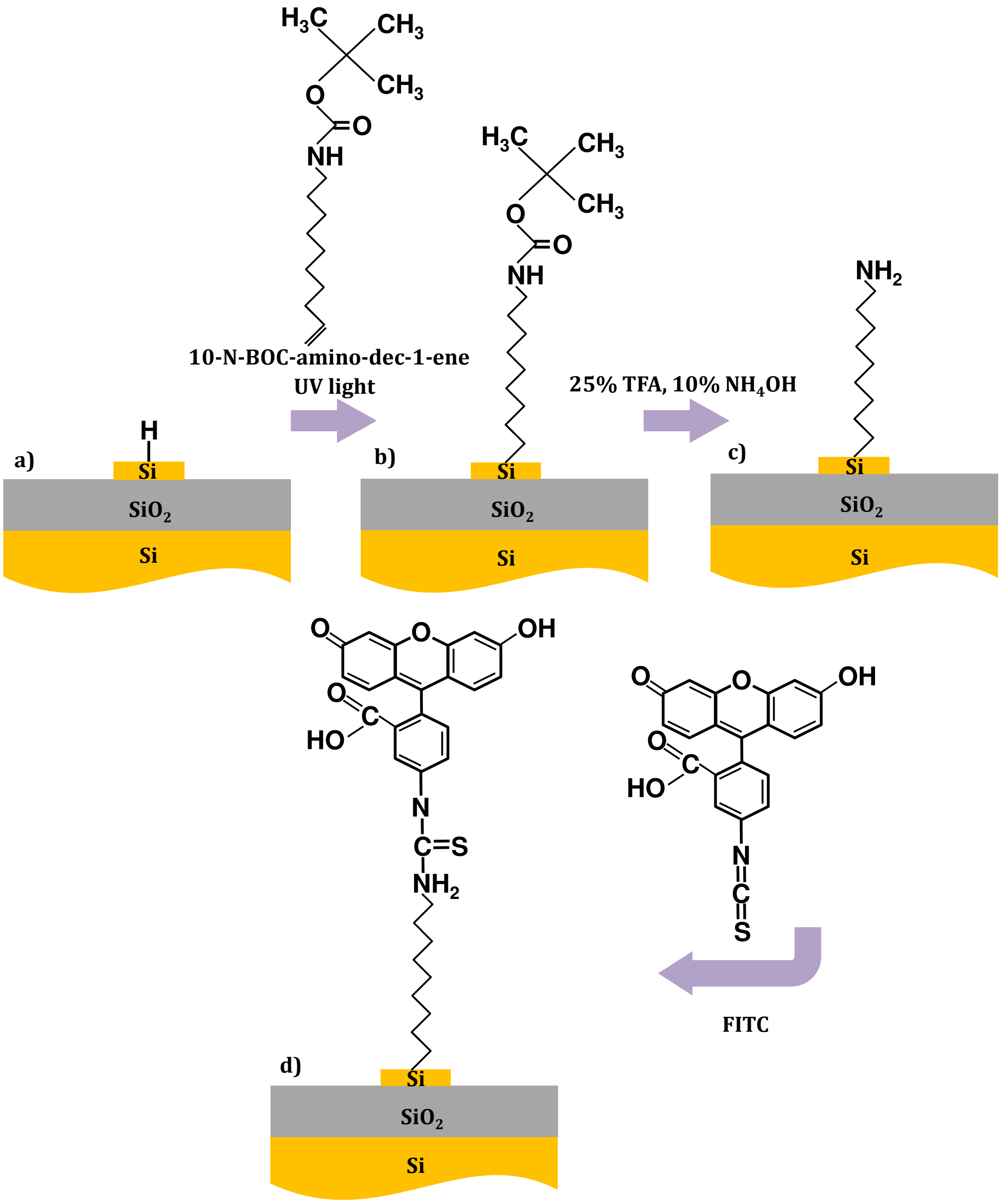

Figure 5.7: Illustration of amino termination of an H-terminated silicon ridge waveguide followed by the attachment of FITC fluorescent tag.

5.3.3 Experiment 1

This experiment was done at the School of Chemistry at the University of Nottingham, UK.

1. 200µl (µdm^3) of HF was measured using a plastic pipette and placed on plastic beaker with 10ml of distilled water. Partially etched Silicon-on-Insulator (SOI) samples were dipped in the HF for 10 mins at ambient temperature and then washed in water and dried with nitrogen.
2. 100µm of 10-N-boc-amino-dec-1-ene was measured using a pipette and dropped on each of samples to completely cover the surface. The samples were then left under a 254nm ultraviolet (UV) light and nitrogen gas at ambient temperature for 12.6 minutes for reasons shown below.

A 125W mercury lamp (purchased from Photochemical Reactors Ltd.) emits 254nm UV radiation at 7×10^{18} photons/s and has a discharge length and diameter of 30mm and 15mm respectively. In [5.19] the sample was exposed to the UV light for 2 hours at an intensity of 2mW/cm^2 whereas [5.18] exposed the sample to the UV light for 2 hours at an intensity of 0.35mW/cm^2 under dry nitrogen gas. The intensity of the UV lamp used for this project was calculated as:

$$Energy = \frac{hc}{\lambda_{UV}} = \frac{6.6 \times 10^{-34} \times 3 \times 10^{8}}{254 \times 10^{-9}} = 7.9 \times 10^{-19} J \quad (5.1)$$

where *h* is the Planchk's constant, *c* is speed of light in a vacuum and *v* is the wavelength.

$$Power = Energy \times \frac{Photons}{s} = 7.9 \times 10^{-19} \times 7 \times 10^{18} = 5.46W \quad (5.2)$$

$$Intensity = \frac{Power}{Area(2\pi rL)} = \frac{5.46}{2\pi \times 15 \times 30} = \frac{19mW}{cm^2} \quad (5.3)$$

To obtain the equivalent energy of 2mW/cm^2 for 2 hours the sample should be irradiated for 12.6 minutes at 19mW/cm^2.

3. The samples were then left in a beaker with 500µl of TFA (purchased from Halocarbon) diluted in 1.5ml of dichloromethane (≥99.8%, purchased from Sigma-Aldrich) for deprotection of the t-BOC group.
4. Samples were rinsed with NH_4OH (35%, purchased from Fisher Scientific) diluted with distilled water to 10% NH_4OH, followed by PBS.
5. Finally, the samples were immersed in a 1:1000 ratio of FITC (>97.5% purchased from Sigma-Aldrich) to PBS solution for an hour, rinsed with PBS and dried with nitrogen gas.

The results were observed at the School of Mechanical, Materials and Manufacturing Engineering at the University of Nottingham, UK. An ECLIPSE LV100ND Microscope system with a DS-Fi2 camera was used to view the samples in this Chapter. The incident light source used was a Blue LED with a peak of 490nm (M490L2 purchased from Thorlabs). Note that instead of using a filter the microscope software was used to cut out all light except for green light. Therefore, even without the FITC label present the images obtained will look green as it can be seen in the control sample in Figure 5.8a.

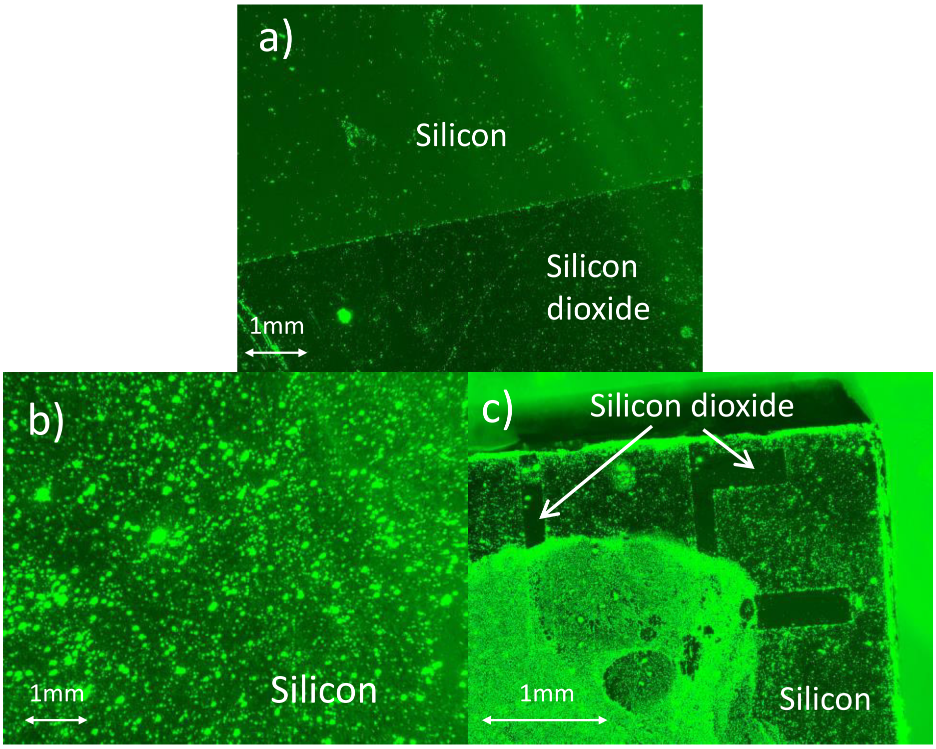

Figure 5.8: Images of silicon and silicon dioxide SOI samples excited by a blue LED and imaged through a camera with red and blue light cut off: a) Silicon and silicon dioxide control sample with no UV irradiation (x10 microscopic view); b) silicon sample with 12.6 minutes of UV irradiation at 19mW/cm² (x10 microscopic view) and c) silicon with silicon dioxide sample with 12.6 minutes of UV irradiation at 19mW/cm² (x5 microscopic view).

Figure 5.8a is a control sample where the top half of the wafer was etched down to the silicon dioxide layer of the SOI wafer. Step 2 of amino attachment was not done on the control sample. The reflections from the silicon and silicon dioxide layer gives two different shades of green when the blue and red light is cut off from the microscope making it difficult to judge from the images if the light is from the reflection of the surface or the fluorescent tag. Figure 5.8b is the silicon surface of the SOI sample and Figure 5.8c shows silicon and silicon dioxide where some patterns were etched down to the silicon dioxide surface of an SOI sample. From Figure 5.8b and c a non-uniform layer of bright spots, which could have been the fluorescent tag, FITC can be seen. From Figure 5.8c a clear affinity towards the silicon surface can be seen. Note that all three samples were dipped in HF for 10 minutes which etched away the native oxide layer formed on the silicon surfaces. Therefore, from Figures 5.8b and c it appears that a non-uniform surface functionalization has occurred on the silicon surface of the SOI samples.

5.3.4 Experiment 2

Silicon ridge waveguides designed in section 3.1.4 have a width of 0.5µm and can extend in length to a few millimetres as shown in section 3.2.1. It is important to obtain a uniformly functionalized surface in order to make sure the narrow waveguides are functionalized suitably. Therefore, in this section experiment 1 was repeated to study the effect of UV exposure time, where two more samples were irradiated with UV light at the same intensity of 19mW/cm^2 for 20 and 40 minutes. Figure 5.9 shows the corresponding images observed under illumination from the blue LED.

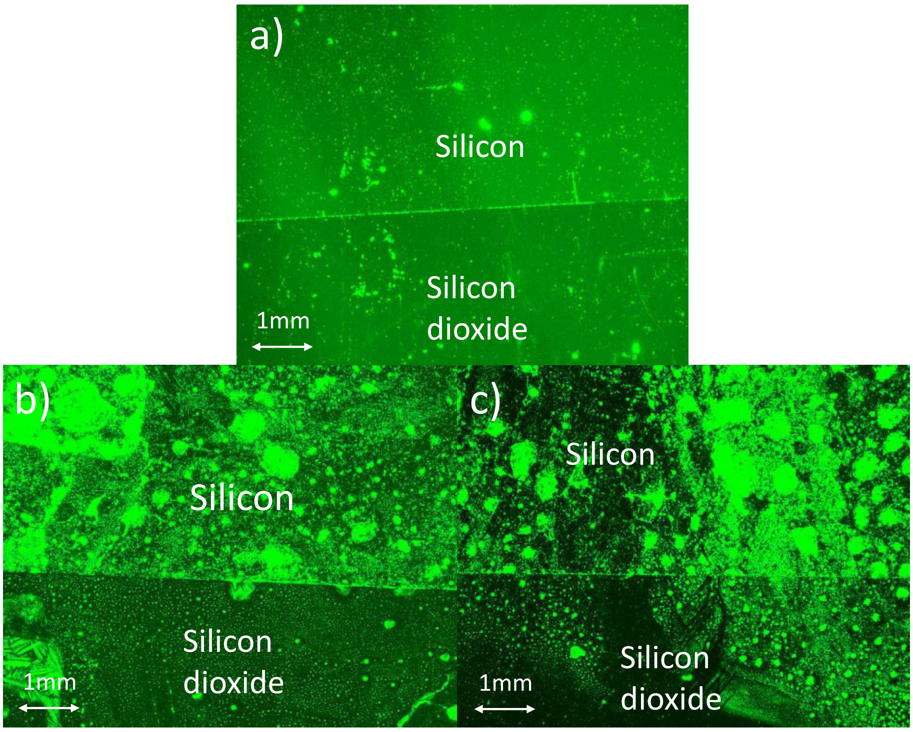

Figure 5.9: Images of silicon and silicon dioxide SOI samples excited by a blue LED and imaged through a camera with red and blue light cut off: a) control sample with no UV irradiation; b) 20 minutes of UV light irradiation at 19mW/cm^2 and c)40 minutes of UV light irradiation at 19mW/cm^2. (x10 microscopic view).

Figure 5.9a is a control sample with a silicon and a silicon dioxide surface where step 2 of amino attachment under the UV light was not done, similar to the sample in Figure 5.8a. From Figure 5.9b it is seen that a larger surface area of silicon is covered in FITC compared to Figure 5.8b. From Figure 5.9c an increase in FITC presence in the silicon dioxide surface can be seen. Therefore, it is concluded that increasing the UV light exposure time increases the area of surface functionalization and further increasing the time allows the surface modification of silicon dioxide surface.

5.3.5 Experiment 3

From experiment 1 and 2 a uniform surface functionalisation had not been achieved. Therefore Experiment 1 was repeated again by replacing the mercury UV lamp with a XL-1000 Microprocessor-controlled UV crosslinker (purchased from Spectroline). This experiment was performed in the nanofabrication facility of the School of Physics at The University of Nottingham, UK. This UV crosslinker provided control over the UV energy, intensity and time.

From experiment 1, 12.6 minutes of UV irradiation at $19mW/cm^2$ (or 2 hours of UV irradiation at $2mW/cm^2$) corresponds to $14.4J/cm^2$. In experiment 3, the energy dosage was varied to 5, 10 and $15J/cm^2$. The images subsequently observed under illumination from the blue LED are shown in Figure 5.10.

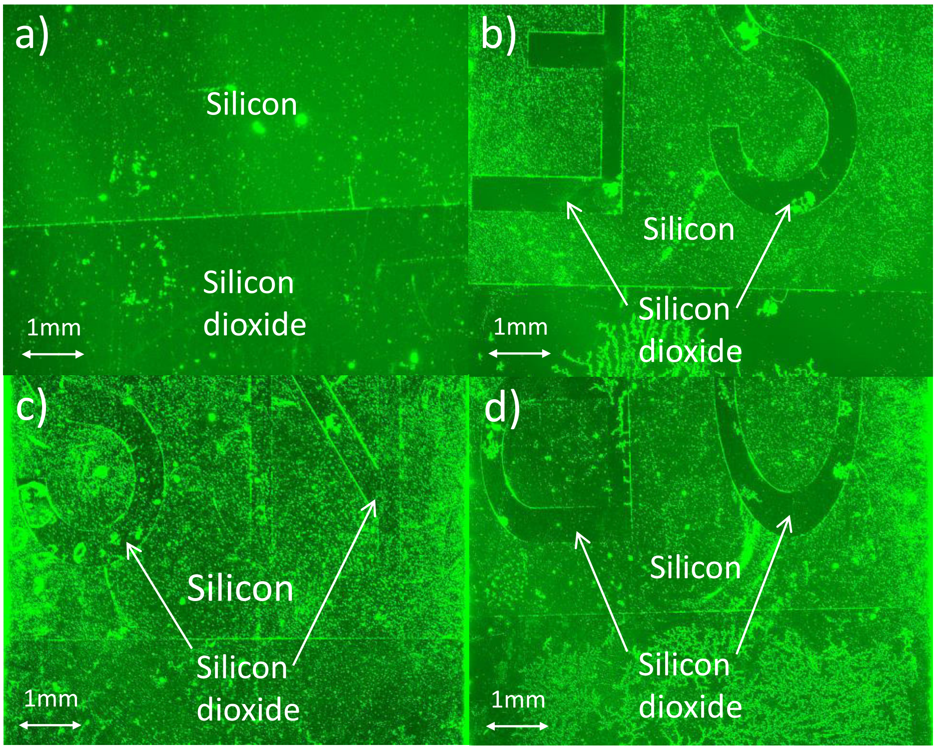

Figure 5.10: Images of silicon and silicon dioxide SOI samples excited by a blue LED and imaged through a camera with the red and blue light cut out: a) control sample with no UV irradiation; b) $5J/cm^2$ of UV light dosage; c) $10J/cm^2$ of UV light dosage and d) $15J/cm^2$ of UV light dosage. (x10 microscopic view).

Figure 5.10a is a control SOI sample with a silicon and silicon dioxide surface where step 2 of amino attachment under UV light was not performed. Figure 5.10b, c and d show silicon and silicon dioxide surfaces of SOI samples which were exposed to 5, 10 and 15J/cm2 of UV light respectively. Figure 5.10b shows FITC attachment on the silicon surface. Figure 5.10c indicates an increase in FITC attachment on the silicon surface, but also some attachment on the silicon dioxide surface. Figure 5.10d shows an increase in FITC attachment on the silicon dioxide surface.

5.3.6 Section summary

In this section, the surface modification of a silicon surface via hyrosilylation and NH_2-terminated monolayer was presented. Initial experiments show that a non-uniform layer of silicon can be modified to attach a FITC tag. Increasing the UV light dosage increased the area of silicon surface modified but after a certain energy dosage the silicon dioxide surface also started to be modified. Further experiments in a more highly controlled environment where the temperature, pressure, flowrate and UV dose can be more precisely controlled, has to be undertaken to perfect this method.

5.4 SURFACE FUNCTIONALISATION BY SILANISATION

The surface functionalisation method described in section 5.3 entails harsh chemicals and UV irradiation which would hinder their application in mass production. A method of surface functionalization is preferred that can be accessible to non-chemists and which avoids any complicated chemical steps or the use of specialist equipment. Functionalisation through OH-terminated silicon surface provides such a method and is described in this section.

5.4.1 Surface passivation of OH-terminated silicon layer

As mentioned in section 5.2 silicon surfaces are typically covered with a native oxide layer of less than 5nm when exposed to air [5.20] and also possess OH bonds on the surface. But the nature of the native oxide is different to that of a wet chemically grown oxide [5.21]. The native oxide is stable and hydrophobic whereas, oxidation achieved through wet chemical treatments would produce an OH-terminated surface with unsaturated surface valencies [5.22].

The oxidation was done by dipping the silicon (100) wafer into a piranha solution comprised of sulfuric acid (H_2SO_4, 98% purchased from Fisher Scientific) and hydrogen peroxide (H_2O_2, 30% purchased from Fisher Scientific) in a 3:1 ratio for 30 seconds [5.22-25]. This treatment also oxidizes any contaminants on the surface.

To increase the OH bonds on the surface a hydroxylation procedure was performed [5.26]. The wafer was placed for 10 minutes in a solution of distilled water, hydrochloric acid (HCl) and hydrogen peroxide (H_2O_2, 30%) in a 6:1:1 ratio at 85˚C.

5.4.2 Amino termination of OH-terminated silicon surface

The most common modification is achieved through salinisation of the native oxide layer [5.8, 23]. Silanisation is the standard procedure of surface functionalisation by a silane (SiH_4) compound that attack hydroxyl groups (OH) and form covalent bonds to the silicon surface. The silane molecule has a functional group (carboxyl-COOH, amino-NH_2 or thiol-SH group) that can react with other desired molecules resulting in an immobilisation of material (antibody in this case) with the silane molecule being the link between the material and Si waveguide [5.12].

The silane molecule used in this project was (3-aminopropyl)triethoxysilane (APTES, ≥98% purchased from Sigma-Aldrich) as shown in Figure 5.11. APTES has an amine (-NH_2) functional group and can be attached to the OH-terminated silicon surface via vapour [5.27, 28] or solution [5.24, 25, 27-29].

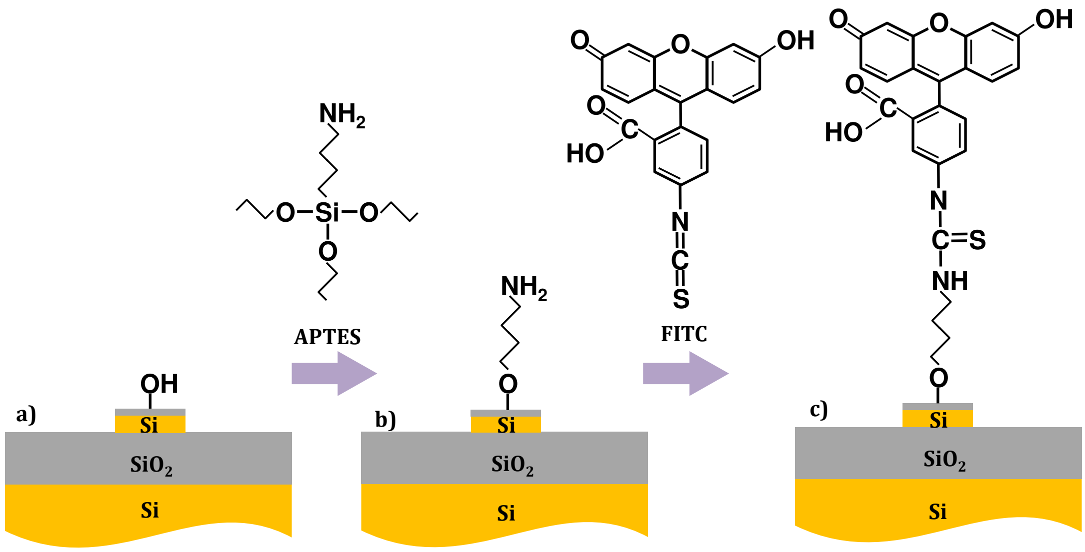

Figure 5.11: Illustration of amino termination of an OH-terminated silicon ridge waveguide followed by the attachment of FITC tag.

Immediately after the oxidation step described in section 5.4.1 the silicon sample was placed in a beaker and the beaker was then placed in a vacuum desiccator with a vial containing 3 drops of (3-aminopropyl)triethoxysilane (APTES). The chamber was heated to 150˚C and pumped down to <1 mbar (0.1 kPa), isolated from the pump and left under vacuum for 4 hours.

The albumin conjugated to fluorescein isothiocyanate (FITC) label (fluorescent tag) is a ready-to-use labelled antibody designed for immunofluorescence. The FITC label was diluted with PBS in a 1:100 ratio and injected to the beaker containing the sample and left for an hour under ambient conditions. The solution was removed and sample was washed with PBS three times again then dried with nitrogen.

5.4.3 Experiment 4

This experiment was done in the School of Life Sciences at The University of Nottingham, UK. The experimental procedure listed below was followed and the effect of each step was studied separately as shown in Table 5.1.

1. Partially etched silicon and silicon dioxide samples were immersed in buffered HF for 45 seconds. This step was done to etch the native oxide layer and leave -H bonds on the surface of the wafer.
2. An oxygen plasma expose was done at room temperature on the samples for 5 minutes. This step was done to leave more -OH bonds on the surface of the chip.
3. Samples were placed in a hydroxilation solution composed of distilled water:HCl:H_2O_2 in the ratio of 6:1:1 for 10 minutes at 85˚C.
4. Samples were placed in a small petri dish containing 0.5ml of APTES which was in turn placed in a vacuum desiccator and a rotary pump was used to create a vacuum of approximately 0.1 atm. Once a vacuum was created the sample was left for 4 hours at room temperature (RT) inside the desiccator.
5. Finally, the samples were immersed in a 1:1000 ratio of FITC to PBS solution for an hour at RT, rinsed with PBS and dried with nitrogen gas.

Table 5.1 shows a summary of the experimental steps performed on partially etched SOI samples shown in Figure 5.12.

Table 5.1: Experimental steps performed in samples shown in Figure 5.12.

Figure	Step 1 (Buffered HF for 45s)	Step 2 (O2 plasma for 5 mins)	Step 3 (hydroxylation for 10 mins at 85C)	Step 4 (APTES for 4 hours in vacuum at RT)	Step 5 (FITC for 1 hours at RT)
Figure 5.12a	×	×	×	×	×
Figure 5.12b	×	×	×	×	√
Figure 5.12c	×	×	×	√	√
Figure 5.12d	√	×	×	√	√
Figure 5.12e	×	×	√	√	√
Figure 5.12f	√	×	√	√	√
Figure 5.12g	√	√	×	√	√

The results were observed in the School of Mechanical, Materials and Manufacturing Engineering at The University of Nottingham, UK. An ECLIPSE LV100ND Microscope system with a DS-Fi2 camera was used to view the samples in this Chapter. The incident light source used was a Blue LED with a peak of 490nm and the reflected light as imaged through a 518nm filter (XF3405/10 purchased from Horiba Jobin). Note that the results in section 5.3 were not captured through a filter and therefore are much brighter in comparison to the results presented in this section.

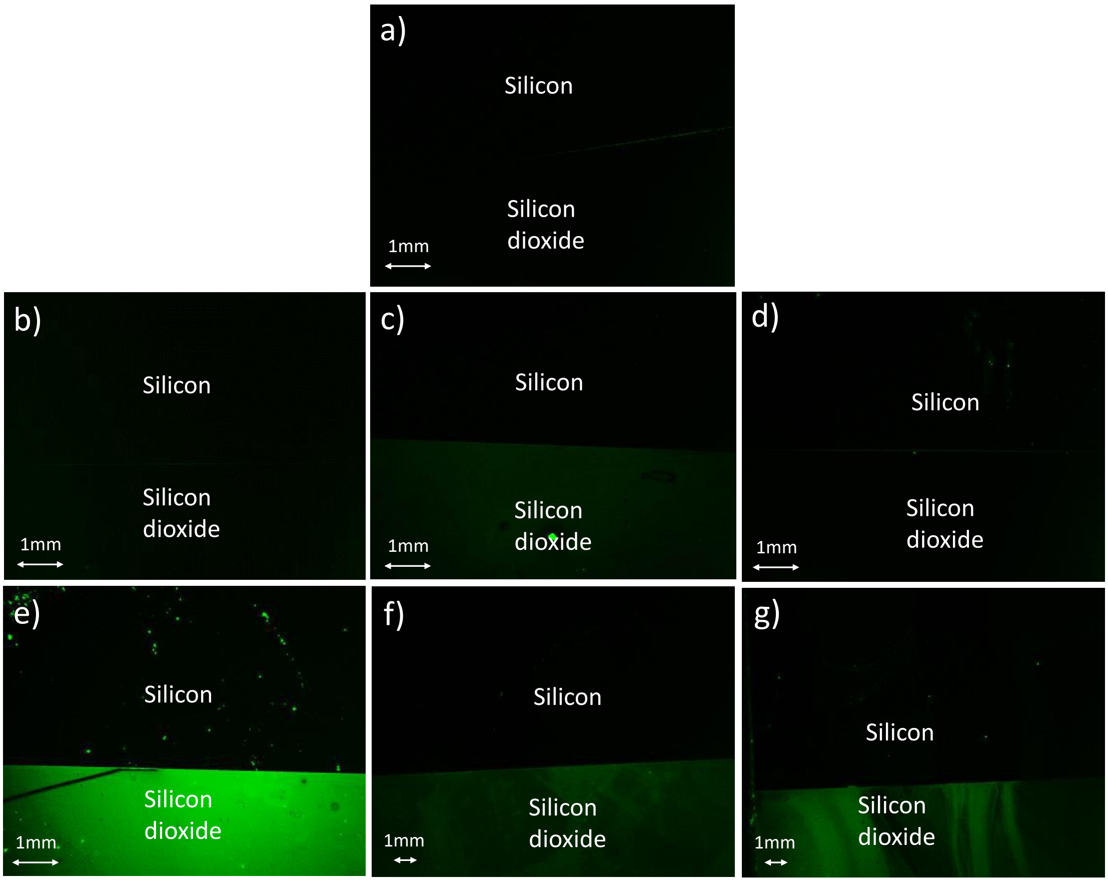

Figure 5.12: Images of silicon and silicon dioxide SOI samples excited by a blue LED and imaged through a 518nm filter: a) control samples; b) step 5 performed; c) steps 4 and 5 performed; d) steps 1, 4 and 5 performed; e) steps 3, 4 and 5 performed; f) steps 1, 3, 4 and 5 performed and g) steps 1, 2, 4, 5 and 6 performed. (x10 and x20 microscopic view).

Figure 5.12a, b, and c are not expected to have any FITC attachment as the surface was not passivated with -OH bonds by the hydroxylation step. But Figure 5.12c shows a faint uniform green colour on the silicon dioxide surface suggesting that the silicon dioxide surface was modified during the etching of the sample which enabled an APTES and FITC to bind to the silicon dioxide surface. The etching process of the wafer was explained in detail in section 4.4.

The SOI sample shown in Figure 5.12d was treated with buffered HF to remove the native oxide and form -H bonds on the silicon; it shows no FITC attachment in the silicon or silicon dioxide surfaces and therefore it can be concluded that APTES does not react with -H bonds.

Figure 5.12e shows the brightest uniform green layer of FITC attachment on the silicon dioxide surface showing that the hydroxylation step did not create -OH bonds on the silicon surface for APTES attachment. The dark scratch on the green silicon dioxide surface is a scratch that occurred when handling the samples with tweezers. This indicates that a layer of FITC was present which was removed by the tweezers.

The SOI samples of Figure 5.12f and g underwent a buffered HF treatment; they also underwent a hydroxylation step and an oxygen plasma step respectively as shown in Table 5.1. The oxygen plasma was expected to create -OH bonds on both the surface of the native oxide and on the oxide layer of the SOI samples just like the hydroxylation step. But Figure 5.12f and g show that the silicon dioxide surfaces are not as bright as the silicon dioxide surface in Figure 5.12e which may be due to the buffered HF step which etches the oxide forming -H bonds on the surface.

It can be concluded from this experiment that an oxygen plasma or hydroxylation process creates -OH bonds on the silicon dioxide layer, and not on the native oxide layer, allowing the binding of APTES followed by the FITC on the silicon dioxide layer. Unlike the experiments presented in section 5.3, experiment 4 showed a uniform layer of FITC attachment. But a requirement of this project is to functionalise the silicon surface or the native oxide on the silicon surface as the light will propagate in silicon waveguides and not silicon dioxide waveguides and therefore this experiment did not meet the requirement.

5.4.4 Experiment 5

This experiment was done at the University of Nottingham, China campus and was intended to replicate the results obtained in experiment 4 and functionalise the native oxide layer present on the silicon surface. 10mm × 10mm piece diced from silicon (100) wafer covered in native oxide were used for this experiment.

The experimental procedure listed below was followed and the effect of each step was studied separately as shown in Table 5.2 and Figure 5.13.

1. Oxidation was done by dipping the SOI wafer into a piranha solution comprised of sulphuric acid (H_2SO_4, 98% purchased from Liyang Guan Yuan Inc.) and hydrogen peroxide (H_2O_2, 30% purchased from Sinopharm Chemical Reagent Co., Ltd) in a 3:1 ratio for 1 minute.
2. To increase the OH bonds on the surface a hydroxylation procedure was performed. The wafer was placed for 10 minutes in a solution of distilled water, hydrochloric acid (HCl, 36-38% purchased from Sinopharm Chemical Reagent Co., Ltd) and hydrogen peroxide in a 6:1:1 ratio at 80˚C.
3. Immediately after the oxidation the SOI was placed in a petri dish and the petri dish was then placed in a vacuum desiccator with a vial containing 3 drops of (3-aminopropyl)triethoxysilane (APTES, ≥98% purchased from Sigma Aldrich). The chamber was pumped down to <1mbar using a rotary pump, isolated from the pump and left under vacuum on a hotplate at 80˚C for 4 hours.
4. FITC (>97.5% purchased from Sigmal Aldrich) was diluted in ethanol (99.7% purchased from Sinopharm Chemical Reagent Co., Ltd) to form a 10mg/ml solution. This was further diluted into a 1:100 ratio of FITC solution to ethanol and injected onto the surface of the SOI and left for one hour at R. T. The sample was then rinsed with ethanol and dried with compressed air.

Table 5.2: Experimental steps performed in samples shown in Figure 5.13.

Sample number	Step 1- Oxidation with Piranha for 1 min	Step 2- Hydroxylation for 10 mins at 80°C	Step 3- APTES 4 hours under vacuum at 80°C	Step 4- FITC:ethanol (1:100) 1 hour at RT
Figure 5.13a	×	×	×	×
Figure 5.13b	×	√	√	√
Figure 5.13c	√	×	√	√
Figure 5.13d	√	√	×	√
Figure 5.13e	√	√	√	×
Figure 5.13f	√	√	√	√

The images in Figure 5.13 were viewed using a fluorescent microscope, N-800F purchased from Novel Optics. The excitation light was at a wavelength between 460-490nm and the reflected light is at a wavelength above 520nm of wavelength.

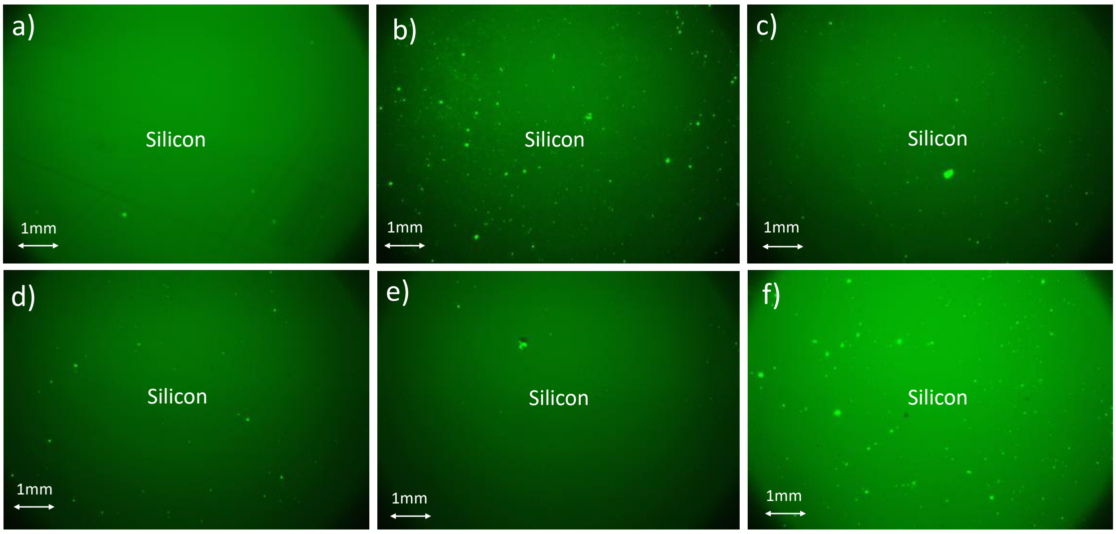

Figure 5.13: Images of silicon with native oxide layer samples excited by a blue LED and imaged through a 518nm filter where: a) unprocessed wafer; b) steps 2, 3 and 4 performed; c) steps 1, 3 and 4 performed; d) steps 1, 2 and 4 performed; e) steps 1, 2 and 3 performed and f) steps 1, 2, 3 and 4 performed. (x10microscopic view).

Figure 5.13b and f show bright green spots on the surface and the fluorescence presented in Figure 5.13f is brighter than the other samples. This indicates that in this sample the hydroxylation step has modified the surface in isolated spots where the APTES followed by FITC was attached.

The additional oxidation step may also have modified the surface uniformly as seen in Figure 5.13f. However, this cannot be confirmed as the difference between the isolated bright spots and the uniform background is distinct.

To confirm the results obtained in experiment 5, the City University of Hong Kong undertook a similar experiment where the vapour deposition of APTES was replaced by dipping the sample in an APTES solution as described as experiment 6 below.

5.4.5 Experiment 6

This experiment was conducted by Dr. Alex Chun-Yuen Wong at the Department of Biology and Chemistry at the City University of Hong Kong as a result of a collaboration. A silicon (100) wafer covered in native oxide was used for this experiment.

1. The samples were dipped in piranha solution for 15 minutes followed by an oxygen plasma for 1 minutes at 30W and 50sccm.
2. The samples were then dipped in APTES SAM (self-assembled monolayer) solution for 12 hours at 90˚C. The APTES solution was comprised of 117µl of APTES in 10ml toluene.
3. Finally, the samples were immersed in a 1:1000 ratio of FITC to PBS solution for two hours at RT, rinsed with PBS and dried with nitrogen gas.

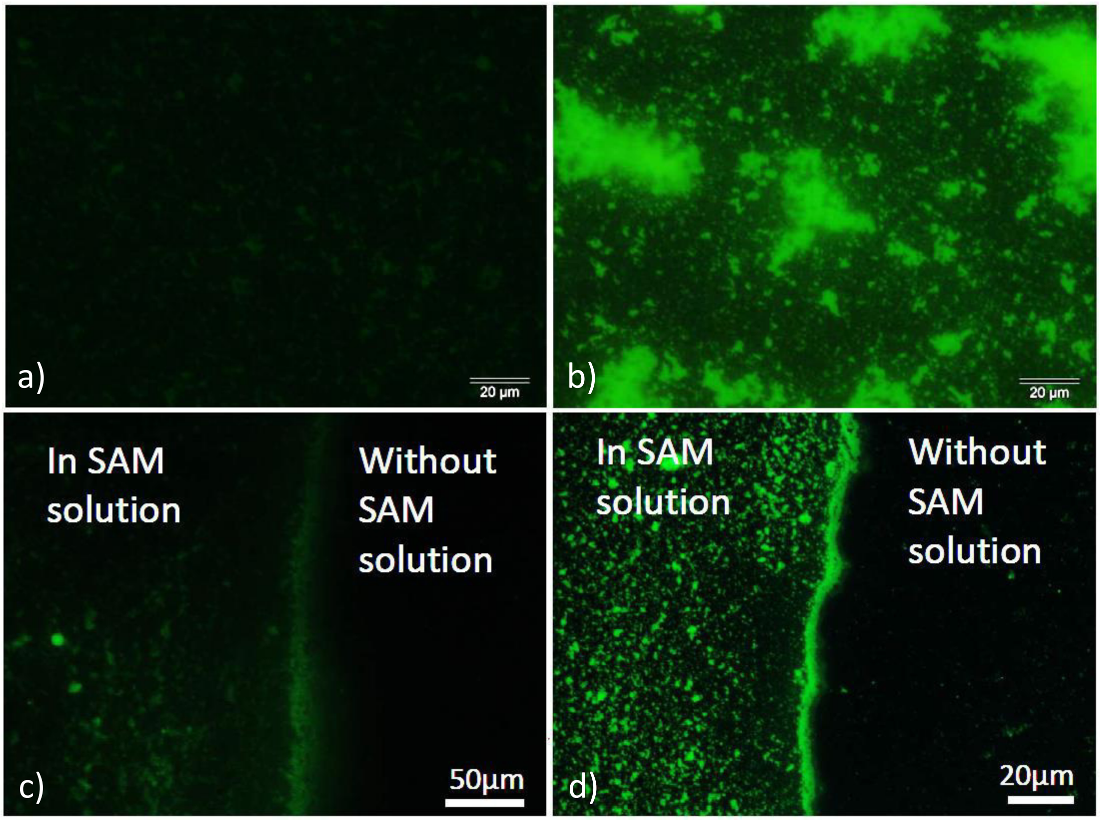

Figure 5.14: Images of silicon with native oxide layer samples excited by a blue LED and imaged through a 518nm filter where the APTES attachment was done at: a) RT b) 90˚C; c) 90˚C and d) 90˚C. (microscopic view).

In Figure 5.14a, step 2 APTES attachment was performed at room temperature and shows no FITC attachment to the surface. Figure 5.14b, c and d are silicon samples with APTES attachment performed at 90˚C, and show that bright green spots corresponding to the presence of FITC are present on the silicon surface. This experiment was similar to the sample in Figure 5.13c where an oxygen plasma was followed by the APTES attachment at 80˚C in a vacuum which did not indicate a FITC attachment. From experiment 6, it can be inferred that the APTES attachment must be done at a higher temperature of 90˚C to obtain an amino-terminated silicon surface.

5.4.6 Section summary

In section 5.4, surface functionalisation by hydroxylation and silanisation was presented. Preliminary experiments show that a non-uniform layer of silicon dioxide can be modified to attach a FITC tag. Increasing the temperature from 80˚C to 90˚C, time from 4 hours to 12 hours, and using APTES solution instead of vapour deposition APTES, allowed the APTES to attach itself to the native oxide layer of the silicon surface. A uniform layer of FITC attachment was not achieved.

5.5 CHAPTER SUMMARY

Two methods of surface functionalisation were presented and experimentally shown with promising results. For the biosensor to work as a heterogenous evanescent wave sensor the antibodies immobilised on the silicon waveguides must react with the target molecule. A uniform surface modification on silicon or the native oxide layer is necessary as the proposed waveguides are narrow and long. Surface functionalisation by hydrosilylation described in section 5.3, entails the use of HF and UV radiation; the inherently dangerous nature of the process is a hindrance to mass production.

Surface functionalisation by hydroxylation and silanisation described in section 5.4, show an affinity to the silicon dioxide surface and not the silicon or the native oxide layer as required. This can be solved by depositing a thick (~1µm) layer of silicon dioxide layer over the whole device but this would reduce the sensitivity of the evanescent wave sensor by 79% as the fraction of the evanescent part of the guided light interacting with the target molecules is reduced.

REFERENCES

[5.1] S. P. Mohanty and E. Kougianos, "Biosensors: a tutorial review," *Potentials, IEEE,* vol. 25, pp. 35-40, 2006.

[5.2] C. Morgan, D. Newman, and C. Price, "Immunosensors: technology and opportunities in laboratory medicine," *Clinical Chemistry,* vol. 42, pp. 193-209, 1996.

[5.3] M. A. Cooper, "Label-free screening of bio-molecular interactions," *Anal. Bioanal Chem,* vol. 377, pp. 834-842, Nov 2003.

[5.4] M.-J. Bañuls, R. Puchades, and Á. Maquieira, "Chemical surface modifications for the development of silicon-based label-free integrated optical (IO) biosensors: A review," *Anal. Chimica Acta,* vol. 777, pp. 1-16, 2013.

[5.5] W. E. Moerner, "New directions in single-molecule imaging and analysis," *Proceedings of the National Academy of Sciences,* vol. 104, pp. 12596-12602, July 31, 2007 2007.

[5.6] X. Fan, I. M. White, S. I. Shopova, H. Zhu, J. D. Suter, and Y. Sun, "Sensitive optical biosensors for unlabeled targets: a review," *Anal. Chim Acta,* vol. 620, pp. 8-26, Jul 14 2008.

[5.7] B. T. Cunningham, *Label-free optical biosensors: An Introduction*. New York: Cambridge University Press, 2009.

[5.8] J. Escorihuela, M. J. Bañuls, J. G. Castelló, V. Toccafondo, J. García-Rupérez, R. Puchades, and Á. Maquieira, "Chemical silicon surface modification and bioreceptor attachment to develop competitive integrated photonic biosensors," *Anal Bioanal Chem,* vol. 404, pp. 2831-2840, 2012.

[5.9] Z. Cui and C. G. Takoudis, "Initial Oxidation of H-Terminated Si (100) in O 3 (950 ppm)/O 2 and Pure O 2," *Journal of The Electrochemical Society,* vol. 150, pp. G694-G701, 2003.

[5.10] T. A. Miura, M. Niwano, D. Shoji, and N. Miyamoto, "Kinetics of oxidation on hydrogen - terminated Si (100) and (111) surfaces stored in air," *Journal of Applied Physics,* vol. 79, pp. 4373-4380, 1996.

[5.11] S. Ciampi, J. B. Harper, and J. J. Gooding, "Wet chemical routes to the assembly of organic monolayers on silicon surfaces via the formation of Si–C bonds: Surface preparation, passivation and functionalization," *Chemical Society Reviews,* vol. 39, pp. 2158-2183, 2010.

[5.12] T. Baumgärtel, C. von Borczyskowski, and H. Graaf, "Selective surface modification of lithographic silicon oxide nanostructures by organofunctional silanes," *Beilstein Journal of Nanotechnology,* vol. 4, pp. 218-226, 2013.

[5.13] J. M. Buriak, "Organometallic chemistry on silicon surfaces: formation of functional monolayers bound through Si–C bonds," *Chemical Communications,* vol. 12, pp. 1051-1060, 1999.

[5.14] Z. Lin, T. Strother, W. Cai, X. Cao, L. M. Smith, and R. J. Hamers, "DNA attachment and hybridization at the silicon (100) surface," *Langmuir,* vol. 18, pp. 788-796, 2002.

[5.15] A. B. Sieval, R. Linke, G. Heij, G. Meijer, H. Zuilhof, and E. J. Sudhölter, "Amino-terminated organic monolayers on hydrogen-terminated silicon surfaces," *Langmuir,* vol. 17, pp. 7554-7559, 2001.

[5.16] R. Coustel, Q. Benoît à la Guillaume, V. Calvo, O. Renault, L. Dubois, F. Duclairoir, and N. Pauc, "Measurement of the surface recombination velocity in organically functionalized silicon nanostructures: The case of silicon on insulator," *The Journal of Physical Chemistry C,* vol. 115, pp. 22265-22270, 2011.

[5.17] D. D. Wayner and R. A. Wolkow, "Organic modification of hydrogen terminated silicon surfaces 1," *Journal of the Chemical Society, Perkin Transactions 2,* pp. 23-34, 2002.

[5.18] W. Cai, J. R. Peck, D. W. van der Weide, and R. J. Hamers, "Direct electrical detection of hybridization at DNA-modified silicon surfaces," *Biosensors and Bioelectronics,* vol. 19, pp. 1013-1019, 2004.

[5.19] T. Strother, R. J. Hamers, and L. M. Smith, "Covalent attachment of oligodeoxyribonucleotides to amine-modified Si (001) surfaces," *Nucleic Acids Research,* vol. 28, pp. 3535-3541, 2000.

[5.20] S. Gilles and F. Jülich, *Chemical modification of silicon surfaces for the application in soft lithography*. Jülich: Forschungszentrum Jülich GmbH, Zentralbibliothek, 2007.

[5.21] H. F. Okorn-Schmidt, "Characterization of silicon surface preparation processes for advanced gate dielectrics," *IBM Journal of Research and Development,* vol. 43, pp. 351-326, 1999.

[5.22] S. Guhathakurta and A. Subramanian, "Effect of hydrofluoric acid in oxidizing acid mixtures on the hydroxylation of silicon surface," *Journal of The Electrochemical Society,* vol. 154, pp. P136-P146, 2007.

[5.23] E. Pavlovic, A. P. Quist, U. Gelius, and S. Oscarsson, "Surface functionalization of silicon oxide at room temperature and atmospheric pressure," *Journal of Colloid and Interface Science,* vol. 254, pp. 200-203, 2002.

[5.24] Y. Guo, J. Y. Ye, C. Divin, B. Huang, T. P. Thomas, J. Baker, James R, and T. B. Norris, "Real-time biomolecular binding detection using a sensitive photonic crystal biosensor," *Analytical Chemistry,* vol. 82, pp. 5211-5218, 2010.

[5.25] N. Aissaoui, L. Bergaoui, J. Landoulsi, J.-F. Lambert, and S. Boujday, "Silane layers on silicon surfaces: mechanism of interaction, stability, and influence on protein adsorption," *Langmuir,* vol. 28, pp. 656-665, 2011.

[5.26] A. K. Mahapatro, A. Scott, A. Manning, and D. B. Janes, "Gold surface with sub-nm roughness realized by evaporation on a molecular adhesion monolayer," *Applied Physics Letters,* vol. 88, p. 151917, 2006.

[5.27] Y. Han, A. Offenhäusser, and S. Ingebrandt, "Detection of DNA hybridization by a field‐effect transistor with covalently attached catcher molecules," *Surface and Interface Analysis,* vol. 38, pp. 176-181, 2006.

[5.28] A. R. Yadav, R. Sriram, J. A. Carter, and B. L. Miller, "Comparative study of solution–phase and vapor–phase deposition of aminosilanes on silicon dioxide surfaces," *Materials Science and Engineering: C,* vol. 35, pp. 283-290, 2014.

[5.29] M. S. Luchansky, A. L. Washburn, T. A. Martin, M. Iqbal, L. C. Gunn, and R. C. Bailey, "Characterization of the evanescent field profile and bound mass sensitivity of a label-free silicon photonic microring resonator biosensing platform," *Biosensors and Bioelectronics,* vol. 26, pp. 1283-1291, 2010.

Chapter 6

6 PHYSICAL AND OPTICAL CHARACTERISATION

Chapters 3 and 4 discussed the design and fabrication respectively of four sets of biosensor devices as listed in Table 3.16. This chapter presents the fabricated devices and some preliminary optical results.

6.1 SET 1-BIOSENSORS DEVICES FABRICATED AT THE UNIVERSITY OF NOTTINGHAM

The first set of devices was fabricated in the nanofabrication facility of the School of Physics and Astronomy at The University of Nottingham, UK, using a 0.32µm silicon-on-insulator (SOI) wafer and a waveguide width fixed at 4µm. Appendix E shows the mask layout and lists the devices fabricated. Figure 6.1-Figure 6.3 show some of the fabricated devices as seen under an optical microscope.

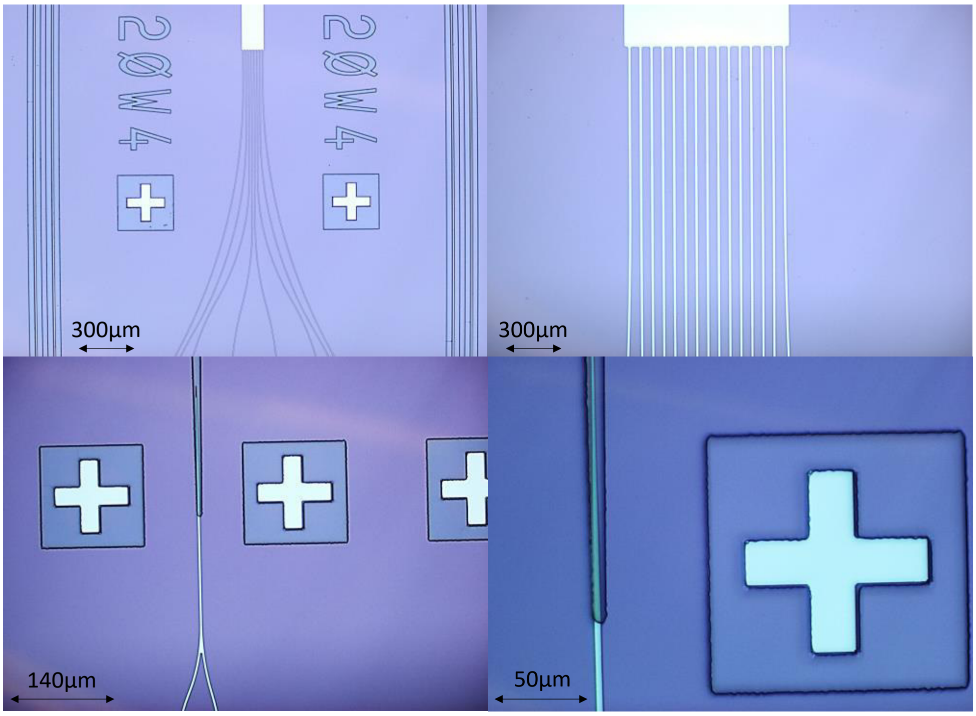

Figure 6.1: a) 1x8 MMI coupler and S-bends, b) 1x15 MMI coupler, c) MZI and SU-8 taper and d) an output waveguide with an SU-8 taper; device set 1 as seen under an optical microscope.

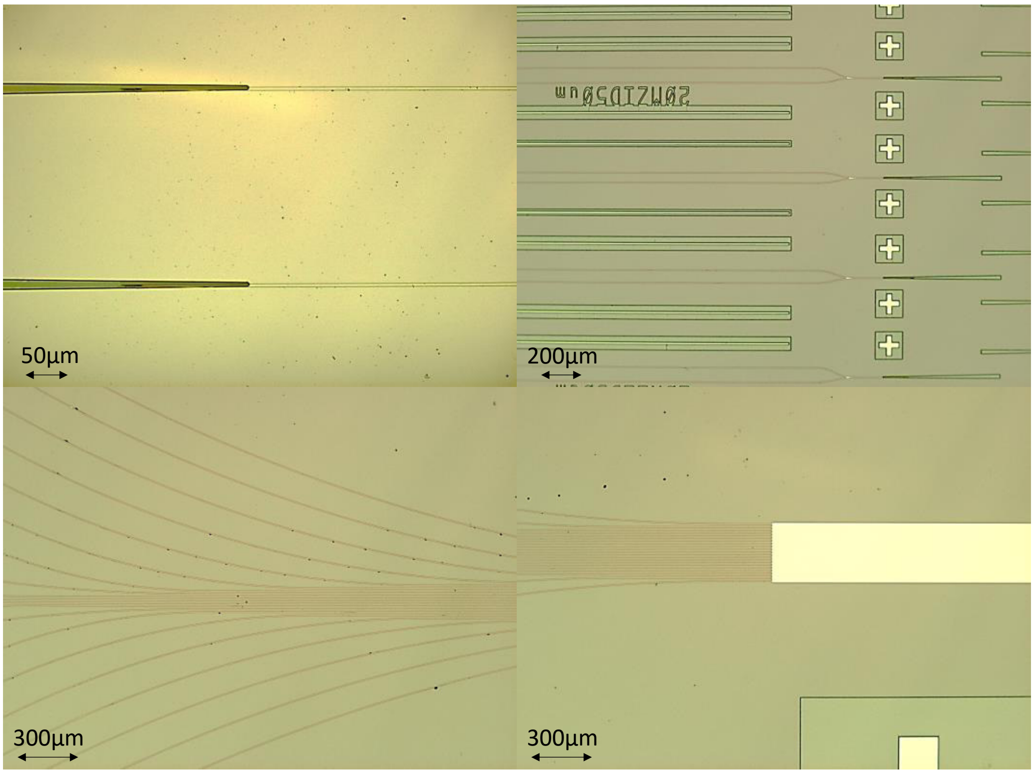

Figure 6.2: a) Output waveguides with SU-8 tapers, b) MZI with SU-8 tapers, c) S-bends and d) 1x30 MMI coupler; device set 1 as seen under an optical microscope.

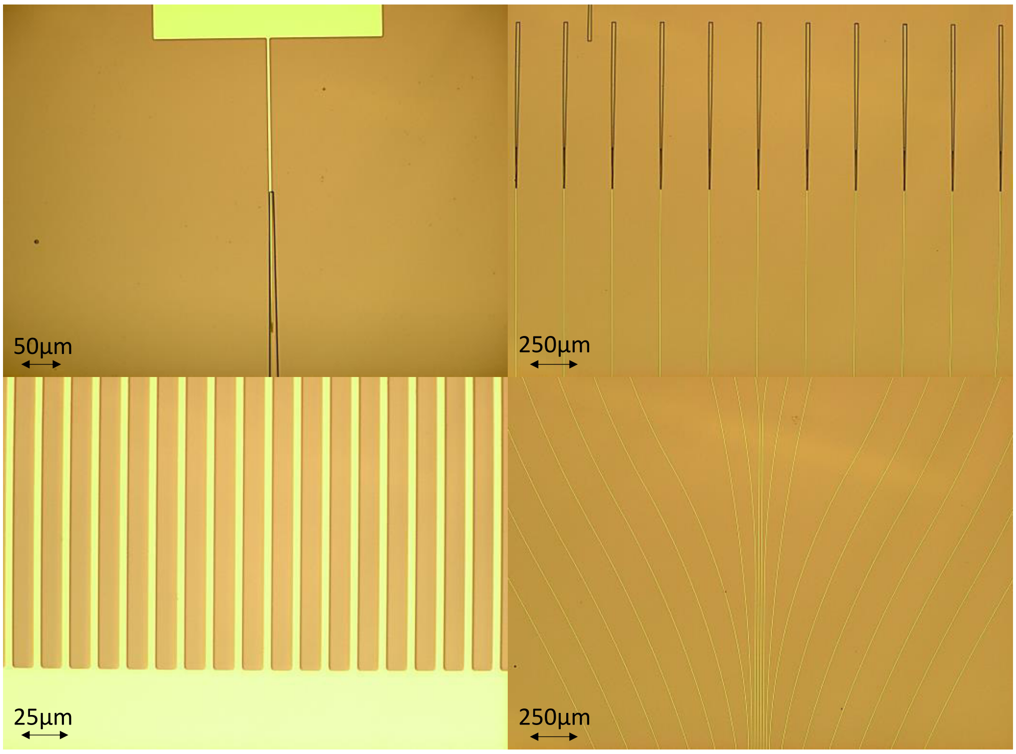

Figure 6.3: a) Input waveguide and SU-8 taper of an MMI coupler, b) Output waveguides and SU-8 tapers of an MM coupler with S-bends, c) Output waveguides of a 1x20 MMI coupler and d) S-bends; device set 1 as seen under an optical microscope.

6.1.1 Experimental set-up

The devices shown in Figure 6.1-Figure 6.3 were tested in the optical laboratory of the School of Mechanical, Material and Manufacturing Engineering at The University of Nottingham, UK.

An optical bench set up was used as shown in Figure 6.4 to evaluate these devices. A tunable laser (Agilent 8164B Lightwave measurement system from 1465µm-1575µm) and a red diode with a wavelength of 651nm were connected to a tapered fibre (OZ optics TSMJ-S3-1550-9/125-0.25-7-2-12-2-AR) with a spot diameter of 2.5µm which was used to couple light into the input SU-8 tapered waveguide of the MMI. A 3-paddle polarization controller and linear polariser was used to polarise the light to launch TM (transverse magnetic)-like modes. A wavelength division multiplexer (Thorlabs WD202A-FC for combing or splitting two signals at 980 and 1550nm) was used to combine the light from the red diode and the tunable laser. Even though the channel for the red light in the wavelength division multiplexer is designed for a 980nm wavelength, some red light is still transmitted through the wavelength division multiplexer. The red laser was used to help align the fibre to the input waveguide.

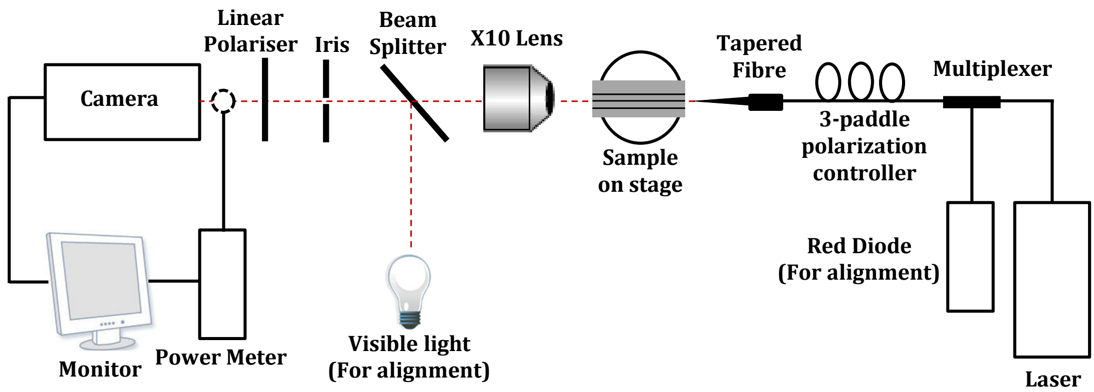

Figure 6.4: Schematic representation of the optical bench set-up.

At the output of the waveguide an object lens focused the light to an infrared camera whose output was displayed on the screen. An iris was used to isolate each output waveguide image on the camera. A power meter (Thorlabs PM100USB Power and energy meter connected to Thorlabs S122C photodiode sensor of 700-1800nm wavelength) was used to measure the light intensity of the light in front of the camera (LINK ELECTRONICS infrared camera).

Figure 6.5 shows the optical bench set-up used at the optical laboratory of the School of Mechanical, Material and Manufacturing Engineering at the University of Nottingham, UK and Figure 6.6 shows the alignment of the tapered fibre, as seen by the red line, to the SU-8 taper input of an MMI coupler as seen through a microscope.

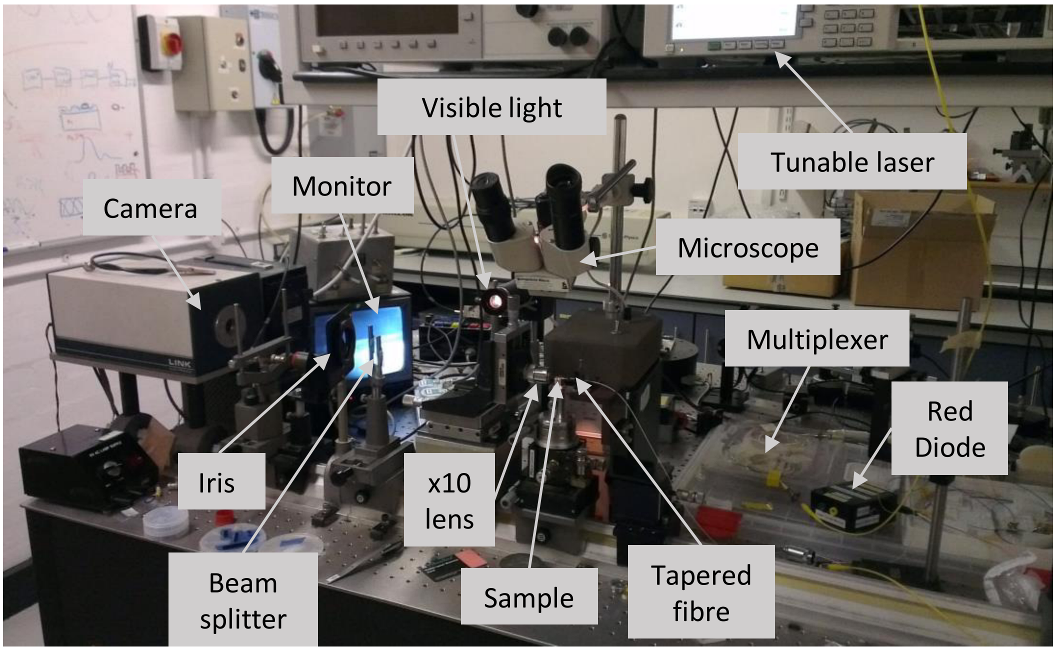

Figure 6.5: Image of the optical bench set-up used at the optical laboratory of the School of Mechanical, Material and Manufacturing Engineering at the University of Nottingham, UK.

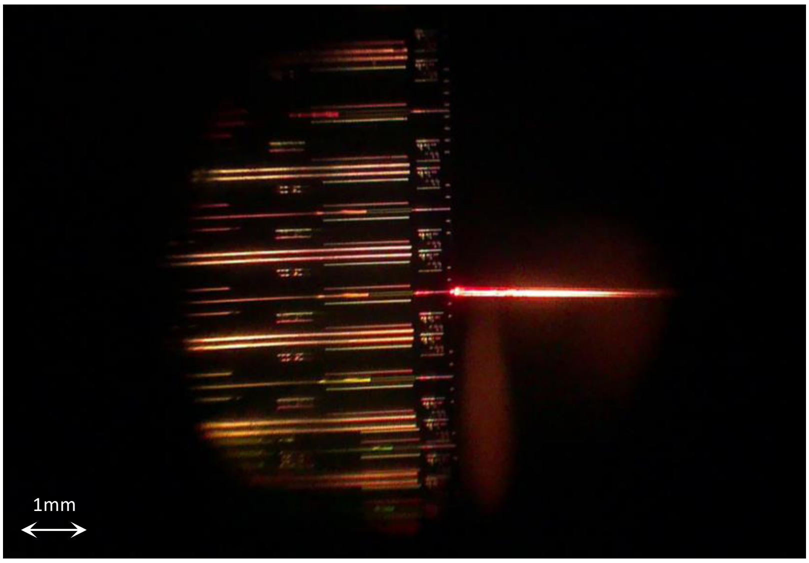

Figure 6.6: Alignment of the tapered fibre to the SU-8 taper input of an MMI coupler as seen through a microscope (x10 microscopic view).

6.1.2 Results

Figure 6.7 shows some images taken of the output light as seen on the monitor with TM polarised input light at an operating wavelength of 1.55µm. Figure 6.7a shows the output of a Mach-Zehnder interferometer (MZI) showing a multimoded output light. This multimode behaviour is as expected since the width of the silicon waveguides was 4µm. Figure 6.7b shows two outputs of a 1x8 MMI coupler spaced 250µm apart. Figure 6.7c andFigure 6.7d show the output waveguides of a 1x15 MMI coupler spaced 15µm apart and a 1x20 MMI coupler spaced 10µm apart. In Figure 6.7c and Figure 6.7d an SU-8 taper was not used to couple the light out of each waveguide.

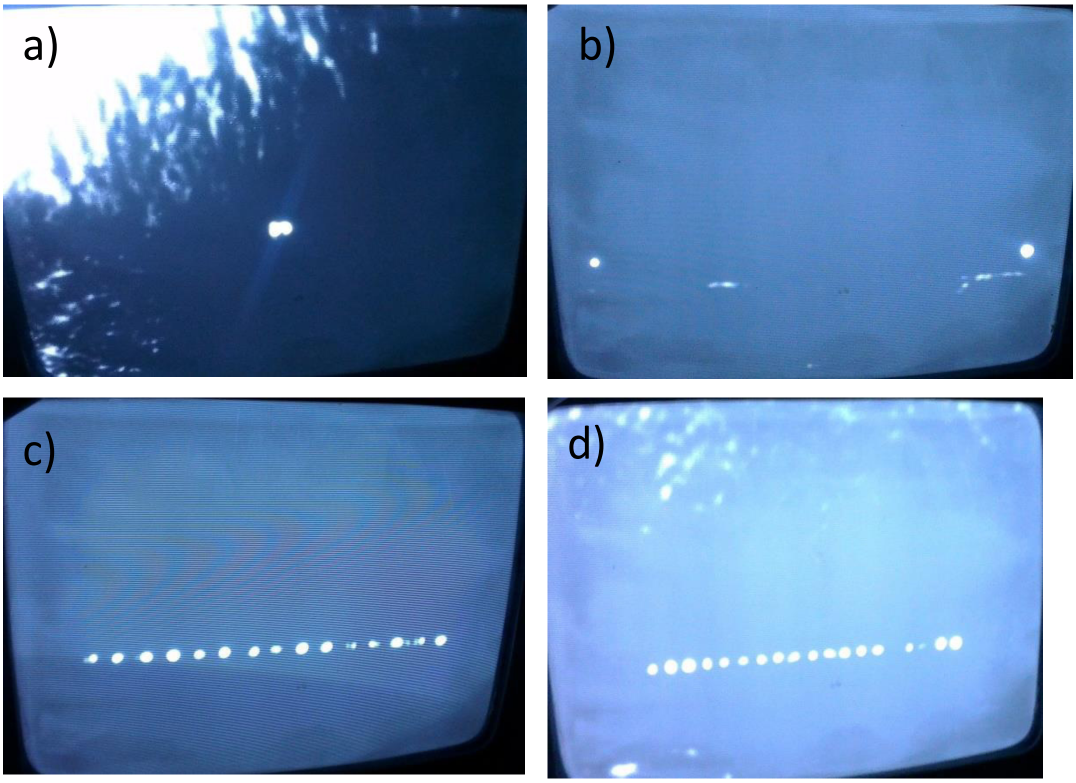

Figure 6.7: Output light as seen on the screen for: a) MZI showing multimoded output; b) two output waveguides of a 1x8 MMI coupler spaced 250µm apart; c) output waveguides of a 1x15 MMI coupler spaced 15µm apart and d) output waveguides of a 1x20 MMI coupler spaced 10µm apart.

Power intensity and loss measurements were not undertaken for the devices in set 1 as the output is multimoded and therefore the devices will not function as intended as was explained in section 3.2.1. However, the results presented show successful realisation of waveguides and power splitters.

6.2 Set 2-Plasmonic interferometers fabricated at The University of Nottingham

The devices in set 2 are all plasmonic interferometers (PI) of various lengths ranging from 4-25µm. According to simulations an optimized PI was designed in section 3.3.2 for an SOI waveguide height and width of 0.32µm and 4µm respectively and a gold height and width of 0.23µm and 13µm respectively to obtain maximum sensitivity.

To realise the PI, the waveguide must be etched by 230nm and a 5nm layer of titanium and 225nm of gold must be embedded as described in section 4.3.4. But controlling the etch depth to that accuracy is extremely difficult. In set 2 the devices had an actual etch depth of 212nm. In the same way, accurately controlling the titanium and gold deposition is also demanding. In the device fabricated, a combined thickness of 245nm of titanium and gold was deposited.

Although the optimum length of the gold layer was found to be 13µm, the closest PI device length fabricated was 12µm as shown in Figure 6.8. See Appendix F for the complete mask layout.

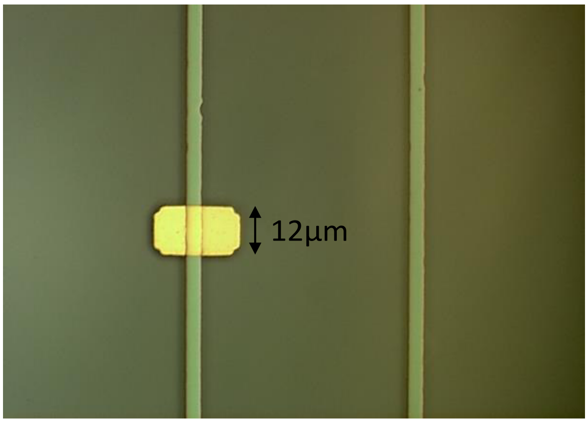

Figure 6.8: PI device fabricated with an SOI waveguide of height and width of 0.32µm and 4µm respectively and a titanium and gold combined height and width of 0.212µm and 12µm respectively. (View from optical microscope).

6.2.1 Results

Figure 6.9 shows the simulated result of the PI shown in Figure 6.8 when exposed to air and water and Figure 6.10 shows the experimental result of the PI when exposed to air. Experimental results for when PI is exposed to water could not be obtained as the sample was less than 3mm wide and placing a drop of water on such a small area without the fabrication of proper a microfluidic channel proved too challenging as the water would get to the input/output facets and also the sample could move causing the alignment of the sample to the tapered fibre to change.

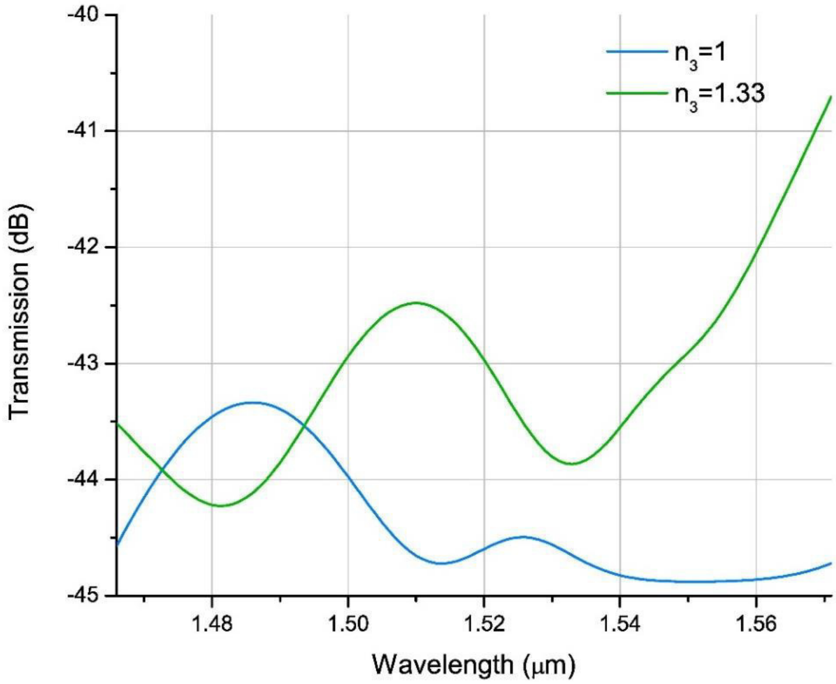

Figure 6.9: Simulated results for fabricated plasmonic interferometer when exposed to air and water.

The simulated result in Figure 6.9 for the fabricated device in Figure 6.8 does not have sharp resonant dips as seen on the simulation result for the optimised structure as shown in section 3.3.2, which has a predicted wavelength shift responsivity of 500nm/RIU. Nevertheless, slight dips in the spectrum, and a predicted wavelength shift responsivity of 97nm/RIU can be seen in Figure 6.9 suggesting that the device functions as intended.

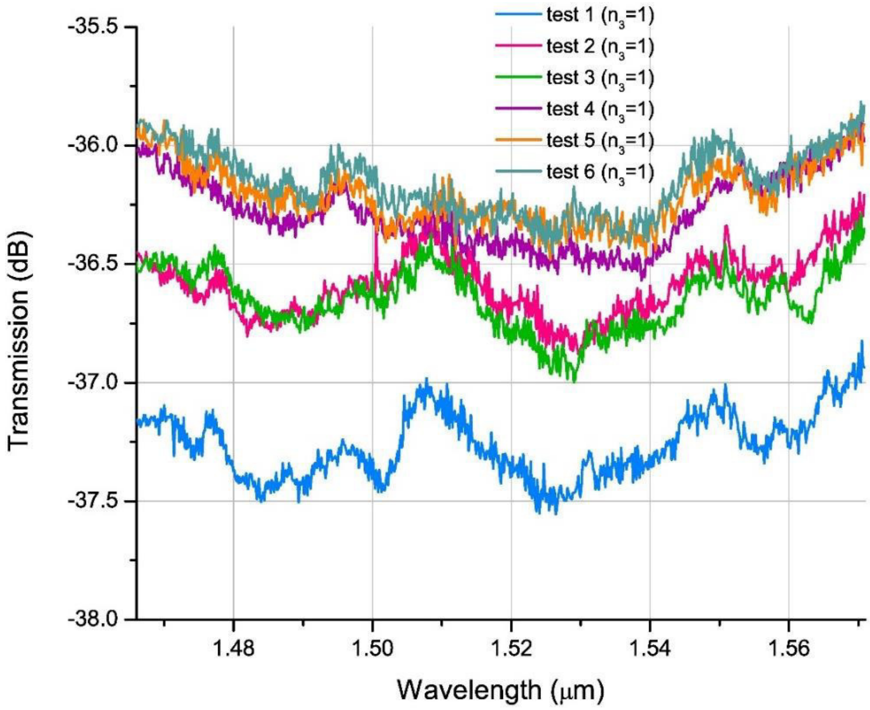

Figure 6.10: Experimental results for fabricated plasmonic interferometer when exposed to air.

In Figure 6.10 the experiment was repeated six times. Tests 1-3 and tests 4-6 were conducted on two different days. Since the graphs from test 1-3 are similar to each other and graphs from tests 4-6 are similar to each other it can be concluded that test 1-3 and 4-6 gives slightly different curves due to different alignments of the device with the tapered fibre or the photodiode and hence different insertion loss.

The general trend of the curves remained the same proving the PI concept. The experimental wavelength shift responsivity was not determined as the cover index was not changed.

6.3 SET 3-BIOSENSOR DEVICES FABRICATED AT THE UNIVERSITY OF SOUTHAMPTON

The third set of biosensor devices (referred to as set 3) were fabricated on a 0.25µm silicon core SOI wafer with 0.8µm wide silicon waveguides. The e-beam writing for these devices was done at the University of Southampton, UK as described in section 4.3.2 and the rest of the fabrication was done in the School of Physics and Astronomy of The University of Nottingham, UK. Figure 6.11 shows some environmental scanning electron microscope (ESEM) images of some of the fabricated devices. See Appendix G for the Mask layout of Set 3. Note that a physical mask was not necessary as the layout was fed to the e-beam software.

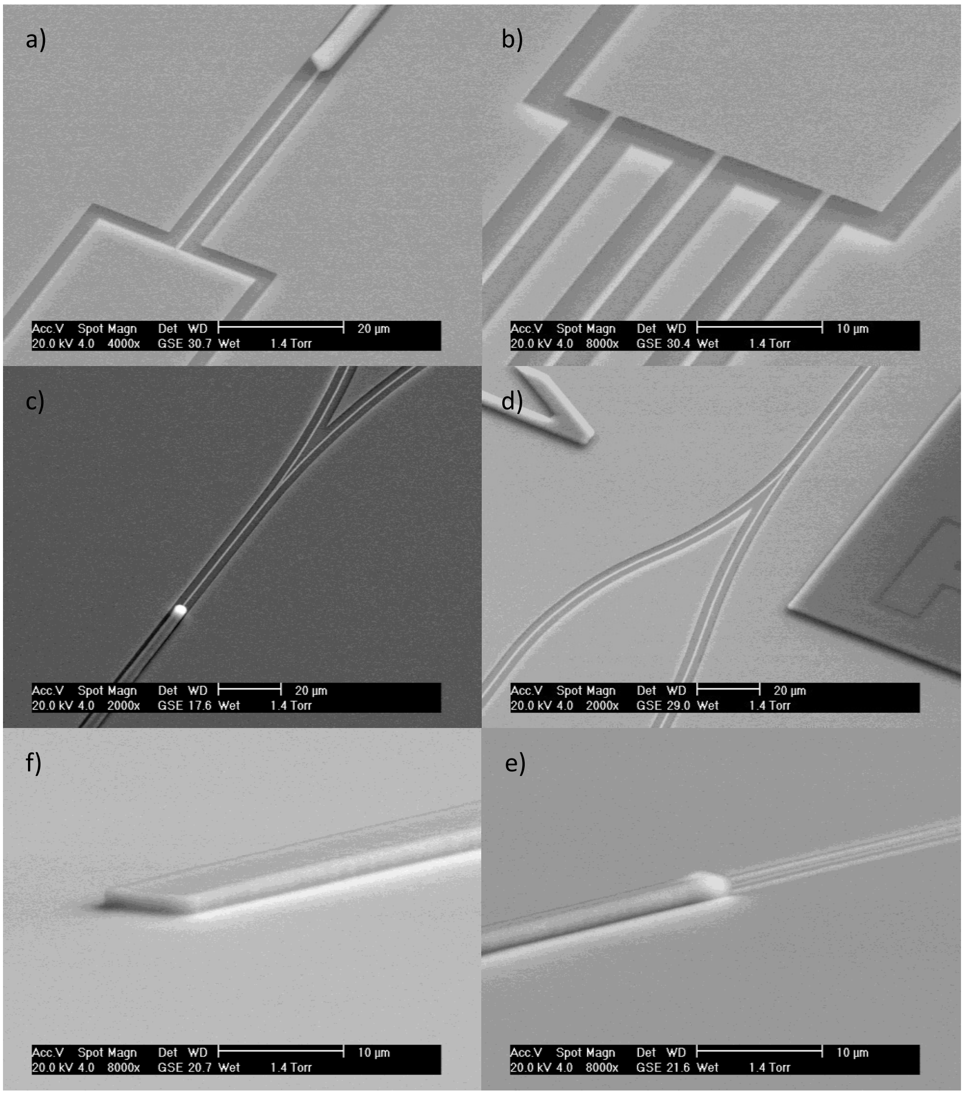

Figure 6.11: ESEM images of: a) Input SU-8taper and waveguide of a MMI coupler; b) output waveguides of a 1x3 MMI coupler; c) output waveguide and SU-8 of MZI; d) MZI with one arm longer than the other; d) 2µm thick SU-8 taper and e) SU-8 taper on a waveguide.

In Figure 6.11a-d a clear 2.5µm trench etched around the device into the oxide layer can be seen; this is as explained in section 4.3.2.

A microfluidic layer was then fabricated from a 50µm thick SU-8 layer as described in section 4.8.2. See Appendix G for complete mask layouts and their description and Appendix I for an image of the mask. Figure 6.12 shows the SU-8 microfluidics channels on some of the devices of set 3.

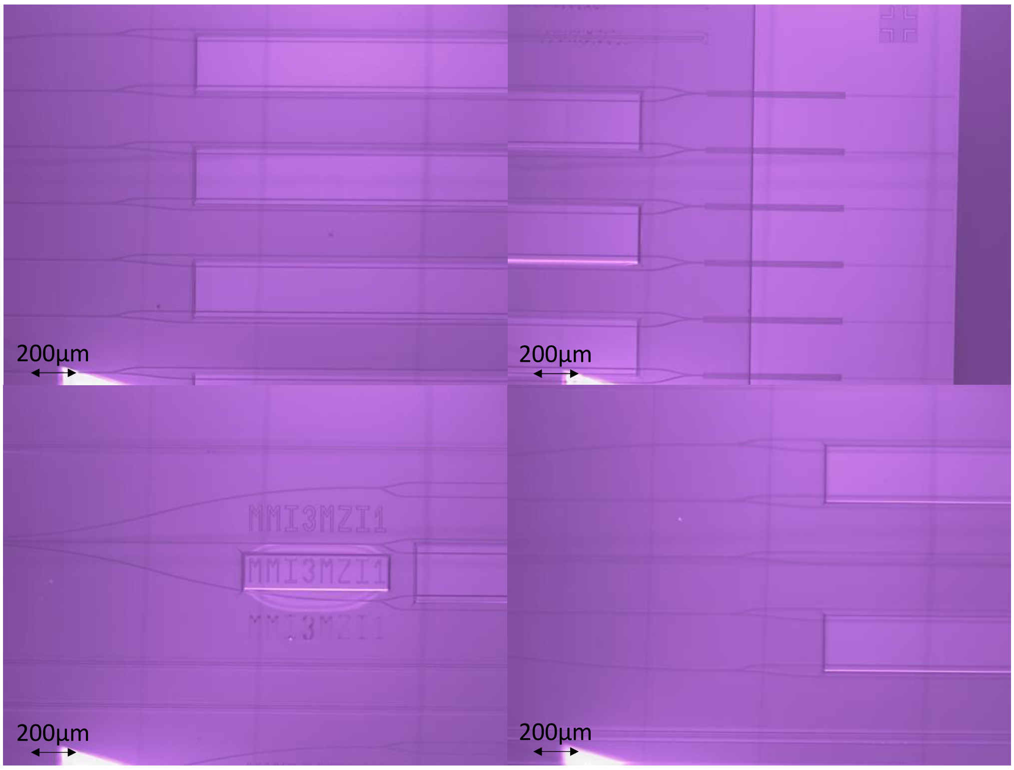

Figure 6.12: Microfluidics channels of set 3 (x4 view from microscope).

6.3.1 Experimental set-up

Devices in set 3 were tested in the optical laboratory of the School of Electrical and Electronic Engineering of the University of Nottingham, China campus. The experimental set-up is the same as the experimental set-up illustrated schematically in Figure 6.4. Figure 6.13 shows an image of the actual optical bench set-up used.

The Infra-red camera (Xeva-1.7-640 purchased from Xenics Infrared Solutions, red diode (650nm100mW purchased from FU LASER) and optical power meter (N77454 purchased from Agilent Technologies) used were different from the ones used in the Nottingham UK campus.

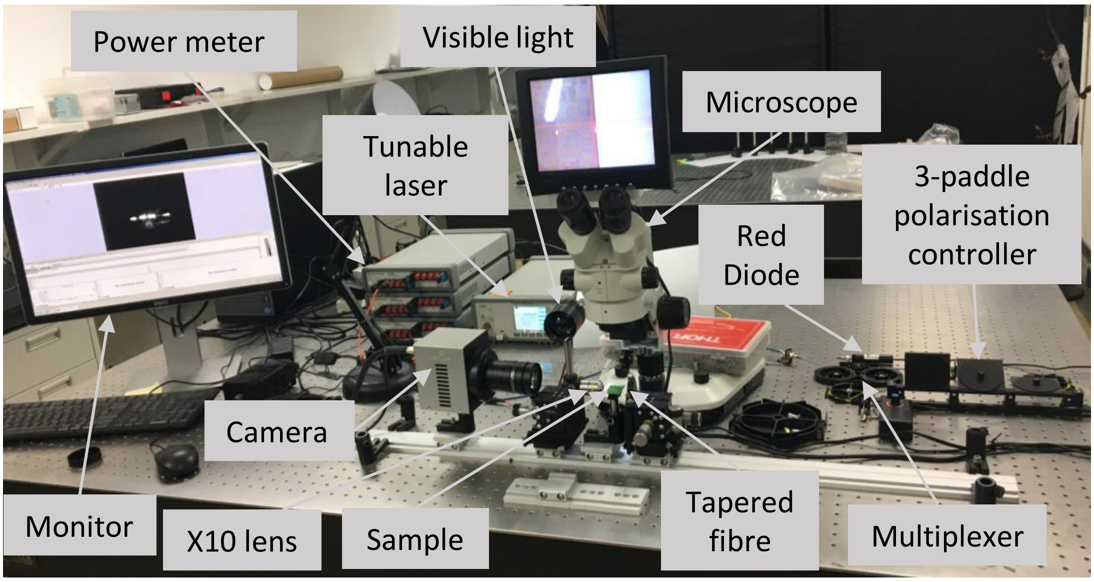

Figure 6.13: Image of the optical bench set-up used at the optical laboratory of the school of Electrical and Electronic Engineering at the University of Nottingham, China.

6.3.2 Results

The devices tested in section 6.1.2 were tested in the optical bench set up shown in Figure 6.13 to test if the optical set-up functions as intended. Figure 6.14 shows a 1x8 MMI splitter with output waveguide spaced 250μm apart. In Figure 6.14 the tunable laser was set to a) 4mW and b) 10mW, the camera gain was set to the lowest setting and the waveguide output was imaged through a x10 lens. While the outputs of the waveguides are clearly visible the camera gain was too large and caused the images to saturate.

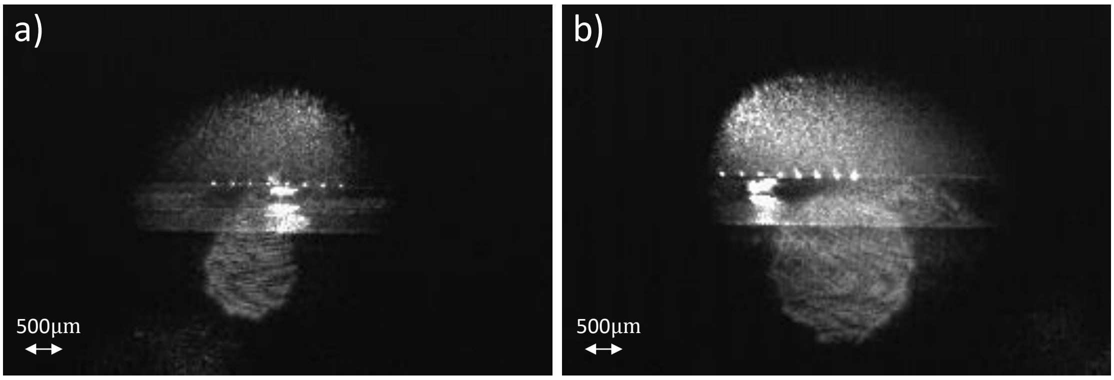

Figure 6.14: Output light as seen on the screen for a 1x8 MMI splitter with input light of: a) 4mW and b) 10mW and output waveguides spaced 250µm apart imaged through a x10 lens.

The lowest power setting on the 81960A tunable laser at a wavelength of 1.55µm was 4mW. So even with the lowest input power and lowest gain on the camera the image showed light in the background and the output power was saturated making it impossible to get accurate readings of loss and any change in the power caused by change in cover index.

The third set of devices with the microfluidics layer was not optically tested as the images obtained by the camera were currently saturated.

6.4 Set 4-Biosensor devices fabricated at Zhejiang University, City University of Hong Kong and The University of Glasgow

The fourth set (set 4) of devices consisted of input/output grating couplers, directional couplers and MZIs with spirals. See Appendix H for the mask layout of set 4. These biosensor devices were designed by Zhejiang University and one set was fabricated and tested at Zhejiang University, China. A second set was fabricated at the City University of Hong Kong, as shown in Figure 6.15-Figure 6.16, while a third set was fabricated at The University of Glasgow, UK, as shown in Figure 6.17-Figure 6.18. The second and third sets of devices were tested at the University of Nottingham, China.

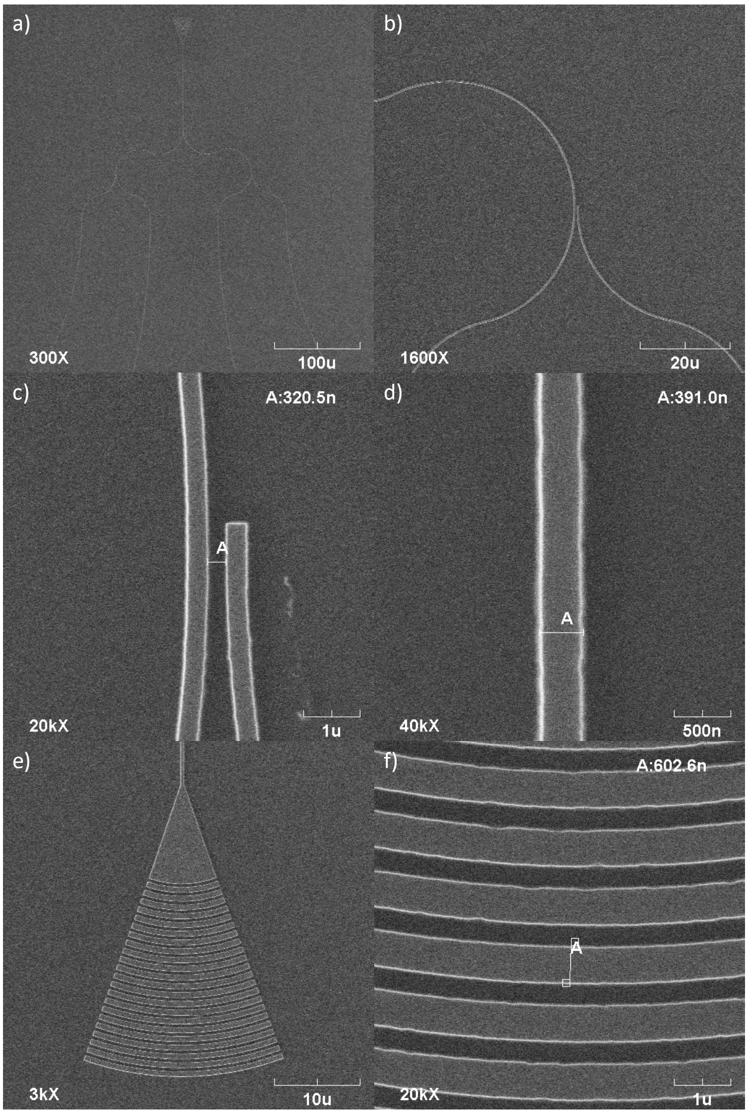

Figure 6.15: SEM images of the biosensor devices fabricated and imaged at the City University of Hong Kong: a) Input grating coupler and cascaded DCs forming a 1x4 splitter; b) DC; c) DC; d) waveguide; e) grating coupler and g) grating coupler.

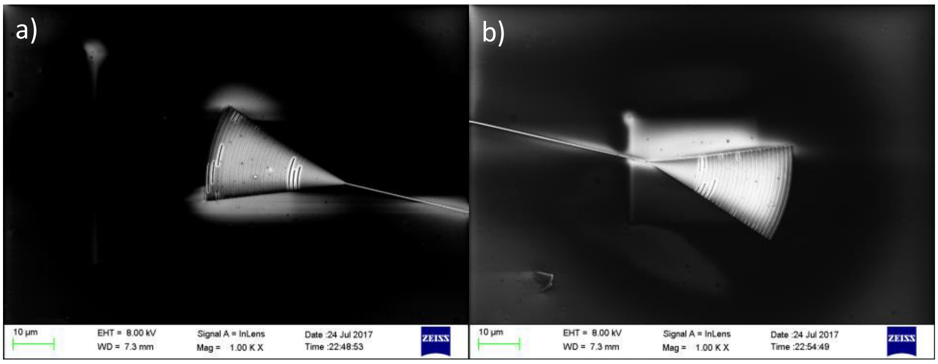

Figure 6.16: SEM images of the biosensor fabricated at the City University of Hong Kong and imaged at The University of Nottingham, China: a) and b) grating couplers.

The SEM images in Figure 6.15 were provided by the City University of Hong Kong and the biosensing devices appears to be intact. Figure 6.16 shows SEM images of the grating couplers of same wafer, but imaged at the University of Nottingham, China. The grating couplers appear to have been over-etched and this might explain why it proved difficult to evaluate them optically as will be described in the next section.

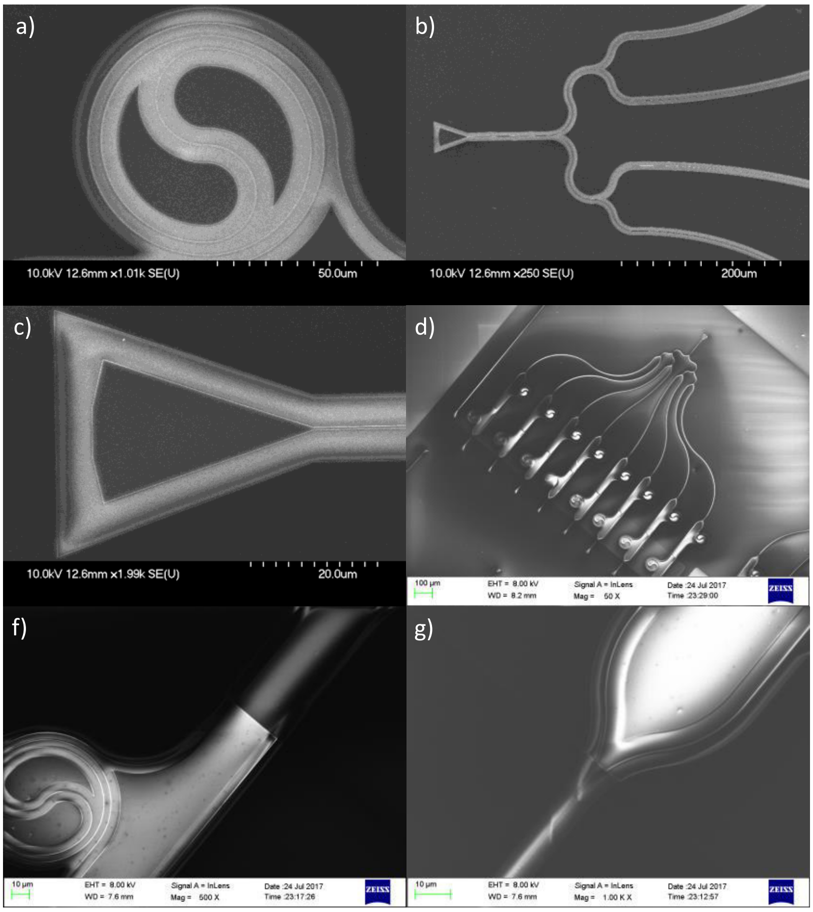

Figure 6.17: SEM images of biosensor devices fabricated at the University of Glasgow, UK, and tested at the University of Nottingham, China: a) spiral arm of a MZI; b) Input grating coupler and cascaded DCs; c) Grating coupler before the 120nm etching; d) complete biosensor comprised of grating couplers, DCs and 8 MZIs with spirals; f) spiral open to the microfluidic channel and g) waveguides of a MZI.

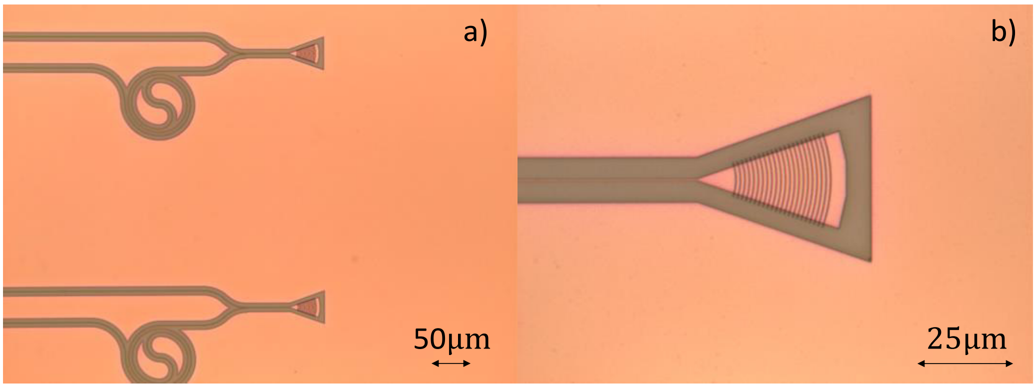

Figure 6.18: Microscope images after the second etching of 120nm of the devices fabricated at The University of Glasgow and tested at The University of Nottingham, China: a) Spiral MZI and grating couplers and b) Grating coupler.

6.4.1 Experimental set-up

Once again, the optical bench was set up as illustrated in Figure 6.4 and shown in Figure 6.13, except the input and output light for these devices had to be at 15˚ to the normal due to the design of the grating couplers. Therefore, fibre holders were 3D printed to hold the input tapered fibre and the output multimode fibre 15˚ from the normal as shown in Figure 6.19.

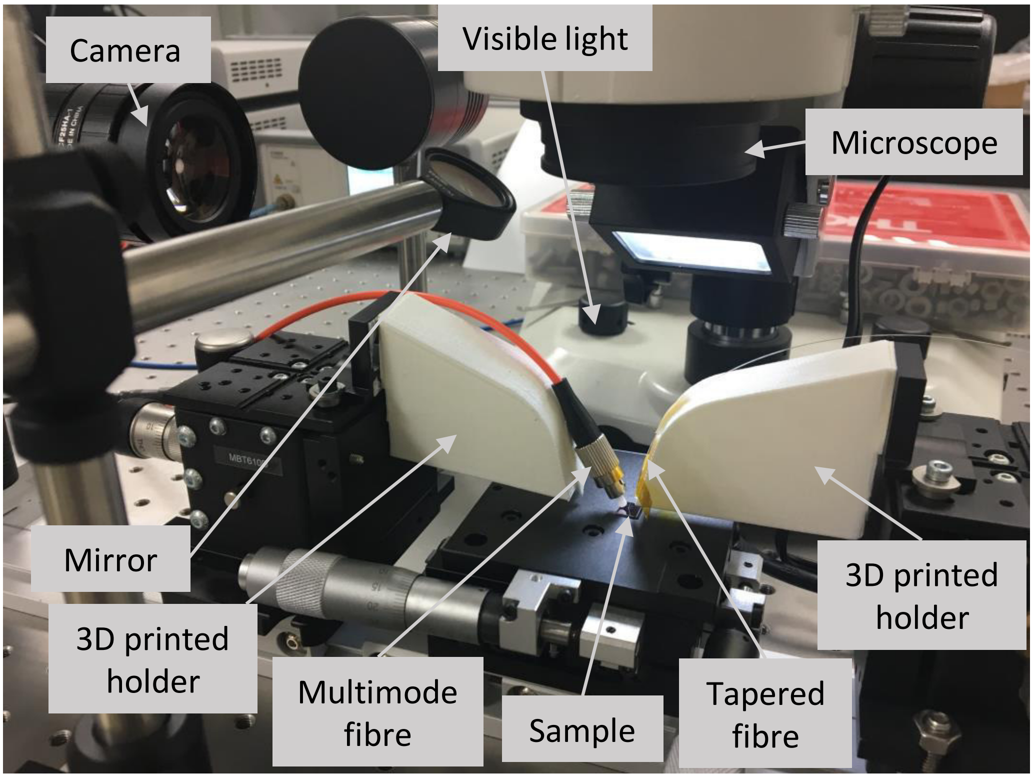

Figure 6.19: image of the experimental set up used for devices in set 4 where 3D printed fibre holders are used to couple light in at 15˚ from the normal and to couple light out of the device at 15˚ from the normal to the sample.

However, as noted above the optical testing at The University of Nottingham, China campus was unable to detect the expected waveguiding in these samples, probably as a result of the over etched grating couplers as shown in Figure 6.16.

6.4.2 Results

The results presented in this sub-section and shown in Figure 6.20-Figure 6.22 were obtained at Zhejiang University, China (by Ming Zhang). They are included here, with the permission of Mr. Zhang, not only to indicate successful realisation of the devices but also because they demonstrate that the fabricated devices show some deviations from expected behaviour which must be further understood and controlled before the proposed devices can be commercialised.

The theoretical loss for each grating coupler was 3dB and 4dB for the TE and TM-like modes respectively. The experimental loss for each grating coupler was about 5.5dB and 7.25dB for the TE and TM-like modes respectively. The straight waveguide loss was about 1dB/cm for the TM-like mode.

The insertion loss results shown in this section does not consider the grating coupler losses; they were normalised against the throughput for a straight waveguide with grating couplers.

Figure 6.20 shows the loss in dB of a 1x4 splitter formed by cascading 2 layers of directional couplers (DCs). The DCs designed by Zhejiang University had a coupling length, $L_c/2$ of 0.8µm and edge-to-edge distance between the waveguides, d of 0.2µm in contrast to the simulations done in section 3.4.5 which gave an optimum $L_\pi/2$ of 11.4µm and d of 0.45µm for the vector TM-like mode at an operating wavelength of 1.55µm.

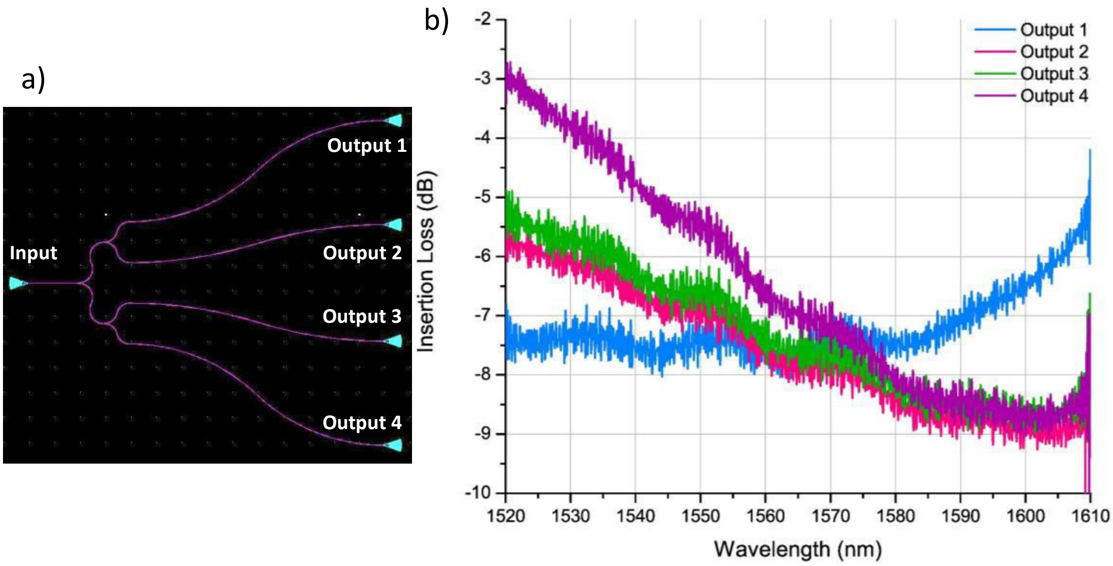

Figure 6.20: 1x4 splitter formed by cascading two layers of DCs a) layout as seen on a GDS edit and b) loss measurements over a wavelength range of 1.52-1.61µm.

At a central wavelength of 1.55µm the insertion loss of each output should be the same for each device but as Figure 6.20 shows the central wavelength shifted to 1.575µm, except for output 1. Output 1 was expected to be similar to output 4, which had the same physical layout on the mask as output 1, but it is not the same.

Figure 6.21b shows loss of a 1x8 splitter formed by cascading three sets of DCs as illustrated in Figure 6.21a. In Figure 6.21b the central wavelength is shifted from 1.55µm to 1.56µm.

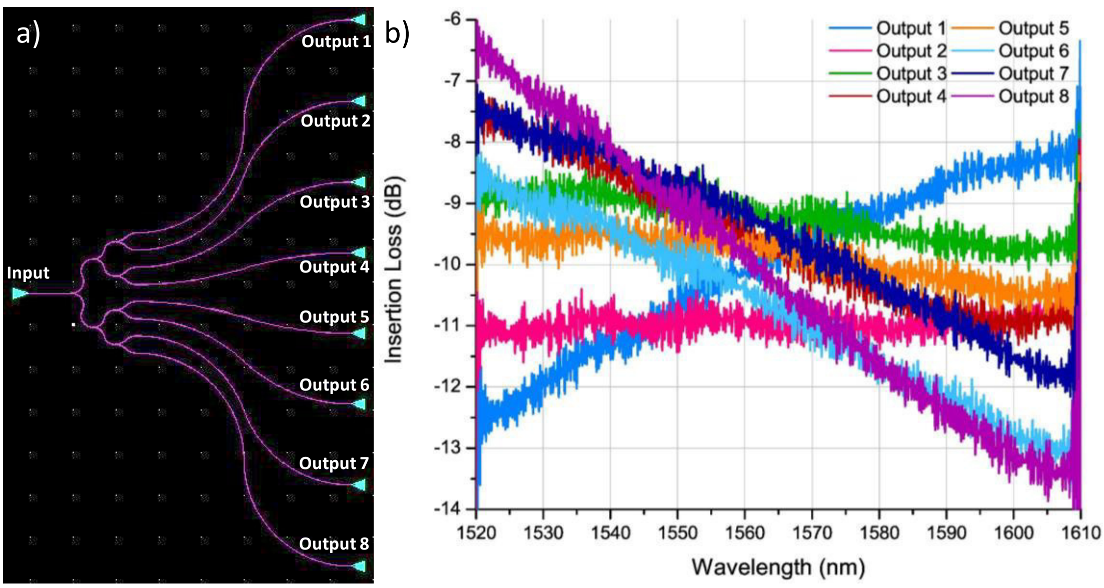

Figure 6.21: Loss of a 1x8 splitter formed by cascading three layers of DCs over a wavelength range of 1.52-1.61µm.

Figure 6.22b shows the loss in dB of a 1x4 splitter formed by cascading two layers of DCs and four spiral MZIs attached to each output scanned over a wavelength range of 1.52-1.61µm. Again output 1 and output 4 should have been similar as the waveguiding path was a mirror image of each other. This suggests an experimental error which might be associated with the alignment of the output grating coupler to the output fibre.

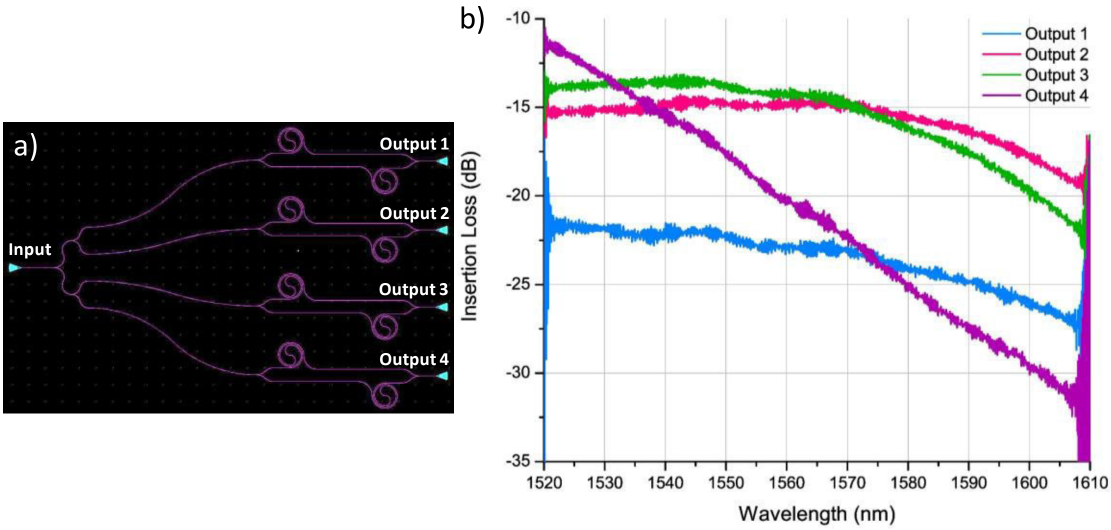

Figure 6.22: Loss of a 1x4 splitter formed by cascading two layers of DCs attached to spiral MZIs over a wavelength range of 1.52-1.61µm.

The set 4 devices shown in Figure 6.15 and Figure 6.17 were optically tested at the Optics laboratory of the School of Electrical and Electronic Engineering at the University of Nottingham, China as shown in Figure 6.23 and Figure 6.24 using the optical set up shown in Figure 6.19.

Figure 6.23 shows the tapered input fibre aligned to the grating coupler of a sensor fabricated at Zhejiang University at 15˚ to the normal. The tunable laser was set to 10mW at a wavelength of 1.55µm and the light polarised to the TM mode. Each device on the chip was about 1mm in length but since the camera output was saturated a clear input and output light cannot be observed.

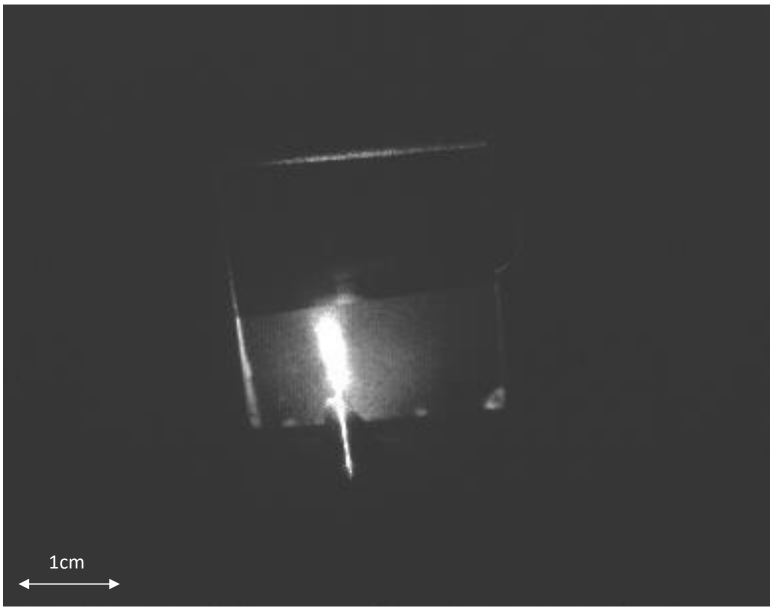

Figure 6.23: Set 4 biosensor device comprised of input/output grating couplers, DCs and MZI with spirals fabricated in Zhejiang University imaged with TM polarised input light at 10mW aligned to the grating coupler.

Figure 6.24a shows the input tapered fibre aligned to the grating coupler of a sensor fabricated at the University of Glasgow at 15˚ to the normal. The tunable laser power was set to 4mW at a wavelength of 1.55µm and the light was polarised to excite the TM-like mode. Again, each sensor device was about 1mm in length and as in Figure 6.23 the camera was saturated as shown in the line scan in Figure 6.24b making it impossible to observe any intensity change caused by the solutions in the microfluidic channels. The line scans in Figure 6.24b correspond to the lines A and B shown in Figure 6.24a.

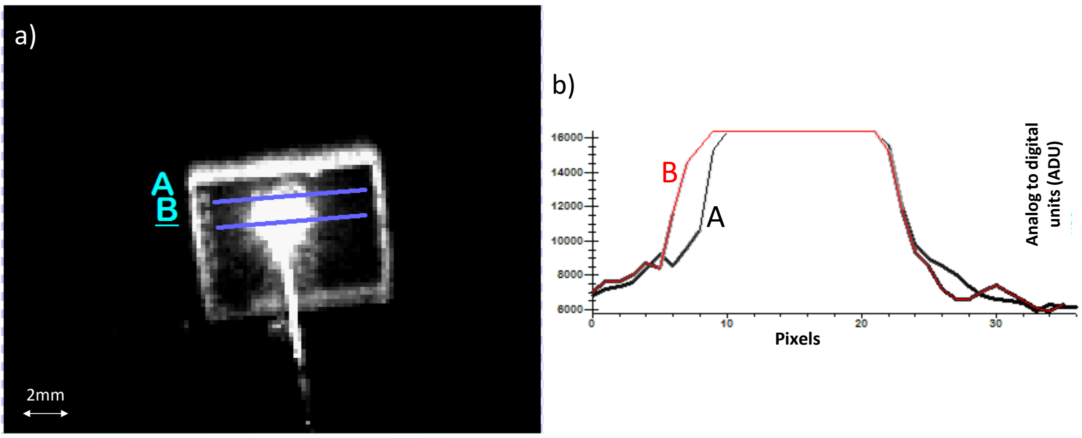

Figure 6.24: Set 4 biosensor device comprised of input/output grating couplers, DCs, MZI with spirals and microfluidic channels fabricated in The University of Glasgow: a) imaged with TM polarised input light at 4mW aligned to the grating coupler and b) line scan of the input and output light showing the problematic saturation.

6.5 Chapter summary

Four sets of devices were fabricated and tested successfully. Although the waveguides were multimoded in set 1, guided light could be captured by the infrared camera as expected. However, the results presented show successful realisation of waveguides and power splitters. Set 1 allowed the development of the fabrication process of the waveguide and microfluidic channels at the University of Nottingham, UK. Through this process the fabrication limitations and challenges were taken into consideration when designing the next set of devices.

The fabricated plasmonic interferometers of set 2 were slightly different from the optimised structure but the simulation of the fabricated device still functioned as intended with a wavelength shift responsivity of 97nm/RIU. The experimental results were as expected and proof of principle was presented successfully for a plasmonic interferometer.

For the optical testing of the biosensor devices in set 3 and 4 an optical lab was set up at the School of Electrical and Electronic Engineering at The University of Nottingham, China campus. With the tunable laser power set to its lowest value of 4mW and the camera gain set to its lowest, the images obtained were saturated making it impossible to image or record the intensity of the sensors.

However, a set of biosensors fabricated (to the same design as set 4) by Zhejiang University was tested by them; their preliminary measurements indicate the device successfully guided light with acceptably low propagation and insertion losses.

Chapter 7

7 CONCLUSIONS AND POTENTIAL FUTURE WORK

This chapter summarises the work presented in this thesis and suggests potential future work to improve on the optical biosensor device.

7.1 CONCLUSIONS

During this PhD work, the design, fabrication and testing of a label-free Silicon-on-Insulator (SOI) optical biosensor was successfully completed.

Label-free SOI optical biosensors based on the evanescent wave principle have been previously demonstrated [7.1, 2]. The novelty of the biosensors in this work lies on the transducer layout, tapered spot size converters and grating couplers, parallel sensing of up to 20 sensors, increased sensitivity and the steps towards surface functionalisation of the silicon waveguides.

The initial stage of this work was to investigate the ideal material for the transducer and the type of waveguide to obtain a high sensitivity ($\Delta N_{eff}/\Delta n_c$) of detection while also considering biocompatibility, easy integration, and established fabrication procedures for mass production. Calculations showed that high index contrast (HIC) materials such as SOI gave the highest sensitivity of 0.47, when the silicon core height was 0.18µm and the upper cladding index, n_c was 1.33 for the TM mode, at an operating wavelength of 1.55µm. SOI based waveguides are also widely used in biomedical applications [7.3-5], allow easy integration and have well established fabrication procedures [7.6, 7].

Simulation investigation performed using the software FIMMWAVE showed that obtaining a high sensitivity of 0.68 is possible if the silicon ridge waveguide height and width was fixed to 0.22µm and 0.27µm respectively and operated in the vector TE-like mode at a wavelength of 1.55µm. The sensitivity can be increased further to 0.77 by using slot waveguides of height and width of 0.22µm and 0.23µm respectively for the vector TE-like mode at a wavelength of 1.55µm. However, the fabrication of such narrow and long waveguides would require sophisticated and expensive fabrication technologies. For wider waveguides, the vector TM-like mode becomes more sensitive than the TE-like mode. To take advantage of the standard industrial SOI fabrication procedure [7.7], the silicon ridge waveguide height and width need to be 0.22µm and 0.5µm respectively and operate in the vector TM-like mode at a wavelength of 1.55µm. Due to the availability of SOI wafers two other ridge waveguide dimensions were also used where the silicon ridge waveguide heights were 0.32µm and 0.25µm and the widths were 4µm and 0.8µm respectively.

Propagation loss due to substrate leakage was calculated and showed that as the silicon dioxide thickness separating the silicon guiding layer from the silicon susbtrate increased, the substrate leakage loss decreased for both the vector TE-like and TM-like modes for an operating wavelength of 1.55µm. The SOI wafers used in this project had a 2µm thick silicon dioxide buffer layer which theoretically gives a substrate leakage loss of 0.23dB/cm for the vector TM-like mode at an operating wavelength of 1.55µm.

The curvature loss for the vector TE-like mode increases as the cover index, n_c, increases whereas the opposite is true for the TM-like mode. For an SOI ridge waveguide of height and width of 0.22µm and 0.5µm respectively and n_c=1.33 operating in the vector TM-like mode at a wavelength of 1.55µm, the calculated curvature loss is 0dB/cm (below calculation error) for a radius of curvature greater than 11µm. Therefore, the minimum radius of curvature was fixed at 15µm for all devices in this project.

Splitting light into two or more waveguides was achieved by Y-junction splitters, directional couplers (DCs) and multimode interference (MMI) couplers. Simulations show that Y-junction splitters require the shortest device length whereas DCs have the smallest insertion loss. Y-junctions splitters are more vulnerable to fabrication errors due to the sharp splitting of waveguides at the junction. To achieve the splitting of more than two outputs the Y-junction splitters and DCs must be cascaded and with each cascaded section the probability of fabrication errors increases. Therefore, each splitting method has its advantages and disadvantages and all three devices were designed, fabricated and tested successfully.

Mach-Zehnder interferometers (MZI) constructed by Y-junction splitters, straight waveguides and spiral waveguides were designed, fabricated and tested successfully. The longer the MZI the more sensitive the sensor became. Simulations showed that if the adsorbed layer of a heterogeneous sensor is greater than 0.7μm the sensor acts like a homogeneous sensor. For a homogenous sensing MZI with length, L, of 1000μm and $\Delta N_{eff}/\Delta n_c$ =0.5 the theoretical MZI sensitivity was 3.1×10^{-7} RIUs. For a MZI with spirals of 10 turns and L=3145μm the theoretical MZI sensitivity was 9.9×10^{-8}.

Increasing the sensitivity is not always optimal as the output power intensity is a co-sinusoidal graph which could result in fringe order ambiguity, directional ambiguity and sensitivity fading. This could be avoided by reducing the length of the MZI, thereby reducing the sensitivity, so that the intensity is always located on one arm of the fringe in an intensity graph.

Another sensor based on SOI considered for this project was a plasmonic interferometer (PI). A PI sensor was designed and fabricated successfully. A PI of length 13μm using a 0.23μm thick gold layer gave a theoretical wavelength shift responsivity of 500nm/RIU. The fabricated PI was of L=12μm and gold layer thickness of 0.245μm, with a theoretical wavelength shift responsivity of 97nm/RIU. Some preliminary testing showed that the device performed as intended but the responsivity was not determined experimentally as microfluidic channels were not fabricated on the PI sensor. Even though PIs require a very small area, the PI sensor has an experimental insertion loss between 36-37dB which prevents the use of PIs in parallel detection.

Butt coupling and grating coupling methods were used to couple light into and out of waveguides in this project. For butt coupling, a tapered spot size converter was successfully fabricated on top of an inverted silicon taper to efficiently couple the light in and out of the waveguides. Simulations show a 97.7% coupling efficiency and 0.1dB insertion loss for an SU-8 spot size converter tapered from 10µm to 0.5µm with a height of 2µm and a silicon waveguide inversely tapered from 0.1µm to 0.5µm for the vector TM-like mode at an operating wavelength of 1.55µm. The total length of the taper was 600µm.

The grating coupler used was 35µm in length and 24µm in width. The theoretical and experimental coupling efficiency was about 4dB and 7.25dB respectively. Grating couplers require a small area compared to the butt coupling method but have a much higher insertion loss.

For heterogenous sensing a bioreceptor layer needs to be added to the transducer. To enable a label free detection, an immunosensor where the target molecule binds to an antibody immobilised on the surface of the MZI was used as the bioreceptor layer. To attach the antibody to the silicon waveguide two selective surface functionalisation methods of silicon surface were experimentally shown with promising results. The attachment of a fluorescent tag to the functionalised surface enabled the imaging and quantification of the functionalised silicon surface.

The first method of surface functionalisation studied, by hydrosilylation and a NH_2-terminated monolayer modified a layer of non-uniform silicon. The second method of surface functionalisation by hydroxylation and silanisation modified a non-uniform layer of silicon dioxide. The experiments were respectively conducted on silicon and silicon dioxide surfaces. For the heterogenous sensor to work efficiently, the long and narrow silicon waveguides or the native oxide on the waveguide need to be functionalised uniformly. But the experiments conducted showed that a highly controlled experimental procedure is required for the uniform modification of the narrow waveguides.

Four sets of devices were fabricated and optically tested successfully. The first set of devices consisted MZIs and MMIs where the silicon waveguide height and width were 0.32µm and 4µm respectively. The waveguides were multimoded but the devices performed as expected. The second set of devices consisted of PIs which also performed as expected as noted above.

The third set of devices were fabricated and consisted of spot size converters, MZIs, MMIs and microfluidic channels. The silicon waveguide height and width were 0.25µm and 4µm respectively. The optical testing was done at the Optical Laboratory at The University of Nottingham, China campus, which was specifically set up for this project. Initial results showed that light imaged through the camera caused the camera to saturate making it difficult to record the intensity of light.

A fourth set of devices consisting of grating couplers, DCs and MZIs with spiral arms and fabricated with silicon waveguide height and width of 0.22µm and 0.5µm respectively. Optical testing performed at The University of Nottingham, China campus, presented saturated camera images, just as with the third set of devices. However, optical loss measurement performed at Zhejiang University showed that the devices operated as expected.

7.2 POTENTIAL FUTURE WORK

In terms of the SOI transducer sensitivity the waveguides and the MZI have been designed to give the maximum sensitivity and lowest insertion loss. However, there are some aspects of the device that can be improved further but which were not studied further due to time constraints. Some of these areas are discussed below.

7.2.1 MMIs and grating couplers

In this project MMIs with tapered input and output waveguides were used. In addition to tapering the input and output waveguides the performance of the MMI can be improved by changing the shape of the MMI cavity [7.8-12] as described in section 3.4.4.

Grating couplers have high insertion loss but require a very small area and reduced alignment sensitivity compared to spot size converters, which is important when considering the cost for future commercialisation of the biosensor. This project used a pre-designed focused grating coupler but recent literature shows new subwavelength structures [7.13], such as apodized [7.14] and focused apodized grating couplers [7.15] designed for the vector TM-like mode, have coupling efficiencies of 3.7dB and 3dB respectively as described in section 3.5.2.

Improving on the designs of MMIs and grating couplers will reduce the size of the biosensor and reduce the insertion loss.

7.2.2 The mid-infrared

Analyte species absorb in the mid infrared (MIR) [7.16, 17] and therefore will not require heterogenous sensing or a bioreceptor layer. Operating as a homogenous sensor with only the microfluidics layer for the control of the flow of fluids would reduce the fabrication steps and costs greatly.

The devices in the project was designed for an operating wavelength of 1.55µm. SOI devices cannot be used for the MIR because silicon dioxide absorbs heavily at wavelengths greater than 3.7μm [7.18]. Instead materials such as chalcogenide glasses can be used to replace SOI and the layout and devices designed in this project can be adapted for chalcogenide glass based waveguides.

In section 2.8.3 the sensitivity of SOI and chalcogenide glass based waveguides were calculated. The simulations showed that the sensitivity is 7 times smaller for the chalcogenide glass waveguides with refractive index of core and substrate of 3.359 and 2.533 respectively for the TM mode at operating wavelengths of 3, 6 and 10μm. The sensitivity could be increased by increasing the refractive index contrast between the core and substrate but the present studies shows that a sensitive homogenous evanescent field based label-free optical biosensor can be designed for the MIR and is worth exploring experimentally in the future.

7.2.3 Working towards a Lab-on-a-chip device

To achieve a lab-on-a-chip device the transducer, bioreceptor and the microfluidics layer must be combined and tested as one device and then packaged to take it from a laboratory apparatus to a portable and cheap sensor.

The primary consideration for packaging is the method of optical interfacing to the chips. In this project, butt coupling and grating coupling were discussed which are the two most common approaches for optical interfacing. While butt coupling provides the advantage of wide optical bandwidth, low insertion loss and the ability to couple both TE and TM polarisations, grating couplers provide easy automated alignment with reduced alignment sensitivity [7.19].

Another factor to consider is the temperature control of the device. Although a reference arm is included in the MZI sensor to remove ambiguity caused by temperature changes, the sensing and refence arms of the MZI will not be identical due to fabrication errors. This can be compensated for using a Thermo-Electric cooler (TEC), which can keep the temperature of the biochip constant during operation.

The final production and operating costs of the sensor will be determined by the materials, photolithography, plasma etching, detection instrumentation and the thoughput (measurements per hour) [7.20]. The cost can be reduced by increasing the number of devices fabricated per wafer and increasing the throughput. Silicon based fabrication technology is a mature mass production process, which potentially can produce chips at very low cost achievable of a few US dollars each.

The work presented in this thesis is a start but much work is yet to be done.

REFERENCES

[7.1] A. Densmore, D. X. Xu, P. Waldron, S. Janz, P. Cheben, J. Lapointe, A. Delage, B. Lamontagne, J. H. Schmid, and E. Post, "A silicon-on-insulator photonic wire based evanescent field sensor," *Photonics Technology Letters, IEEE,* vol. 18, pp. 2520-2522, 2006.

[7.2] B. Sepulveda, J. S. Del Rio, M. Moreno, F. Blanco, K. Mayora, C. Domínguez, and L. M. Lechuga, "Optical biosensor microsystems based on the integration of highly sensitive Mach–Zehnder interferometer devices," *Journal of optics A: Pure and Applied Optics,* vol. 8, p. S561, 2006.

[7.3] J. L. Coffer, *Semiconducting silicon nanowires for biomedical applications*. Cambridge: Elsevier, 2014.

[7.4] M.-J. Bañuls, R. Puchades, and Á. Maquieira, "Chemical surface modifications for the development of silicon-based label-free integrated optical (IO) biosensors: A review," *Anal. Chimica Acta,* vol. 777, pp. 1-16, 2013.

[7.5] S. Ciampi, J. B. Harper, and J. J. Gooding, "Wet chemical routes to the assembly of organic monolayers on silicon surfaces via the formation of Si–C bonds: Surface preparation, passivation and functionalization," *Chemical Society Reviews,* vol. 39, pp. 2158-2183, 2010.

[7.6] O. Kononchuk and B.-Y. Nguyen, *Silicon-on-insulator (SOI) technology: Manufacture and Applications*. Cambridge: Elsevier, 2014.

[7.7] A. E.-J. Lim, J. Song, Q. Fang, C. Li, X. Tu, N. Duan, K. K. Chen, R. P.-C. Tern, and T.-Y. Liow, "Review of silicon photonics foundry efforts," *IEEE Journal of Selected Topics in Quantum Electronics,* vol. 20, pp. 405-416, 2014.

[7.8] A. Maese-Novo, R. Halir, S. Romero-García, D. Pérez-Galacho, L. Zavargo-Peche, A. Ortega-Moñux, I. Molina-Fernández, J. Wangüemert-Pérez, and P. Cheben, "Wavelength independent multimode interference coupler," *Optics Express,* vol. 21, pp. 7033-7040, 2013.

[7.9] D. S. Levy, R. Scarmozzino, Y. M. Li, and R. M. Osgood Jr, "A new design for ultracompact multimode interference-based 2 x 2 couplers," *Photonics Technology Letters, IEEE,* vol. 10, pp. 96-98, 1998.

[7.10] J.-J. Wu, "A multimode interference coupler with exponentially tapered waveguide," *Progress In Electromagnetics Research C,* vol. 1, pp. 113-122, 2008.

[7.11] C. Themistos, M. Rajarajan, B. M. A. Rahman, S. S. A. Obayya, and K. T. V. Grattan, "Rigorous Comparison of Parabolically Tapered and Conventional Multimode-Interference-Based 3-dB Power Splitters in InGaAsP/InP Waveguides," *Appl. Opt.,* vol. 43, pp. 5228-5235, 2004.

[7.12] P. A. Besse, E. Gini, M. Bachmann, and H. Melchior, "New 2x2 and 1x3 multimode interference couplers with free selection of power splitting ratios," *Lightwave Technology, Journal of,* vol. 14, pp. 2286-2293, 1996.

[7.13] R. Halir, P. J. Bock, P. Cheben, A. Ortega‐Moñux, C. Alonso‐Ramos, J. H. Schmid, J. Lapointe, D. X. Xu, J. G. Wangüemert‐Pérez, and Í. Molina‐Fernández, "Waveguide sub‐wavelength structures: a review of principles and applications," *Laser & Photonics Reviews,* vol. 9, pp. 25-49, 2015.

[7.14] R. Halir, P. Cheben, J. Schmid, R. Ma, D. Bedard, S. Janz, D.-X. Xu, A. Densmore, J. Lapointe, and I. Molina-Fernández, "Continuously apodized fiber-to-chip surface grating coupler with refractive index engineered subwavelength structure," *Optics Letters,* vol. 35, pp. 3243-3245, 2010.

[7.15] Z. Cheng, X. Chen, C. Y. Wong, K. Xu, and H. K. Tsang, "Apodized focusing subwavelength grating couplers for suspended membrane waveguides," *Applied Physics Letters,* vol. 101, p. 101104, 2012.

[7.16] B. J. Eggleton, B. Luther-Davies, and K. Richardson, "Chalcogenide photonics," *Nat. Photon,* vol. 5, pp. 141-148, 2011.

[7.17] A. B. Seddon, "A prospective for new mid-infrared medical endoscopy using chalcogenide glasses," *International Journal of Applied Glass Science,* vol. 2, pp. 177-191, 2011.

[7.18] R. A. Soref, S. J. Emelett, and W. R. Buchwald, "Silicon waveguided components for the long-wave infrared region," *Journal of optics A: Pure and Applied Optics,* vol. 8, p. 840, 2006.

[7.19] L. Chrostowski and M. Hochberg, *Silicon photonics design: from devices to systems*. Cambridge: Cambridge University Press, 2015.

[7.20] B. T. Cunningham, *Label-free optical biosensors: An Introduction*. New York: Cambridge University Press, 2009.

Appendix A

MATLAB code for cut-off heights of an SOI waveguide for TE-like and TM-like modes at a wavelength of 1.55µm

```
clear all; close all; clc;

n1=1.33;
n2=3.5;
n3=1.45;

lam=1.55*10^-6;
k0=(2*pi)/lam;

q2=sqrt((((2*pi)/lam)^2)*((n2^2)-(n3^2)));
p1=sqrt((((2*pi)/lam)^2)*((n3^2)-(n1^2)));

m=[0,1,2,3,4,5];

TM_hcut=((atan(((n2^2)*p1)/((n1^2)*q2)))+(m*pi))/q2
TE_hcut=((atan((p1)/q2))+(m*pi))/q2*

plot(m,TE_hcut/1e-6,'b',m,TM_hcut/1e-6,'r')
title('Cut off widths in a slab for modes 0-5')
xlabel('mode');
ylabel('Cut-off width (um)');
grid on;
legend('TE mode','TM mode');
```

Appendix B

MATLAB code for cut-off heights for the fundamental TE-like and TM-like mode of an SOI waveguide at a wavelength of 1-10µm

```
clear all
clc
No_of_points=10000;
lambda=linspace(1e-6,10e-6,No_of_points);%(start,end,number_of
values)
[nr,nm]=size(lambda);
TM_hcut=zeros(nr,nm);
TE_hcut=zeros(nr,nm);

n1=1.33;
n2=3.5;
n3=1.45;

for K=1:No_of_points
k0=(2*pi)/lambda(:,K);
q2=sqrt(((k0)^2)*((n2^2)-(n3^2)));
p1=sqrt(((k0)^2)*((n3^2)-(n1^2)));
m=0;
TM_hcut(:,K)=((atan(((n2^2)*p1)/((n1^2)*q2)))+(m*pi))/(q2*10^-6);
TE_hcut(:,K)=((atan((p1)/q2))+(m*pi))/(q2*10^-6);
end

figure(1)
plot(lambda/1e-6,TE_hcut/1e-6,'b','LineWidth',1.5);hold on;
plot(lambda/1e-6,TM_hcut/1e-6,'r','LineWidth',1.5);hold off;
xlabel('Wavelength (um)');
ylabel('Cut-off height (um)');
title('Cut-off height for fundamental mode (TE and TM)');
grid on;
legend('TE mode','TM mode');
```

Appendix C

MATLAB code for calculating Radius of Curvature from an equation

```
clear all;
close all;

L=20;
Plhs=0;
Prhs=5;
Z=[0:0.01:L];
y=Plhs*(1-(sin((Z*pi)/(L*2))).^2)+Prhs*(sin((Z*pi)/(L*2))).^2;

hold on
grid on
subplot(2,1,1)
plot(Z,y)

xlabel('L (um)');
ylabel('x (um)');
title('S-function curve');

A=((pi^2)/4)*((Prhs-Plhs)^2)*((sin((pi*Z)/L)).^2)/(L^2);
B=((pi^2)/2)*(Prhs-Plhs)*cos((pi*Z)/L)/(L^2);
r=((1+A).^(3/2))./B;

r2=abs(real(r));

subplot(2,1,2)
plot(Z,r2)

xlabel('L (um)');
ylabel('Radius of curvature (um)');
title('Radius of curvature along the S-function curve');
```

Appendix D

MATLAB code for Mach-Zehnder Interferometer (MZI) with Archimedean Spiral of 4 turns

```
turns=4;
h=175;% horizontal offset for second spiral
v=25; % vertical offset for second spiral

R2=(turns+9)*pi; %Final radius of archemedian spiral
R=9.5*pi; % Initial radius of archemedian spiral
r=R/2; %minimum radius=14.9225 fixed % used for S-bend

n=0.01;
t =[R:n:R2];
r1=t;
r2=-t;
X1=r1.*cos(t);
Y1=r1.*sin(t);
X2=r2.*cos(t);
Y2=r2.*sin(t);

title(['Turns=', num2str(turns)])
hold on
grid on

plot(X1,Y1,'b','LineWidth',0.5) %first Archimedean spiral
plot(X2,Y2,'r','LineWidth',0.5) %first Archimedean spiral
plot(h+X1,-v+Y1,'b','LineWidth',0.5) %second Archimedean spiral
plot(h+X2,-v+Y2,'r','LineWidth',0.5) %second Archimedean spiral

axis equal
axis tight
xlabel('Length (um)')
ylabel('Width (um)')
f=@(t) sqrt((t.^2)+1);
len = integral(f,R,R2) %length of one Archimedean spiral
Total_length=2*len+2*pi*r+pi*R2+h %length of one arm

t1=[0:n:pi];
x3=r*sin(t1);
y3=r+r*cos(t1);
plot(x3,y3,'r',-x3,-y3,'b')  %first S-bend
plot(h+x3,-v+y3,'r',h-x3,-v-y3,'b')  %second S-bend

t2=[0:n:pi/2];
x4=-2*R2+R2*sin(t2);
y4=-R2*cos(t2);
plot(x4,y4,'b',-x4,-y4,'r') %first 2 arcs
plot(h+x4,-v+y4,'b',h-x4,-v-y4,'r') %second 2 arcs

x5=2*R2;
```

```
x6=h+2*R2;
x7=h-2*R2;
y5=R2;
plot([x5,x6],[y5,y5],'r') %top line
plot([x7,-x5],[-v-y5,-v-y5],'b') % bottom line

plot ([x6,x6+h],[y5-v,y5-v])
XY=[x4,fliplr(X1),-x3,fliplr(x3),X2,fliplr(-x4),x5,x6;y4,fliplr(Y1),-
y3,fliplr(y3),Y2,fliplr(-y4),y5,y5];
XY2=[x7,-x5,h+x4,fliplr(h+X1),h-x3,fliplr(h+x3),h+X2,fliplr(h-
x4),x6,x6+h;-v-y5,-v-y5,-v+y4,fliplr(-v+Y1),-v-y3,fliplr(-v+y3),-
v+Y2,fliplr(-v-y4),y5-v,y5-v];

csvwrite('spiral_4_top.csv',XY.'); %Write top arm to file
csvwrite('spiral_4_bottom.csv',XY2.'); %Write bottom arm to file
```

Appendix E

Set 1 Mask Layout and Description

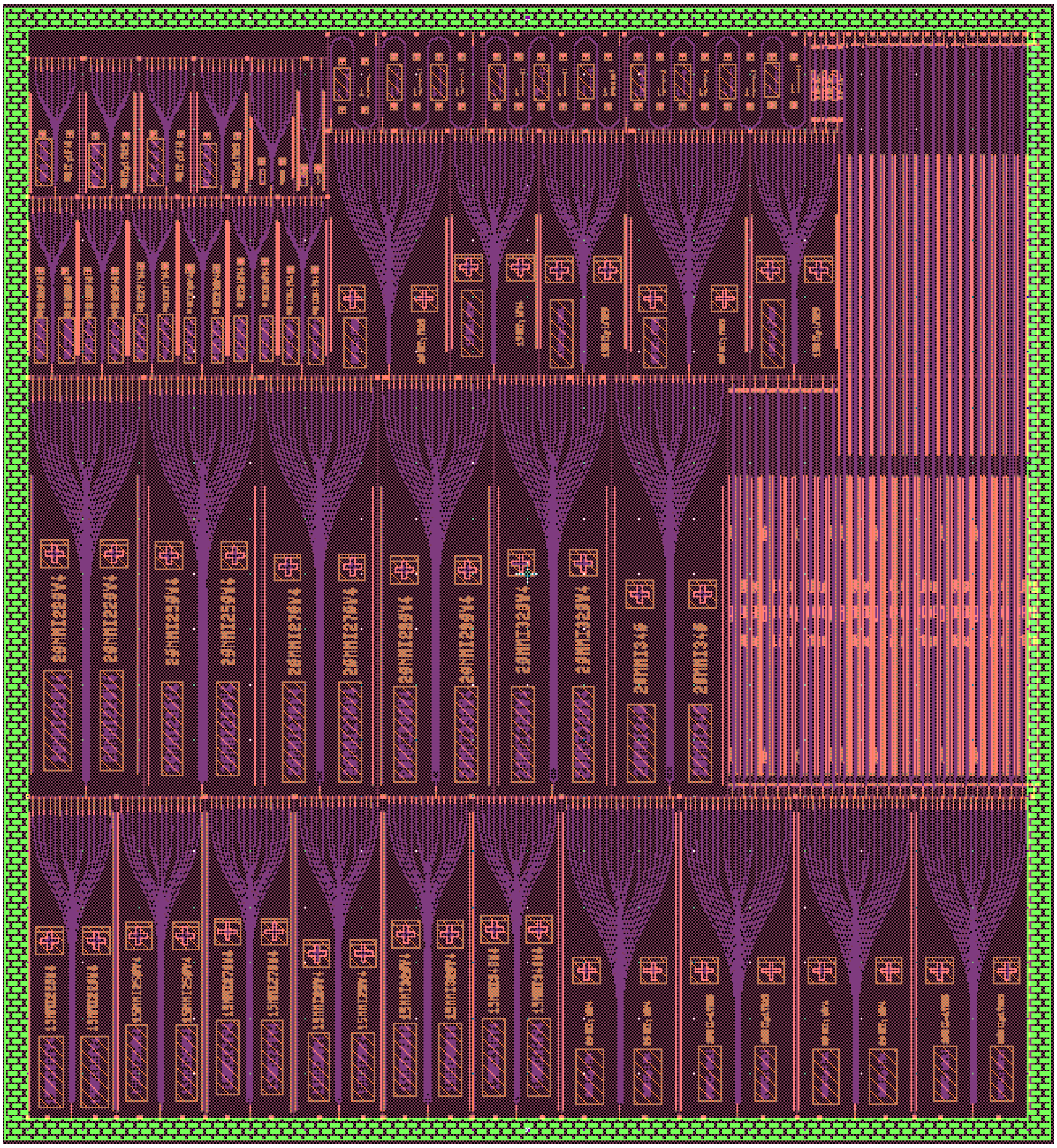

Figure 1: Mask Layer 1 and 2 of set 1.

Cell Name	Description
8MMI220W4	1x8 MMI with output waveguide adjacent separation 15um, Input/output tapers, S-bend waveguides, ridge width of 4um, Si core thickness of 220nm
8MMI250W4	1x8 MMI with output waveguide adjacent separation 15um, Input/output tapers, S-bend waveguides, ridge width of 4um, Si core thickness of 250nm
8MMI270W4	1x8 MMI with output waveguide adjacent separation 15um, Input/output tapers, S-bend waveguides, ridge width of 4um, Si core thickness of 270nm
8MMI290W4	1x8 MMI with output waveguide adjacent separation 15um, Input/output tapers, S-bend waveguides, ridge width of 4um, Si core thickness of 290nm
8MMI320W4	1x8 MMI with output waveguide adjacent separation 15um, Input/output tapers, S-bend waveguides, ridge width of 4um, Si core thickness of 320nm
8MMI340W4	1x8 MMI with output waveguide adjacent separation 15um, Input/output tapers, S-bend waveguides, ridge width of 4um, Si core thickness of 340nm
15MMI220W4	1x15 MMI with output waveguide adjacent separation 15um, Input/output tapers, S-bend waveguides, ridge width of 4um, Si core thickness of 220nm
15MMI250W4	1x15 MMI with output waveguide adjacent separation 15um, Input/output tapers, S-bend waveguides, ridge width of 4um, Si core thickness of 250nm
15MMI270W4	1x15 MMI with output waveguide adjacent separation 15um, Input/output tapers, S-bend waveguides, ridge width of 4um, Si core thickness of 270nm

15MMI290W4	1x15 MMI with output waveguide adjacent separation 15um, Input/output tapers, S-bend waveguides, ridge width of 4um, Si core thickness of 290nm
15MMI320W4	1x15 MMI with output waveguide adjacent separation 15um, Input/output tapers, S-bend waveguides, ridge width of 4um, Si core thickness of 320nm
15MMI340W4	1x15 MMI with output waveguide adjacent separation 15um, Input/output tapers, S-bend waveguides, ridge width of 4um, Si core thickness of 340nm
20MMI220W4	1x20 MMI with output waveguide adjacent separation 15um, Input/output tapers, S-bend waveguides, ridge width of 4um, Si core thickness of 220nm
20MMI250W4	1x20 MMI with output waveguide adjacent separation 15um, Input/output tapers, S-bend waveguides, ridge width of 4um, Si core thickness of 250nm
20MMI270W4	1x20 MMI with output waveguide adjacent separation 15um, Input/output tapers, S-bend waveguides, ridge width of 4um, Si core thickness of 270nm
20MMI290W4	1x20 MMI with output waveguide adjacent separation 15um, Input/output tapers, S-bend waveguides, ridge width of 4um, Si core thickness of 290nm
20MMI320W4	1x20 MMI with output waveguide adjacent separation 15um, Input/output tapers, S-bend waveguides, ridge width of 4um, Si core thickness of 320nm
20MMI340W4	1x20 MMI with output waveguide adjacent separation 15um, Input/output tapers, S-bend waveguides, ridge width of 4um, Si core thickness of 340nm
8MMIp10W4	1x20 MMI with output waveguide adjacent separation 10um, Input/output tapers, S-bend waveguides, ridge width of 4um, Si core thickness of 250nm

8MMIp10W25	1x20 MMI with output waveguide adjacent separation 10um, Input/output tapers, S-bend waveguides, ridge width of 25um, Si core thickness of 250nm
15MMIp10W4	1x15 MMI with output waveguide adjacent separation 10um, Input/output tapers, S-bend waveguides, ridge width of 4um, Si core thickness of 250nm
15MMIp10W25	1x15 MMI with output waveguide adjacent separation 10um, Input/output tapers, S-bend waveguides, ridge width of 25um, Si core thickness of 250nm
20MMIp10W4	1x20 MMI with output waveguide adjacent separation 10um, Input/output tapers, S-bend waveguides, ridge width of 4um, Si core thickness of 250nm
20MMIp10W25	1x20 MMI with output waveguide adjacent separation 10um, Input/output tapers, S-bend waveguides, ridge width of 25um, Si core thickness of 250nm
8MMIp5W25	1x8 MMI with output waveguide adjacent separation 5um, Input/output tapers, S-bend waveguides, ridge width of 25um, Si core thickness of 250nm
15MMIp5W25	1x15 MMI with output waveguide adjacent separation 5um, Input/output tapers, S-bend waveguides, ridge width of 25um, Si core thickness of 250nm
20MMIp5W25	1x20 MMI with output waveguide adjacent separation 5um, Input/output tapers, S-bend waveguides, ridge width of 25um, Si core thickness of 250nm
Y-3J	3 ways split, with input/output tapers
MZID50um	MZI with two arms’ path difference of 50 um
MZID25um	MZI with two arms’ path difference of 25 um
MZID0um	MZI with no path difference with two arms
Loss measurement	Straight optical path lengths connected by 5mm radius semi-circles

Appendix F

Set 2 Mask Layout and Description

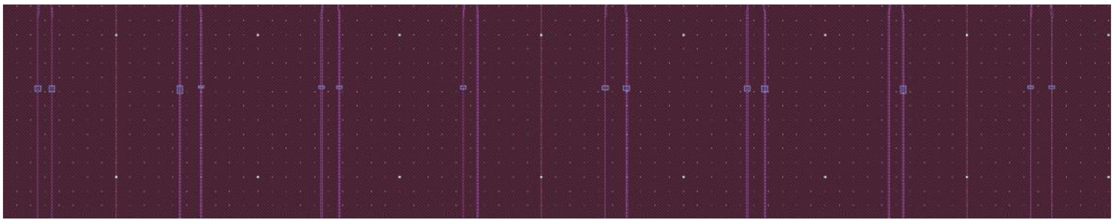

Figure 1: Mask layer 1 and 2 of Set 2 Plasmonic interferometers.

Mask layer 1 of set 1 was used to fabricate the waveguides of set 2. Another Mask containing windows of varying lengths from 4-25µm and width of 10µm was made for the gold deposition of the plasmonic interferometer.

Appendix G

Set 3 Mask Layout and Description

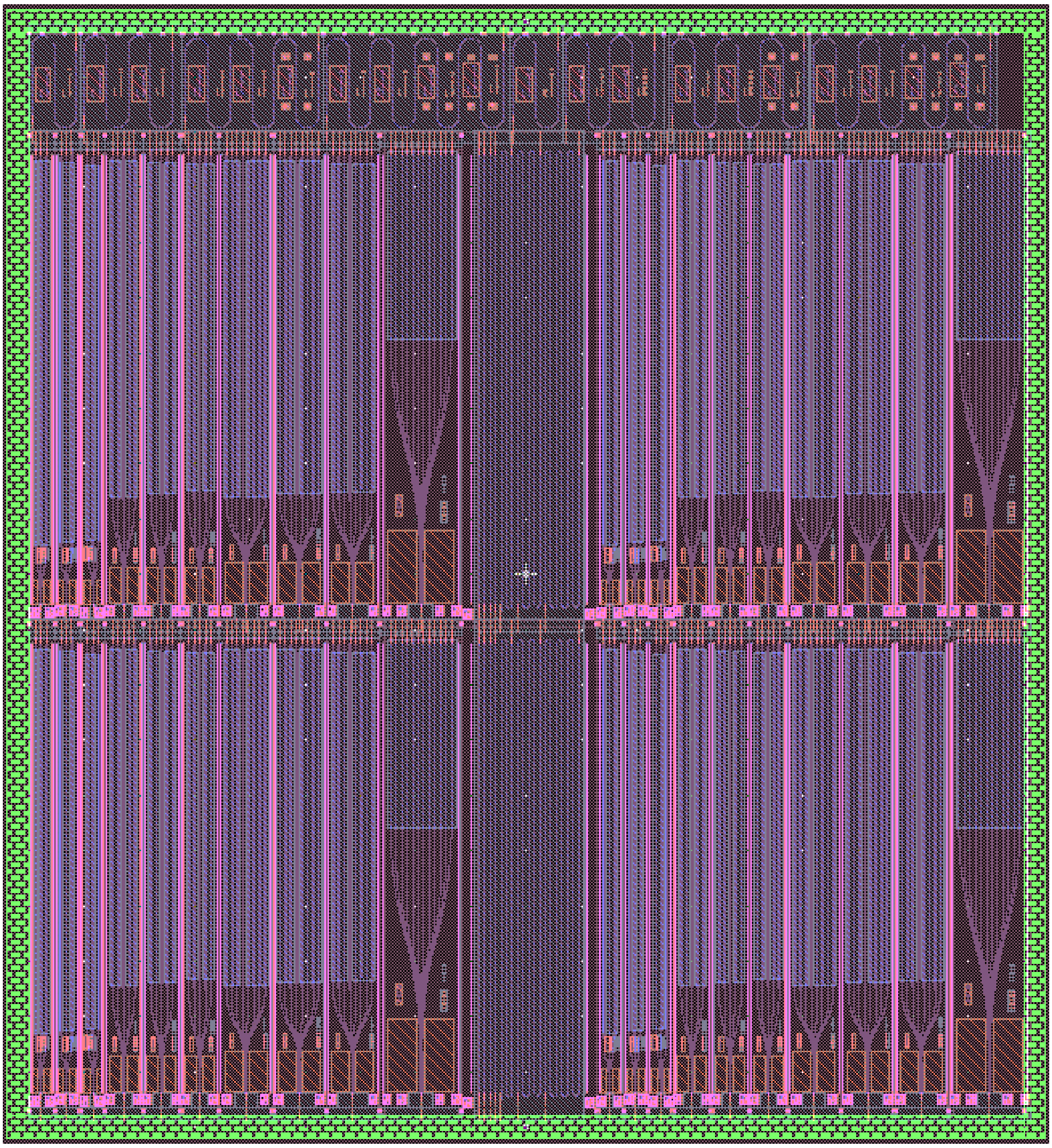

Figure 1: Mask Layer 1, 2 and 3 of set 3.

Cell Name	Description
MMI3MZI1	1x3 MMI with output waveguide adjacent separation 10um, 3 MZIs the arms are 25µm and 37.5µm from the centre giving an inbuilt phase offset, Input/output tapers, S-bend waveguides, ridge width of 0.8um, Si core thickness of 250nm and microfluidic channel
MMI3MZI2	1x3 MMI with output waveguide adjacent separation 10um, 3 MZIs the one arm is 250µm longer than the other arm giving an inbuilt phase offset, Input/output tapers, S-bend waveguides, ridge width of 0.8um, Si core thickness of 250nm and microfluidic channel
MMI3MZI3	1x3 MMI with output waveguide adjacent separation 10um, 3 MZIs the one arm is 500µm longer than the other arm giving an inbuilt phase offset, Input/output tapers, S-bend waveguides, ridge width of 0.8um, Si core thickness of 250nm and microfluidic channel
MMI5MZI1	1x5 MMI with output waveguide adjacent separation 10um, 5 MZIs the arms are 25µm and 37.5µm from the centre giving an inbuilt phase offset, Input/output tapers, S-bend waveguides, ridge width of 0.8um, Si core thickness of 250nm and microfluidic channel
MMI5MZI2	1x5 MMI with output waveguide adjacent separation 10um, 5 MZIs the one arm is 250µm longer than the other arm giving an inbuilt phase offset, Input/output tapers, S-bend waveguides, ridge width of 0.8um, Si core thickness of 250nm and microfluidic channel
MMI5MZI3	1x5 MMI with output waveguide adjacent separation 10um, 5 MZIs the one arm is 500µm longer than the other

	arm giving an inbuilt phase offset, Input/output tapers, S-bend waveguides, ridge width of 0.8um, Si core thickness of 250nm and microfluidic channel
MMI8MZI1	1x8 MMI with output waveguide adjacent separation 10um, 8 MZIs the arms are 25µm and 37.5µm from the centre giving an inbuilt phase offset, Input/output tapers, S-bend waveguides, ridge width of 0.8um, Si core thickness of 250nm and microfluidic channel
MMI8MZI2	1x8 MMI with output waveguide adjacent separation 10um, 8 MZIs the one arm is 250µm longer than the other arm giving an inbuilt phase offset, Input/output tapers, S-bend waveguides, ridge width of 0.8um, Si core thickness of 250nm and microfluidic channel
MMI8MZI3	1x8 MMI with output waveguide adjacent separation 10um, 8 MZIs the one arm is 500µm longer than the other arm giving an inbuilt phase offset, Input/output tapers, S-bend waveguides, ridge width of 0.8um, Si core thickness of 250nm and microfluidic channel
MMI12YI	1x12 MMI with output waveguide adjacent separation 10um, 1x12 MMI with output waveguide adjacent separation 10um and microfluidic channel
Loss measurements	Straight and bent waveguides of 250µm radius of curvature, ridge width 0.8µm and Si core thickness of 250µm
Loss measurements	Straight and bent waveguides of 250µm radius of curvature, ridge width 0.8µm and Si core thickness of 250µm

Appendix H

Set 4 Mask Layout and Description

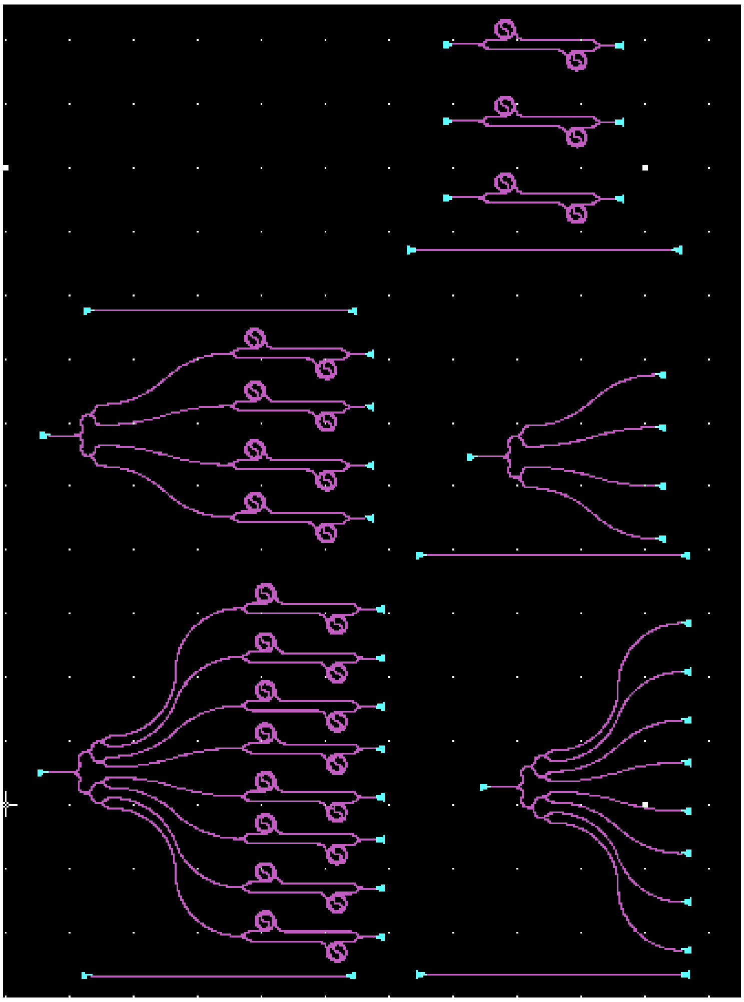

Figure 1: Mask layer 1 and 2 of Set 4.

Mask layer 1 was for the photolithography of waveguides which are 0.5µm of width and 0.22µm of height. Mask layer 2 was for the photolithography of the grating couplers which are etched 0.12um. A physical mask was not required for both layers as e-beam lithography method as used.

Layer 1 consists of 1000um long straight waveguides, 3 MZIs with spirals, a 1x4 splitter comprised of DCs, a 1x8 splitter comprised of DCs, a 1x4 MMI with 4 MZI with spirals and a 1x8 MMI with 8 MZI with spirals.

Appendix I

Pictures of the physical masks manufactured

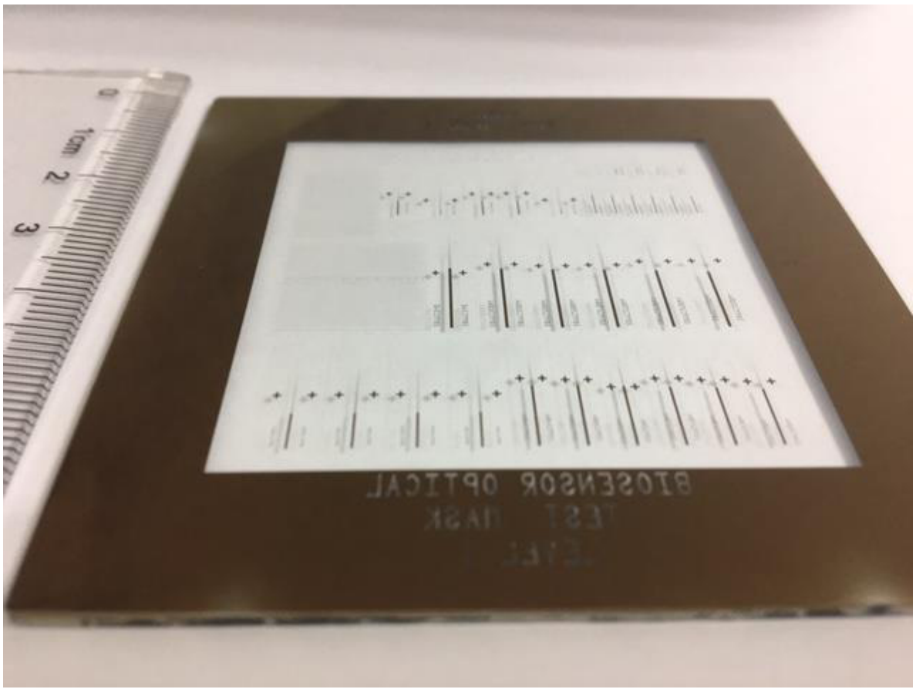

Figure 1: Set 1 Mask Layer 1 (Waveguide layer) for Silicon core 0.32µm.

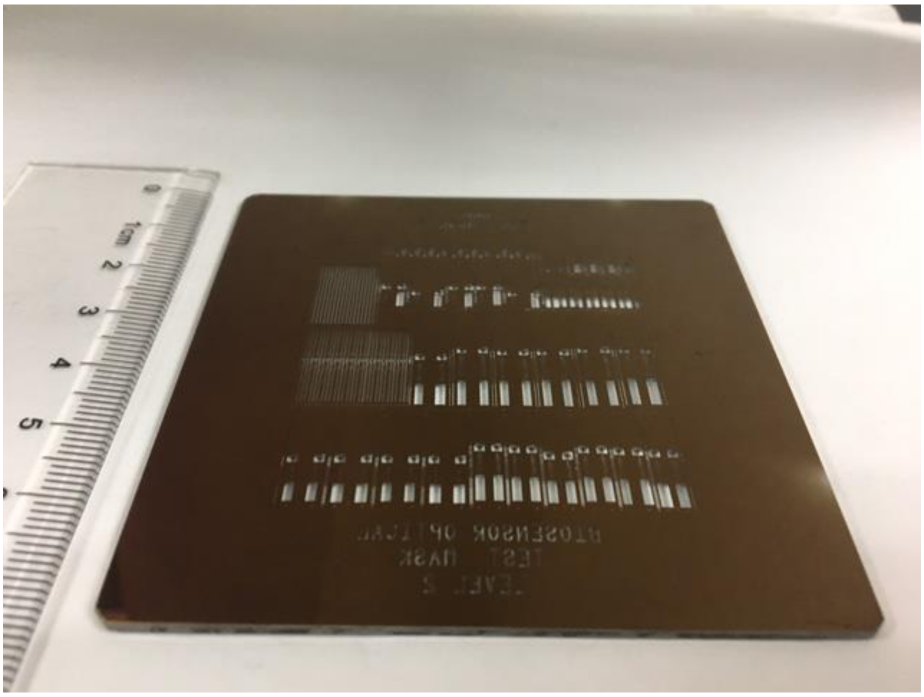

Figure 2: Set 1 Mask Layer 2 (2µm SU-8 taper layer) for Silicon core 0.32µm.

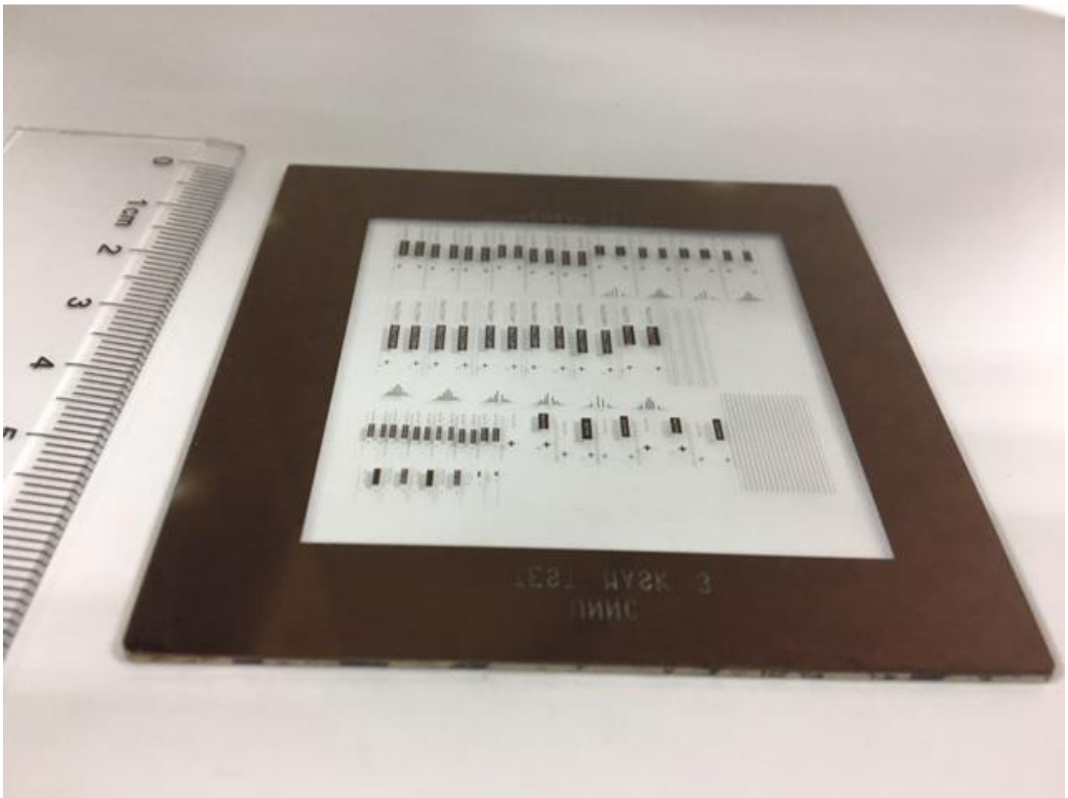

Figure 3: Set 2 Mask layer 2 -Plasmonic layer (gold layer) for Silicon core 0.32µm.

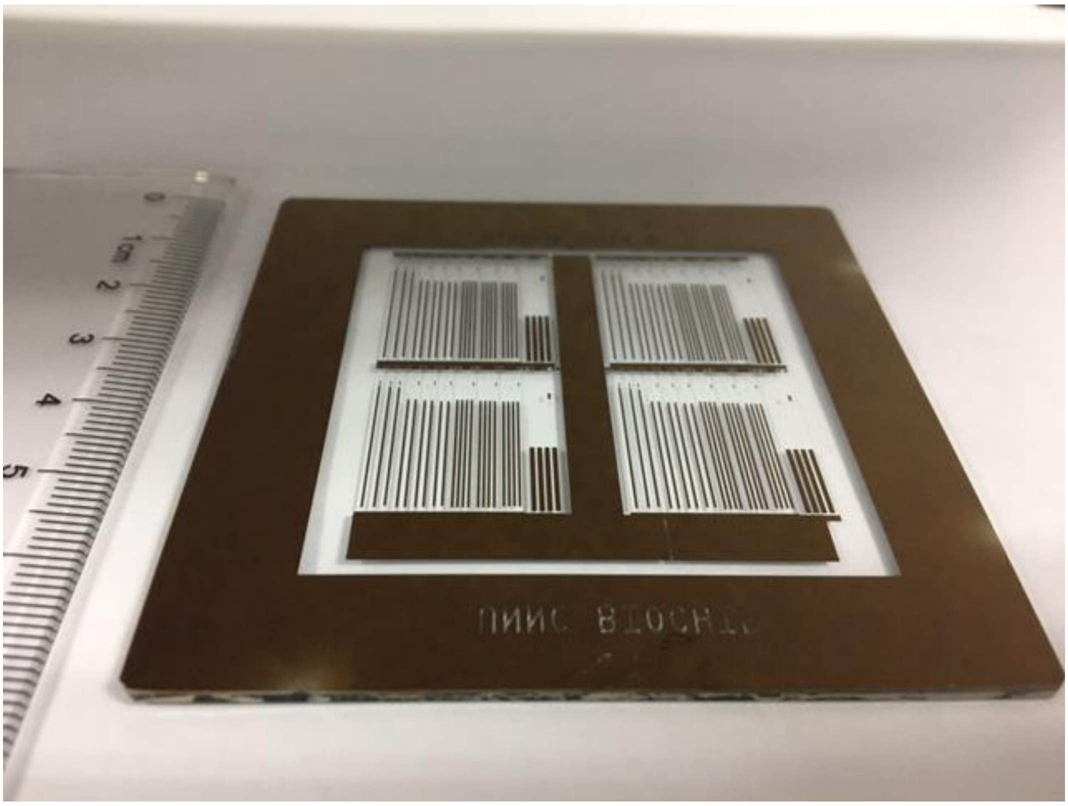

Figure 4: Set 3 Mask Layer 3 (Waveguide layer) for Silicon core 0.25µm.

Figure 5: Set 3 Mask Layer 2 (2µm SU-8 taper layer) for Silicon core 0.25µm.

Appendix J

Microfluidic Device Fabrication Protocol

Microfluidic Device Fabrication Protocol

Location B23 Cleanish Room

Equipment:

1kg 0.1kg silicone elastower .

Sylgard 184 1.1 kg Base and Curing Agent kit (Dow Corning, re-order from Farnell)
Scales (usually located on workbench opposite B23)
1x disposable pipette
1x disposable transparent plastic cup
1x disposable plastic fork
100ml unused Petri dishes
Vacuum Pump
60 C oven

Latex / Nitrile Gloves
0.5mm or 1.5mm Biopsy punch
Dissection microscope (currently in B14)
Scalpel and Tweezers
Compressed air (N_2)
Scotch Tape
Distilled H_2O
Disposable 5ml syringes

For microfluidic devices
1x Silicon wafer with microfluidic channel design embossed on upper surface

Mixing the PDMS

PDMS consists of two compounds, a Base monomer gel and a Curing Agent (cross-linking) liquid. These must be mixed in the ratio **10:1 by weight** NOT volume.

The quantity of PDMS to be mixed will depend on the intended application. Estimate the quantity needed before mixing in order to reudce wasted product.

For casting **microfluidic** devices on a Silicon wafer in a 100mm petri dish, **35g** will be needed
Thus the proportions should be (to within 0.5g) 4g Curing Agent : 40g Base

- Place the empty plastic cup on the scales and zero the display.
- Weigh out the Curing Agent using the pipette and zero again.
- Weigh out the Base directly from the container. Take care to avoid spillage or over-dispensing of volume.

- The PDMS must be thoroughly mixed for the curing agent to cross link with the base monomers. Whip the PDMS into a froth using the plastic fork for at least 5 minutes, making sure to pick up any adhering to the cup sides.

De-gassing

Now the PDMS is mixed but contains a considerable quantity of air in the bubbles. This must be removed.

- Open the vacuum pump and remove the middle shelf.
- Place the cup on the bottom of the pump and replace the lid.
- Switch on the pump using the floor extension lead.
- The valve at the top of the pump should be fully open, allowing atmosphere in. Slowly twist the valve to seal the pump and allow vacuum. The PDMS will begin to rise up the sides of the cup. Carefully align the valve so that the PDMS level is close to the top of the cup but is not overflowing.
- Leave the pump to run for at least 15 minutes until no bubbles remain.
- Switch off the pump and partially open the valve to admit atmosphere.
- Remove the lid once the vacuum seal has dissipated

Pouring and further de-gassing

If creating microfluidics devices take the Petri dish from the oven and place on the scales. Zero the reading and add 35g of PDMS.

- Pouring the PDMS will reintroduce bubbles, and a large air space will be present under the Silicon wafer. For each mould place the Petri dish in the vacuum pump and de-gas until there are no bubbles remaining near the device channels. The air space under the Silicon wafer will take some time to remove.
- When re-admitting atmosphere only open the valve slightly – a rapid pressure change can crack the Petri dish.

Curing

Place the Petri dishes into the oven and leave for at least 1 hour and ideally overnight.

Extracting the device

For a microfluidic channel the device must be cut out of the cured material. Cut parallel to the channel length and taper at the channel ends, leaving at least 3mm clearance around the channel. The Silicon cannot be damaged by the scalpel; cut all the way to the bottom. Use the tweezers to lever the device free of the mould.

Port Creation and surface cleaning

- Under the dissection microscope, and working from the channel side, punch through the PDMS at each port with the Biopsy punch.
- Use the syringe to drive dH_2O from the top side through the ports to remove any debris, and nitrogen dry the device.
- Apply and remove scotch tape 3x on channel side to clean the surface
- Extract a coverslip and clean with lens tissue

Bond according to protocol on Plasma Oven